N°d'ordre NNT : xxx

THESE de DOCTORAT DE L'UNIVERSITE DE LYON
opérée au sein de l'Ecole centrale de Lyon

Ecole Doctorale N° 162
Mécanique, Energétique, Génie civil, Acoustique

Spécialité de doctorat :
Mécanique des fluides

Soutenue publiquement le 3 Mai 2017, par :
ZHOU Lu

NUMERICAL MODELLING OF SCOUR IN STEADY FLOWS

Jury

LI Ming	Lecturer	University of Liverpool	Rapporteur
FUHRMAN David	Associate Professor	Technical University of Denmark	Rapporteur
ROCA Marta	Principal Engineer	HR Wallingford	Examinatrice
RIVIÈRE Nicolas	Professeur	INSA Lyon, LMFA	Examinateur
PERKINS Richard	Professeur	Ecole Centrale de Lyon, LMFA	Directeur de thèse

Abstract

This thesis describes the development of a numerical model for local scour caused by bed-mounted obstacles, combining the hydrodynamic and morphological processes.

The basis of the numerical model is the multiphase flow field solver in the open-source CFD toolbox OpenFOAM® which is released by OpenCFD Ltd. The hydrodynamic module of the model solves the Reynolds Averaged Navier-Stokes (RANS) equations with either a k-ε or a k-ω model. There are two interfaces in the simulation domain: the free surface between water and air, which is tracked using the Volume of Fluid (VOF) method, and the interface between the water and the sediment, which is represented by a finite area mesh constructed from the bottom boundary of the finite volume mesh. A morphological module which has been developed as part of the project consists of three components: a sediment transport model which includes suspended load and bed load transport; the Exner equation to compute the bed deformation, and a sand-sliding mechanism to restrict the bed slope angle to be smaller than the angle of repose. The morphological changes are incorporated into the hydrodynamic field through deformation of the computational mesh. Additional boundary conditions and parallel computing corrections are also added into the model.

Each individual part of the model has been validated separately with corresponding preliminary test cases including the rough wall functions, the performance of the VOF method, the suspended load transport model and the sand-sliding mechanism. The numerical model is then applied to study two-dimensional scour caused by a submerged jet issuing from an opening under sluice gate. Comparison of the simulation results with the experimental measurements proves the ability of the model for conducting two-dimensional simulations and the limitations of the model are also discussed.

Finally, the model is applied to study the three-dimensional flow field and scour formation around an obstacle in flow. Initially, the bed deformation is not activated in the model. The horseshoe vortex formed in front of an obstacle in water and the turbulent flow field around a cylinder on smooth and rough beds are simulated. Two types of simulations for the hydrodynamic module are used: a rigid lid simulation with a slip boundary condition to represent the air-water interface, and a free surface simulation including both the water and air domains with the free surface tracked by the VOF method. The influences of the

variation of the water depth on the flow field are identified and discussed. Comparison with the experimental data also confirms the importance of the water surface variation on the flow field. Next, the bed is allowed to deform in the model. The temporal development of three-dimensional scour around a cylinder on live-bed in a steady current is simulated. The development of the scour with time and the computed maximum scour depths in front of and behind the cylinder agree quite well with the experimental measurements. The influences of the scour process on the flow field are also studied and the performance of the numerical model is discussed.

Keywords: Local scour, Sediment transport, Free-surface flow, Mesh deformation

Abstract in French

Cette thèse porte sur le développement d'un modèle numérique de l'affouillement causée par des obstacles montés sur le lit, combinant les processus hydrodynamiques et morphologiques.

Le modèle numérique est basé sur le solveur de champ d'écoulement polyphasique de l'outil CFD open-source OpenFOAM® qui est distribué par OpenCFD Ltd. Le module hydrodynamique du modèle résout les équations de Navier-Stokes avec moyennes de Reynolds (RANS) et les modèles des turbulences k-ε ou k-ω. Il existe deux interfaces dans le domaine de simulation: la surface libre entre l'eau et l'air, qui est suivi par la méthode de Volume de Fluide (VOF); et l'interface entre l'eau et le lit du sédiment, qui est représentée par un maillage de surface finie déformable construit à partir de la limite en bas du maillage de volume fini. En outre, un module morphologique qui a été développé dans le cadre du projet se compose de trois composantes: un modèle de transport de sédiments comprenant la charge suspendue et le charriage; l'équation d'Exner pour mesurer la déformation du lit; et un mécanisme de glissement du sable pour limiter la pente du lit à être plus petite que l'angle de repos du sédiment. Le changement morphologique est incorporé dans le modèle hydrodynamique par la déformation du maillage. Des conditions limites spéciales et des corrections nécessaires pour le calcul en parallèle sont également ajoutées au modèle.

Chaque partie du modèle est validée séparément avec les tests préliminaires correspondants, y compris les fonctions de paroi rugueuse, les performances de la méthode VOF, le modèle de transport de charge suspendu et le mécanisme de glissement de sable. Le modèle numérique est ensuite appliqué pour étudier un affouillent bidimensionnelle causé par un jet immergé provenant d'une ouverture sous écluse. Comparaison des résultats de la simulation avec des données expérimentales prouve la capacité du modèle. Et les limites du modèle sont également discutées.

Enfin, le modèle est appliqué à l'étude du champ d'écoulement tridimensionnel et de la formation d'affouillement autour d'un obstacle dans l'écoulement. Tout d'abord, la déformation du lit n'est pas activée. Le tourbillon en fer à cheval devant un obstacle et le champ d'écoulement turbulent autour d'un cylindre sur un lit lisse ou rugueux sont simulés. Deux types de simulation pour le module hydrodynamique sont effectués: une simulation qui utilise une surface fixe et rigide pour représenter l'interface air-eau, et une

simulation incluant à la fois les domaines de l'eau et de l'air avec la surface libre suivie par la méthode VOF. Les influences de la surface libre sur le champ d'écoulement sont identifiées et discutées. La comparaison avec les données expérimentales confirme l'importance de la déformation de la surface libre sur le champ d'écoulement. Ensuite, le lit est autorisé à se déformer et le développement temporel de l'affouillement tridimensionnelle autour d'un cylindre sur le lit est simulé. Le développement temporel d'affouillement et le profondeur maximale du trou calculé devant et derrière le cylindre conviennent assez bien avec les mesures expérimentales. Les influences de l'affouillement sur le champ d'écoulement sont aussi étudiées et la performance du modèle numérique développé est discutée.

Mots-clefs: Affouillement, Transport de sédiments, Écoulement de surface libre, Déformation du maillage

Table of contents

List of figures

List of tables

Nomenclature

Roman Symbols

$\boldsymbol{e}$	Unit vector
$\boldsymbol{f}$	External volume force
$\boldsymbol{F}_D$	Drag force
$\boldsymbol{F}_f$	Friction force
$\boldsymbol{f}_\sigma$	Volume force of surface tension
$\boldsymbol{g}$	Gravity acceleration vector
$\boldsymbol{n}$	Normal vector
$\boldsymbol{P}$	Coordinate of a point or a cell centre
$\boldsymbol{q}_b$	Bed load transport rate vector
$\boldsymbol{R}$	Reynolds stress tensor
$\boldsymbol{S}$	(i) Outward-pointing face area vector; (ii) Strain rate tensor
$\boldsymbol{U}$	Velocity vector
$\boldsymbol{U}_f$	Friction velocity vector
$\boldsymbol{V_s}$	Fall velocity of the sediment particles
$\boldsymbol{v}$	Velocity of mesh points movements
$\boldsymbol{W}$	Gravity force
A	Amplification of the bed shear stress

a	(i) Constant for bed load calculation; (ii) Reference height for suspended load concentration profile
B	Constant for wall functions
C	Volumetric concentration of the suspended load
C_1	Turbulence closure coefficient
C_2	Turbulence closure coefficient
C_μ	Turbulence closure coefficient
c_b	Concentration of the suspended load near bed
C_D	Drag force coefficient
c_e	Equilibrium concentration of the suspended load at a reference level
C_f	Slop effect constant of the bed load transport formula
C_L	Lift force coefficient
c_p	Phase velocity of the surface wave
C_s	Roughness constant of wall function
C_t	Combined force coefficient
Co	Courant number
D	Deposition rate of the sediment
d	Diameter of the sediment particles
$d_\star$	Dimensionless diameter of the particles
E	Entrainment rate of the sediment
f	(i) Face of a cell; (ii) Frequency
H	Water level height
h	Bed level height
H_d	Maximum height of the sand dunes

H_s Maximum scour depth

k Turbulence kinetic energy

k_s Equivalent roughness height

m Mass

n Porosity of sediment bed

P Centre of a control volume

p Pressure

p_b Modified pressure

s Density ratio between sediment particle and water

St Strouhal number

T Dimensionless excess shear stress

t Time

U_τ Tangential velocity of the flow near the bed

V Volume

z_p Distance from the wall to the first centre near the wall

Greek Symbols

α (i) Volume fraction of the water phase; (ii) Turbulence closure coefficient

β (i) Bed slope angle; (ii) Turbulence closure coefficient

$\beta^\star$ Turbulence closure coefficient

Δ_D Height of the first cell node above the bed

Δ_d Reference height from the bed

ε Turbulence dissipation rate

γ Diffusion coefficient

κ von Kármán constant

κ_α	Curvature of free surface
λ	Wave length
μ_d	Dynamic friction coefficient
μ_m	Dynamic molecular viscosity
μ_s	Static friction coefficient
μ_t	Dynamic eddy viscosity
ν_m	Kinematic molecular viscosity
ν_t	Kinematic eddy viscosity
ω	Characteristic frequency of turbulence
Φ	Arbitrary physical property of the fluid
Φ_b	Non-dimensional form of the transport rate
ϕ_r	Repose angle of the sediment
ρ	Density
ρ_f	Density of the flow
ρ_s	Density of the sediment
σ_ε	Turbulence closure coefficient
σ_ω	Turbulence closure coefficient
σ_c	Schmidt number
σ_g	Geometric standard deviation on sediment grain distribution
σ_k	Turbulence closure coefficient
σ_T	Surface tension coefficient
θ	Shields parameter
θ_c	Critical Shields parameter
θ_{c0}	Critical Shields parameter for a horizontal bed

φ (i) Off-centring coefficient of the time discretization scheme; (ii) Angle between the bed shear stress and the direction of the steepest bed slope

τ_b Wall shear stress vector

τ_{bf} Bed shear stress related to bed form

τ_{bs} Bed shear stress related to skin friction

Superscripts

$\square^+$ Dimensionless value given in terms of wall coordinates

Subscripts

$\square_0$ Property for phase $\alpha = 0$

$\square_1$ Property for phase $\alpha = 1$

$\square_b$ Related to bed or to bed load

$\square_c$ Critical value of a property

$\square_e$ Equilibrium property

$\square_m$ Molecular property

$\square_t$ Turbulent property

Acronyms / Abbreviations

CFD Computational Fluid Dynamics

DNS Direct Numerical Simulation

FAM Finite Area Method

FFT Fast Fourier Transform

FVM Finite Volume Method

LDA Laser-Doppler Anemometer

LDS Laser Distance Sensor

LES Large Eddy Simulation

PISO Pressure Implicite with Splitting of Operators

PIV Particle Image Velocimetry

RANS Reynolds Averaged Navier-Stokes

SIMPLE Semi-Implicit Method for Pressure-Linked Equations

URANS Unsteady Reynolds Averaged Navier-Stokes

VOF Volume of Fluid Method

Chapter 1

Introduction

1.1 Motivations and Objectives

On June 19, 1938, the Custer Creek train wreck, the worst rail disaster in Montana history, happened when a bridge, whose foundations were washed away by a flash flood, collapsed beneath Milwaukee Road's Olympian as the train crossed Custer Creek, and killed at least 47 people. On the night of 4 March 2001, the Hintze Ribeiro disaster occurred when the Hintze Ribeiro Bridge, made of steel and concrete, collapsed in Entre-os-Rios, Castelo de Paiva, Portugal, killing 59 people, including those in a bus and three cars that were crossing the Douro river. According to the national authorities, the collapse was caused by "two decades of uncontrolled sand extraction, which compromised the stability of the bridge's pillars, together with underestimating the warnings from divers and technicians" (Sousa and Bastos, 2013). Only the sand extractors were prosecuted and sued. The Schoharie Creek Bridge collapse on April 5, 1987 is another example of disasters caused by bridge scour. So it is important to be able to predict the location and depth of scour holes that might develop in different flow conditions.

Scour can occur wherever hydraulic structures such as bridge piers and offshore structure foundations cause a local acceleration of the flow, generating vortex structures close to the bed, creating high pressure gradients in the surrounding sediments. Local bed scour around objects has been a continuous research interest and numerous experimental and numerical studies have been done about this subject. The physical modelling of this phenomenon produce more reliable results but sometimes it is hampered by problems of scaling. For non-cohesive sediment situations, if we reduce the scale too much, the scaled sediment will become cohesive and the behaviour will change. Moreover, it is difficult to maintain both the Reynolds number and the Froude number unchanged. And the costs to conduct such

(a)

(b)

Fig. 1.1 Bed scour formed around obstacles in flow: (a) scour around a circular cylinder bridge pier (from http://www.thermotun.com/), (b) scour around a rectangular cylinder bridge pier (from http://thestagnationpoint.blogspot.fr/).

tests can be very high in some situations. So numerical simulations offer, in principle, an interesting alternative.

However, numerical modelling of the growth of a scour hole poses its own challenges. First of all, the flow field itself will be a turbulent flow, often highly three-dimensional, with a free surface between water and air. Secondly, the growth of a scour hole is a combination of many complex processes. The depth and position of scour holes depend on the processes of sediment erosion, transport and deposition which in turn depend on a range of parameters including the sediment size distribution, the form of the obstacle, the depth and velocity of the flow, etc. Finally, the coupling between the flow field and the bed erosion is hard to implement in a numerical simulation but has a strong influence on the scour development. The geometry of the flow field will change with the sediment transport processes and the bed erosion. The sediment entrained and suspended in the flow will also influence the properties of the flow field. Even though a lot of studies have been performed to investigate the coupling mechanism between the flow field and sediment transport processes, many of these influences are still unclear and therefore difficult to implement precisely in numerical models.

The main objective of this thesis is to establish a numerical model which is able to predict the position and depth of scour holes and the temporal development of local scour around objects. The numerical model we have developed consist of two modules – a hydrodynamic module which simulates the flow field, including the influence of the free surface effect and the turbulence of the flow field, and a morphological module which calculates the sediment transport, including the suspended load transport and the bed load transport, and imposes the bed deformation. The coupling between the flow field and the bed deformation is implemented through dynamic deformation of the computational mesh for the flow field. The numerical model established should also require moderate calculating resources whilst still providing practically useful results, so that it can be used in the future in engineering practice as a tool to guide the construction and protection of structures in flow. The model can also be a potential research tool for simulating and studying scour formation and developments in various situations.

1.2 Methodology of the Study

This study is a numerical study of the local bed scour and a numerical model established for both two dimensional and three dimensional simulations is based on the platform of an open source computational fluid dynamics (CFD) code named OpenFOAM® . OpenFOAM® is developed primarily by OpenCFD Ltd since 2004, distributed by OpenCFD Ltd and the OpenFOAM® Foundation. It provides a platform for numerical solution of

partial differential equations involved in CFD and its dynamic mesh feature provides the possibility of cooperating the bed deformation into the flow field simulation. Moreover, the accessibility of the source code of OpenFOAM® also facilitate the addition of features which are necessary to built the model. The version FOAM-extend-3.1 is used which is released by the OpenFOAM® Extend-Project. The goal of the Extend-Project is to open the OpenFOAM® CFD toolbox to community contributed extensions in the spirit of the open-source development model.

The flow field is solved using the multiphase flow solver *interDyMFoam* provided by OpenFOAM® . On to this we have added components for computing sediment transport and evolution of the bed. The performance of the model is tested by the experimental cases selected from the literature. Firstly, some individual components of the model are tested with preliminary test cases. Then the overall performance of the model is tested by simulating the development of a complex three dimensional scour around a cylinder in current flow.

Most of the simulations were done with the computing clusters in PMCS2I (Pôle de Modélisation et de Calcul en Sciences de l'Ingénieur et de l'Information) of Ecole Centrale de Lyon. Multi-processor computing server *Kepler* and *Newton* were used. Therefore, most of the simulations were performed in parallel to accelerate the computation especially for the three dimensional simulations.

1.3 Outline of the Thesis

The rest of the thesis is organized as follows.

In next section, chapter 1 concludes with a literature review of previous experimental and numerical studies of scour formed in different flow conditions.

Chapter 2 gives a brief introduction of the hydrodynamic module of the model. The governing equations of turbulent flow field with free surface effects and the numerical methods used for solving them are introduced. The special treatment for rough boundaries is also discussed. Preliminary test cases are introduced to test the performance of several crucial components of the hydrodynamic module.

Chapter 3 elaborates the morphological module of the model. The sediment transport models, including the suspended load and the bed load, the calculation of bed level changes and bed deformation mechanisms are described. The chapter ends with a presentation of the overall simulation flow chart and the parallelization of the model.

Chapter 4 describes the numerical simulation of a two dimensional bed scour caused by a submerged jet. The details of the laboratory study and the set-ups of the simulation are

introduced. The simulation results are compared with the experimental measurements to validate the model.

Chapter 5 presents the application of the model to simulate three dimensional flow field and scour around an obstacle in a current. By analysing the simulations results for the horseshoe vortex in front of a cubic obstacle and for the flow field around a cylinder, the importance of including the free surface in the simulation is discussed. The numerical simulation for the scour formed around a cylinder is presented and the influence of the scour hole on the flow field is studied. The simulated temporal development of the scour profile is presented and compared with the experimental measurements and the performance of the numerical model is discussed.

Chapter 6 offers some conclusions and perspectives.

In the appendices, the derivation of the transport equation for volume fraction coefficient used in this thesis and the details of the sand-sliding mechanism implemented in the model are given.

1.4 Review of Previous Research

A great deal of research has been devoted to the problem of understanding and modelling scour around structures, using both experimental and numerical approaches. The model built in this work has only been applied to study a two dimensional scour caused by submerged jet and a three dimensional scour around a single cylinder in current. But it has the possibility to be applied in the future to study scour formed in other situations. So in this literature review, different studies addressed the problem of scour from currents, from waves or from the combined action of the two, formed in various conditions are introduced. Many existing important books and papers about researches of local scour provide very good summaries of previous research such as Kraus (1988), Hoffmans and Verheij (1997), Whitehouse (1998), Melville and Coleman (2000), Sumer and Fredsøe (2002), van Rijn (2005) and van Rijn (2013).

1.4.1 Experimental and Field Studies

Here we first give a brief literature review of the experimental research both in the laboratory and in the field on local scour in various conditions.

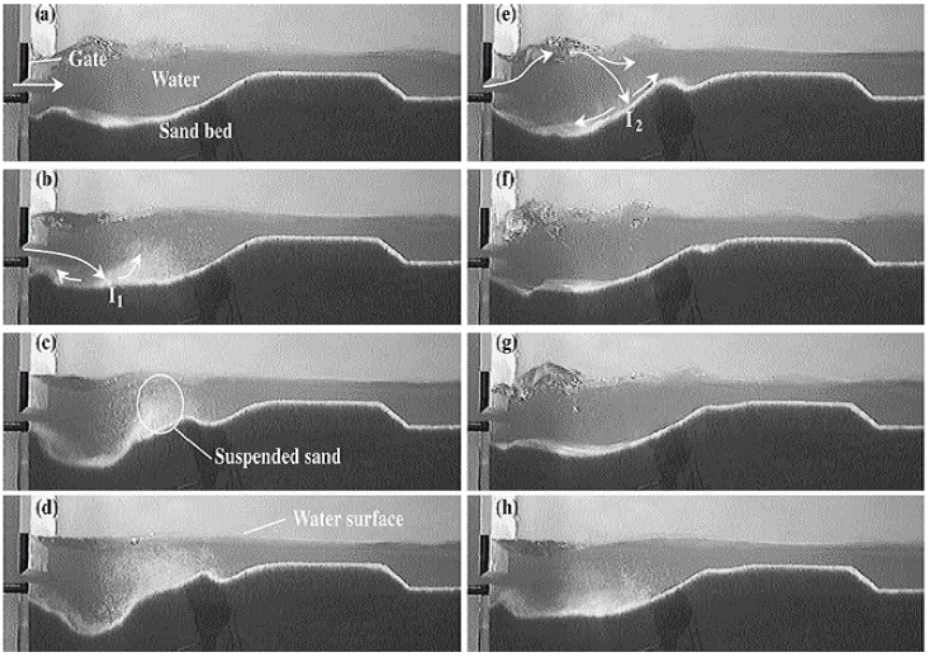

(a)

(b)

Fig. 1.2 Experimental studies of the local bed scour: (a) scour caused by a submerged jet, from Balachandar et al. (2000), (b) scour around a cylinder, from Guo et al. (2012).

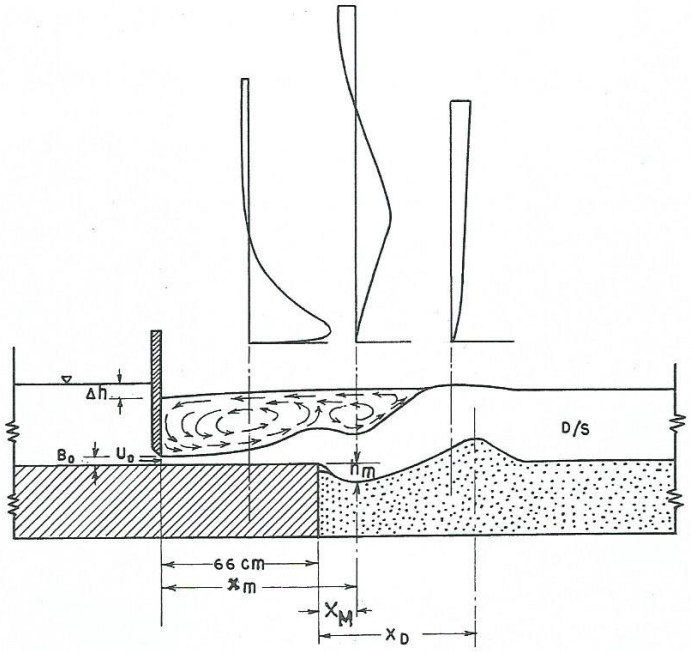

Fig. 1.3 Flow pattern and scour downstream of a submerged jet issuing from a sluice opening over an apron, from Chatterjee and Ghosh (1980).

Scour downstream of sluice gates or barrages

The local scour downstream of a structure such as a barrage or a sluice gate in a unidirectional current has been studied by many researchers. The scour that occurs in this condition can sometimes be treated as a two-dimensional scour as the variation of the flow field and the scour depth in the third direction are often very small compared with those in the other two directions. Usually, the maximum scour depth in the equilibrium state and the temporal development of the scour profile are the primary objectives of study.

Breusers (1965) and Breusers (1967) studied experimentally the downstream scour holes in a bed with non-cohesive sediment caused by the flow over and under an estuary closure structure in tidal channels. They propose an empirical relationship for the time dependence of the development of scour depth in this condition:

$$H_s = h(\frac{t}{T_s})^{0.38} \tag{1.1}$$

where H_s is the maximum scour depth, h is the upstream water depth, T_s is the time at which $d_s = h_0$. The importance of the time scale in the design of structures where a temporary exposure of the bed to scouring effects occurs is stressed and some experimental data on this time scale and the conformity between various experiments are given.

Chatterjee and Ghosh (1980) and Chatterjee et al. (1994) measured the scour hole formed in a non-cohesive bed caused by a submerged jet issuing from a sluice opening over an apron and empirical relationships between the maximum scour depth and time were also given. The velocity field of the submerged jet when the scour hole reaches the equilibrium state were also measured and studied.

Balachandar et al. (2000) also conducted experiments to study local scour occurring downstream of a submerged jet under sluice gate and they observed that the scour process consisted of two phases – a scouring phase, in which the jet is directed towards the bed so that the scour hole develops and a refilling phase when the jet is directed towards the free surface and sediment that has been eroded and then deposited falls back and refills the scour hole. These two phases alternate until an equilibrium situation is attained.

Subsequently, Faruque et al. (2006), Sarathi et al. (2008) and Sui et al. (2008) performed similar experiments but as a three-dimensional problem, with an axisymmetric jet to investigate the influence of channel width, tail-water depth and densimetric Froude number on the equilibrium scour profile.

Scour near seawalls and breakwaters

Seawalls and breakwaters are built to protect the mainland against retreat or inundation. The scour near these types of hydraulic structures has also been widely studied using field data and experiments. In this condition, scour can be formed at the toe of the wall or on both ends of the wall. The scouring in this condition is a combination of several processes. Firstly, the interaction between the incident and reflected flow can cause a wave-induced drift velocity above the sand bed near the structure, putting the sediment into suspension. Secondly, besides the transport of the suspended sediment induced by the long-shore current, wave breaking at or near the wall also enhances the offshore-directed transport of the sediment. Finally, the increased turbulence and circulations generated at the down-drift end of the wall will also lead to scour and retreat of the shoreline.

Irie and Nadaoka (1984) and Irie et al. (1986) presented two and three dimensional experiments on scour in front of wall-type breakwaters and rubble-type breakwaters. The relation between flow condition and the formation of different types of scour is discussed and the formula for estimating maximum scour depth and position were given.

Fowler (1992) presented laboratory experiments consisting of 22 tests to evaluate methods for estimating wave-induced scour depth at vertical seawalls. In the study, both regular and irregular waves were used to move sand placed on the seaward side of a simulated vertical seawall. All of the bottom profiles generated by the 18 irregular wave tests in the study supported a rule-of-thumb method, which states that maximum scour depth will be less than

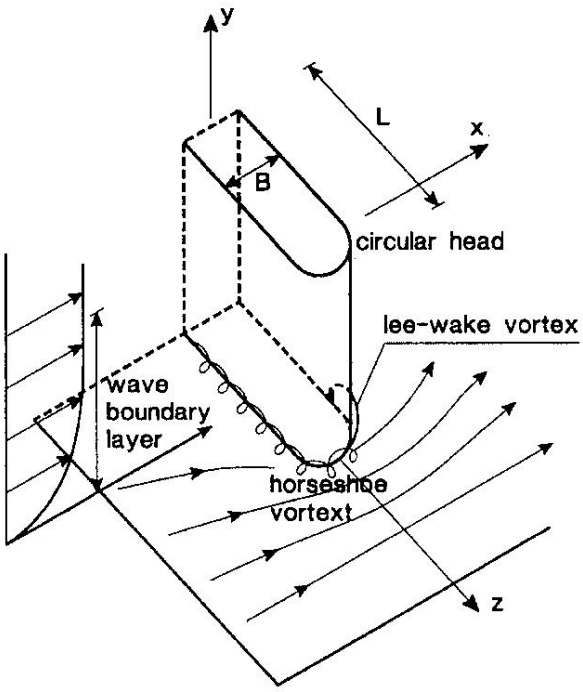

Fig. 1.4 Flow pattern near tip of wall-type breakwater, from van Rijn (2013).

or equal to the incident unbroken deep water wave height. To examine the effects of regular versus irregular waves in movable-bed laboratory studies, four additional test cases were run using regular waves. In each of the four regular wave cases, scour depth increased by approximately 15 percent compared with corresponding irregular wave tests.

Hughes and Kamphuis (1996) presented experiments of scour at inlet navigation structures including ebb and flood flows. A new scour mechanism was identified for situations where the ebb-flow discharge is redirected by a navigation structure. As the ebb flow is deflected, flow velocities increase and a scour trench forms adjacent to the jetty. In this paper, formulations from inviscid jet theory were used to develop a prediction for maximum flow velocity in terms of entrance channel velocity and inlet geometry. A simplified scour prediction method was also provided. Preliminary conclusions were offered concerning the scour produced by flood flow combined with waves.

Sumer and Fredsøe (1997) presented the results of an experimental investigation on near-bed flow patterns, bed shear stress amplification and scour around the head of a vertical-wall breakwater, using regular waves. The Keulegan-Carpenter number, based on the diameter of the breakwater head, was found to be the major parameter that governs the flow and the equilibrium scour depth. An empirical formula was proposed for the width of the protection layer as a function of the Keulegan-Carpenter number. Also, the effects of head shape,

the angle of attack and the presence of a co-directional current were investigated. As a complement of this study, Fredsøe and Sumer (1997) dealt with the case of rubble-mound breakwater based on data of Lillycrop and Hughes (1993).

Rahman and Haque (2003) presented field data of scour depths near abutment-type structures collected from major rivers in Bangladesh and modified the original Lacey formula by introducing the structure length as a parameter.

Scour around vertical cylinders

Studies of the scour around vertical cylinders are usually divided into two flow conditions which are referred to as clear water scour and live-bed scour. In the clear water scour condition, there is no sediment transport upstream of the cylinder whilst in the live-bed scour condition, sediment transport occurs even without cylinders in flow. Both types of scour have been investigated in studies like those of Lim (1997) and Kothyari et al. (1992). Detailed studies based on field measurements and experiments can be found in Melville and Sutherland (1988), Melville (1997) and Melville and Coleman (2000). The flow pattern around a cylindrical pipe is shown in Fig. (1.5) and is characterized by (van Rijn, 2013):

- Water surface roller in front of the pipe.
- Downward flow in front of the pipe.
- vortex-shedding in the separation zone.
- Wake flow downstream of the pipe.
- Generation of horseshoe-vortices in the scour hole.

Breusers et al. (1977) analysed field and experimental data and found that, for a single pipe in uniform bed material, the maximum scour depth is influenced by the pipe diameter, the velocity and the depth of the flow, the shape of the pipe and the angle of incidence of the flow. They also proposed a formula to estimate the maximum scour depth with these parameters.

Rance (1980) studied the maximum scour depth around piles of different cross-sections (circular, hexagonal and square piles) induced by waves and currents together. He proposed formulae to estimate the relationship between the maximum scour depth and the diameter of the piles with different cross-sections.

Sumer and Fredsøe (1998) and Sumer and Fredsøe (2001b) studied the wave-induced scour around a large circular cylinder and a group of vertical piles. For a single cylinder, rigid and movable bed experiments were performed and the velocities in the flow field

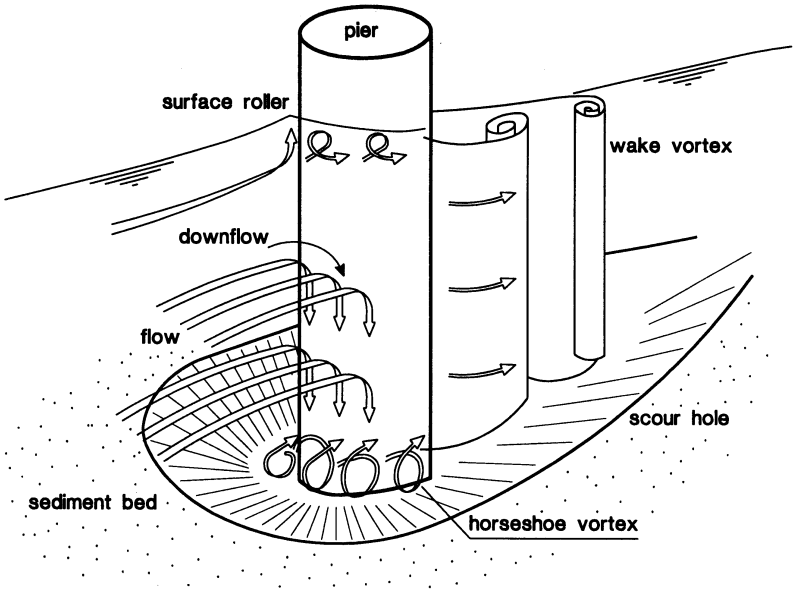

Fig. 1.5 Flow pattern and scour near a vertical pile, from van Rijn (2013).

were measured. As for the scour around a pile group, various configurations were tested in side-by-side and in-line arrangements for two and three piles. They concluded that the spacing between the piles influences the scour depth and the side-by-side arrangements will increase the scour depth while the in-line arrangement will decrease the scour depth. Sumer and Fredsøe (2001a) also studied the scour around a vertical pile but with waves in combination with current and proposed empirical expressions relating the scour depth to the Keulegan–Carpenter number.

Oscar et al. (2008) presented experiments to study the characteristics of developing scour-holes around a sand-embedded circular cylinder. In the experiment, measurements of the scour hole were taken by a Laser Distance Sensor (LDS) in different azimuthal half-planes in order to study the spatio-temporal variation of geometric properties in developing scour hole. This measurements showed that scour starts upstream and on the sides of the cylinder and then surrounds the cylinder, propagating to the region behind the cylinder. Slopes of the developing scour-holes presented three regions with different inclinations, which were attributed to vortex action. This work also provided an experimental database for numerical simulation.

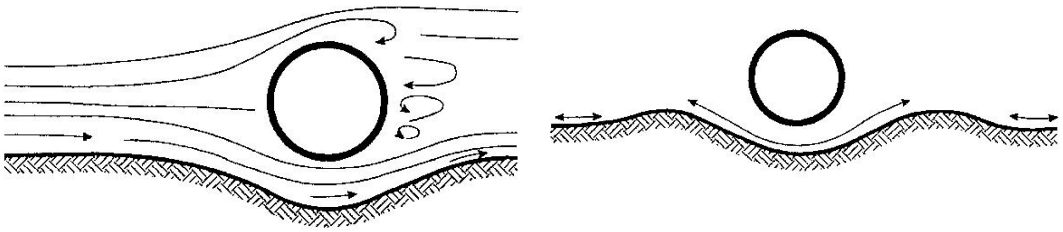

(a) Scour in unidirectional flow (b) [Scour in oscillatory flow

Fig. 1.6 Flow pattern and scour near horizontal pipelines, from van Rijn (2013).

Scour under horizontal cylinders

The presence of the pipeline in the flow near the bed changes the local flow field. The velocity near the pipe will initiate and intensify the erosion on the bed. The mechanisms can be divided into three groups (van Rijn, 2013):

- Flow induced pressure differences: if the flow is perpendicular to the pipeline, there is a pressure difference between the upstream and the downstream part of the pipeline. These pressure differences can cause movement of the ground water which carries the sediment away.
- Vortices near the pipeline: the vortices generated upstream and downstream of the pipeline can transport the sediment away as suspended load and bed load.
- Imperfections in the seabed near the pipeline: The variations of the bed near the pipeline may result in the presence of gaps between the pipeline and the bed which enhance the erosion of the bed under the pipeline.

Kjeldsen et al. (1973) performed flume experiments with uniform flow near pipelines resting on the bottom. Two different flumes with uniform flow perpendicular to the longitudinal axis of the pipes were used for the experiments. On the basis of these experiments the following has been estimated for uniform flow: 1. The development with time of the scouring processes. 2. The different scour patterns near the pipes when they are resting on the bottom and when they are more or less buried in the sand. 3. Possibilities with relevant parameters to extend the observed results for use on prototypes.

Sumer and Fredsøe (1990) present the results of an experimental investigation on scour below pipelines exposed to waves. They point out that the effect of the lee-wake of the pipe is the key element in the scour process, and they demonstrate that the Keulegan-Carpenter number is the main parameter that governs the equilibrium scour depth. In the paper, an equation is established to relate the equilibrium scour depth with the Keulegan-Carpenter

number for the live-bed situation and for a pipe in contact with the bed. The influence of the Shields parameter on the final scour depth is found to be quite weak. It is also found that the surface roughness of the pipe has practically no influence on the scour process. The pipe position with respect to the bed appears to be an important parameter in determining the equilibrium scour depth.

Çevik and Yüksel (1999) describe experimental investigations of scour depth around offshore pipelines with respect to water depth under regular waves. Based on the experimental measurements of velocities and beach profiles, a new equation is proposed, relating the maximum equilibrium scour depth to the modified Ursell number for the live bed condition around a rigid pipe fixed initially in contact with the bed.

Moncada-M and Aguirre-Pe (1999) present experimental research on the scour produced under a pipe exposed to a stream. Experiments were performed in a rectangular laboratory channel where the bed was composed of loose granular particles of two different diameters. Pipes of four different sizes were located either on top of the bed or at varying distances above it. They found that the Froude number was an important parameter in the definition of the scour process while the Reynolds number of the pipe exerts a negligible influence on the scour process. Good correlations between the Froude number of the flow and the most important characteristic dimensions of the scour hole were obtained, and generic relationships that allow the prediction of the characteristic dimensions of the scour hole were proposed.

A pipeline laid close to seabed and exposed to the action of currents can also vibrate and the local scour may be coupled with vortex-induced vibration. Many researchers have investigated the influence of the coupling between the vortex-induced vibration and scour.

Sumer et al. (1988) describe an experimental investigation of the scour with the pipe vibrating only in the transverse direction. The experimental results showed that the vibration of the pipe close to an erodible sand bed is ultimately dominated by vortex shedding due to the extra soil erosion, even though the pipe is placed very close to the original undisturbed bed. Recently, local scour around a transversely vibrating pipeline has been investigated experimentally by Gao et al. (2006).

1.4.2 Numerical Studies

Recently, with the rapid development of CFD, numerical study of local scour has become more feasible and hence more popular. Numerical models for simulation of scour usually consist of two distinct elements: a hydrodynamic module to solve the fluid flow, and a morphological module to deal with the sediment transport and bed erosion.

The hydrodynamic module solves the Navier-Stokes equations for the flow field. The sediment-laden flow can be treated as a two-phase flow, which includes the water phase

and the sediment phase, or as a one-phase flow, in which the two phases are modelled as a mixture. The two-phase flow model can be categorized into the Euler-Euler type and the Euler-Lagrange type. The Euler-Lagrange type of model treats the sediment phase as motions of a certain number of individual particles. This approach succeeds in capturing the individual and collective dynamics of natural sand grains and many very good numerical models of the Euler-Lagrange type have been proposed recently such as those by Li et al. (2014), Finn et al. (2016) and Sun and Xiao (2016). However, this approach requires rather a large number of particles to simulate practical problems and this can necessitate large computational resources and times. The Euler-Euler approaches describes the dispersed phase in a similar way to that used for the continuous phase and efforts have been directed to this type of model like Li et al. (2008), Jha and Bombardelli (2010) and Chen et al. (2011). However, as pointed out in Chen et al. (2011), the Euler-Euler type of two-phase model is usually very complicated. The two-phase model needs to solve the continuity and momentum equation for both of the two phases and the most difficult part is to properly describe the turbulence characteristics of the two phases. So in hydraulic and coastal engineering applications, including scour hole estimations, the single phase model is more commonly used.

The most popular single-phase model is to neglect the effects of the dispersed phase on the continuous phases and solve the volumetric concentration of the dispersed phase using an advection-diffusion model. The advection-diffusion model has been successfully applied to many numerical study of scour problems, for example, in the studies of Liang et al. (2005b) and Roulund et al. (2005). However, it should be noted that the advection-diffusion model which neglects the effects of the dispersed phase is only valid for dilute problems where the suspended load concentration is not large enough to influence the principle properties of the flow field. In this thesis, the advection-diffusion model is chosen, as in most of the scour problems, the dilute flow condition can be satisfied and the bed load transport has much more influence than the suspended load transport on the form and depth of scour hole. Moreover, the model established should only require limited calculating resources if it is to be useful for solving practical problems.

Another issue concerning the hydrodynamic module is whether to include free surface effects in the model. The interface between the water and air varies when the flow encounters the obstacle and causes variations in the water depth. If the variation is not very small compared with the water depth, this can have an important influence on the flow field and thus on the scour formation. This situation is very common in scour problems as the obstacles that cause the scour can have very large dimensions and the variation of the flow depth can be quite strong. Recently, many numerical models for scour or bed erosion problems include the free surface effect in the model, such as Liu and García (2008). In this thesis, as in almost all

the simulation cases, the flow is quite shallow compared with the obstacles dimension, so the free surface effect is included in the model. An analysis of the free surface variation and the influence of the free surface on the simulation results of the flow field has also been given.

The last important issue concerning the hydrodynamic module is to properly choose the turbulence closure for solving the Navier-Stokes Equations. The flows in scour problems are often turbulent flows. A direct numerical simulation (DNS) (Orszag, 1970) of the full Navier-Stokes equations will resolve the whole range of spatial and temporal scales of the turbulence, but the computational meshes must be fine enough to resolve the smallest dissipative scale (Kolmogorov microscales), which for the problem that interests us, can be of the order of 1×10^{-5} m. The computational resources required to solve this sort of problem exceed what is currently practical, so this approach is not suitable for those problems. The most commonly used turbulence closures are Reynolds Averaged Navier-Stokes (RANS) and Large Eddy Simulation (LES). Various studies have investigated the influence of the choice of turbulence model on the results of scour simulations. Aghaee and Hakimzadeh (2010) simulated the scour caused by bridge piers with both RANS and LES turbulence models and concluded that although the LES simulates the flow field more accurately, especially for the periodic behaviour of the vortex shedding, a RANS model was generally sufficient to give a satisfactory estimate of scour development. In this study, therefore, we have used a RANS turbulence model.

The morphological module for scour simulations generally includes a sediment transport model and a mass conservation equation (the Exner equation) to calculate the bed level change. There are many possible choices for the sediment transport model which usually includes both suspended load and bed load. As mentioned before, the suspended load in scour problems is often solved by the advection-diffusion model with a reference concentration given at a certain reference height. The reference concentration is usually given by empirical models of sediment entrainment. Two entrainment models commonly used can be found in Rijn (1984) and García and Parker (1991).

To determine the bed load, many empirical equations from laboratory flume data have been given by previous studies. Most of them depend on the bed shear stress τ_b, i.e. the Shields parameter θ, the density ratio between the sediment and the flow $s = \rho_s/\rho_f$ and the sediment particle diameter d. In order to facilitate the expression, a non-dimensional form of transport rate which is referred as the Einstein number in some papers Φ_b is defined:

$$\Phi_b = \frac{\|\boldsymbol{q}_b\|}{\sqrt{(s-1)gd^3}} \tag{1.2}$$

Table 1.1 Existing formulas to estimate bed load, from Hassanzadeh (2012).

Author	Formula
Meyer-Peter(1934)	$\Phi = 8(\theta - 0.047)^{1.5}$
Shields(1936)	$\Phi = 10C_{z\star}(\theta - 0.076)\theta^{1.5}, \quad C_{z\star} = \frac{C_z}{s\sqrt{g}}$
Einstein-Brown(1942)	$\Phi = 23.6\theta^3$
Kalinske(1947)	$\Phi = 10\theta^{2.5}$
Bonnefille(1963)	$\Phi = 5.5\theta^{1.5}(4.26\theta^{0.5} - 1)^{1.25}$
Hassanzadeh(2007)	$\Phi = 24\theta^{2.5}$

where $\boldsymbol{q}_b$ is the bed load transport rate with dimension and Some of the commonly used bed load transport models are presented in Table 1.1. The Shields parameter θ is defined as:

$$\theta = \frac{\tau_b}{\rho_f(s-1)gd_{50}} \tag{1.3}$$

where τ_b is the wall shear stress tangential to the bed.

Some of important and very often referenced papers of numerical simulation of local scour in recent years are briefly summarized below.

Brørs (1999) proposed a numerical model to simulate the flow and scour at pipelines. The flow field was computed using a k-ε turbulence closure model and the sediment transport was computed using the model proposed by Soulsby (1993). Differences between the measured and computed flow fields were attributed to lack of resolution in the finite element grid.

Liang et al. (2005a) and Liang et al. (2005b) successfully simulated the development of a scour hole underneath an offshore pipeline using a RANS model with k-ε and k-ω closure models, and an LES model with the Smagorinsky sub-grid scale model for the flow field. The suspended sediment transport was modelled using an advection-diffusion model and the bed load transport was calculated using the model proposed in Van Rijn (1987). In addition, a sand-sliding mechanism was included to smooth the irregular bed level change. The results showed that the k-ε model is sufficient for scour prediction, and that a sand-sliding mechanism is necessary to produce a reasonable scour profile.

Roulund et al. (2005) conducted a numerical and experimental investigation of flow and scour around a circular pile exposed to a steady current. The flow was simulated using the hydrodynamic model EllipSys3D with a k-ω turbulence model, and the free surface effects were neglected. And the bed load sediment transport model proposed by Engelund and Fredsøe (1976) was used and generalised to account for the three dimensional effects as well

as te bed-slope modifications. They did not consider the suspended load transport in their model and a steady-state flow model was used which didn't account for the unsteady effects in the flow field.

Liu and García (2008) developed a numerical model to simulate local scour around bridge piers using the volume-of-fluid (VOF) method to track the free surface between water and air, and the moving mesh method to modify the simulation domain. They also chose the k-ε model and the bed load sediment transport model proposed by Engelund and Fredsøe (1976). The simulation results for the flow field and scour profiles agreed well with the measurements. However, their model did not include a sand-sliding mechanism to limit the bed slope at scour holes.

Khosronejad et al. (2012) carried out numerical simulations and laboratory experiments on scour caused by different forms of bridge piers using the fluid-structure interaction curvilinear immersed boundary (FSI-CURVIB) method with a k-ω closure model; the sediment transport modelling was similar to that described in Khosronejad et al. (2011). Their study shows that the pier bluntness has an important influence on the predictive capabilities of the simulation model.

Fuhrman et al. (2014) and Larsen et al. (2016) established a fully-coupled hydrodynamic/morphological numerical model for simulating wave-induced and wave-plus-current scour beneath submarine pipelines. The model solves the RANS equations with k-ω turbulence closure for the hydrodynamic component on a computational mesh where near-bed cells below a reference level are removed and the morphological component of the model is solved separately on a surface mesh which is the same technique used by Jacobsen et al. (2014). The bed load transport model used is the same with the one described by Roulund et al. (2005) and the suspended load is also included in the model. Simulations involving waves over a wide range of Keulegan-Carpenter number combined with current flows with different current-strength were conducted using the model and a new and generalized expression for the scour time-scale in combined wave-plus-current environments was proposed.

Baykal et al. (2015) and Baykal et al. (2017) studied the flow and scour around a vertical pile exposed to current flow or waves and the backfilling process of the scour hole with the same numerical model used in Fuhrman et al. (2014). The simulation results were compared with the experimental measurements from Roulund et al. (2005), Sumer et al. (1997) and Sumer et al. (2012) to validate the model and the influences of the suspended load, the unsteady flow features such as the horseshoe vortex and lee-wake vortices on the scour were discussed.

It should be noticed that the numerical studies of Liu and García (2008), Fuhrman et al. (2014), Larsen et al. (2016), Baykal et al. (2015) and Baykal et al. (2017) were all conducted

using the CFD tool OpenFOAM® . Many commercial software packages have also been adapted to simulate scour, and some have given reasonable results.

Wang and Jia (1999) simulated the scour hole developing around bridge piers using CCHE3D and they examined the importance of various flow effects on sediment transport.

Boroomand et al. (2007) modelled an offset jet using FLUENT with a two-phase model. The model calculated the scour development from a force balance on individual particles involving the buoyancy, drag, lift, virtual mass and particle interaction forces and solved the continuity and momentum equations for each phase. The results are quite good except for the sediment concentration near bed.

Abdelaziz et al. (2010) used FLOW3D software to simulate the flow field, and a sediment transport model integrated into the model to simulate scour. The bed slope effects and a sand-sliding mechanism were also taken into account. They got good agreement with data for the complex flow field and scour depth, but the slope downstream of the deposition dune may be over-estimated.

Chapter 2

Modelling Free Surface Turbulent Flows

This chapter provides of a brief introduction to the hydrodynamical module of the numerical model. The hydrodynamical module described in this thesis has been performed using the open-source computational tool OpenFOAM® to provide a numerical solution of the Navier-stockes equations. More detailed information of OpenFOAM® and of the multi-phase flow solver *interDyMFoam* can be found in Jasak (1996) and Rusche (2002). The tool has been adapted in a number of ways to solve the equations to describe the flow field and those adaptations are presented in details in Chapter 3. In this Chapter, first of all, we summarise the governing equations of the model including a brief introduction of the Volume of Fluid (VOF) method which is used to reconstruct the interface between air and water. Secondly, we introduce the numerical methods to solve the governing equations and the treatment for rough surfaces in the numerical model. Finally, two preliminary test cases are presented which aim at verifying the rough wall functions and the multiphase flow solver's ability to track the free surface.

2.1 Fluid Flow Model

The motion of a fluid can be described by the Navier-Stokes equations. As we discussed in the literature review, the RANS model is used in this study. In this section we will give a summary of the governing equations of the model by adopting the Eulerian description, including the turbulence closure and the free surface effect.

2.1.1 Reynolds-Averaged Navier-Stokes Equations

The governing equations for the fluid flow are the incompressible continuity equation and the Reynolds-averaged Navier-Stokes equations:

$$\nabla \cdot \boldsymbol{U} = 0 \tag{2.1}$$

$$\frac{\partial \rho \boldsymbol{U}}{\partial t} + \nabla \cdot (\rho \boldsymbol{U}\boldsymbol{U}^T) = -\nabla p + \nabla \cdot (2\mu_m \boldsymbol{S} + \rho \boldsymbol{R}) + \rho \boldsymbol{f} \tag{2.2}$$

where ρ is the fluid density, $\boldsymbol{U}$ is the fluid velocity, $\boldsymbol{S}$ is the strain rate tensor $\boldsymbol{S} = \frac{1}{2}(\nabla \boldsymbol{U} + (\nabla \boldsymbol{U})^T)$, μ_m is the fluid dynamic molecular viscosity, $\boldsymbol{R}$ is the Reynolds stress tensor calculated from turbulence closure models used in this work, p is the pressure and $\boldsymbol{f}$ is the external volume force. The left side of the equation consists of the time-dependent and convective terms of the velocity, whereas the right side includes the effects of viscosity and the external forces. ∇ is the gradient operator given as:

$$\nabla = (\frac{\partial}{\partial x}, \frac{\partial}{\partial y}, \frac{\partial}{\partial z})^T \tag{2.3}$$

By adopting the Boussinesq eddy viscosity assumption, the momentum transfer caused by turbulent eddies can be modelled with an eddy viscosity. This is in analogy with how the momentum transfer caused by the molecular motion in the flow can be described by the molecular viscosity. And the deviatoric anisotropic stress is considered proportional to the traceless mean rate of strain. So the Reynolds stress tensor can be written in the following way:

$$\boldsymbol{R} = -\overline{\boldsymbol{u}'\boldsymbol{u}'^T} = 2\frac{\mu_t}{\rho}\boldsymbol{S} - \frac{2}{3}k\boldsymbol{I} \tag{2.4}$$

where μ_t is the eddy viscosity, k is the turbulent kinetic energy, u' is the fluctuating component of the velocity and $\boldsymbol{I} = \delta_{ij}$. Various turbulence closure models are available in OpenFOAM® and in this work we have used two of them - the standard k-ε model (Launder and Spalding, 1974) is used for two-dimensional simulations and the k-ω Shear Stress Transport (k-ω SST) model (Menter and Esch, 2001) (Menter et al., 2003) is used for three-dimensional simulations. The choice of the turbulence models is based on the flow conditions of the test case. The k-ε model is able to predict flow behaviour with reasonable accuracy for a wide range of turbulent flows and the k-ω SST model often produces better results in adverse pressure gradients and separating flows (Menter, 1992).

k-ε model The k-ε model calculates the turbulent viscosity as:

$$\mu_t = C_\mu \rho \frac{k^2}{\varepsilon} \tag{2.5}$$

where ε represents the turbulent dissipation rate. k and ε are modelled by:

$$\frac{\partial \rho k}{\partial t} + \nabla \cdot (\rho \boldsymbol{U} k) = \nabla \cdot \left[(\mu_m + \frac{\mu_t}{\sigma_k}) \nabla k \right] + P_k - \rho \varepsilon \tag{2.6}$$

$$\frac{\partial \rho \varepsilon}{\partial t} + \nabla \cdot (\rho \boldsymbol{U} \varepsilon) = \nabla \cdot \left[(\mu_m + \frac{\mu_t}{\sigma_k}) \nabla \varepsilon \right] + C_1 \frac{\varepsilon}{k} P_k - C_2 \rho \frac{\varepsilon^2}{k} \tag{2.7}$$

where P_k is the rate of production of turbulence, given by:

$$P_k = \mu_t (\nabla \times \boldsymbol{U}) \cdot (\nabla \times \boldsymbol{U})^T \tag{2.8}$$

The constants C_μ, C_1, C_2, σ_k and σ_ε which appear in Eq.(2.6), Eq.(2.7) and Eq.(2.8) take the values given in Launder and Spalding (1974): $C_\mu = 0.09$, $C_1 = 1.44$, $C_2 = 1.92$, $\sigma_k = 1.0$, $\sigma_\varepsilon = 1.3$.

k-ω SST model The k-ω SST model is also a two-equation model for the turbulence kinetic energy k and the turbulence specific dissipation rate ω. The governing equations for k and ω are:

$$\frac{\partial \rho k}{\partial t} + \nabla \cdot (\rho \boldsymbol{U} k) = \nabla \cdot [(\mu_m + \sigma_k \mu_t) \nabla k] + P_k - \beta^\star \omega k \tag{2.9}$$

$$\frac{\partial \rho \omega}{\partial t} + \nabla \cdot (\rho \boldsymbol{U} \omega) = \nabla \cdot [(\mu_m + \sigma_\omega \mu_t) \nabla \omega] + \gamma \frac{\omega}{k} P_k - \rho \beta \omega^2 + 2(1 - F_1) \frac{\rho \sigma_{\omega 2}}{\omega} \nabla k \cdot (\nabla \omega)^T \tag{2.10}$$

and F_1 is defined as:

$$F_1 = \tanh(Arg_1^4) \tag{2.11}$$

$$Arg_1 = \min \left[\max \left(\frac{\sqrt{k}}{\beta^\star \omega d}, \frac{500 \mu_m}{\rho d^2 \omega} \right), \frac{4 \rho \sigma_{\omega 2} k}{CD_{k\omega} d^2} \right] \tag{2.12}$$

$$CD_{k\omega} = \max \left(\frac{2 \rho \sigma_{\omega 2}}{\omega} \nabla k \cdot (\nabla \omega)^T, 10^{-10} \right) \tag{2.13}$$

where d is the distance from the wall. The turbulent eddy viscosity is computed from:

$$\mu_t = \frac{\rho k a_1}{max(a_1\omega, b_1 S F_2)} \tag{2.14}$$

$$S = \sqrt{2S:S} \tag{2.15}$$

$$F_2 = \tanh(Arg_2^2) \tag{2.16}$$

$$Arg_2^2 = \max\left(\frac{2\sqrt{k}}{\beta^\star \omega d}, \frac{500\mu_m}{\rho d^2 \omega}\right) \tag{2.17}$$

Each of the constants is a blend of an inner and an outer constant, blended via:

$$\Phi = F_1\Phi_1 + (1 - F_1)\Phi_2 \tag{2.18}$$

where Φ represent a random constant, Φ_1 is the inner value and Φ_2 is the outer value. The constants in the expressions take the following values $\gamma_1 = 5/9$, $\gamma_2 = 0.44$, $\beta^\star = 0.09$, $\beta_1 = 0.075$, $\beta_2 = 0.0828$, $\sigma_{k1} = 0.85$, $\sigma_{k2} = 1.0$, $\sigma_{\omega 1} = 0.5$, $\sigma_{\omega 2} = 0.856$, $a_1 = 0.31$ and $b_1 = 1.0$.

2.1.2 Free Surface Effects

The conventional VOF method proposed by Hirt and Nichols (1981) is used to simulate flow field of two immiscible fluids. This method uses an indicator to represent the volume fraction of one phase in each mesh cells. The detailed description of the implementation in OpenFOAM® can be found in Ubbink (1997a).

In this thesis, α is used to represent the volume fraction of the water phase, so $\alpha = 1$ means the cell is filled with water and $\alpha = 0$ means the cell is filled with air and $0 \leq \alpha \leq 1$ means the cell includes the interface between air and water. In this way, the domain is considered to be filled with a single composite fluid, which is referred as the effective fluid, whose properties can be calculated from a weighted average of the properties of the component fluids. Any physical property Φ of the effective fluid is then given by:

$$\Phi = \Phi_1\alpha + \Phi_0(1 - \alpha) \tag{2.19}$$

where the subscripts 1 and 0 indicate respectively the value in the water phase and in the air phase.

For scour simulation problems with a free surface, the external volume force includes gravity and surface tension at the free surface. Thus, with the VOF method, the volume force term for the multiphase flow field can be interpreted as:

$$\rho \boldsymbol{f} = \rho \boldsymbol{g} + \boldsymbol{f}_\sigma \tag{2.20}$$

where $\boldsymbol{g}$ is the gravitational acceleration and $\boldsymbol{f}_\sigma$ represents the surface tension effects at the free surface. The surface tension is calculated from:

$$\boldsymbol{f}_\sigma = \sigma_T \kappa_\alpha \nabla \alpha \tag{2.21}$$

$$\kappa_\alpha = -\nabla \cdot \left(\frac{\nabla \alpha}{|\nabla \alpha|} \right) \tag{2.22}$$

where κ_α is the curvature of the interface and σ_T is the coefficient of surface tension which, in this study, is $0.074\,\mathrm{kg \cdot s^{-2}}$ for an air-water interface at 20 °C.

In order to facilitate the pressure boundary condition set-up, the pressure used in Eq.(2.2) in the solver is the modified pressure p_d:

$$p_d = p - \rho \boldsymbol{g} \cdot \boldsymbol{x} \tag{2.23}$$

where $\boldsymbol{x} = (x, y, z)$ is the coordinate vector of the position and p is the total pressure.

Combined with Eq.(2.20), Eq.(2.21) and Eq.(2.23), Eq.(2.2) can be rearranged as:

$$\frac{\partial \rho \boldsymbol{U}}{\partial t} + \nabla \cdot (\rho \boldsymbol{U} \boldsymbol{U}^T) = -\nabla p_d - \boldsymbol{g} \cdot \boldsymbol{x} \nabla \rho + \nabla \cdot (2\mu_m \boldsymbol{S} + \rho \boldsymbol{R}) + \rho \boldsymbol{g} + \sigma_T \kappa_\alpha \nabla \alpha \tag{2.24}$$

The transport equations for the indicator α are solved simultaneously with the RANS equations. The transport equations can be expressed as:

$$\frac{\partial \alpha}{\partial t} + \nabla \cdot (\boldsymbol{U} \alpha) = 0 \tag{2.25}$$

One major problem of the free surface simulation is to guarantee the mass conservation of each phase. The mass conservation is crucial to the calculation of surface curvature which is required for the determination of the surface tension and the pressure gradient across the free surface (Rusche, 2002). In order to guarantee the conservation of the phase fraction, a modified transport equation is solved in OpenFOAM® , as proposed by Weller (2002). An

additional convective term is introduced into the transport equation:

$$\frac{\partial \alpha}{\partial t} + \nabla \cdot \boldsymbol{U}\alpha + \nabla \cdot \boldsymbol{U}_r \alpha(1-\alpha) = 0 \tag{2.26}$$

where $\boldsymbol{U}_r = \boldsymbol{U}_1 - \boldsymbol{U}_0$ is the relative velocity. The details of the derivation can be found in Appendix A.

The additional convection term in Eq.(2.26) is also called the compression term (Berberović et al., 2009) and it serves an artificial contribution to the convection of the phase fraction α, which makes the free surface sharper to increase the resolution of the free surface. The term will only have a non-zero value within the interface region so it does not have any influence in the single phase regions. However, the mesh in the interface region still needs to be fine enough to reduce modelling errors, especially for the two phases with high density ratios.

2.2 Numerical Implementation

In this section, we will introduce the numeral methods and procedures that are used in this work to establish the numerical model, including the wall functions for simulating the effects of rough surfaces on the flow field provided by OpenFOAM® .

2.2.1 Discretization Procedure

In order to solve the fluid motion over a domain, the discretization practice is needed to transform the equitations into a corresponding system of algebraic equations. The details of the discretization approaches can be found in Jasak (1996) and here we will only give a brief introduction.

Spatial discretization To obtain a numerical solutions to the relevant equations within a given domain, it is first necessary to discretize the doamin into a finite number of points at which the required variables will be calculated. In the OpenFOAM® code, the space is discretized using the Finite Volume Method (FVM); the computational domain is divided into control volumes, which can be different sizes and different shapes. The equations to be solved are integrated over each control volume with the integrals of the divergence terms in the equation converted to integrals over the surface of the volume, using the Gauss divergence theorem. For a vector $\boldsymbol{a}(\boldsymbol{x},t)$ within a control volume P, we have :

$$\int_{V_p} \nabla \cdot \boldsymbol{a} dV = \oint_{\partial V_P} \boldsymbol{a} \cdot d\boldsymbol{S} = \sum_{S_f} \left(\int_{S_f} \boldsymbol{a} \cdot d\boldsymbol{S} \right) \tag{2.27}$$

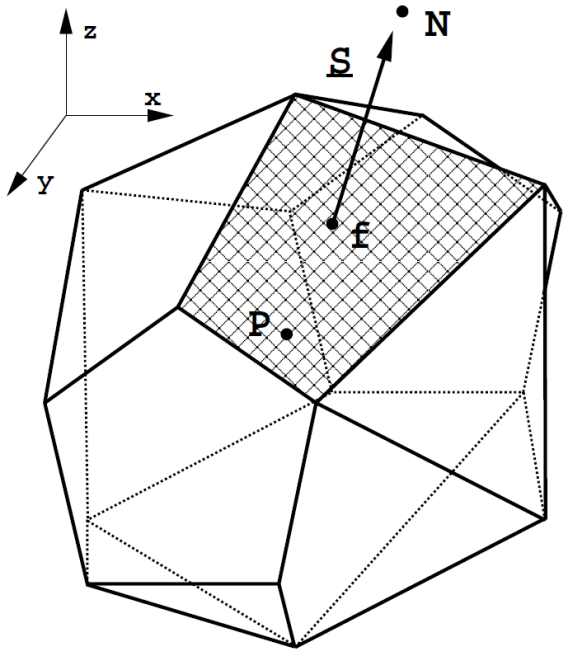

Fig. 2.1 Control Volume, from Jasak (1996).

where V_P is the volume of the cell, S_f are the surface areas of the constituent faces and $\boldsymbol{S}$ is the outward-pointing face area vector. We assume a linear variation in space, which makes the space discretization a second-order accurate method. The term on the left and the term on the right can therefore be calculated respectively from:

$$\int_{V_p} \nabla \cdot \boldsymbol{a} dV = (\nabla \cdot \boldsymbol{a}) \int_{V_P} dV + \left[\int_{V_P} (\boldsymbol{x} - \boldsymbol{x_P}) dV \right] \cdot [\nabla (\nabla \cdot \boldsymbol{a})_P] = (\nabla \cdot \boldsymbol{a}) V_P \tag{2.28}$$

$$\int_{S_f} \boldsymbol{a} \cdot d\boldsymbol{S} = \left(\int_{S_f} d\boldsymbol{S} \right) \cdot \boldsymbol{a}_f + \left[\int_{S_f} (\boldsymbol{x} - \boldsymbol{x_f}) d\boldsymbol{S} \right] : (\nabla \boldsymbol{a})_f = \boldsymbol{S} \cdot \boldsymbol{a}_f \tag{2.29}$$

where the subscript f means the value at centre of face. Combining Eq.(2.27), Eq.(2.28) and Eq.(2.29), the divergence of vector $\boldsymbol{a}$ in the control volume can be calculated as:

$$\nabla \cdot \boldsymbol{a} = \frac{\sum_f \boldsymbol{S} \cdot \boldsymbol{a}_f}{V_P} \tag{2.30}$$

The convection term, the diffusion term and the source terms in Eq.(2.24) can therefore be discretized respectively and multiple differencing schemes for the convection term and an orthogonal correction approach for the diffusion term are available in OpenFOAM® .

Temporal discretization OpenFOAM® provides several different time discretization methods and the ones that will be used in this work are presented here. To achieve temporal discretization, a linear variation in time is assumed. So for any value Φ we have:

$$\Phi^{t+\Delta t} = \Phi^t + \Delta t \left(\frac{\partial \Phi}{\partial t}\right)^t \tag{2.31}$$

Thus, the time derivative term in Eq.(2.24) can be calculated by:

$$\left(\frac{\partial \rho \boldsymbol{U}}{\partial t}\right)_P = \frac{\rho_P \boldsymbol{U}_P^{t+\Delta t} - \rho_P \boldsymbol{U}_P^t}{\Delta t} \tag{2.32}$$

Different time discretization methods treat the temporal variation of the velocity and other properties in other terms of the Eq.(2.24) differently. The most commonly used time discretization methods in OpenFOAM® is the Euler implicit method which expresses the values in terms of the new time step. It is a first order method and is enough for most of the cases. Another choice is the Crank-Nicholson method which takes into account the temporal variations of the values using linear assumption which makes it a second order implicit method. The Crank-Nicholson method cannot guarantee boundedness of the solution, so a combination of Euler implicit and Crank-Nicholson method is possible in OpenFOAM® by setting an off-centring coefficient φ:

$$\varphi = \begin{cases} 1 & \textbf{pure Crank-Nicholson method} \\ 0 & \textbf{pure Euler method} \end{cases} \tag{2.33}$$

generally $\varphi = 0.9$ is used which helps to guarantee both of the boundedness and stability of the simulation.

A backward differencing scheme is also provided in OpenFOAM® which is a second-order method. It doesn't take into account the temporal variation of the values but instead of a linear assumption of the variation in time, the second order of the Taylor series expansion is included:

$$\left(\frac{\partial \rho \boldsymbol{U}}{\partial t}\right)_P = \frac{\frac{3}{2}\rho_P \boldsymbol{U}_P^{t+\Delta t} - 2\rho_P \boldsymbol{U}_P^t + \frac{1}{2}\rho_P \boldsymbol{U}_P^{t-\Delta t}}{\Delta t} \tag{2.34}$$

In this thesis, for steady state problems, the time derivatives are set to be zero and an under-relaxation method is used. For transient problems, the Euler implicit is used because the Crank-Nicholson takes longer time.

2.2.2 Pressure-Velocity Solution Procedure

In OpenFOAM® , most fluid dynamics solver applications use either the pressure-implicit split-operator (PISO) (Issa, 1986) algorithm, the semi-implicit method for pressure-linked equations (SIMPLE) algorithm (Patankar and Spalding, 1972), or a combined PIMPLE algorithm. PISO and PIMPLE are used for transient problems and SIMPLE for steady-state problems.

SIMPLE algorithm For a steady-state problem, it is not necessary to fully resolve the linear pressure-velocity coupling, as the changes between consecutive solutions are no longer small. The basic steps in the solution update are as follows:

1. An approximation of the velocity field is obtained by solving the momentum equation. The pressure gradient term is calculated using the pressure distribution from the previous iteration or an initial guess.

2. The pressure equation is formulated and solved in order to obtain the new pressure distribution.

3. Velocities are corrected and a new set of conservative fluxes is calculated.

The discretized momentum equation and pressure correction equation are solved implicitly, where the velocity correction is solved explicitly. This is the reason why it is called 'Semi-Implicit Method'. The SIMPLE algorithm is developed to reach the steady state very fast and does not contain time derivation. To provide a stable simulation, the relaxation factors are used and the new value of a field $\phi^{\star}_{n+1}$ is a combination of the value obtained from the previous iteration ϕ_n and the current iteration ϕ_{n+1}:

$$\phi^{\star}_{n+1} = \phi_n + \gamma(\phi_{n+1} - \phi_n) \tag{2.35}$$

where γ represents the relaxation factors for ϕ.

PISO algorithm For solving a transient problem, the PISO loop is used. The solution procedure for one time step is as follows:

1. Solve the momentum equation to calculate the velocity field using the best-guess initial pressure gradient values. This step is the 'Momentum Predictor' step.

2. The velocity field obtained in the first step is used to get a new estimate of the pressure field.

3. The velocity field is corrected using the updated estimate of the pressure field.

4. Step 2 and 3 are then repeated until the difference between successive estimates for the pressure-velocity system is less than some threshold value. The pressure and velocity fields for the current time-step are then obtained and the new conservative fluxes are calculated.

PIMPLE algorithm When using PISO algorithm to solve a transient problem, the time step should be limited by $Co < 1.0$ to ensure the stability of the simulation, which means that it is very expensive to solve a real time problem in transient manner for long time especially with very complex geometries. In order to accelerate the simulation, in OpenFOAM® , a combination of SIMPLE and PISO algorithms is possible which allows the time step to reach $Co \geq 1.0$ and it is called the PIMPLE algorithm. So in this work, the turbulent flow field is solved using the PIMPLE loop. While PIMPLE solves the governing equations, the looping is controlled by user-defined parameters *nCorrectors*, *nNonOrthogonalCorrectors* and *nOuterCorrectors* and the PIMPLE algorithm calculates the pressure-momentum coupling in one time step for with different algorithms for each correctors:

nCorrectors:it sets the number of times the algorithm solves the pressure equation and momentum corrector in each step and is typically set to be 2 or 3.

nNonOrthogonalCorrectors: it specifies the number of times the explicit non-orthogonal correction is repeated and it is typically set to be 0 if the mesh is orthogonal and can be set up to 20 if the mesh is highly non-orthogonal.

nOuterCorrectors: it enables looping over the entire system of equations within on time step, representing the total number of times the system is solved. It is set to be larger than 1 and the last time of the correction of the pressure-momentum coupling uses PISO algorithm while the previous correction of the pressure-momentum coupling uses SIMPLE algorithm with a relaxation factor. If *nOuterCorrectors* is set to be 1, then it is a pure PISO algorithm.

In OpenFOAM® , the convergence of a solver is controlled by the relative tolerance between the initial and final residual. The tolerance can be separately defined for each variable and the residual used to evaluate the tolerance is the sum of the residual over all the mesh cells.

2.2.3 Adaptive Time Step Control

In the model, a self-adapting time step is used to adjust the time step according to the Courant number Co of the cell faces:

$$Co = \frac{\boldsymbol{U}_f \cdot \boldsymbol{S}_f}{\boldsymbol{d} \cdot \boldsymbol{S}_f} \Delta t \tag{2.36}$$

where $\boldsymbol{d}$ is the vector connecting the centroids of the two adjacent cells who share the face f and the values of $\boldsymbol{U}_f$ and Δt are obtained from the previous time step. The time step for the present Δt^n is calculated based on the maximum Courant number of the previous time step Co^{n-1} by:

$$\Delta t^n = \min\left(\frac{Co_{max}}{Co^{n-1}}\Delta t^{n-1}, (1+\lambda_1\frac{Co_{max}}{Co^{n-1}})\Delta t^{n-1}, \lambda_2 \Delta t^{n-1}, \Delta t_{max})\right) \tag{2.37}$$

where λ_1 and λ_2 are constants used to restrict oscillation of the time step to avoid instability of the simulation, Co_{max} is the maximum Courant number and Δt_{max} is the maximum time step. When initiating the simulation, Co_{max} and Δt_{max} can be defined by the user. An initial time step Δt_{init} is also defined when setting up the case. But in order to avoid any sudden change of the time step, the actual initial time step $\Delta t^{\star}_{init}$ used in the simulation is calculated from:

$$\Delta t^{\star}_{init} = \min\left(\frac{Co_{max}\Delta t_{init}}{Co^0}, \Delta t_{max}\right) \tag{2.38}$$

When using VOF method, the transport equation for the volume fraction is solved with several sub-cycles within a time step to increase the accuracy of the simulation. The sub-cycles also allows the global time step to be larger for solving other equations which accelerates the simulation. The number of sub-cycles n_s can be user-defined and the time step for each sub-cycle is calculated from:

$$\Delta t_s = \frac{\Delta t}{n_s} \tag{2.39}$$

The overall procedure of the transient solver for simulating flow with free surface can then be summarized as follows (Lopes, 2013):

1. Initiate all the variables and boundary conditions.

2. Calculate the Courant number and adjust the time-step.

3. Solve the phase fraction transport equation using the volumetric fluxes from the previous time step and go through the sub-cycles.

4. Calculate the viscosity and density fields with the updated phase fraction and calculate the curvature of the free surface.

5. Assemble and solve the momentum predictor.

6. Go through the PISO or PIMPLE loop until the pre-defined tolerance for the pressure-velocity system is reached.

7. Advance to the next time-step and start again from step 2.

2.2.4 Rough Wall Treatment

For numerical simulation of scour, the bed is usually made of sand grains which makes it a rough surface instead of a smooth one. Besides, the predictions of sediment transport rate depends on the estimation of the resistance to the flows on the bed. So the roughness of the bed is an important factor in our simulation.

The bed roughness is usually given in terms of the equivalent Nikuradse roughness height (k_s). Nikuradse (1933) glued uniformly sized sand grains to the internal surface of pipes and studied the steady flows over densely packed sand grains and fitted the velocity profiles with the logarithmic law of the wall:

$$U = \frac{U_f}{\kappa} \ln \frac{z}{z_0} \tag{2.40}$$

where $\kappa = 0.41$ is the von Kármán constant, U_f is the friction velocity, z is the distance to the wall and z_0 is the distance from the boundary at which the idealized velocity given by the law of the wall goes to zero and following Nikuradse (1933), z_0 is equal to $k_s/30$.

For natural sediment, the equivalent roughness is expected to be between 1 and 5 times the characteristic sand grain size which could be d_{50}, d_{84} or d_{90}. Some are shown in Table 2.1.

Table 2.1 Relationship between k_s and sand grain sizes proposed by different authors.

Hey (1979)	$3.5d_{84}$
Whiting and Dietrich (1990)	$2.95d_{84}$
Ferguson (2013)	$(3.1 \sim 4)d_{84}$
Kamphuis (1947)	$2d_{90}$
van Rijn (1982)	$3d_{90}$
Ferguson (2013)	$(2.8 \sim 3.5)d_{84}$

At high Shields parameter values, the sediment can move along the bottom in a layer as sheet flow. The presence of the sheet flow will increases the apparent roughness height. This

is probably caused by increased energy dissipation in the sheet flow layer due to interaction between individual sediment grains as well as between the sediment and the fluid (Camenen et al., 2009). Ribberink (1998) proposed a relationship between the roughness height and the Shields parameter after performing a series of experiments.

$$k_s = d_{50}[1+6(\theta-1)] \quad \textbf{for} \quad \theta > 1 \tag{2.41}$$

In this thesis, only current flow is studied and the equivalent roughness height is decided respectively according to the experimental data of each simulation case. As for oscillatory flows, Nielsen (1992) performed a very detailed study for equivalent roughness height of beds made of natural sand in oscillatory flows based on data collected by Carsons et al. (1929) and Lofquist (1986).

With RANS, OpenFOAM® provides a set of wall functions including one that allows the user to define the roughness height of the wall surface and the ones that are used in this work are presented below.

kqRWallfunction This is a boundary condition for k field which is actually a zero gradient condition.

epsilonWallfucntion This is a boundary condition for ε field for k-ε turbulent model. The production and dissipation of turbulent kinetic energy is assumed to be in equilibrium and the logarithmic law of the wall is also used to set the value of ε in the near wall cells.

$$\varepsilon = \frac{C_\mu^{\frac{3}{4}} k^{\frac{3}{2}}}{\kappa z_p} \tag{2.42}$$

where z_p is the distance from the wall to the first centre near the wall.

omegaWallfucntion This is a boundary condition for ω field for k-ω turbulent model. It provides a wall constraint on turbulence specific dissipation ω for both low and high Reynolds number turbulence models. In the near wall cells, the centroid values for ω are set from:

$$\omega_{vis} = \frac{6(\nu_m + \nu_t)}{\beta z_p^2} \tag{2.43}$$

$$\omega_{log} = \frac{\sqrt{k}}{C_\mu^{1/4} \kappa z_p} \tag{2.44}$$

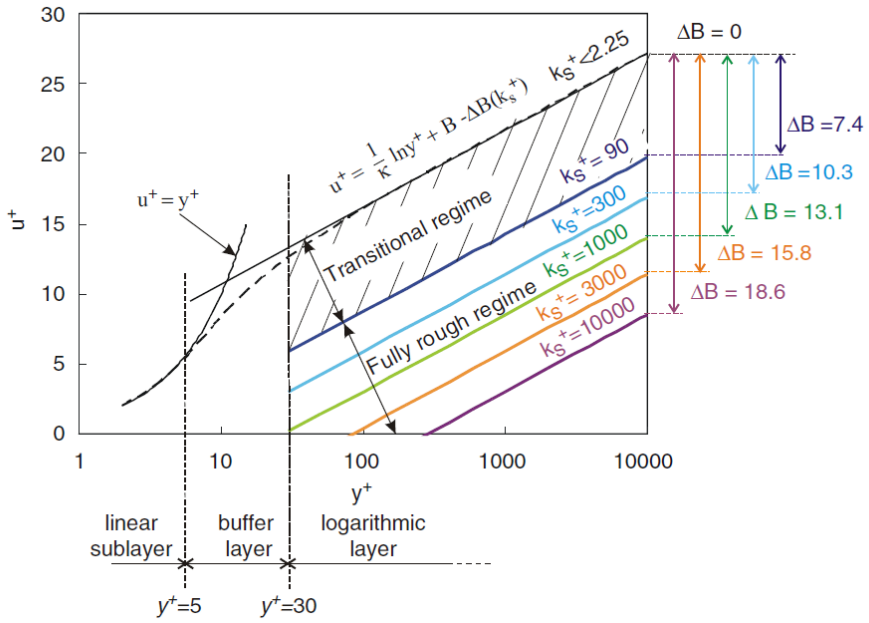

Fig. 2.2 Law of the wall for smooth and sand-grain roughened surfaces with the dimensionless sand-grain roughness height k_s as a parameter, from Blocken et al. (2007).

where ω_{vis} is the value calculated for the viscous layer and ω_{log} for the log law layer and the final value of ω is calculated as a blending of these two values:

$$\omega = \sqrt{\omega_{vis}^2 + \omega_{log}^2} \tag{2.45}$$

nutRoughWallfunction This is a boundary condition for ν_t field. It calculates the wall shear stress for a rough wall based on the law of the wall and the shear stress later is included as a body force in the momentum equations for calculating the tangent velocity in near wall cells. The conventional law of the wall for rough surface can be written as (Blocken et al., 2007):

$$U^+ = \frac{U}{U_f} = \frac{1}{\kappa}\ln(z^+) + B - \Delta B(k_s^+) \tag{2.46}$$

$$z^+ = \frac{U_f z_p}{\nu_m} \qquad k_s^+ = \frac{U_f k_s}{\nu_m} \tag{2.47}$$

where B is the constant for smooth wall function which is generally taken as $B \sim 5.2$. Fig. (2.2) gives a more direct interpretation for the law of the wall.

To use this boundary condition, two inputs are required: the equivalent roughness height k_s and the roughness constant C_s which usually takes the value $0.5 \sim 1.0$. The velocity profile

in log law region generated from this wall function should be:

$$\frac{U}{U_f} = \frac{1}{\kappa}\ln(\frac{Ez^+}{1+C_s k_s^+}) \tag{2.48}$$

The friction velocity U_f is calculated from the turbulence model:

$$U_f = k^{\frac{1}{2}} C_\mu^{\frac{1}{4}} \tag{2.49}$$

where E is the smooth wall constant written inside the logarithm $E = e^{\kappa B}$.

Combine the Eq.(2.46) and Eq/ (2.48), we can find that:

$$\Delta B = \frac{1}{\kappa}\ln(1+C_s k_s^+) \tag{2.50}$$

The kinematic eddy viscosity in the grid cells closest to the wall (ν_t) is therefore calculated by:

$$\nu_t = \nu_m \left[\frac{z^+\kappa}{\ln\left\{Ez^+/(1+C_s k_s^+)\right\}} - 1\right] \tag{2.51}$$

In order to use the rough wall function correctly, z_p should locate in the logarithmic layer of the boundary layer which means that $z^+ >= 30$. Moreover, Blocken et al. (2007) argued that the first cell height should also be at least equal to or larger than the Nikuradse's roughness length. Frisch (1989) shows that even with $z_p \geqslant 0.2k_s$, the simulation results can still be accurate. However, in OpenFOAM® , the cell aspect ratio should be less than 1000 to prevent extra numerical errors (Cavar et al., 2016). As a result, $z_p/z_0 = 10$ is recommended in Martinez (2011).

2.3 Preliminary Test Cases for the Hydrodynamic Module

In this section, we will test the performance of the rough wall functions and the free surface tracking features of the hydrodynamical module with two simple test cases since these two features are very important for producing an accurate simulation results of the flow field. We will also introduce the general folder structure and the files necessary for running a simulation using OpenFOAM® .

2.3.1 Case Folder Structure

A typical file system for a simulation case in OpenFOAM® is shown in Fig. (2.3) which has three major folders necessary for most of the simulations: *0*, *constant* and *system*.

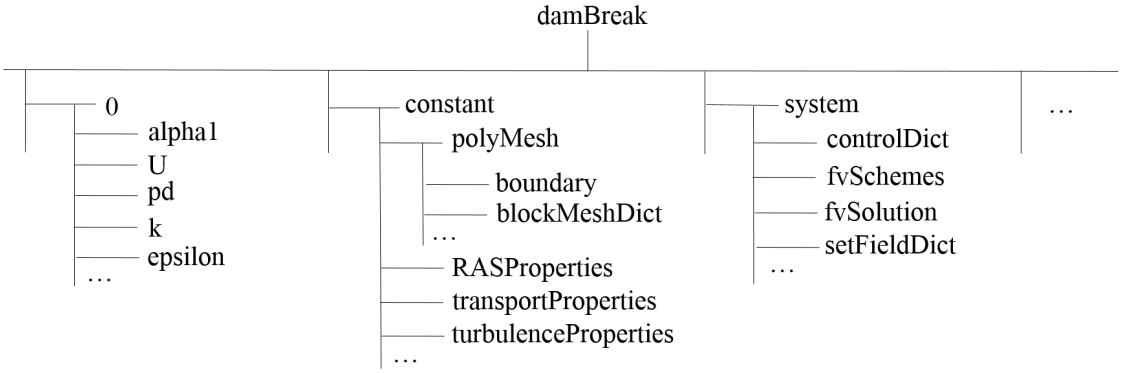

Fig. 2.3 The general folder system for constructing a simulation case in OpenFOAM® .

In folder *0*, the initial values and boundary conditions for all the variables used in the simulation are defined. In folder *constant*, the constant coefficients and other settings which will not vary during the simulations are defined. The most important files in this folder are:

- *blockMeshDict*: this file defines mesh informations which will be used by the *blockMesh* utility to generate the computational mesh.
- *boundary*: this file defines the boundary types and the faces belonging to each boundary patch
- *transportProperties*: this file defines properties of the fluids in the simulation such as density, viscosity and so on.
- *turbulenceProperties*: this file defines turbulence models used in the simulation.

The choices which control the simulation are registered in the folder *system*, including:

- *controlDict*: this file defines the time step controls and the read and write options.
- *fvSchemes*: this file specifies the numerical schemes used to perform the temporal and spacial discretization.
- *fvSolutions*: the solvers used to solve different equations and the tolerances are defined in this file.

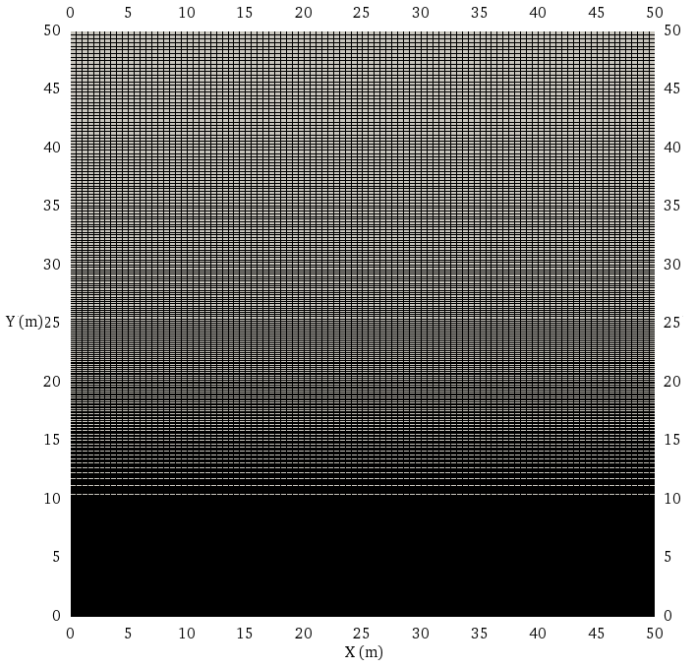

Fig. 2.4 Mesh generated for simulating flow over homogeneous bed.

Many other files can be added into this folder, for example, the files which can be read by the utilities of OpenFOAM® to perform the pre-processing and post-processing of the simulation.

2.3.2 Test Case: Flow Over Homogeneous Bed

In order to test the performance of the rough wall functions in OpenFOAM® , test cases of flow over homogeneous bed with different equivalent roughness height are simulated.

Mesh generation and boundary conditions The mesh is generated with *blockMesh* utility of OpenFOAM® and is shown in Fig. (2.4). The simulation domain is $50\,\mathrm{m} \times 50\,\mathrm{m}$ and the number of cells are 100×400. The same mesh is used to simulate the flow over homogeneous land with smooth bed $k_s = 0\,\mathrm{m}$ and with rough bed of different equivalent roughness height $k_s = 0.005\,\mathrm{m}$, $k_s = 0.01\,\mathrm{m}$, $k_s = 0.05\,\mathrm{m}$ and $k_s = 0.1\,\mathrm{m}$. Details of the simulations can be found in Table 2.2.

The initial velocity is set to be uniform all over the domain. The steady state solver *simpleFoam* is used which solves the Navier-stocks equation for a single phase with SIMPLE algorithm. The simulation ends when the predefined tolerances for pressure and velocity fields are reached. The k-ε turbulence model is used. The boundary conditions are presented below:

Table 2.2 Details of the simulations for flow over homogeneous bed.

Run	k_s (m)	k_s^+	z^+	U_f (m/s)
1	0	\	912	0.0286
2	0.005	182	1165	0.0365
3	0.01	392	1252	0.0392
4	0.05	2322	1484	0.0464
5	0.1	5047	1612	0.0505

- **Top boundary**: The slip boundary condition is used for all the fields at the top boundary.
- **Inlet and outlet boundaries**: The cyclic boundary condition is applied for inlet and outlet boundaries. A mean velocity is defined for the whole domain and the pressure gradient is calculated from the mean velocity to compensate the energy loss in the domain.
- **Bottom boundary**: The velocity at the wall is set to be zero and the pressure is set to be zero gradient. For k, ε and ν_t fields, the corresponding wall functions with different equivalent roughness height k_s are used.
- **Front and back boundaries**: As the simulation is in 2D, the *empty* boundary condition is used.

Simulation results The velocity profiles obtained from the simulations for different beds are shown in Fig. (2.5)

The simulation results are then compared with the results obtained from the log law of the wall Eq.(2.46) using U_f obtained from the simulation results and the comparison is shown in Fig. (2.6). The good agreement between the simulation results and results of Eq.(2.46) verifies the accuracy of the rough wall functions in OpenFOAM® .

2.3.3 Test Case: Dam Break

The hydrodynamical module of the numerical model for scour simulation is constructed using the *interDyMFoam* solver, which is a combination of a multiphase flow solver *interFoam* and a dynamic mesh feature. In this part, we use a simple test case to check the performance of the *interFoam* solver for solving two incompressible immiscible fluids and tracking the interface between the two phases. The test case chosen is a classical 'dam break' simulation, which is one of the tutorial cases provided by Foam-extend-3.1. With this test case, only

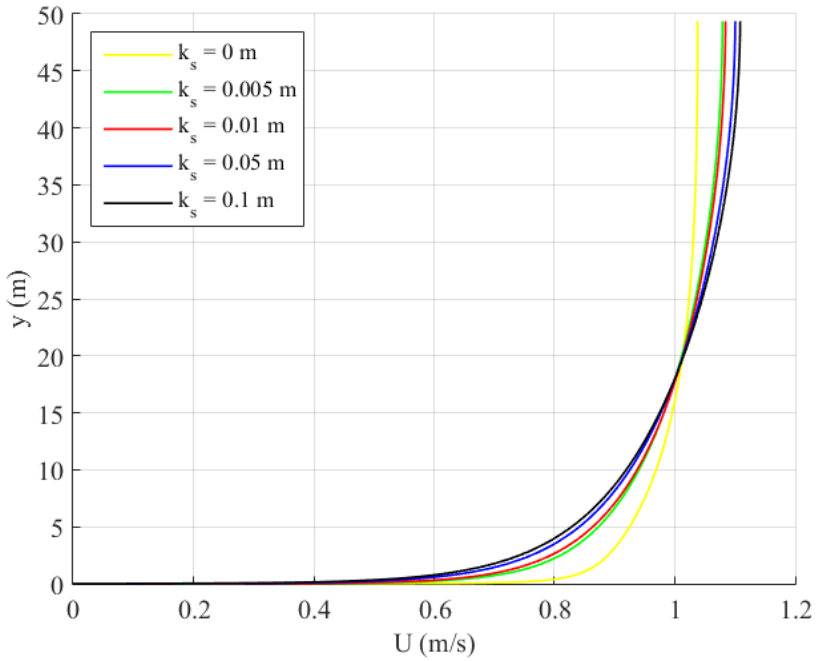

Fig. 2.5 Velocity profiles for different equivalent roughness height k_s obtained from the numerical simulation (y represents the vertical coordinate).

qualitative comparison with the experimental measurements was given as no quantitative results were found for this case and we intended to just check the solver already established in OpenFOAM® . If more quantitative comparison is required, many similar cases can be used such as Aureli et al. (2004).

The test case has been investigated experimentally and numerically by Koshizuka (1995), Ubbink (1997b) and Greaves (2006). It simulates a collapse of a water column with an obstacle placed in the way of the wave front as shown in Fig. (2.7). A water column of width $L = 0.146\,\text{m}$ and height $2L$ is held in place at $t = 0\,\text{s}$. Then the restraint is removed instantaneously and the water column collapses under gravity and hits first a rectangular obstacle of $b = 0.024\,\text{m}$ wide and $2b$ high placed on the bottom of a tank which is $4L$ wide and $4L$ high, with the leading edge at the centre of the tank.

Mesh generation and boundary conditions The mesh is generated by the *blockMesh* utility. In order to test the influence of mesh refinement on the accuracy of the *interFoam* solver, three different meshes were generated: mesh A with 46×50 cells, mesh B with 90×86 cells, and mesh C with 180×172 cells. The meshes are shown in Fig. (2.8).

The initial velocity and modified pressure are set to be zero over all the domain. The volume fraction α is set to be 1 at the water column and 0 else where. The k-ε turbulence

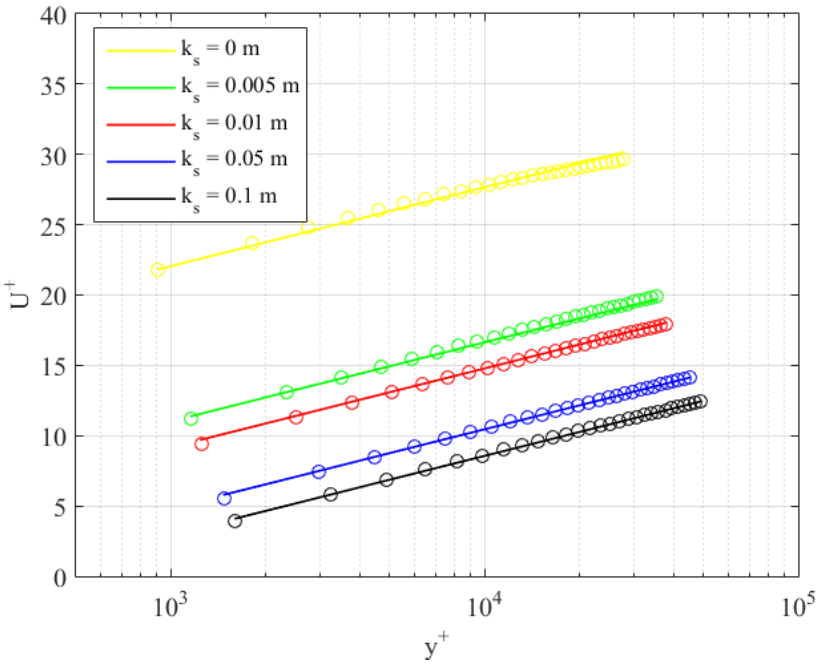

Fig. 2.6 Comparison of the simulated velocity profile and the velocity profile obtained from Eq.(2.46) for different k_s. ∘ represents the simulation results, − represents the theoretical results. y^+ here is defined the same as z^+ in Eq.(2.46).

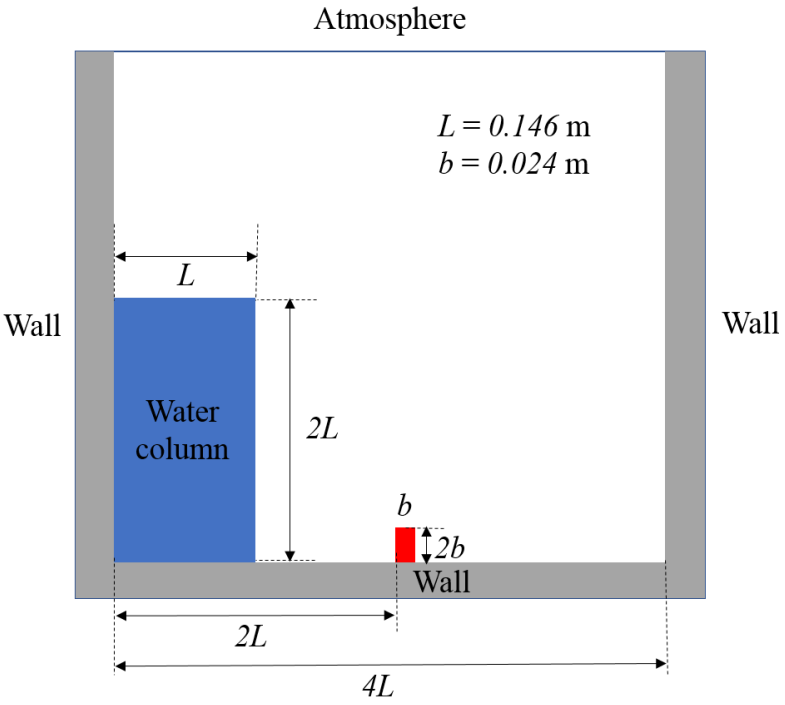

Fig. 2.7 Sketch of the test case 'dam break'.

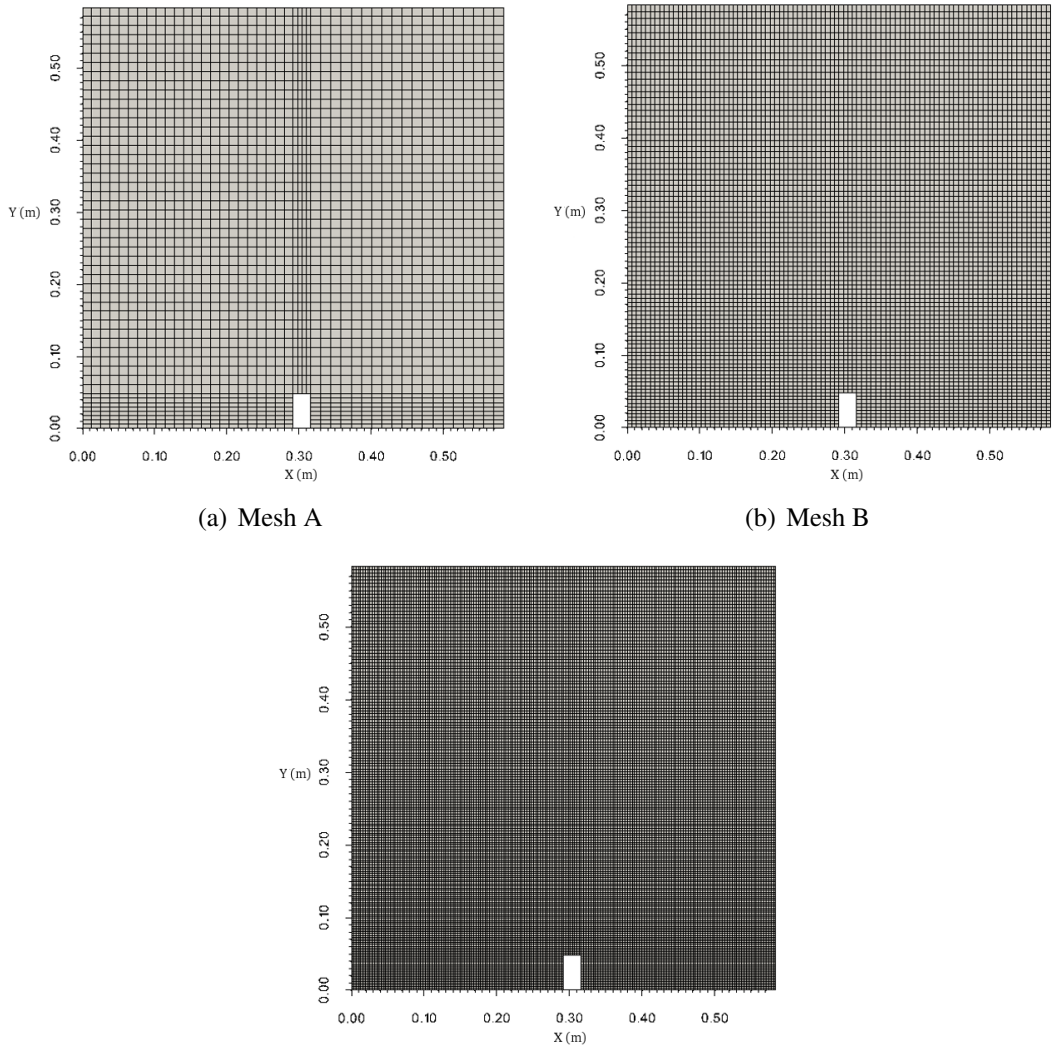

(a) Mesh A

(b) Mesh B

(c) Mesh C

Fig. 2.8 The meshes generated. Mesh A: 46×50, Mesh B: 90×86, Mesh C: 180×172.

model is used and as this is a transient problem, the time step is controlled by $Co < 0.7$. The boundary conditions defined are presented below:

- **Top boundary**: The top boundary is connected to the atmosphere so both outflow and inflow should be permitted. The combination of the *totalPressure* condition on pressure and *pressureInletOutletVelocity* on velocity is extremely common for representing the atmosphere in simulation where some inflow occurs and the inlet flow velocity is not known. The *totalPressure* boundary condition specifies:

$$p = \begin{cases} p_0 \\ p_0 - \frac{1}{2}\|\boldsymbol{U}\|^2 \end{cases} \tag{2.52}$$

  where p_0 can be user-specified. The *pressureInletOutletVelocity* boundary condition for velocity field sets the gradient of all the components of the velocity to be zero except for the tangential component for inflow, which is set to be a fixed value defaulting to 0. Then for the field α, k and ε, an *inletOutlet* condition is used which sets the gradient of the value to be zero when the flow is outwards and a fixed value defined by the user when the flow is inwards.

- **Bottom and side boundaries**: The bottom and side boundaries are all walls. For the pressure field, the *fixedFluxPressure* boundary condition is applied which adjusts the pressure gradient so that the boundary flux matches the velocity boundary condition for solvers that include body forces such as gravity and surface tension. The velocity field is set to be zero at all the *wall* type of boundaries. The gradient of α is set to be zero as the surface tension of the water at the wall boundaries is ignored. Finally, for the k and ε fields, the wall functions are used, as explained in 2.2.4.

- **Front and back boundaries**: As the simulation is in 2D, an *empty* type boundary condition is used for the front and back boundaries.

Simulation results At the start of the simulation, the water column collapses, and the water flows outwards until it encounters the obstacle. The water is then projected upwards and outwards as an air borne jet, which eventually impacts on the boundary wall. The comparison between the simulation results using three different meshes and the still photographs taken by Koshizuka (1995) at $t = 0\,\text{s}$, $t = 0.1\,\text{s}$, $t = 0.2\,\text{s}$, $t = 0.3\,\text{s}$, $t = 0.4\,\text{s}$, $t = 0.5\,\text{s}$ are shown in Fig. (2.9) and Fig. (2.10). Comparison of the simulation results for the three meshes shows that the mesh refinement produces a clearer and sharper interface. However, even with a

rather coarse mesh, the general form of the free surface is correct although there are errors in some of the details.

2.4 Conclusions

In this chapter, we have introduced the basic concepts and methods for simulating turbulent flow with free surface. We started from the governing equations for incompressible flow with turbulent closures and free surface effect. Then the numerical approaches and procedures implemented in the model for solving the equations are introduced. Finally, two simple test cases are simulated to test the performance of the hydrodynamical module of the model: the test case of flow over homogeneous bed with different roughness height to verify the accuracy of the rough wall functions provided by OpenFOAM® ; and the test case 'dam break' with coarse and fine meshes to test the ability of the multiphase solver for tracking the free surface between air and water.

In the next chapter, we will focus on the morphological module of the numerical model which includes the processes of entrainment, transport and deposition of the sediment and the corresponding deformation of the bed. The morphological module is essential to the model and its implementation is the major job of this thesis.

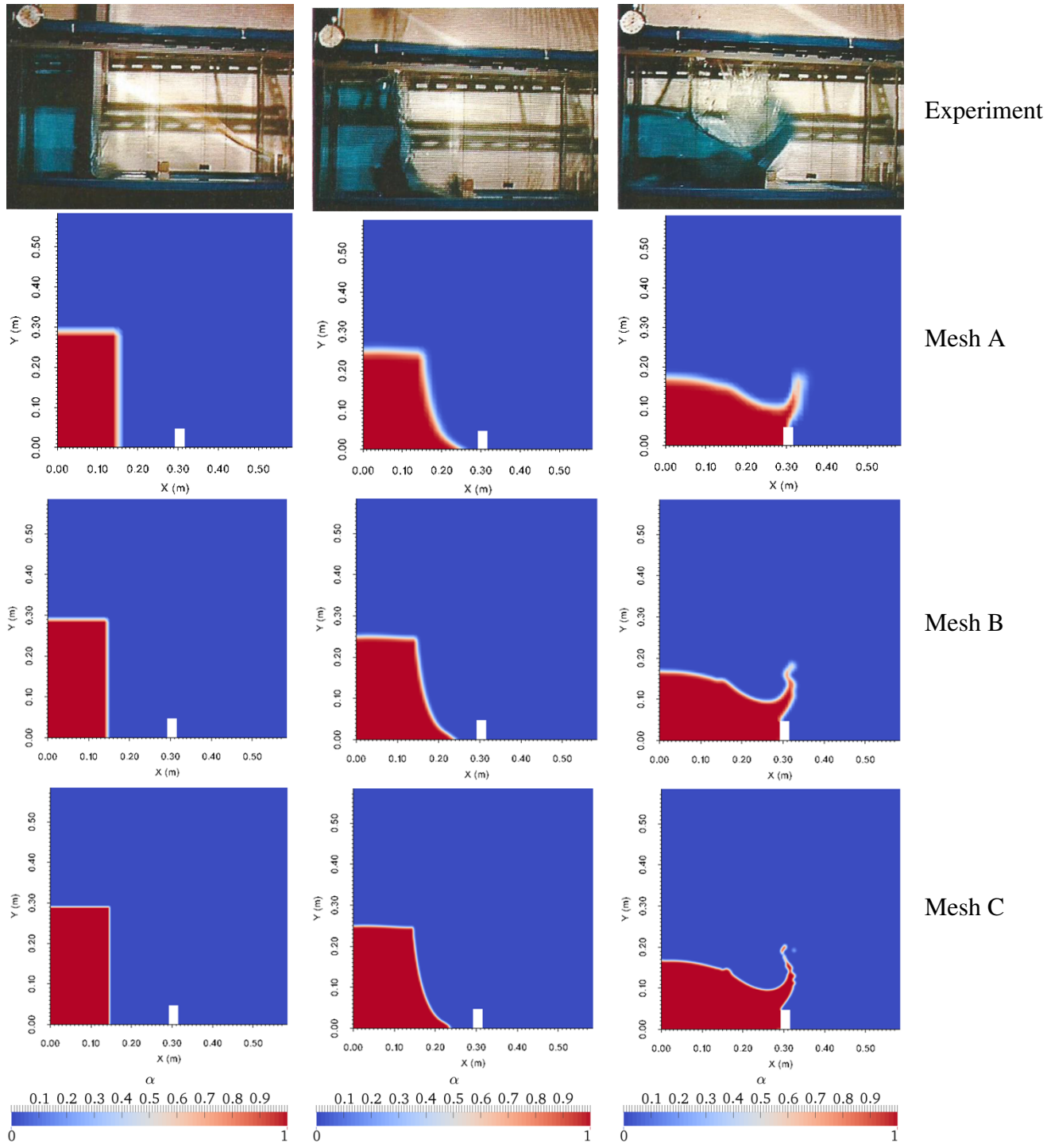

(a) $t = 0\,\mathrm{s}$ (b) $t = 0.1\,\mathrm{s}$ (c) $t = 0.2\,\mathrm{s}$

Fig. 2.9 Comparison between the simulation results using three different meshes and the photographs taken in the experiment of the 'dam break' test case at $t = 0\,\mathrm{s}$, $t = 0.1\,\mathrm{s}$, $t = 0.2\,\mathrm{s}$.

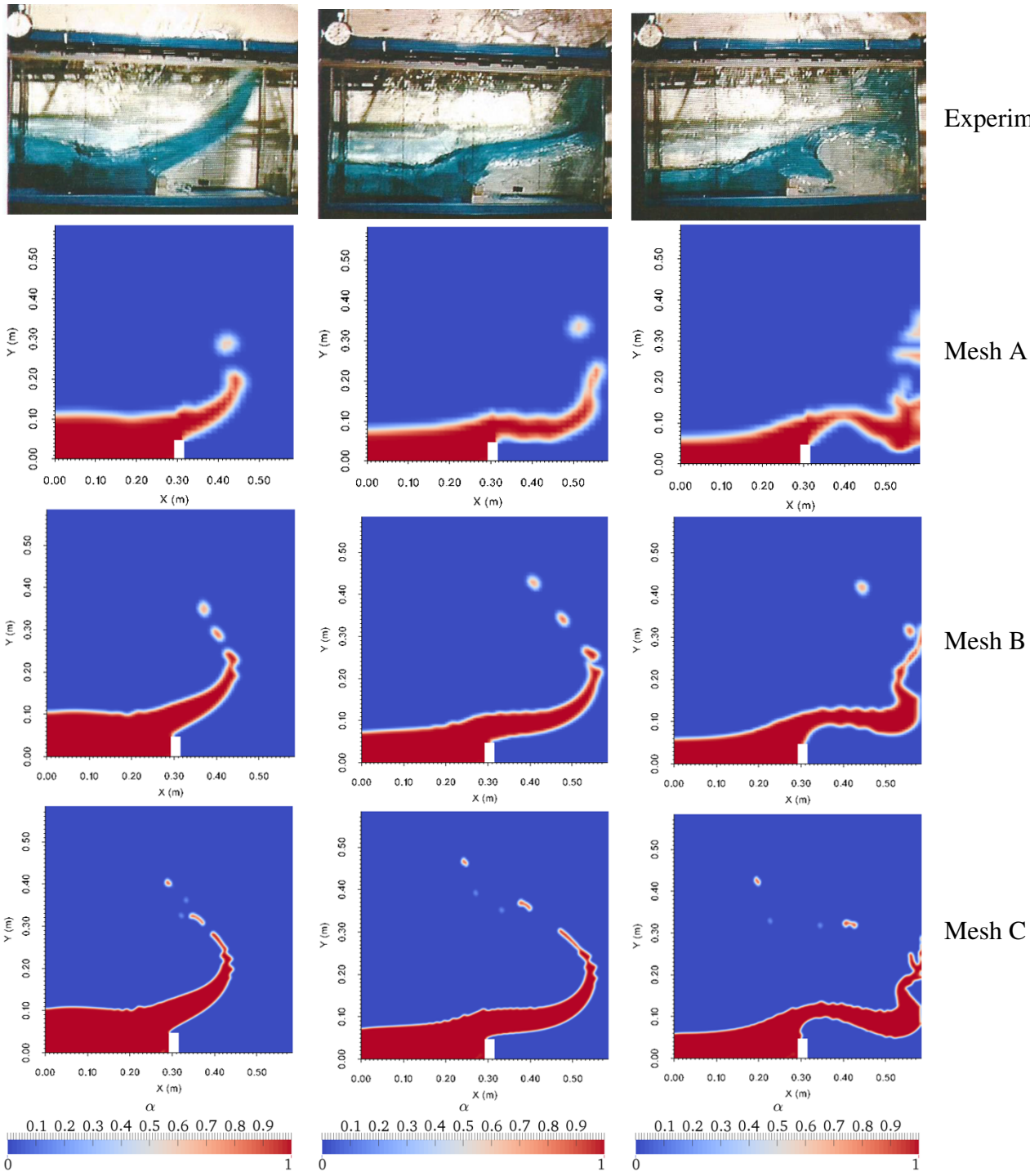

(a) $t = 0.3\,\mathrm{s}$ (b) $t = 0.4\,\mathrm{s}$ (c) $t = 0.5\,\mathrm{s}$

Fig. 2.10 Comparison between the simulation results using three different meshes and the photographs taken in the experiment of the 'dam break' test case at $t = 0.3\,\mathrm{s}$, $t = 0.4\,\mathrm{s}$, $t = 0.5\,\mathrm{s}$.

Chapter 3

Sediment Transport and Bed Erosion

This chapter consists of a brief presentation of non-cohesive sediment transport in flow. We will introduce the suspended load transport and bed load transport models that are implemented in our numerical model, including the entrainment and deposition rate calculations which serve as a boundary condition in this study. Next, we present the calculation of bed level change with a sand-sliding mechanism to restrict the bed slope, and the corresponding mesh deformation feature in our model. The final section of this chapter discusses the implementation of the model on parallel architectures and the modifications that this necessitates.

3.1 Sediment Transport

Sediments are small particles of different sizes like sand, gravel, clay, silt and so on. The sediments can be transported by water and thus cause erosion of the sediment bed, transforming the bed into a variety of different shapes like ripples and dunes. In this study, the bed is considered to be made of non-cohesive sediments and the sizes of sediment grain correspond mainly to sand (62 µm - 2 mm) as shown in Table 3.1, which is the type of the sediment particles generally involved in the local scour problems.

3.1.1 The Threshold of Movement

First of all, we look at a single sediment particle resting on horizontal bed in flowing water to study the stability of the particle. The condition can be characterized by the shear Reynolds number $Re_\star$ and the Shields parameter θ:

$$Re_\star = \frac{U_f d}{\nu} \tag{3.1}$$

Table 3.1 Classification of the sediment by their sizes from British Standard BS 1377:1975 Raudkivi (1998).

Groups	Subgroups	Diameter d_p
clay	very fine clay	0.24 ¯m - 0.5 ¯m
	find clay	0.5 ¯m - 1.0 ¯m
	medium clay	1 ¯m - 2 ¯m
	coarse clay	2 ¯m - 4 ¯m
silt	very fine silt	4 ¯m - 8 ¯m
	file silt	8 ¯m - 16 ¯m
	medium silt	16 ¯m - 31 ¯m
	coarse silt	31 ¯m - 62 ¯m
sand	very fine sand	62 ¯m - 125 ¯m
	fine sand	125 ¯m - 250 ¯m
	medium sand	250 ¯m - 500 ¯m
	coarse sand	0.5 mm - 1.0 mm
	very coarse sand	1 mm - 2 mm
gravel	very fine gravel	2 mm - 4 mm
	fine gravel	4 mm - 8 mm
	medium gravel	8 mm - 16 mm
	coarse gravel	16 mm - 32 mm
	very coarse gravel	32 mm - 64 mm
cobbles	small cobbles	64 mm - 128 mm
	large cobbles	128 mm - 256 mm
boulders	small boulder	256 mm - 512 mm
	medium boulders	512 mm - 1024 mm
	large boulders	1024 mm - 2048 mm
	very large boulders	2048 mm - 4096 mm

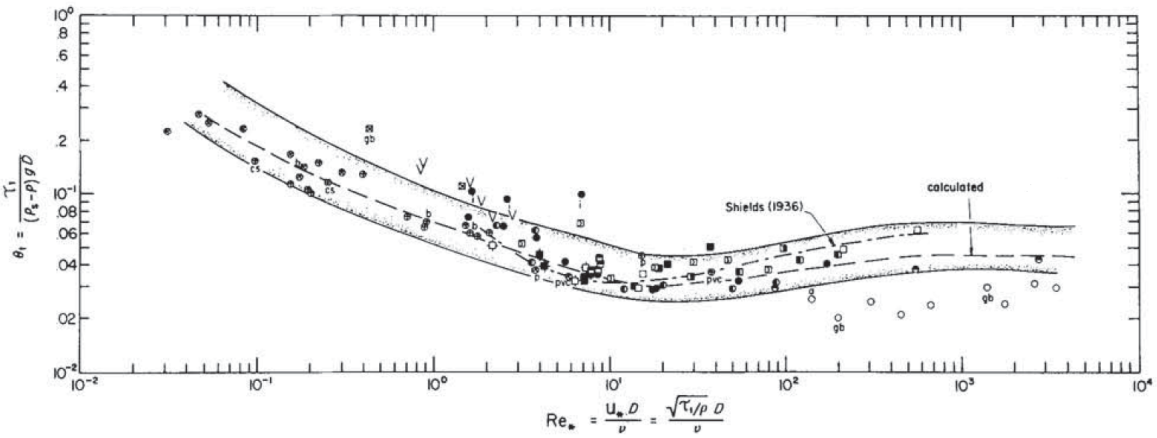

Fig. 3.1 The modified Shields diagram. Symbols are measured data from several studies of threshold of motion for different granular materials in flows, from Miller et al. (1977).

where ν is the kinematic viscosity of the flow and θ is defined the same as in Eq.(1.3).

As the velocity of the flow increases, the shear stress becomes larger and the particle will start to move. For a particle at the threshold of moving, the Shields parameter for the particle becomes equal to the critical Shields parameter calculated from the critical shear stress. The relationship between the critical Shields parameter and the shear Reynolds number was determined experimentally by Schields (1936) who found that the results could be plotted in a shaded region. This diagram is called the Shields diagram, and it can be used to find the critical shear stress for a known particle in a flow or to find the particles which will be eroded in a known flow condition. The Shields diagram is later studied by many other researchers and a modified version of the Shields diagram is shown in Fig. (3.1).

In numerical simulations, it is not convenient to check the Shields diagram for the critical Shields parameter. So an alternative method is used in the model based on a curve fitted to the data proposed by Soulsby (1997):

$$\theta_{c0} = \frac{0.3}{1+1.2d_\star} + 0.055(1-e^{-0.02d_\star}) \tag{3.2}$$

where θ_{c0} is the critical Shields parameter for the horizontal bed and $d_\star$ is the dimensionless diameter of the particle, defined as:

$$d_\star = d\left[\frac{(s-1)g}{\nu^2}\right]^{1/3} \tag{3.3}$$

The Shields diagram and Eq.(3.2) only consider the situation of the horizontal bed. In order to take into account the slope of the bed, a modification is needed to calculate the

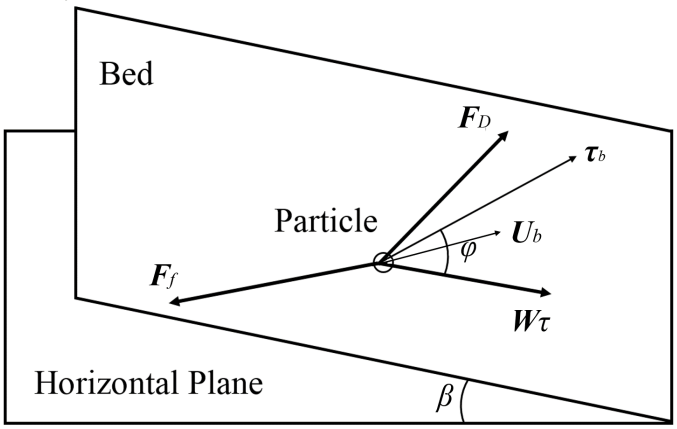

Fig. 3.2 A single moving particle on a sloping bed. $\boldsymbol{F}_D$ is the combination of drag force and lift force , $\boldsymbol{F}_f$ is the friction force, $\boldsymbol{W}_\tau$ is the gravity force component tangential to the bed, $\boldsymbol{\tau}_b$ is the bed shear stress and $\boldsymbol{U}_b$ is the mean velocity of the moving particle.

critical Shields parameter θ_c (Liu, 2008):

$$\theta_c = \theta_{c0}\left(\cos\beta\sqrt{1-\frac{\sin^2\varphi\tan^2\beta}{\mu_s^2}}-\frac{\cos\varphi\sin\beta}{\mu_s}\right) \tag{3.4}$$

where μ_s is the static friction coefficient of the bed. The angles in Eq.(3.4) are defined in Fig. (3.2), where φ is the angle between the bed shear stress and the direction of the steepest slope and β is the bed slope angle. In the numerical model developed for this work, Eq.(3.2) and Eq.(3.4) are used to calculate the critical Shields parameter, which plays an important role in the morphological module of the model.

When the bed shear stress exceeds the critical value for the particles on the bed, the sediment particles will start to move. The sediments can move close to the bed by saltation, rolling or sliding, referred to as the bed load, or move in suspension in the flow, referred to as the suspended load. These two components of the sediment transport are included in the model and their implementation is described in the following sections.

3.1.2 Suspended Load Transport

The volumetric concentration of the suspended sediment C is governed by the traditional advection-diffusion equation:

$$\frac{\partial C}{\partial t}+\nabla\cdot[(\boldsymbol{U}+\boldsymbol{V}_s)C]=\nabla\cdot\left[\left(\nu_m+\frac{\nu_t}{\sigma_c}\right)\nabla C\right]+C_f\nabla\alpha \tag{3.5}$$

Table 3.2 Relations between Re_p and value of m, from Tsai and Tsai (2000).

Re_p	≤ 0.1	0.2	0.5	1	2	5	10	20	50	100	200	$\geq$500
m	4.91	4.89	4.83	4.78	4.69	4.51	4.25	3.89	3.33	2.92	2.58	2.25

where $\boldsymbol{V}_s$ is the settling velocity of sediment in the flow and σ_c is the Schmidt number which is a dimensionless number defined as the ratio of momentum diffusivity and mass diffusivity. The last term on the right side of the equation imposes a zero-flux boundary condition on the sediment at the free surface, because the sediment cannot diffuse into the air phase. This term is zero in regions contain only water or air, but in the interface regions, if the suspended sediment concentration at free surface C_f is not zero, this term will add an equal but opposite flux of suspended sediment from the air into the water so that the net flux across the free surface equals zero.

The settling velocity $\boldsymbol{V}_s$ of the sediment is calculated by:

$$\boldsymbol{V}_s = \frac{(s-1)d^2\boldsymbol{g}}{18\nu + [0.75(s-1)d^3 g]^{0.5}} \tag{3.6}$$

In this model we do not assume that the settling velocity varies with the sediment concentration ('hindered settling'), but this effect could easily be incorporated in the equation. For example, Liang et al. (2005b) used Eq.(3.7) proposed by Soulsby (1997) to calculate the settling velocity in clear water and the interaction between the settling grains is included by decreasing the settling velocity as the concentration of sediment increases using an empirical formula Eq.(3.8) proposed by Richardson and Zaki (1997).

$$\boldsymbol{V}_{s0} = \frac{\nu}{d}\left[(10.36^2 + 1.049 d_\star^3)^{\frac{1}{2}} - 10.36\right]\frac{\boldsymbol{g}}{g} \tag{3.7}$$

$$\frac{\boldsymbol{V}_s}{\boldsymbol{V}_{s0}} = (1-C)^m \tag{3.8}$$

where m is a related to the particle's Reynolds number Re_p which is calculated from:

$$Re_p = \frac{\|\boldsymbol{V}_s\| d}{\nu} \tag{3.9}$$

and the value of Re_p can be found in Tsai and Tsai (2000) as in Table 3.2.

Whether it is feasible to add the excess turbulence caused by suspended load in the flow field has also been considered. The study by Jacobsen (2011) and the experiments done by Sumer et al. (2003) for pure current flow and small shear stress conditions suggested that this

could have an important effect, but more work will need to be done to incorporate this effect correctly into our model.

On the bed boundary, there are exchanges of the sediment between the suspended load and the sediment on the bed. The source of the suspended sediment comes from the entrainment process at the bed and the suspended sediment could also be deposited onto the bed. In order to simulate these processes, we define E as the entrainment rate and D as the deposition rate. E and D are calculated using a similar method to that proposed by Zyserman and Fredsøe (1988) and Liu and García (2008). The entrainment rate is obtained from c_e, which is the equilibrium concentration of suspended load at a reference level:

$$E = c_e \|\boldsymbol{V}_s\| \tag{3.10}$$

In this work, c_e is calculated using the empirical formula proposed by Van Rijn (1987):

$$c_e = 0.015 \frac{d_{50} T^{1.5}}{\Delta_d d_\star^{0.3}} \tag{3.11}$$

where Δ_d is the reference height and is taken as the height of the first cell layer centre closest to the bed of each simulation case and T is the dimensionless excess shear stress or the transport stage parameter which is calculated from:

$$T = \frac{\theta - \theta_c}{\theta_c} \tag{3.12}$$

The entrainment model we used in this work does not have a upper limit and therefore can not guarantee a maximum suspended load concentration in flow. In this work, we have verified that none of the simulations including the suspended load model give a suspended load concentration non-physically high. So this model works fine in this work. But a upper limit of c_e could also be added into the entrainment model to avoid the risk.

The deposition rate is obtained from the concentration in the first layer of grid cells above the bed from the previous time step c_b:

$$D = c_b \|\boldsymbol{V}_s\| \tag{3.13}$$

The entrainment and deposition processes are included in the calculation of the suspended load as a boundary condition of Eq.(3.5). So at the bed boundary, the concentration of suspended load C_b for time step $t + \Delta t$ is calculated from:

$$C_{b,t+\Delta t} = C_{b,t} + \frac{\Delta t (D_t - E_t)}{\Delta_D} \tag{3.14}$$

where Δ_D is the height of the first cell node closest to the bed.

3.1.3 Bed Load Transport

The bed load calculation formula used in this work is the one proposed by Engelund and Fredsøe (1976), because this formula has been used in many studies such as those of Jacobsen (2011), Liu (2008) and Roulund et al. (2005), and proved to give satisfactory results. The bed load transport rate is calculated as follows:

$$\boldsymbol{q}_b = \frac{1}{6}\pi d^3 \frac{p_b}{d^2}\boldsymbol{U}_b \tag{3.15}$$

where $\boldsymbol{q}_b$ is the bed load transport rate, p_b is the probability of moving particles near the bed and $\boldsymbol{U}_b$ is the mean transport velocity of the sediment particles moving as bed load. The probability p_b is given by:

$$p_b = \left[1 + \left(\frac{\frac{1}{6}\pi\mu_d}{\theta - \theta_c}\right)^4\right]^{-1/4} \tag{3.16}$$

where μ_d is the dynamic friction coefficient of the bed which should be smaller than the static friction coefficient μ_s.

In our model, the assumption of Engelund and Fredsøe (1976) is adopted which calculates $\boldsymbol{U}_b$ from:

$$\boldsymbol{U}_b = (1 - 0.7\sqrt{\theta_c/\theta})\boldsymbol{U}_\tau \tag{3.17}$$

$$\boldsymbol{U}_\tau = a\boldsymbol{U}_f \tag{3.18}$$

where $\boldsymbol{U}_\tau$ is defined as the tangential velocity of the flow near the bed, $a = 10$ and $\boldsymbol{U}_f$ is the friction velocity vector which has the same direction with the tangential wall shear stress on the bed. So the Einstein number obtained from Eq.(1.2) is :

$$\Phi_b = 5p_b(\sqrt{\theta} - 0.7\sqrt{\theta_c}) \tag{3.19}$$

This formula does not take into account the influences of the bed slope on the direction of the bed load transport and assumes that the direction of the bed load transport is the same with the direction of the wall shear stress on the bed. In two-dimensional simulations, this formula is applicable without problems. But in three-dimensional simulations, the effects of the bed slope on the direction of the bed load transport can be included to improve the

accuracy of the model. In Roulund et al. (2005), the original formula was generalized to include this effect in three-dimensional simulations.

If we assume that the sediment particles move in uniform velocity, the total force on the particles should be zero. So for a particle moving on the bed, its mean velocity $\boldsymbol{U}_b$ can be calculated by solving the equation:

$$\boldsymbol{F}_D + \boldsymbol{W}_\tau + \boldsymbol{F}_f = \boldsymbol{0} \tag{3.20}$$

where $\boldsymbol{F}_D$ is a combined agitating force which includes the drag force and the lift force, $\boldsymbol{W}_\tau$ is the component of the gravity tangential to the bed and $\boldsymbol{F}_f$ is the friction force. These three forces in the equation can be calculated from:

$$\boldsymbol{W}_\tau = \boldsymbol{W} - (\boldsymbol{W} \cdot \boldsymbol{N})\boldsymbol{N} \tag{3.21}$$

$$\boldsymbol{F}_f = (\boldsymbol{W} \cdot \boldsymbol{N})\mu_d \frac{\boldsymbol{U}_b}{\|\boldsymbol{U}_b\|} \tag{3.22}$$

$$\boldsymbol{F}_D = \frac{1}{2}\rho_f C_t \frac{\pi}{4} d^2 \|\boldsymbol{U}_r\| \boldsymbol{U}_r \tag{3.23}$$

where $\boldsymbol{N}$ is the unit local normal vector of the bed, $\boldsymbol{W}$ is the gravity force and $\boldsymbol{U}_r$ is the relative velocity which is defined as:

$$\boldsymbol{U}_r = \boldsymbol{U}_\tau - \boldsymbol{U}_b \tag{3.24}$$

C_t is the combined force coefficient and is defined as $C_t = C_D + \mu_d C_L$, where C_D is the drag force coefficient and C_L is the lift force coefficient. The value of C_t is calculated from the formula proposed by Fernandez Luque and Van Beek (1976):

$$C_t = \frac{4\mu_s}{3a^2(\frac{1}{2}\theta_{c0})}. \tag{3.25}$$

The gravity force is calculated from:

$$\boldsymbol{W} = \frac{\pi}{6}\rho_f (s-1) d^3 \boldsymbol{g} \tag{3.26}$$

Substitution of Eq.(3.21), Eq.(3.22), Eq.(3.23) and Eq.(3.24) into Eq.(3.20) yields a combination of 3 non-linear equations with 3 unknown variables which are the three components of $\boldsymbol{U}_b$.

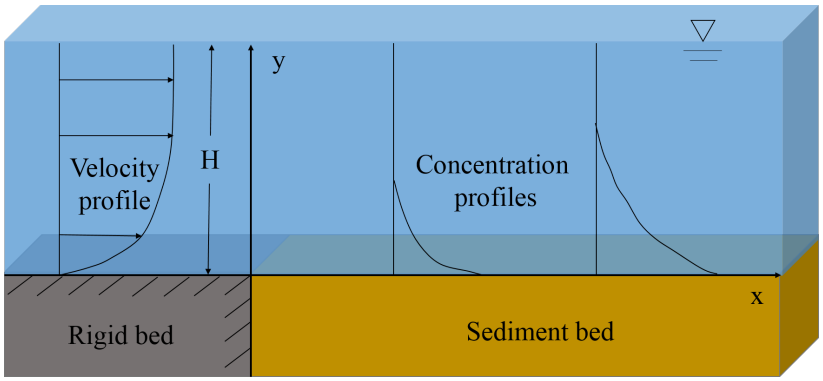

Fig. 3.3 Schema of the net entrainment test case.

This formula proposed by Roulund et al. (2005) has already been successfully implemented in the model and the equations are solved using the Newton-Raphson technique for each cell surfaces on the bottom boundary of the mesh to calculate $\boldsymbol{U}_b$ on the bed. However, the simulations conducted in the thesis does not include this effect and the bed load is assumed to move in the same direction with the tangential wall shear stress on the bed. The new bed load model implemented will be used in the future to study the importance of this effect on the scour formation.

3.1.4 Test Case: Net Entrainment

A net entrainment case is simulated to test the suspended load transport model's performance. This test case is based on the experiments done by van Rijn (1986) in a flume of the Delft Hydraulics Laboratory. The bed load transport model's performance will be verified later through the simulation of local scour, which will be presented in the following chapter.

The model configuration for the net entrainment case is shown in Fig. (3.3). The water depth is $H = 0.25\,\mathrm{m}$ and mean velocity is $\overline{U} = 0.67\,\mathrm{m/s}$. The inlet flow is clear water, free of sediments. It flows first over a rigid bed and then a loose sediment bed where the sediments are entrained. So all the suspended load in the flow comes from the entrainment of the sediment. The length of rigid bed and sediment bed are respectively $20H$ and $40H$. The representative sediment particle diameter is $d_{50} = 0.230\,\mathrm{mm}$ and the velocity and concentration profiles are measured at $x/H = 4$, $x/H = 10$, $x/H = 20$, $x/H = 40$ for 4 points at levels $y = 15\,\mathrm{mm}$, $y = 25\,\mathrm{mm}$, $y = 50\,\mathrm{mm}$, $y = 100\,\mathrm{mm}$ above the bed.

For the flow field, the k-ε turbulence model is used. The free surface effect is also included with the VOF method introduced in the previous chapter. The bed load transport model is not included in this simulation because we are only testing the suspended load transport model and the sediment bed does not deform even though it is eroded. The influence

of the bed form is included in this simulation through rough wall function and the Nikuradse roughness height k_s for the loose sediment bed is set to be $k_s = 0.01\,\mathrm{m}$ as suggested by van Rijn (1986). The Schmidt number is set to be $\sigma_c = 0.8$. The simulation starts with still and clear water in the channel. So the development of the velocity profile together with concentration profiles are all simulated in this test case.

The mesh is two-dimensional and it is constructed by the *blockMesh* utility. The mesh is uniform and it contains 37500 cells with grid resolution $\Delta x_{min} = 0.02\,\mathrm{m}$ and $\Delta y_{min} = 0.01\,\mathrm{m}$. A preliminary test has been done to confirm that the mesh resolution is fine enough. The time steps which are controlled by the Courant number $Co < 0.7$ in this simulations. The convergence criteria for the transient solver are set to be 10^{-6} for pressure, velocity and suspended load concentration fields and 10^{-8} for k and ε fields. The test case requires about 1 h for simulating 240 s in real time. The boundary conditions are set as follows:

- **Top boundary**: The top boundary is connected to the atmosphere so the boundary conditions for flow field are set to be the same as in the dam-break case presented in Section 2.3.3. The boundary condition for suspended load concentration C is set to be zero as there should be no suspended load in the air region.

- **Bottom boundary**: The bottom boundary is solid bed so the *fixedFluxPressure* boundary condition is applied for pressure field and zero vector is given to the velocity field. The gradient of α is set to be zero and rough wall functions are used for k and ε fields. The gradient of the suspended load concentration C at the bed is set to be zero-gradient so the bed is considered to be an infinite source of sediments.

- **Inlet and outlet boundaries**: The *fixedFluxPressure* boundary condition is applied for the pressure field at the inlet and outlet boundaries. The velocity of the water inlet boundary is set to be uniform while for air inlet boundary and outlet boundary of both air and water regions, the zero-gradient condition is applied. Both k and ε are set to be constant values at the inlet and zero-gradient at the outlet. For the suspended load concentration C, the inlet value is set to be zero as the inlet flow should be clear water and the outlet value is set to be zero-gradient.

- **Front and back boundaries**: As the simulation is in 2D, an *empty* type boundary condition is used for all the fields for the front and back boundaries.

The settling velocity calculated by our model is $\boldsymbol{V}_s = 0.0216\,\mathrm{m/s}$. It is very close to the value $0.022\,\mathrm{m/s}$ used by Liang et al. (2005b) which also includes the same test case. The bed shear stress calculated at $x = 40H$ is $\|\boldsymbol{\tau}_b\| = 2.3\,\mathrm{Pa}$, which agrees well with the measured

value. However, in this case, the large bed roughness includes the bed form effects and therefore the bed shear stress calculated is the total bed shear stress which is composed of the skin friction component τ_{bs} and the bed form component τ_{bf}. Only the bed shear stress caused due to the skin friction should be used in Eq.(3.11) to calculate the entrainment rate. As the bed in this case is covered with ripples, so according to Celik and Rodi (1991), the skin friction component of the bed shear stress should be calculated by:

$$\tau_{bs} = \left[1 - \left(\frac{k_s}{H}\right)^{0.06}\right] \tau_b \tag{3.27}$$

The simulation results of the velocity profile which demonstrate the development of the boundary layer are shown in Fig. (3.4). The free surface level at the corresponding positions is also marked in these figures. We can see from the simulation results that the water depth becomes a little bit lower as the boundary layer develops which can be explained by the increasing energy loss due to the bed friction. The concentration profiles obtained by simulation are then compared with the measured profiles in Fig. (3.5). It can be seen that the overall agreement of the results is really good, which proves that the sediment entrainment and deposition processes as well as the suspended load concentration profiles are correctly simulated by our model. Moreover, the suspended load concentration becomes zero in the air region ($y > 0.25\,\mathrm{m}$) even when it is not zero at the free surface which demonstrates that the suspended load model can correctly prevent the unwanted diffusion of the suspended load into the air region. (The non-zero part located slightly above the free surface is due to the linear interpolation between the zero value in cell just above the free surface and the non zero value in the cell which contains the free surface.) Finally, Fig. (3.6) shows the suspended load concentration profile obtained from the numerical simulation together with the theoretical profile, which is a modified Rouse equation proposed by van Rijn (1986):

$y < 0.5H$:

$$\frac{C}{C_a} = \left[\frac{a(H-y)}{y(H-a)}\right]^{\frac{V_s}{\kappa U_f}} \tag{3.28}$$

$y \geq 0.5H$:

$$\frac{C}{C_a} = \left[\frac{a}{H-a}\right]^{\frac{V_s}{\kappa U_f}} \exp\left\{-4\frac{V_s}{\kappa U_f}\left(\frac{y}{H} - 0.5\right)\right\} \tag{3.29}$$

where C_a is the concentration of suspended sediment at a reference height a which is defined in this work to be equal to Δ_d. It should be noticed that the theoretical profile is based on some assumptions. It is applied for a stream in equilibrium where the rate of upward

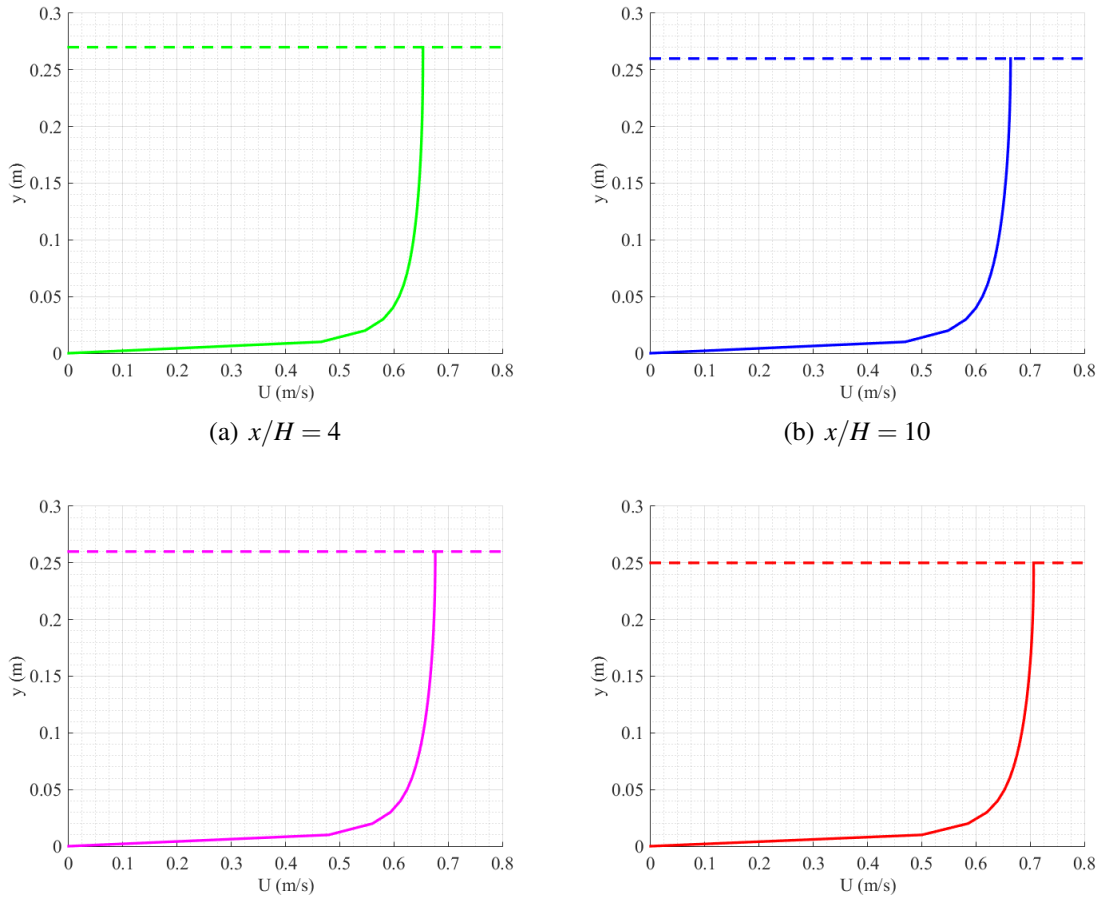

(a) $x/H = 4$ (b) $x/H = 10$

(c) $x/H = 20$ (d) $x/H = 40$

Fig. 3.4 Boundary layer development in the numerical simulation. The dotted line represents the free surface height where $\alpha \approx 0.5$.

sediment transfer by turbulence will be equalled by the downward movement due to settling and it assumes that the shear stress varies linearly with depth as imposed by the mixing length model. In this test case, the simulation used the k-ω model and the flow and the suspended load are not in equilibrium condition, so the theoretical profile is just given here as a reference, calculated with the water depth H, the friction velocity U_f and the suspended load at the reference height C_a obtained from the simulation results at $x/H = 40$. The theoretical profile calculated with the simulation results at other positions won't change the theoretical profile very much and as the boundary layer becomes fully developed and the suspended load concentration reaches its equilibrium, the concentration profile should agree more with the theoretical profile.

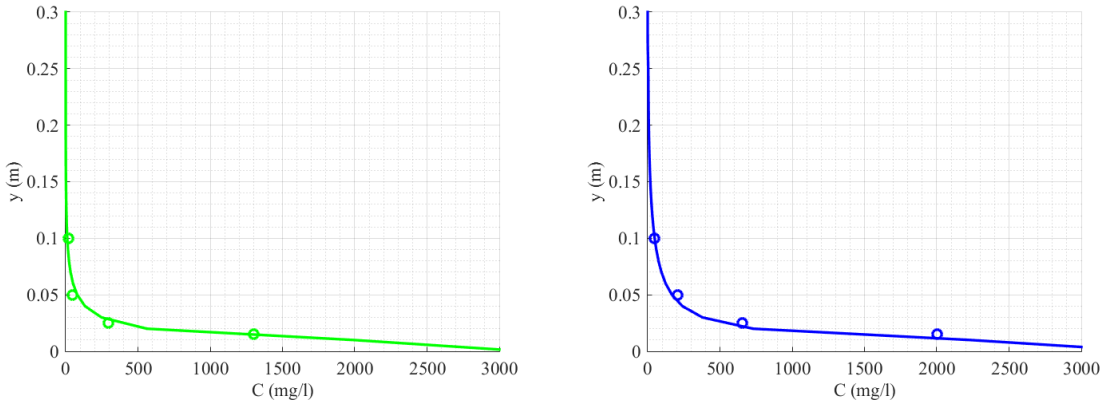

(a) $x/H = 4$

(b) $x/H = 10$

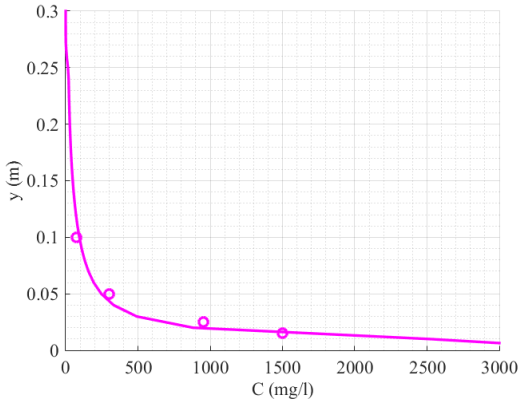

(c) $x/H = 20$

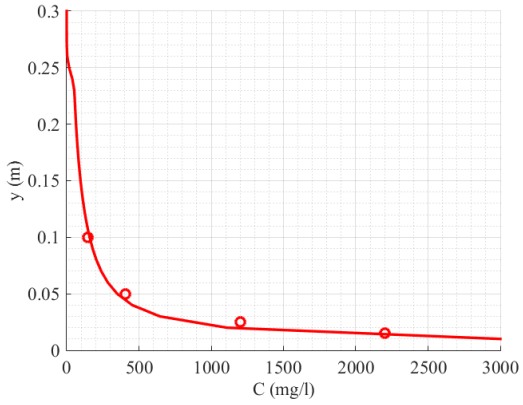

(d) $x/H = 40$

Fig. 3.5 Comparison of the suspended load concentration profile obtained from the numerical simulations and the experimental measurements from van Rijn (1986) for the net entrainment test case. – represents the simulation results, ○ represents the measured results.

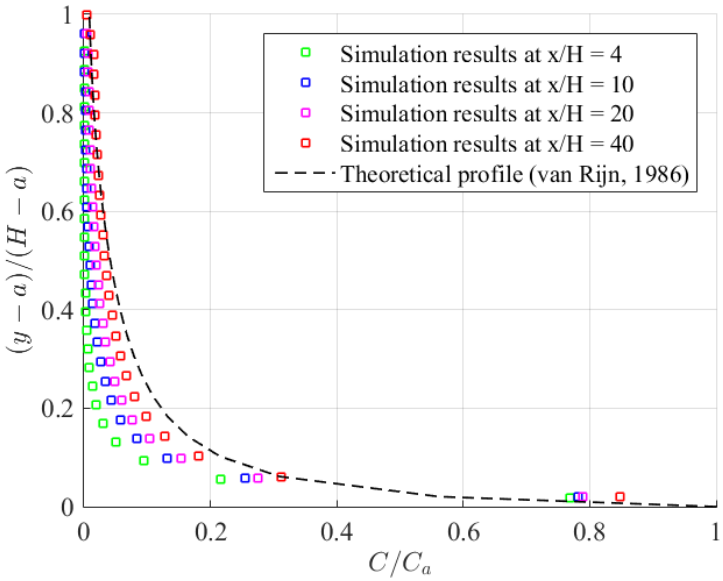

Fig. 3.6 Comparison of the suspended load concentration profile obtained from the numerical simulation and the theoretical profile from van Rijn (1986).

3.2 Sediment Bed Deformation

With the sediment transport rate modelled in the previous section, the bed deformation can be calculated by the continuity equation for the sediment. The deformation of bed is implemented as the movement of the bottom boundary of the mesh and the deformed mesh then needs to be smoothed to avoid large distortions in certain cells. The dynamic mesh feature provided by OpenFOAM makes it possible to move the mesh based on a given displacement of the mesh points and to smooth the mesh accordingly. Moreover, a sand-sliding mechanism is added into the model to limit the bed slope to the critical bed slop of the sediment, which is usually taken as the repose angle of the sediment and is proven to be essential for modelling the form of the bed after deformation.

3.2.1 Continuity Equation for Sediment

The bed deformation level is calculated from the continuity equation for sediment, which is also called the Exner equation (Fredsøe and Deigaard, 1992):

$$\frac{\partial h}{\partial t} = -\frac{1}{1-n}(\nabla \cdot \boldsymbol{q}_b - E + D) \tag{3.30}$$

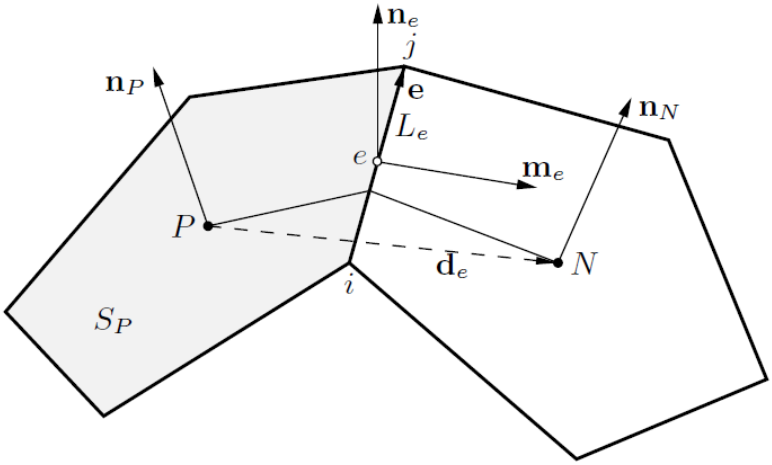

Fig. 3.7 Polygonal control area, from Tukovic and Jasak (2008).

where n is the porosity of the sediment bed. This equation should be solved only on the bed surface and takes into account the curvature of the surface. So the finite area method (FAM) provided in Foam-extend is used for solving the continuity equation in our model.

FAM is the a two-dimensional FVM on a curved surface in three dimension. Like FVM, the computational space domain, which is a surface, is split into a finite number of convex polygonal control areas bounded by straight edges. The computational surface can be curved which means special treatment is required for solving equations on the computational surface. Details of the spatial discretization of the finite area method are provided in Tukovic and Jasak (2008) and here we only will give a brief introduction. Fig. (3.7) shows a schema of two adjacent control areas with centroids P and N and a shared edge $\boldsymbol{e}$ which has a length L_e. The normal vector of the control areas and the edge are respectively $\boldsymbol{n}_P$, $\boldsymbol{n}_N$ and $\boldsymbol{n}_e$ and the vector $\boldsymbol{m}_e$ is the vector perpendicular to vectors $\boldsymbol{e}$ and $\boldsymbol{n}_e$

In order to take account of the curvature of the discretized surface, a linear transformation of the centroid-based values to edge-based values is carried out before solving the equations. When the edge-based value has been calculated, it is transformed back to centroid-based values. The definition of the edge-based local coordinate system can be seen in Fig. (3.8) where $\boldsymbol{t}_e$ is the unit vector tangential to the geodetic line $\overline{PeN}$ at point e.

The edge-based value, taking the velocity $\boldsymbol{U}_e$ as an example, can be calculated from:

$$\boldsymbol{U}_e = (\boldsymbol{T}_e)^T \cdot [e_x \boldsymbol{T}_p \cdot \boldsymbol{U}_p + (1 - e_x)\boldsymbol{T}_N \cdot \boldsymbol{U}_N] \tag{3.31}$$

where T_P, T_N and T_e are transformation tensors from the global Cartesian coordinate system to the edge-based local coordinate system and e_x is the interpolation factor which is calculated

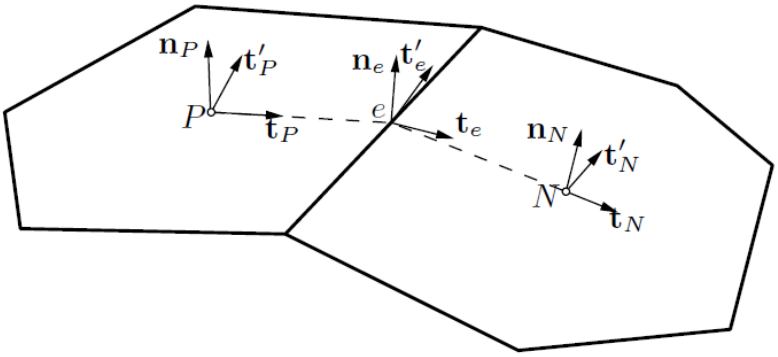

Fig. 3.8 Edge-based local coordinate system, from Tukovic and Jasak (2008).

as the ratio of the geodetic distance $\overline{eN}$ and $\overline{PeN}$:

$$e_x = \frac{\overline{eN}}{\overline{Pe} + \overline{eN}} \tag{3.32}$$

Thus, a finite area mesh is built from the bottom boundary of the three-dimensional finite volume mesh for the flow field. The bed shear stress calculated with finite volume mesh from the velocity field is mapped onto the finite area mesh and the bed load transport model is then solved directly on the finite area mesh. The bed load transport rate $\boldsymbol{q}_b$, the entrainment rate E and the deposition rate D are all calculated on the finite area mesh and finally the bed level change is obtained by solving Eq.(3.30) on the finite area mesh.

3.2.2 Dynamic Mesh Deformation

The bed level change calculated from Eq.(3.30) gives information about the displacement of surface centres of the finite area mesh which is also the displacements of the surface centres on the bottom boundary of the finite volume mesh as shown in Fig. (3.9).

The mesh deformation feature of OpenFOAM however, requires the displacement of mesh points to deform the mesh. So the displacements of surface centres are transformed through interpolation to the displacements of surface mesh points. The mesh points on the bottom boundary of finite volume mesh then move according to the displacement information given.

After the deformation of the bottom boundary, the mesh needs to be smoothed to avoid large distortions in certain cells. OpenFOAM provides a mesh smoothing mechanism which smooths the mesh by solving the Laplace equation on the whole mesh domain:

$$\nabla \cdot (\gamma \nabla \boldsymbol{v}) = 0 \tag{3.33}$$

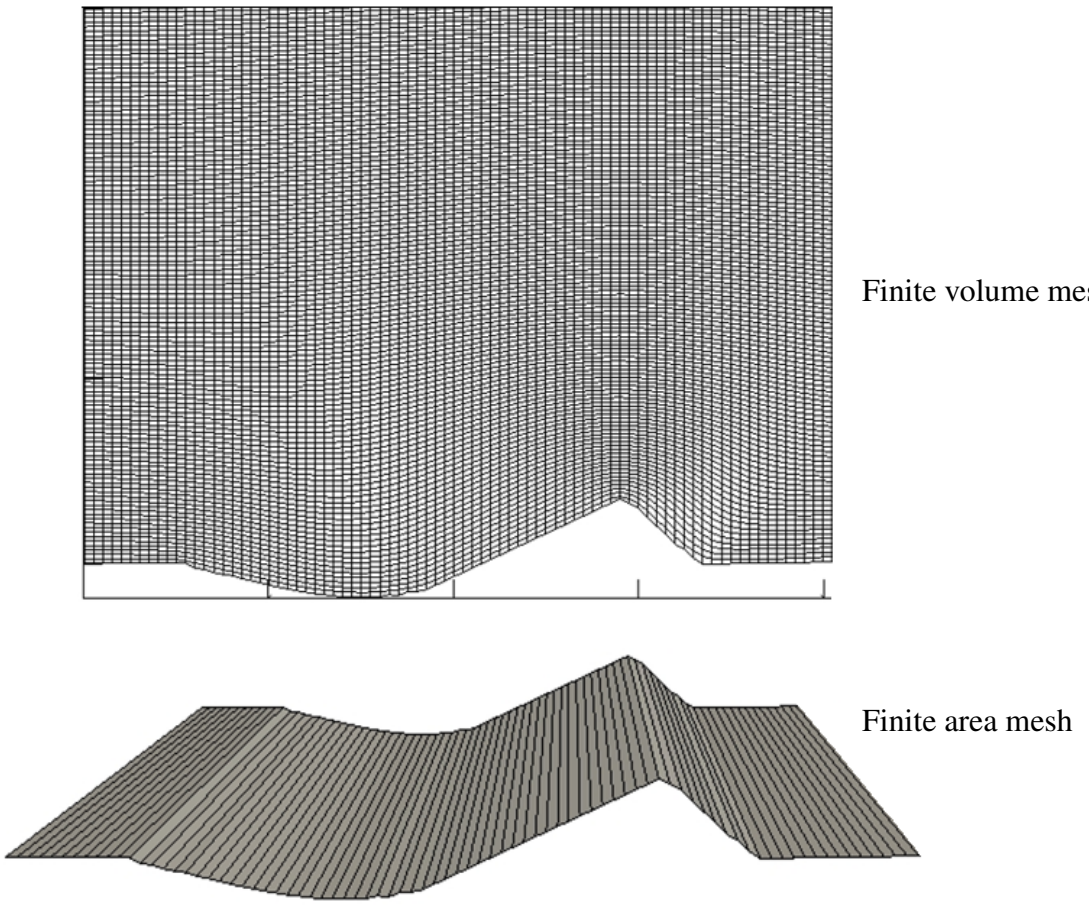

Fig. 3.9 Displacement of finite area mesh and finite volume mesh.

where v is the displacement velocity of grid cell centres and γ is a diffusion coefficient whose value depends on the dynamic conditions of the simulation (for further details, see Jasak and Tukovic (2006)). Then the whole finite volume mesh is smoothed according to the solution of Eq.(3.33).

The bed deformation calculated from the Exner equation can cause stability problems as discussed in several previous studies (Johnson and Zyserman, 2002) (Callaghan et al., 2006). The instability can be caused by the non-linear relationship between the sediment transport rate and bed level change and the existence of numerical errors. So numerical filters are commonly applied to the bed level change or the bed load transport rate calculated to avoid the instability as in Jensen et al. (1999) and in Niemann et al. (2011). On the other hand, some modified numerical schemes are proposed to avoid the instability of Exner equation. The Weighted Essentially Non-Oscillatory (WENO) scheme proposed by Liu et al. (1994) and the Non-Oscillatory Centred Scheme (NOCS) used by Callaghan et al. (2006) and Marieu et al. (2008) are two examples of this.

In our study, when calculating the bed level change, i.e., the displacements of the surface mesh centres Δh, the dynamic mesh feature interpolates the displacements of surface mesh centres calculated from Eq.(3.30) to obtain the displacements of the surface mesh points and the new surface mesh is defined by the new positions of the surface mesh points. As a result, the actual bed level change is obtained by:

$$\Delta h^j = 0.25(\Delta h^{j-1} + \Delta h^{j+1}) + 0.5\Delta h^j \tag{3.34}$$

where j indicates the surface's label. Eq.(3.34) acts already as a numerical filter on the boundary mesh movement and helps to stabilize the simulation so no other filters are used in this work. It should be noticed that Δh is not the bed level height but the variation of the bed level height.

3.2.3 Sand-Sliding Mechanism

A sand-sliding mechanism is necessary to limit the bed slope to be below the critical bed slope which is normally considered to be the same as the repose angle of the sediment. A test by Liang et al. (2005b) which is shown in Fig. (3.10) illustrates the importance of the sand-sliding mechanism. We can see that the scour hole simulated without the sand-sliding mechanism allows very large movement of mesh points, and this can cause large distortions of the mesh and failure of the simulation.

The sand-sliding mechanism included is the method used in Marieu et al. (2008) which is illustrated in Fig. (3.11). The bed slope angle of each surface on the finite area mesh

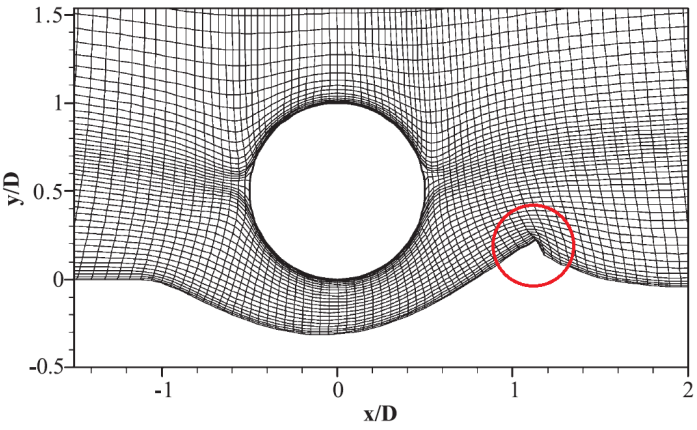

(a)

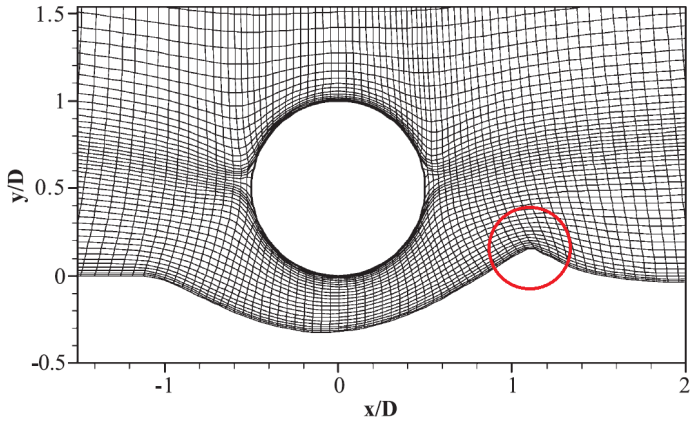

(b)

Fig. 3.10 Simulation of scour below a pipe line with and without sand-sliding model: (a) without sand-sliding model, (b) with sand-sliding model, from Liang et al. (2005b).

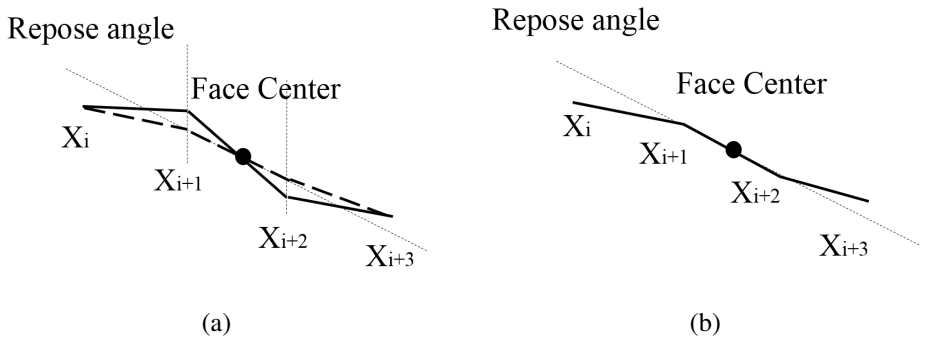

Fig. 3.11 Correction of the bed slope with the sand-sliding mechanism: (a) bed slope before correction, (b) bed slope after correction.

is checked. If the bed slope is larger than the critical bed slope then the surface is rotated around its surface centre to change the bed slope to the critical bed slope. Then the check starts again until no surface slope exceeds the critical bed slope. The details of the algorithm to perform the sand-sliding and the mass conservation problems are presented in Appendix B. The implementation of the sand-sliding mechanism in our model has been verified using a test case as described in section 3.2.5.

3.2.4 Morphological Update Routine

The time step of the morphological module is not the same as that of the hydrodynamic module, because the bed form varies very slowly compared with the evolution of the velocity field. The recalculation of the bed form, and consequent re-meshing of the flow domain, are computationally quite intensive, so we decided to use a larger time step for morphological module in the model to reduce the overall computational time.

Practically, this dual time step is implemented in the code using an indicator N which is initially set to zero. N increments by 1 every time a hydrodynamic time step is completed, and when N exceeds some predetermined threshold M, the morphological module is invoked to recalculated the bed form, using as its time step the total number of elapsed hydrodynamic time steps since its previous invocation. N is then reset to zero. The overall flow chart for the numerical model is shown in Fig. (3.12).

A preliminary test has been done to validate this dual time step method for the two-dimensional scour simulation in this work. We simulated the same case, firstly with identical time steps for the hydrodynamic and morphological modules, i.e., $M = 1$, and then with a time step for the morphological module that was ten times that for the hydrodynamic module, i.e., $M = 10$. The results were almost identical, so we can conclude that using $M = 10$ for

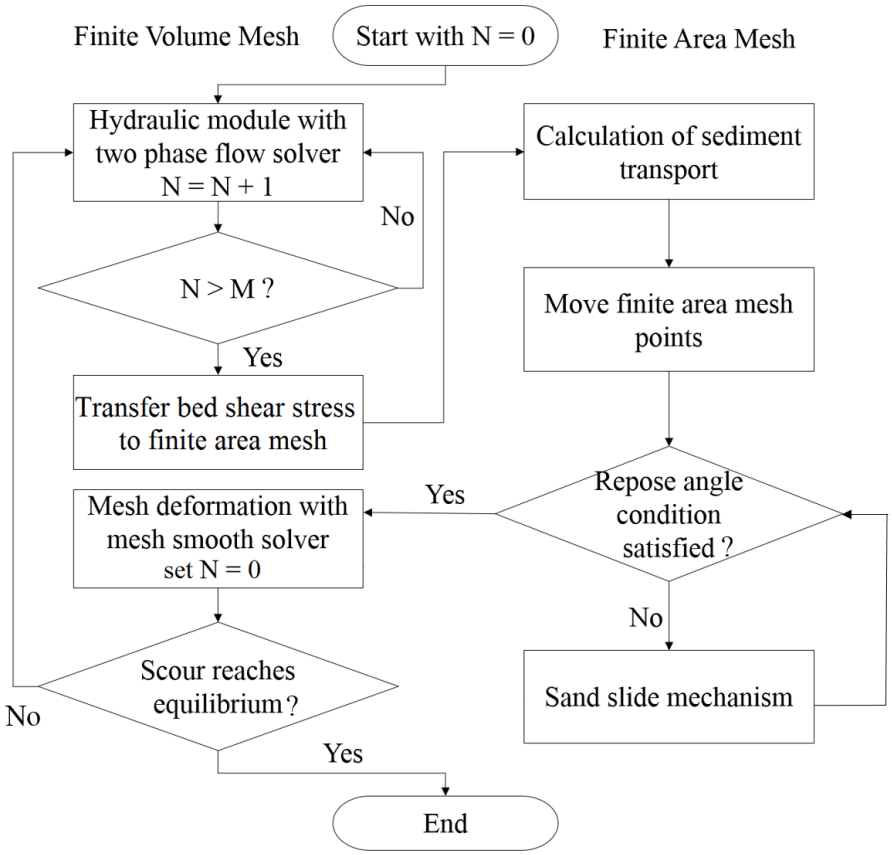

Fig. 3.12 The overall flow chart of the numerical model.

the morphological module will not influence the final results in this simulation. For the three-dimensional simulation of scour around a cylinder in current, the dual time step is set to be $M = 5$, which should also be an acceptable value. However, a higher value of M may considerably accelerate the simulation, so more discussions should be done in the future to choose a more proper value of M.

3.2.5 Test Case: Avalanche of a Sand Heap

A heap of sand with initial slopes larger than the pre-determined critical bed slope is used as test case for the performance of the sand-sliding mechanism. A sketch of the case can be seen in Fig. (3.13). The left slope angle is 40° and the right slope angle is 35°. The critical bed slope is set to be 30° so both of the slopes need to be corrected, but the correction will be different on each side. This test case is designed to test only the sand-sliding mechanism so no flow field or sediment transport models are included in the simulation. Therefore, no equations are solved except for the Laplace equations for smoothing the finite volume mesh.

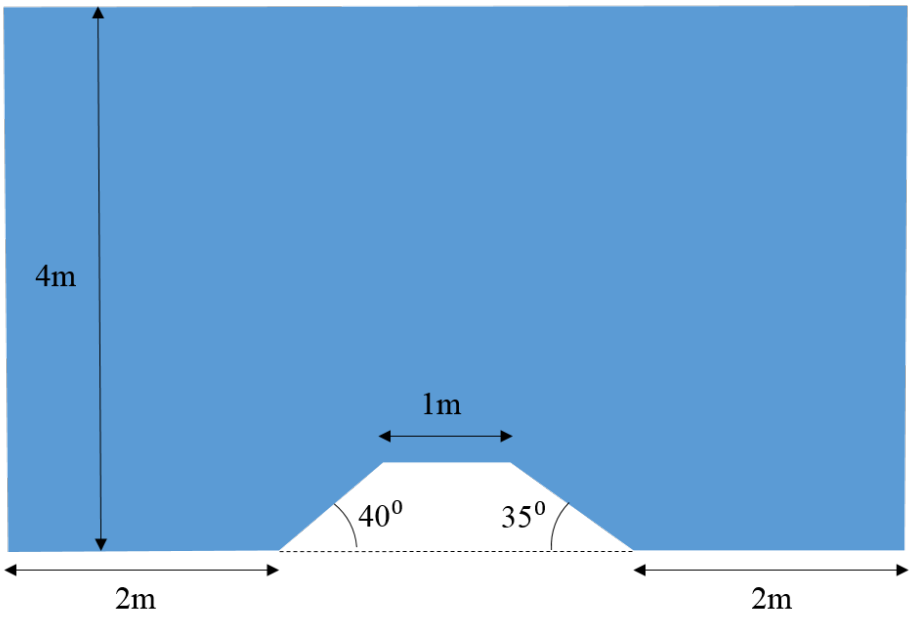

Fig. 3.13 Test case: Avalanche of a heap of sand.

The computational mesh for this test case is two-dimensional and is generated by *blockMesh* utility which contains 18000 cells with grid resolution $\Delta x_{min} = 0.04\,\text{m}$ and $\Delta y_{min} = 0.04\,\text{m}$. The convergence criteria for mesh point displacements solver is set to be 10^{-6}. The boundary conditions for the mesh point displacements are fixed to zero for all the boundaries except for the bottom boundary where the values are given by the sand-sliding mechanism.

The displacements of the mesh points after the sand-sliding procedure are shown in Fig. (3.14). The initial and final mesh are shown in Fig. (3.15). This test demonstrates that the sand-sliding mechanism works correctly to restrict the bed slope to the critical bed slope.

3.3 Parallelization of the Model

In order to reduce the computational time , it was decided to parallelize the model. But we encountered several practical problems in implementing this. First of all, the finite area mesh does not support mesh deformation in parallel in Foam-extend. So when decomposing the mesh, the bottom boundary of the finite volume mesh needs to be assigned to the same processor. Secondly, the parallel calculation on the deforming finite volume mesh also caused problems. In this section, we will introduce the methodology of parallel computing in OpenFOAM, and the correction mechanism added in the model to solve some problems due to parallelization.

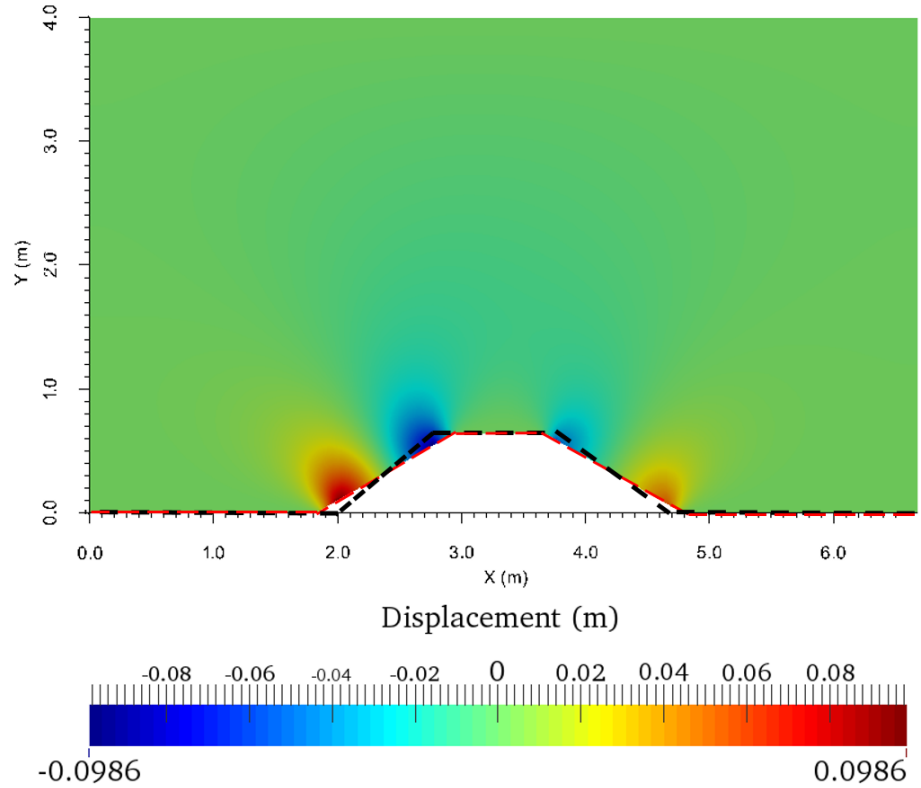

Fig. 3.14 Displacements of mesh points after the sand-sliding mechanism. The black dashed line represents the initial bottom boundary of the mesh and the red dashed line represents the bottom boundary of the mesh after sand-sliding mechanism.

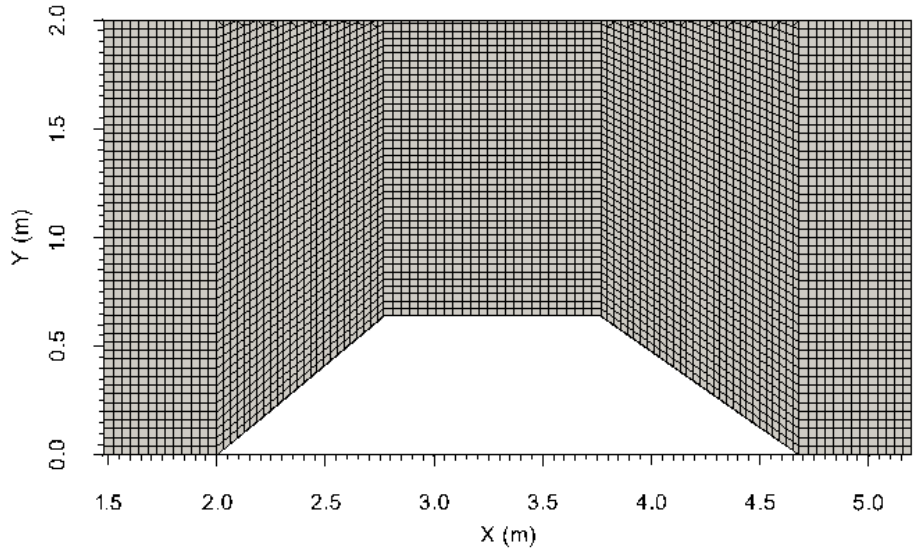

(a) Initial mesh.

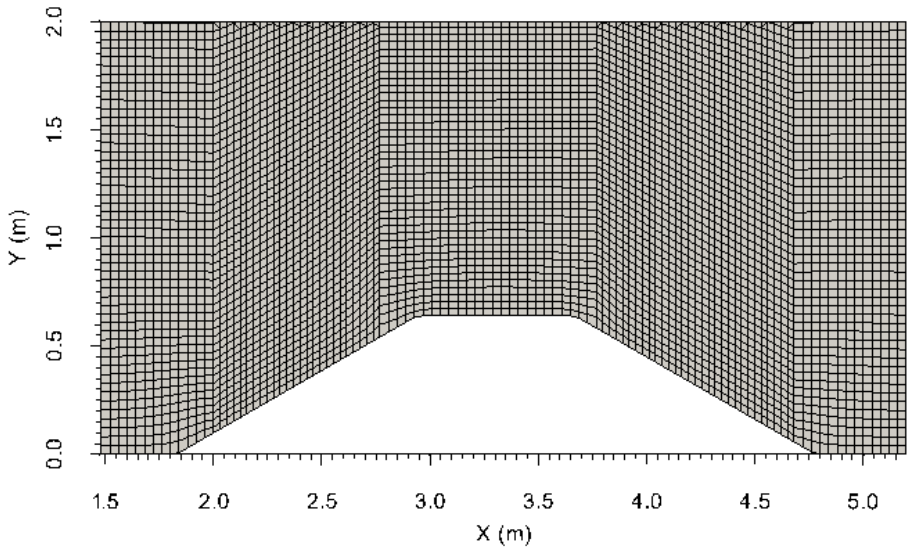

(b) Deformed mesh after sand-sliding mechanism.

Fig. 3.15 Deformation of the mesh before and after the sand-sliding mechanism.

3.3.1 Domain Decomposition Methodology

Several decomposition methods are proposed in OpenFOAM. Among them, four types of commonly used methods are: *simple*, *hierarchical*, *metis* and *manual*. The details of these methods are presented below.

- **Simple decomposition**: Split the domain into sub-domains only by direction. The user can choose the number of sub-domains in each direction.
- **Hierarchical decomposition**: Same as simple decomposition, except that the user can specify the order of decomposition.
- **Metis decomposition**: This decomposition approach automatically decomposes the domain and gives an optimal solution with a minimal number of boundaries. It no longer requires user's input but the user can give an optional keyword to specify different performance factor between processors.
- **Manual decomposition**: Manually specify the location of each mesh cell.

After the decomposition, the mesh faces can be divided into three groups:

1. Internal faces: The internal faces are in the interior of the mesh.
2. Boundary faces: The boundary faces form boundaries even before the decomposition.
3. Inter-processor boundary faces: The inter-processor boundary faces used to be internal faces before the decomposition of the mesh but become boundary faces after the decomposition. These faces are duplicated and represented on 2 processors. No face may belong to more than 2 sub-domains. These inter-processor boundary faces form new boundaries which are called the processor boundaries.

Traditionally, FVM parallelization uses the *halo layer* approach: data for cells next to a processor boundary are duplicated. However, in OpenFOAM, the *zero halo layer* approach is used. Each cell belongs to one and only one processor without inherent overlap for computational points (Jasak, 2012). Only the inter-processor boundary faces and the mesh points belong to these faces are duplicated as shown in Fig. (3.16). A boundary type called 'processor' is defined and will be given to processor boundaries automatically which includes communication functions and information about the neighbor boundaries which contain the same faces. The communication between processors is done by Message Passing Interface (MPI).

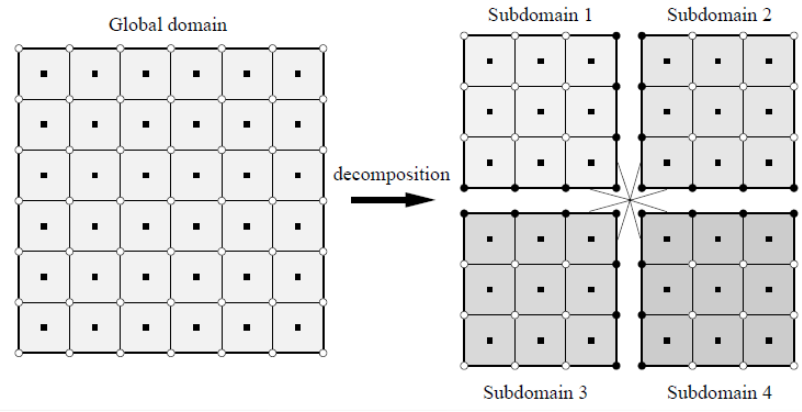

Fig. 3.16 Decomposition of the global domain, from Jasak (2012).

3.3.2 MPI Communication Description

OpenFOAM framework implements MPI message passing by Pstream, which serves as a parallel communication protocol. It is a shared library which contains two sub classes named IPstream and OPstream, respectively for receiving data and sending data. MPI environment routines are used to initialize and terminate MPI parallel running. Several commonly used routines are:

- *MPI_Init*: Initialize the MPI environment.
- *MPI_Comm_size*: Determine the number of processors.
- *MPI_Comm_rank*: Determine the rank of processors within group.
- *MPI_Abort*: Terminate all MPI process when error is happened.
- *MPI_Finalize*: Terminate the MPI enviroment, last MPI routine call.

If the simulation is running in parallel, the first three routines mentioned above are called by *Foam::Pstream::init* which is referenced from the main function. When the simulation is terminated, the later two routines are referenced by the main function and the *Foam::handler* function.

For communication schemes between processors, two candidates are embedded in OpenFOAM: linear communication and binomial tree communication.

Linear communication is also called master-slave communication or self scheduling. The idea is that each slave processor sends the value of its own sub-domain to the master processor. The master processor then performs operations on gathered data and after that,

broadcasts the data to each slave processors. The slave processors can only communicate with the master processor, and the coordination is done by the master processor.

When the number of processors involved in communication is greater than 16, scatter and gather operations will use a binomial tree-based algorithm. Details of the binomial tree-based algorithm can be found in Preiss (2008). In this scheme, the data communication in each step only involves a peer-to-peer scheme which reduces the communication overhead. Pješivac-Grbović et al. (2007) show that a tree-based communication scheme is more efficient than linear-based schemes when the numbers of nodes becomes large; also when the number of messages is large but their size is relatively small, the quality of communication can benefit from a binomial tree algorithm. These two communication schemes are shown in Fig. (3.17).

The operations of collective communication can be divided into two types: Data movement, which includes data scatter and gather operations; and Reduction, which is based on data movement operation to not only collect and scatter data from all processors, but also conduct certain computations with the data.

The data movement operations can be done in three ways:

1. *Pstream::gather* and *Pstream::scatter*: These classes only consider the standard data movement. One processor gathers data from all other processors according to the communication schedule. The user-defined calculations will be performed on the gathered data. After all the data have been processed, the processor will scatter data back to each processor. The gathered data here consist of single values and the calculation is done within the gather function.

2. *Pstrem:: gatherList* and *Pstream::scatterList*: These classes are similar to previous classes, but the data gathered can be a list of values from each processor. No calculation will be performed during the gather and only the master processor holds all the lists. Then the master processor will broadcast all the lists to each processor.

3. *Pstream::combineGather* and *Pstream::combineScatter*: These classes are similar to the standard gather and scatter classes, but more data types and calculations could be allowed.

The reduction operations can reduce all types of the variables defined in OpenFOAM. The types of operators allowed include *sum*, *min*, *max*, etc.

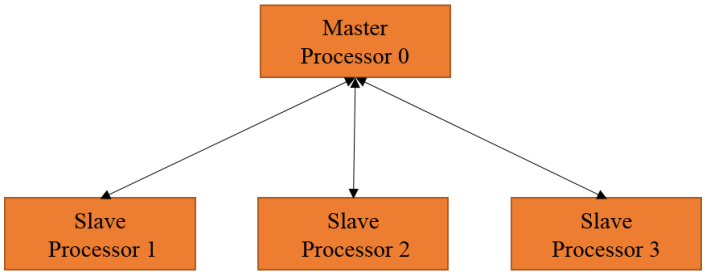

(a)

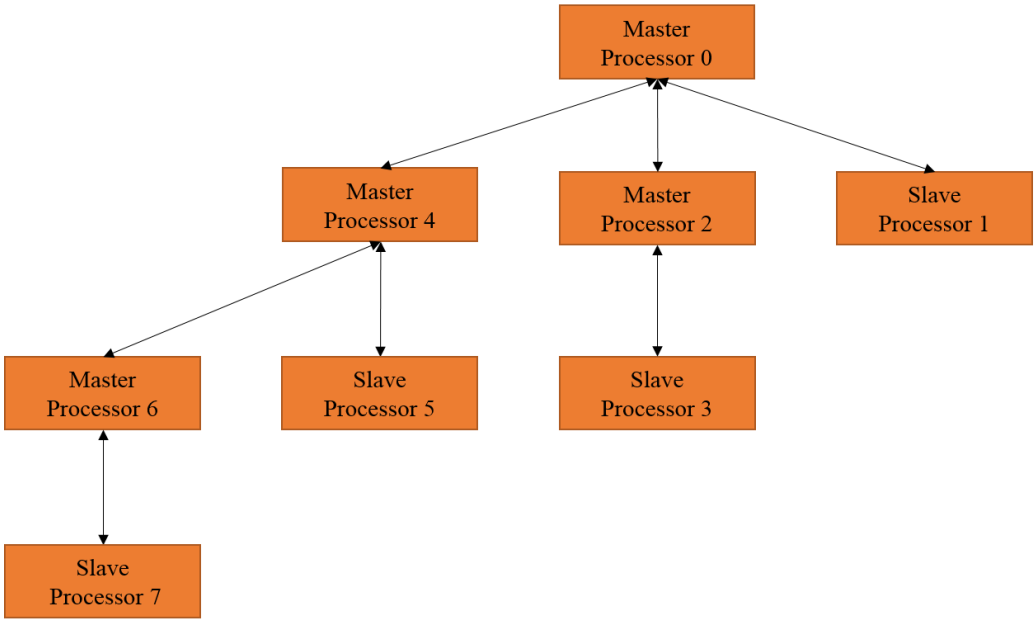

(b)

Fig. 3.17 Communication schemes between processors: (a) linear communication schemes, (b) binomials tree communication schemes.

3.3.3 Correction of Displacements on Processor Boundaries

When establishing and testing the model, a problem arose caused by the parallelization; the displacements of points on the processor boundaries were not calculated correctly, and were usually smaller than they should have been. This was caused by the interpolation routine used to transfer the displacement of mesh cell centres to mesh points on the processor boundaries, because the routine could not use values from cells assigned to neighbouring processors, even though those values should also influence the displacement of the duplicated processor boundary points.

To correct for this, we introduced a routine to gather the required displacements of mesh cell centres from neighbouring processors, based on *Pstrem::gatherList* and *Pstream::scatterList* classes. Examples of the non-corrected deformed mesh and corrected deformed mesh are shown in Fig. (3.18). In this exemple, the mesh is two-dimensional and is generated by *blockMesh* utility which contains 6600 cells with grid resolution $\Delta x_{min} = 0.02\,\mathrm{m}$ and $\Delta y_{min} = 0.01\,\mathrm{m}$. During the deformation, the bottom boundary of the mesh moves downward and the mesh is then smoothed. When calculating in parallel, the mesh is decomposed into four sub-domains with two sub-domains in each direction. We can see that without correction mechanism, the mesh points on processor boundaries do not move correctly which can cause very serious problems to the simulation. With correction mechanism, the displacements of mesh points on processor boundaries can be correctly calculated and the mesh is very well smoothed. In conclusion, the correction mechanism is necessary and it works as intended.

3.4 Conclusions

A morphological module has been developed to compute the sediment transport and the consequent deformation of an erodible bed. The suspended load is calculated by solving an advection-diffusion equation with a boundary condition defined using the entrainment and deposition rates. The bed load transport rate is calculated using the empirical formula proposed by Engelund and Fredsøe (1976). The performance of the suspended load transport has been validated by simulating the entrainment of the sediment from a flat bed and comparing with the measured data from van Rijn (1986). The changes in bed level are obtained by solving the continuity equation for sediments on a finite area mesh constructed from the bottom boundary of the finite volume mesh which represents the bed surface. Once the new bed form has been computed on the finite area mesh, the finite volume mesh is deformed to follow the new bed contours, and is smoothed by solving the Laplace equations for displacements of mesh points. Moreover, a sand-sliding mechanism, which is essential to the stability of the simulation, is included in the model and has been validated by computing

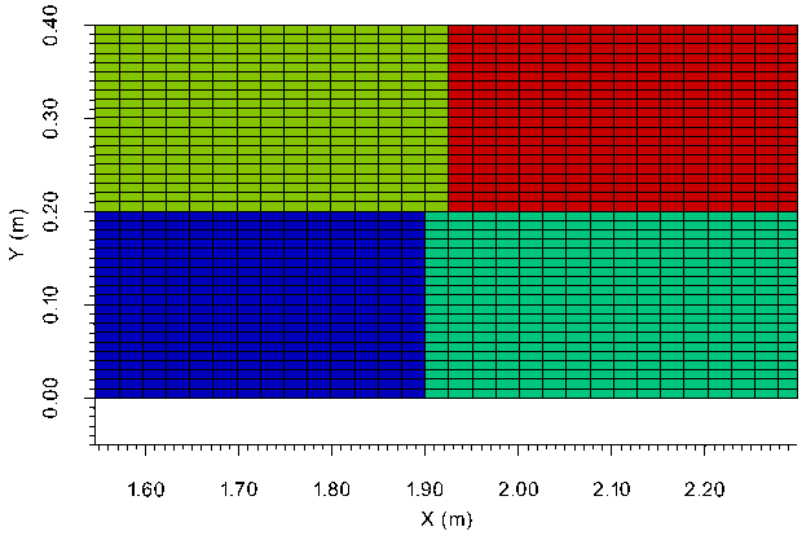

(a) Initial mesh. Each colour represents the cells assigned to the same processor.

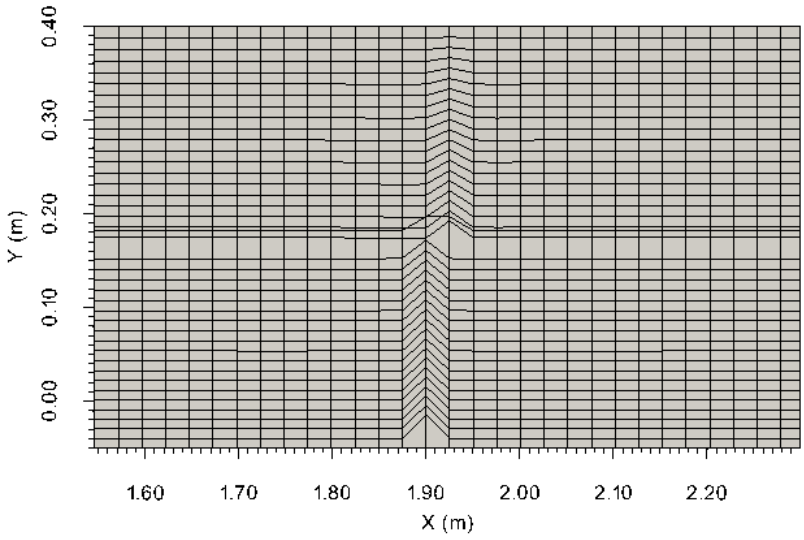

(b) Deformed mesh without correction.

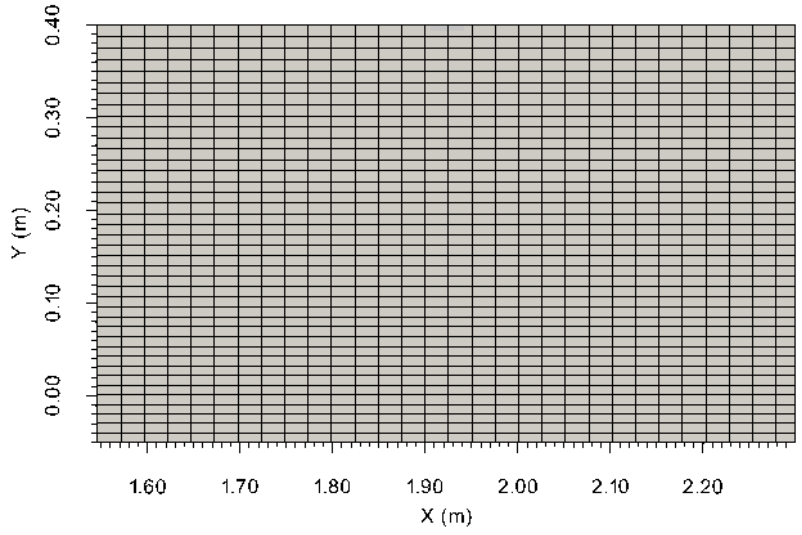

(c) Deformed mesh after correction.

Fig. 3.18 Validation of the correction mechanism for mesh deformation in parallel.

the avalanche of a heap of sand. The time step for the morphological module is set to be larger than that of the hydrodynamic module to reduce the computational time, and a correction mechanism has been included in the model to ensure the correct displacements of the mesh points on processor boundaries. The performance of the complete model will be validated by simulating a two-dimensional scour caused by a submerged jet which will be presented in Chapter 4.

Chapter 4

Two Dimensional Simulation of Submerged Jet Scour

To test the performance of the numerical model established, a two-dimensional scour caused by a submerged jet issuing under a sluice gate with an apron was chosen as the test case. The experimental measurements of the flow field and the development of the scour of this test case were introduced by Chatterjee and Ghosh (1980) and Chatterjee et al. (1994). In this chapter, we will present first the experimental and numerical set-up of the test case. Then the simulation results are compared with the experimental data. At last we will discuss the performance and the limitation of the numerical model. The work in this chapter has been presented in Zhou and Perkins (2016).

4.1 Laboratory Study Details

Chatterjee and Ghosh (1980) and Chatterjee et al. (1994) presented experiments to study the phenomena of local scour and sediment transport due to a horizontal jet issuing from a sluice. The jet flows over a rigid apron, then onto an erodible bed. Based on experimental data, the scour characteristics have been correlated through the development of empirical expressions for the time to reach equilibrium stage, the locations of maximum scour depth and peak of dune, and the variation of maximum scour depth with time. In this section, we will introduce the details of the experimental study of the test case which will be used later to test the performance of the numerical model established.

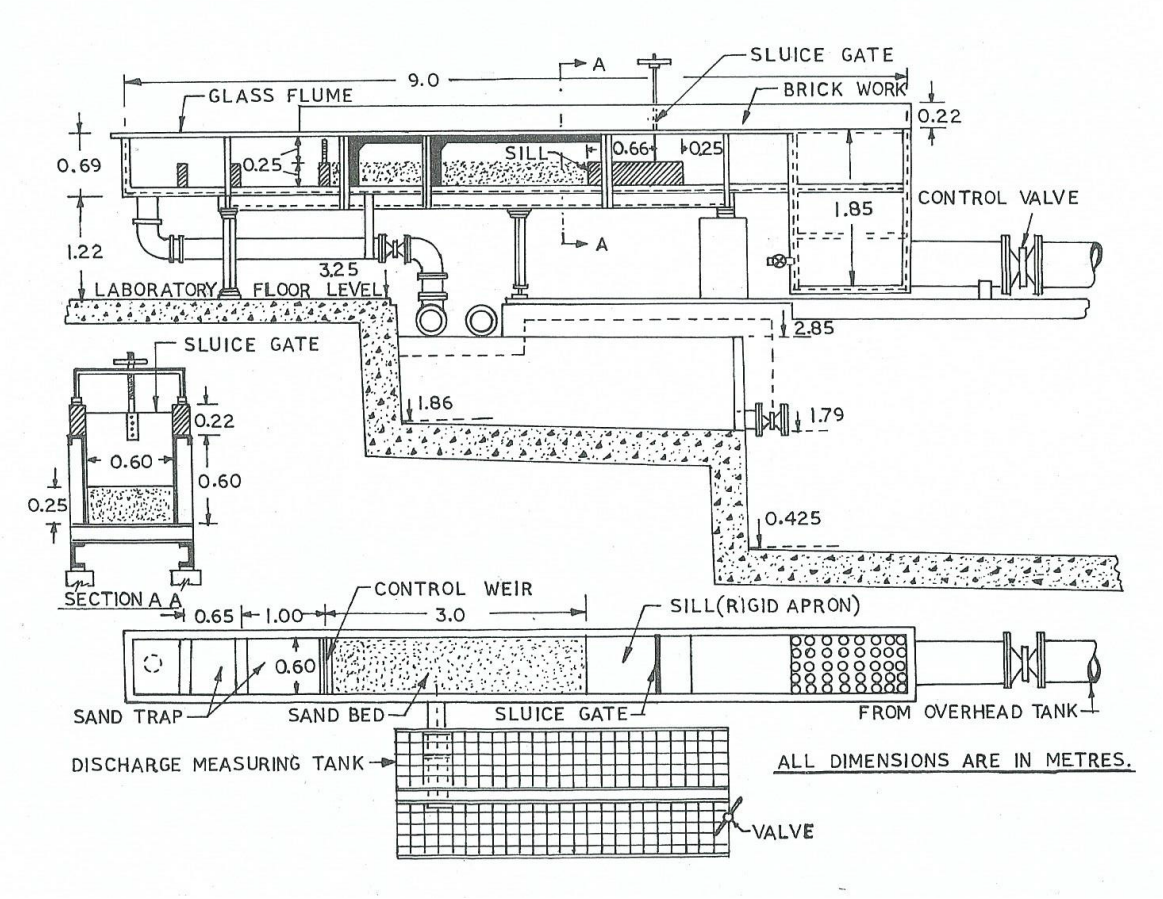

Fig. 4.1 Schematic of experimental set-up, from Chatterjee et al. (1994).

4.1.1 Experimental Set-Up

The experiments have been conducted in a glass-walled flume, as shown in Fig. (4.1). The length of the rigid apron after the sluice gate is 0.66 m and the flume is 0.6 m wide and 3 m long. The flume is supplied with water from a tank through an inlet pipe and a stilling pool and the downstream end of the flume is connected to an outlet pipe that discharges water into a measuring tank to measures the volumetric discharge rate. The velocity and dynamic pressure were measured with a micropitot tube and a preston tube.

The experiments have been performed on two erodible beds, one consisting of sand and the other of gravel. The experiments performed with sand bed are the ones that we wanted to simulated so only the information of the sand used in the experiments is given in this thesis.

The grain-size distribution curve of the sand is presented in Fig. (4.2). The d_{50} of the sand is 760 µm and the density of the sand is 2650 kg/m^3. The estimated settling velocity V_s given in Chatterjee and Ghosh (1980) is 0.122 m/s and the porosity of the sand given is 0.43. The sand repose angle measured in the experiment is 29°. The characteristics of the bed

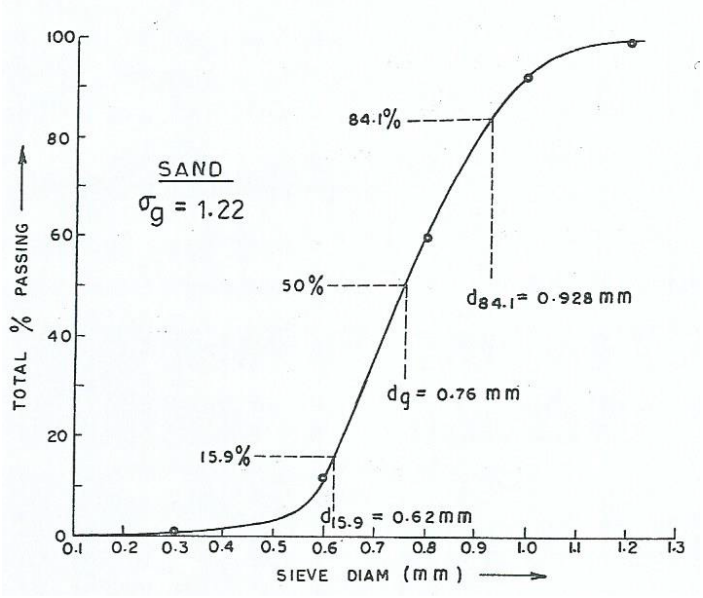

Fig. 4.2 Grain size distribution curve, from Chatterjee et al. (1994).

material are summarized in Table 4.1 where σ_g represents the geometric standard deviation on sediment grain distribution and ϕ_r represents the repose angle of the sediment.

Table 4.1 Characteristics of bed materials.

Bed material	d_{50} (mm)	σ_g	s	n	V_s (m/s)	ϕ_r (°)
Sand	0.76	1.22	2.65	0.43	0.122	29

4.1.2 Flow Establishment and Measurements

The experimental runs have been undertaken for several different gate openings and for various discharges. Before starting a run, the initial bed level is marked on the glass wall of the flume. Then a two-dimensional submerged horizontal jet is created by applying a suitable head difference across the sluice opening. The flow depth over the erodible bed is maintained by operating the control weir at the downstream end of the flume. As soon as the water flowing from the sluice opening reaches the erodible bed, the movement of bed materials from the end of the rigid apron starts and the geometry of the scour hole starts to change with time. The scour profiles were marked on the glass wall of the flume at various times and then traced on paper. The scour hole is considered to reach equilibrium stage when no movement of grains is observed at the location of maximum depth.

For each run, the experiment was performed twice. The first time was to measure the scour profiles at various instant of time and at the equilibrium stage. The velocity distribution at equilibrium stage at several locations along the central plane of the jet, the downstream flow depth in the undisturbed zone and the discharge have also been measured. The second time is to measure the dynamic pressure using a Preston tube at the location of maximum scour at various instants of time during the development of scour hole.

The run number 2 is the case that we will simulate and the significant test data of this run are presented in Table 4.2. The gate opening B_0 for this run is 0.02 m and the head difference Δh is 0.118 m. The measured efflux jet velocity U_0 was 1.56 m/s and the discharge per unit width q was 0.0204 m^2/s. The time needed to reach equilibrium scour depth T was measured to be 30 min. The temporal development of scour profile measured in this run will be used to compare with the simulation results of the numerical model presented in this thesis. The Froude number Fr, which is a dimensionless number defined as the ratio of the flow inertia to the external field, is calculated for this test case. By definition, the Froude number is obtained from:

$$Fr = \frac{U_0}{\sqrt{g_0 L_0}} \tag{4.1}$$

where U_0 is a characteristic flow velocity, g_0 is a characteristic external field and L_0 is a characteristic length. When applied to the simulation of open channel flow with shallow water waves as we simulated, the Froude number is calculated by:

$$Fr = \frac{U}{\sqrt{gH}} \tag{4.2}$$

where U is the undisturbed mean flow velocity, g is the gravity and H is the water depth. The Froude number in this case equals 0.063 and is very small, so the free surface should not be disturbed much by the variation of the bed form.

Table 4.2 Significant experimental test data.

Run number	B_0 (m)	Δh (m)	T (min)	U_0 (m/s)	q (m^2/s)	H (m)	Fr
2	0.02	0.118	30	1.56	0.0204	0.291	0.063

4.2 Numerical Simulation Details

In this section, we will introduce the numerical set-up of the two-dimensional submerged jet scour test case. The part after the sluice gate and before the control wire is the domain of the

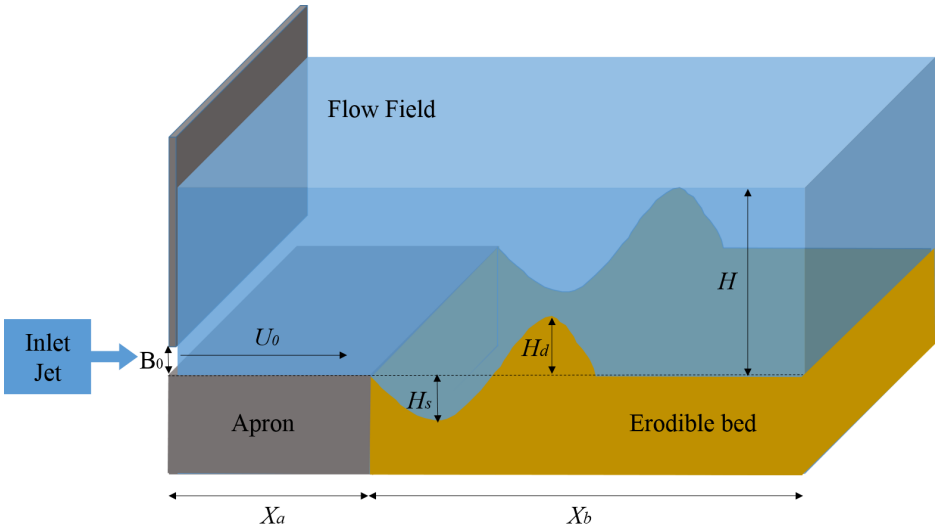

Fig. 4.3 Sketch of the two-dimensional submerged jet scour simulation.

simulation, including the air, water, free surface, rigid apron and erodible bed. A sketch of the simulation domain is shown in Fig. (4.3) where $X_a = 0.66\,\text{m}$, $X_b = 3\,\text{m}$, H_s represents the maximum scour depth and H_d represents the maximum height of sand dune.

4.2.1 Numerical Set-Up

The flow conditions and the sand properties are set to be the same as those in the experiment. For the flow field, RANS modelling with k-ε turbulence model is used. For the sediment transport model, the sand grain used in the experiment is quite large so the settling velocity in water is very high. A preliminary test of the simulation showed that the suspended load concentration was very small and almost had no influence on the scour formation. So the suspended load transport in this test case is neglected.

The density of water is set to be $1 \times 10^3\,\text{kg/m}^3$ and the kinematic viscosity of water is set to be $1 \times 10^{-6}\,\text{m}^2/\text{s}$. The density and kinematic viscosity of air are set to be $1\,\text{kg/m}^3$ and $1.48 \times 10^{-5}\,\text{m}^2/\text{s}$. The friction coefficient of the sand is set to be $\mu_s = 0.554$ which corresponds to the 29° repose angle of the sediment. The *inverse distance* diffusivity is chosen for the dynamic mesh feature which calculates the diffusivity based on the inverse of the distance from each cell centre to the erodible bottom boundary. The time steps were control by the Courant number with $Co < 0.7$ to avoid instability of the simulation. The convergence criteria were set to be 10^{-8} for pressure, velocity, k and ε fields and 10^{-6} for displacements of mesh points.

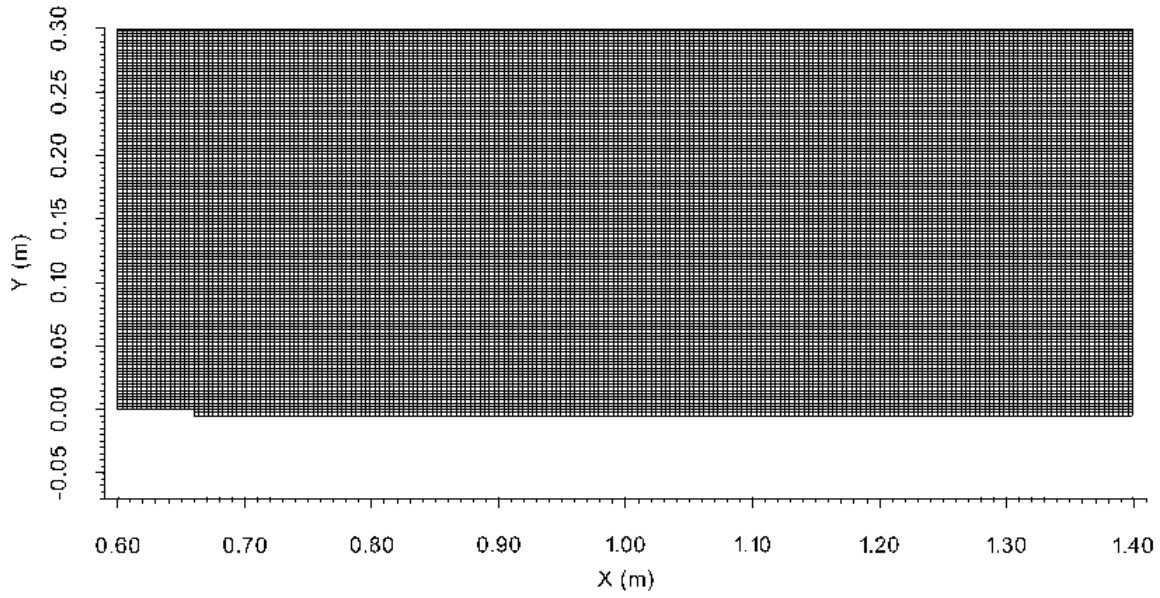

Fig. 4.4 Initial mesh of the two-dimensional submerged jet scour simulation.

4.2.2 Mesh Construction and Boundary Conditions

The finite volume mesh is constructed using *blockMesh* utility of Foam-extend. It is a pseudo 3D mesh with only one layer in the third direction and contains 215000 cells. The initial mesh was defined with constant, uniform values of $\Delta x = 0.003\,\text{m}$ and $\Delta y = 0.002\,\text{m}$. As the simulation progresses, and the computational mesh deforms to follow the eroding bed, the values of Δy for each cell will change, but Δx remains untouched through out the simulation as all mesh points move only in the y direction (the vertical direction) during the deformation. A grid independence test has been done to prove that a finer mesh will not produce very different simulation results. The height of the erodible bed is set to be $z = -0.005\,\text{m}$ while the height of the rigid apron is $z = 0\,\text{m}$ to facilitate the mesh deformation and avoid very large distortions at the connection area between the rigid bed and the erodible bed. Moreover, we found that the bed profile given by the experimental measurement does not conserve the mass of the sediment. The surface of the scour hole region is larger than the surface of the dune region. While in the numerical model, the mass of the sediment should be conserved. With the erodible bed's height initially set as $z = -0.005\,\text{m}$, this also compensates this difference and the numerical simulation could produce the results agree better with the experimental measurements.

Then the finite area mesh is constructed from the bottom boundary of the finite volume mesh which represents the erodible bed which contains 900 cells. Main part of the initial mesh is shown in Fig. (4.4). The boundary conditions defined are presented below:

- **Top boundary**: The top boundary represents the atmosphere so it is set to be the same as in the previous simulations.

- **Rigid bed and erodible bed boundaries**: Both of these two boundaries are *wall* type of boundaries. So the pressure field, the velocity field, α, k and ε are all set to be the same as in the previous simulations. The only difference between the boundary conditions set-ups for the rigid bed and the erodible bed is that the rigid bed uses smooth wall functions while the erodible bed uses rough wall functions with $k_s = 0.004\,56\,\mathrm{m}$.

- **Inlet and outlet boundaries**: The *fixedFluxPressure* boundary condition is applied for pressure field for both inlet and outlet boundaries. A fixed inlet flow rate condition is given to the water inlet boundary and a zero-gradient velocity boundary condition is given to the air inlet boundary. The velocity for the outlet boundary is hard to decide as the water depth in the experiment is controlled by the weir at the outlet but in the numerical simulation it is difficult to fix the water depth at the outlet. In order to solve this problem, the initial water depth is set to be the one that measured in the experiment and a fixed mean velocity is given at the water outlet which guarantees the same inlet flow rate and outlet flow rate. The outlet boundary condition for the air flow is set to be zero-gradient. Thus, the velocity boundary conditions set at the outlet boundaries can adjust the water depth automatically and let it remain at the original height. The field of k and ε are both set to a constant value at the inlet and zero-gradient at outlet.

- **Front and back boundaries**: As the simulation is in 2D, an *empty* type boundary condition is used for all the fields for the front and back boundaries.

4.3 Simulation Results and Discussions

In this section, we will present the simulation results of flow field and scour profile of the two-dimensional submerged jet scour test case, and the simulation results have also been compared with the experimental measurements to test the performance of the numerical model. The numerical simulation takes about 160 h to simulate 30 min experiment in real time with 8 processors. Main part of the deformed mesh at the equilibrium state is shown in Fig. (4.5) and enlarged parts of the deformed mesh at the scour hole and the dune regions are shown in Fig. (4.6). We can see that the deformed mesh is very well smoothed.

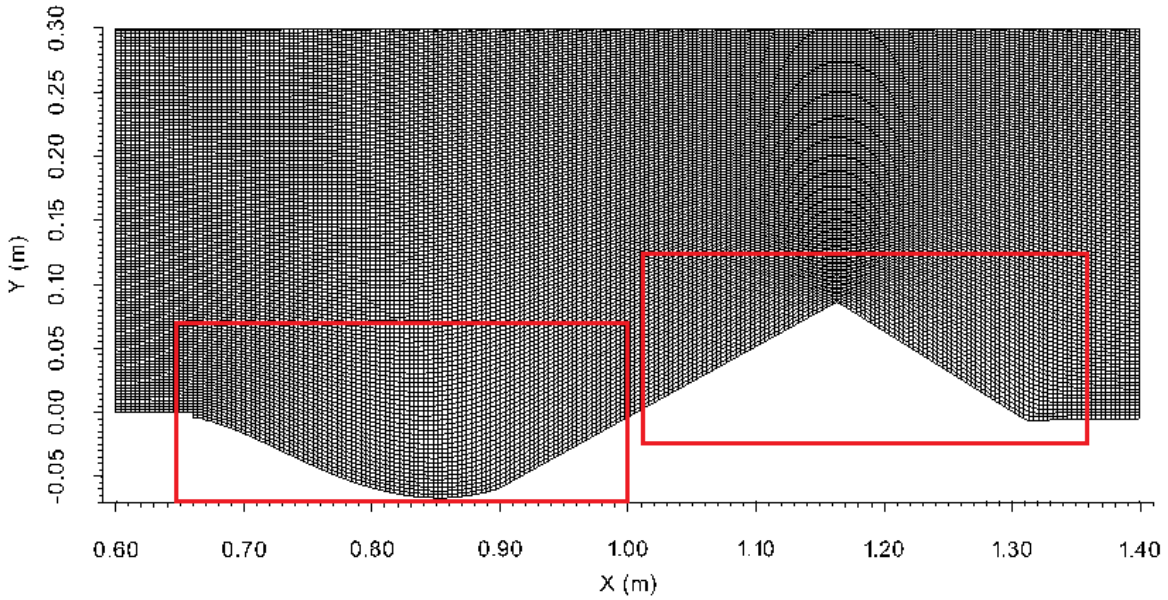

Fig. 4.5 Deformed mesh at equilibrium state. The red square marks the enlarged parts in Fig. (4.6).

4.3.1 Flow Field Simulation Results

The numerical simulation results for the free surface, magnitude velocity and velocity vectors at equilibrium state are shown in Fig. (4.7).

The free surface does not vary much and remains almost horizontal. However, we can observe a blurred zone near the left boundary which is different from the rest of the free surface. In VOF method, the density and the velocity of the fluid in each cell containing a free surface is computed from the weighted-average of the relevant properties of the two phases, using the volume fraction indicator for the cell. So for most of the free surface, the interface between the water and the air is therefore represented by a single layer of cells in which the volume fraction indicator takes a value between 0 and 1, and outside this layer the indicator is either 0, for air, or 1, for water. However, at the upstream end of the simulation, immediately downstream from the sluice gate, this inter-facial layer becomes thicker as shown in Fig. (4.7(a)). From the velocity vector field we can see that this is also a separation zone where the flow hit the sluice gate and the water phase goes downward and the air phase goes upward which may cause some numerical artefacts. The velocity in this region are relatively low, and certainly not sufficient to explain any significant perturbation of the free surface. However, this inaccuracy should not have any influence on the calculation of sediment transport or the erosion.

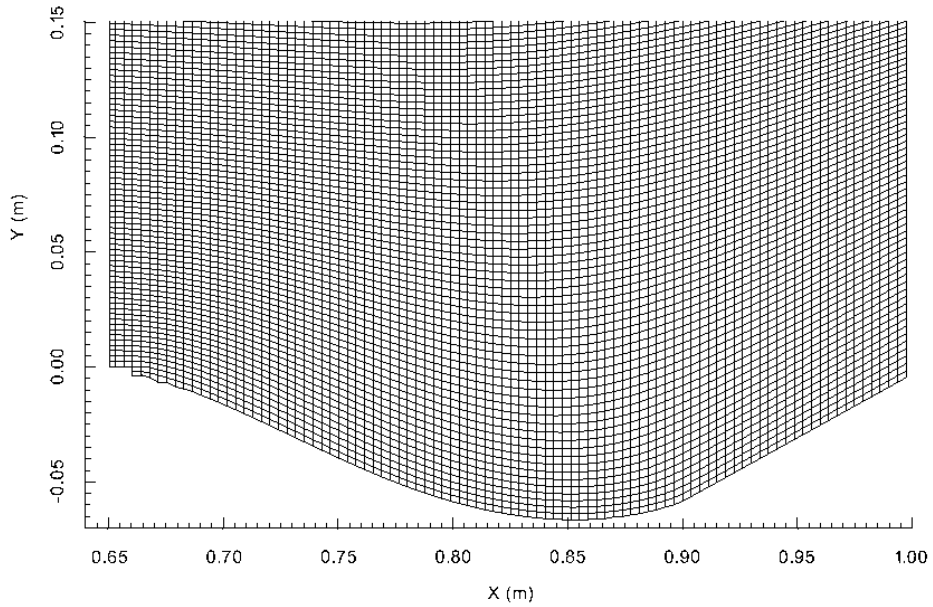

(a) Deformed mesh at the scour hole.

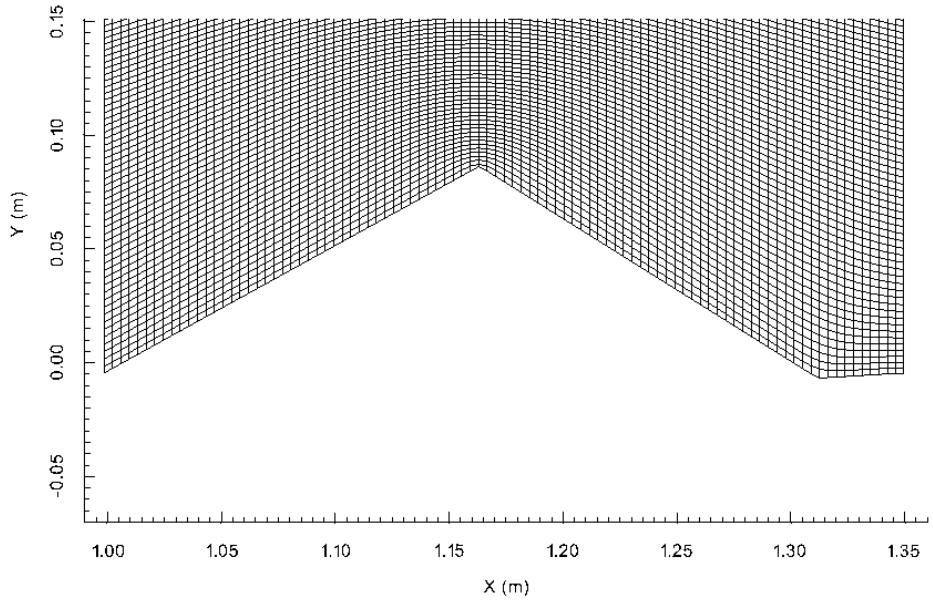

(b) Deformed mesh at the deposition dune.

Fig. 4.6 Enlarged parts of the deformed mesh at equilibrium state.

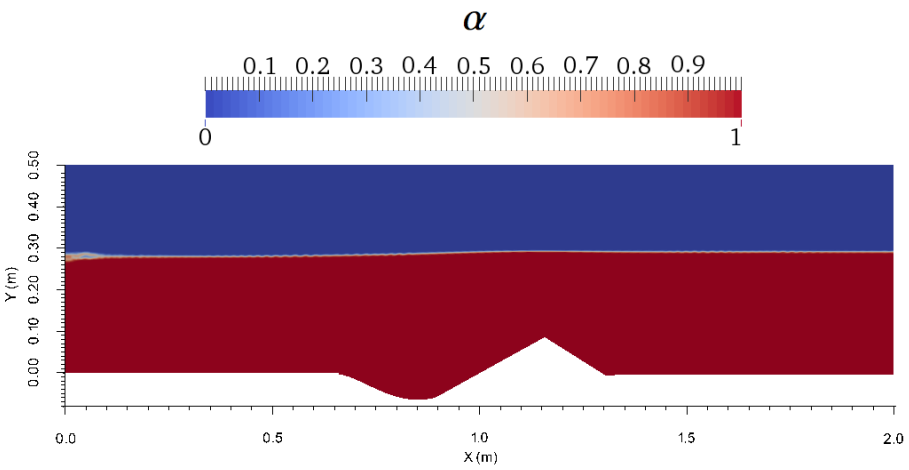

(a) Volume fraction indicator field.

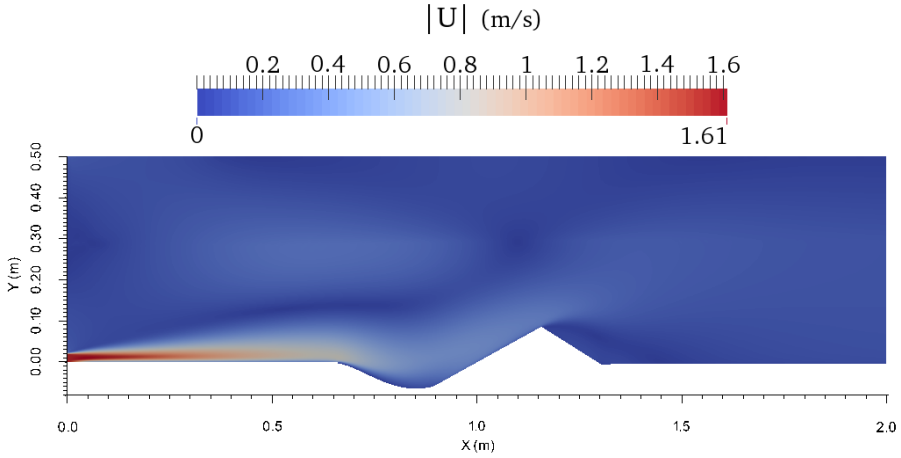

(b) Magnitude of velocity field.

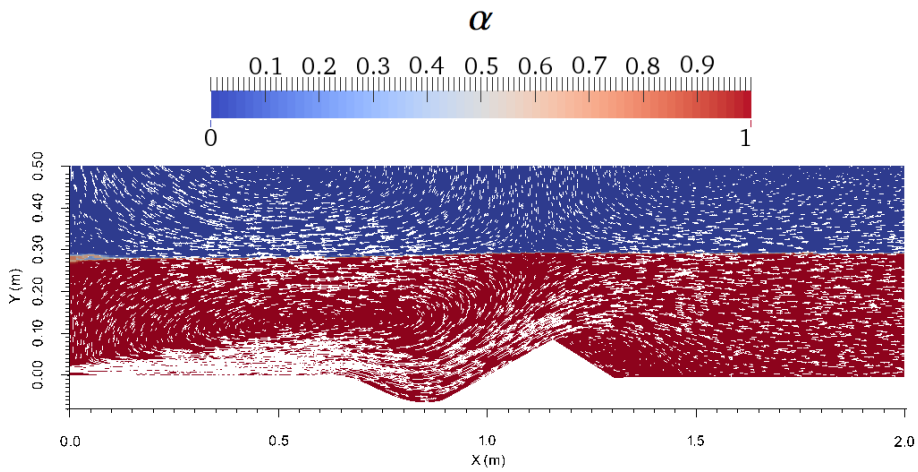

(c) Velocity vector field.

Fig. 4.7 Numerical simulation results of flow field at equilibrium state.

The velocity magnitude field shows the development of the submerged jet along the bed and the velocity vector field shows the reverse flow on the downstream side of the dune and the circular flow in the inlet area. Moreover, the velocity vector field also indicates that the air near the free surface is driven by the movement of the water. The simulation results for the flow field velocity are compared with the experimental measurements form Chatterjee and Ghosh (1980). In the experiment, the velocity field was measured at equilibrium state. In this study, in order to identify the influences of the scour on the flow field, the velocity field was first plotted for a similar simulation but with a fixed bed, then plotted for a simulation with the deformed bed at equilibrium state. The comparison of these two velocity fields and the measured data is shown in Fig. (4.8).

Fig. (4.8(a)) shows the velocity profile in y direction at $x = 0.6\,\mathrm{m}$ which locates at the rigid apron. The velocity profile with and without scour does not show much difference. We can see from this figure that the scour hole may reduce slightly the velocity of the reverse flow. Moreover, the simulation results are in good agreement with the experimental data near the bed and for further away from the bottom, the simulated velocity is slightly lower than the measured one and becomes negative more quickly. The difference between the inlet condition may be responsible for this slight under estimation as in the experiment the submerged horizontal jet is created by applying a suitable head difference across the sluice opening while in the simulation, the jet is created by an uniform inlet velocity equal to the measured jet efflux velocity. The fact that the micropitot tube can not properly measure very small velocities can also be responsible for the difference.

Fig. (4.8(b)) shows the variation of the maximum horizontal velocity along the bed and the corresponding profile of the bed. We can see from the figure that the scour hole does have an influence on the diffusion characteristics of the submerged jet which accelerates the flow at the scour hole region and decelerates the flow at the slop of the sand dune. We can also conclude from the figure that the simulation results at the equilibrium state agree quite well with the experimental measurements.

4.3.2 Temporal Development of Scour

The computed evolution of the bed profile is plotted in Fig. (4.9). We can see the evolution of the scour hole and the dune's height with time. To validate the simulation results, the simulated profile are compared with the measured profile, for 7 different instants up to the time at which the equilibrium scour depth is reached at $t = 1800\,\mathrm{s}$, and the comparison can be found in Fig. (4.10). The evolution of the scour depth H_s and the deposition dune's height H_d are plotted in Fig. (4.11).

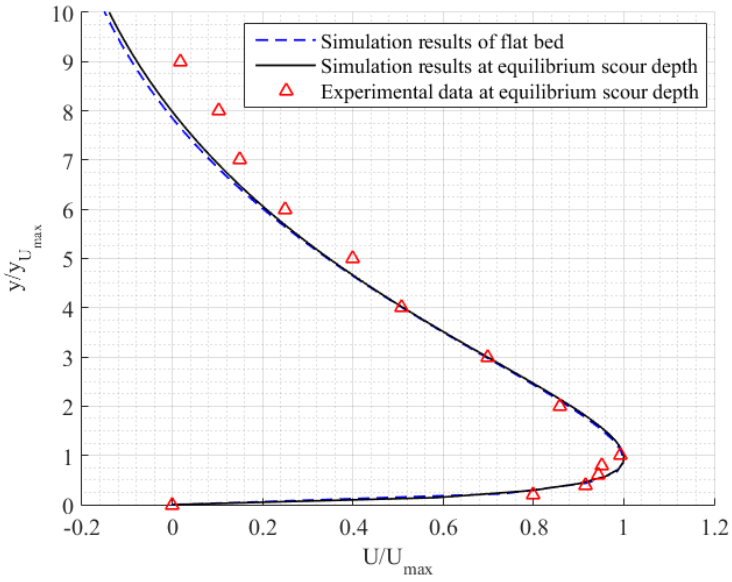

(a) Velocity profile in y direction at x= 0.6m.

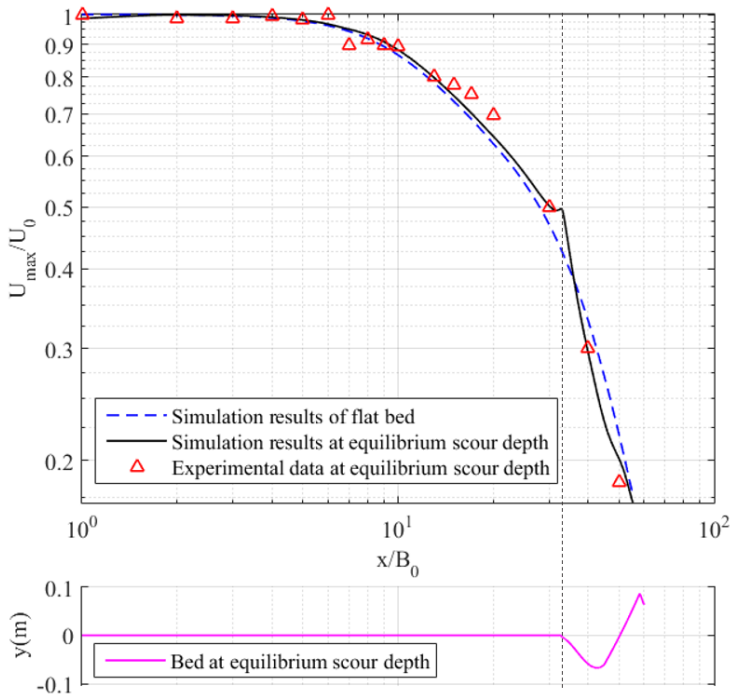

(b) Variation of the maximum horizontal velocity along the bed.

Fig. 4.8 Comparison between simulated and measured velocity of flow field at equilibrium state. U_0 is the inlet velocity and B_0 is height of the inlet gate opening.

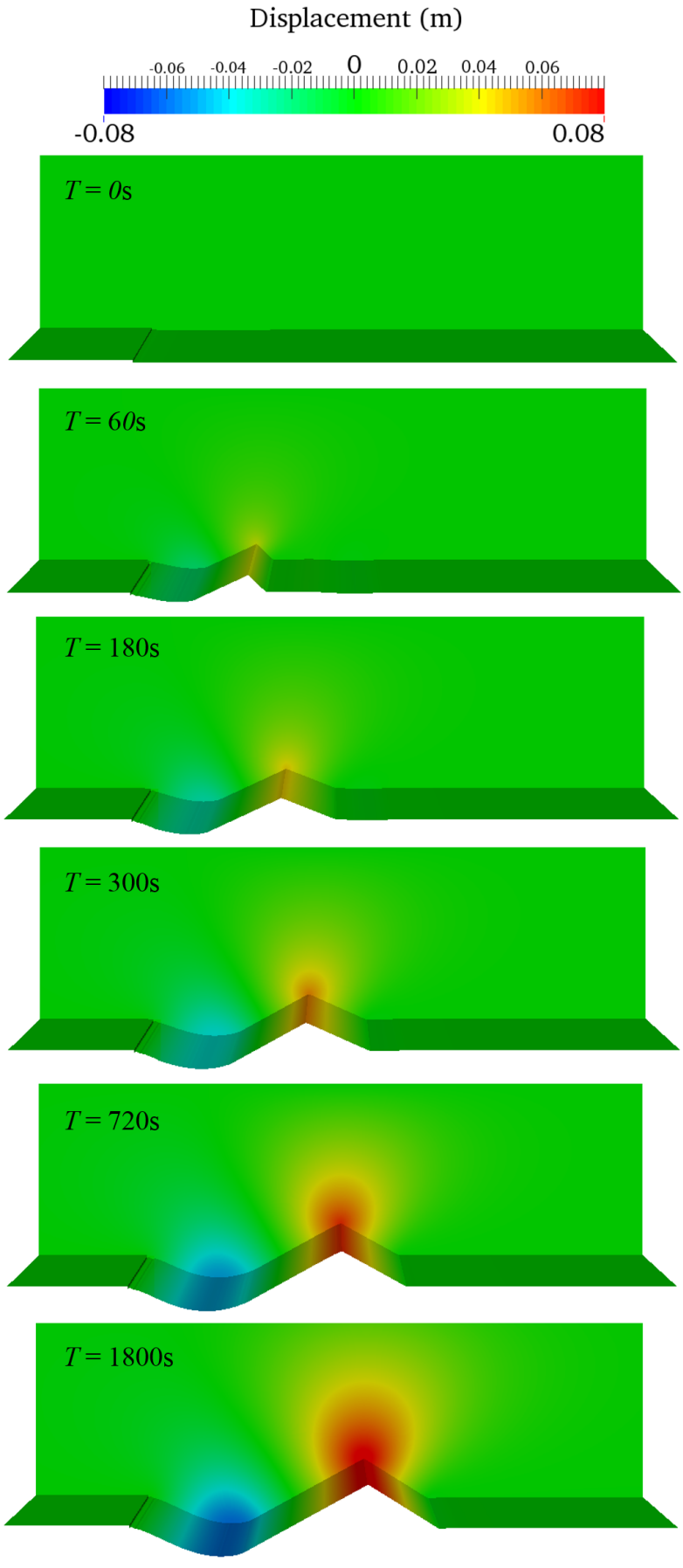

Fig. 4.9 Simulation results of scour profile at $t = 0\,\text{s}$, $t = 60\,\text{s}$, $t = 180\,\text{s}$, $t = 300\,\text{s}$, $t = 720\,\text{s}$ and $t = 1800\,\text{s}$.

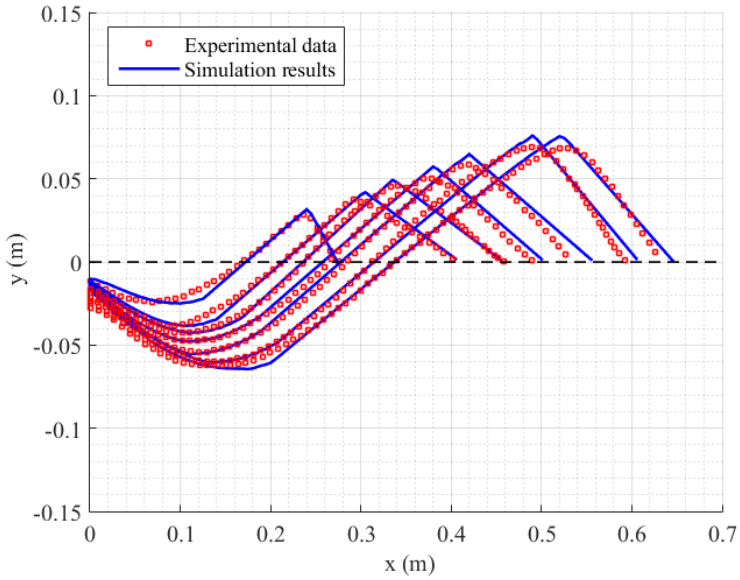

Fig. 4.10 Comparison of the simulated and measured temporal development of scour profile at $t = 60\,\mathrm{s}$, $t = 180\,\mathrm{s}$, $t = 300\,\mathrm{s}$, $t = 480\,\mathrm{s}$, $t = 720\,\mathrm{s}$, $t = 1200\,\mathrm{s}$ and $t = 1800\,\mathrm{s}$.

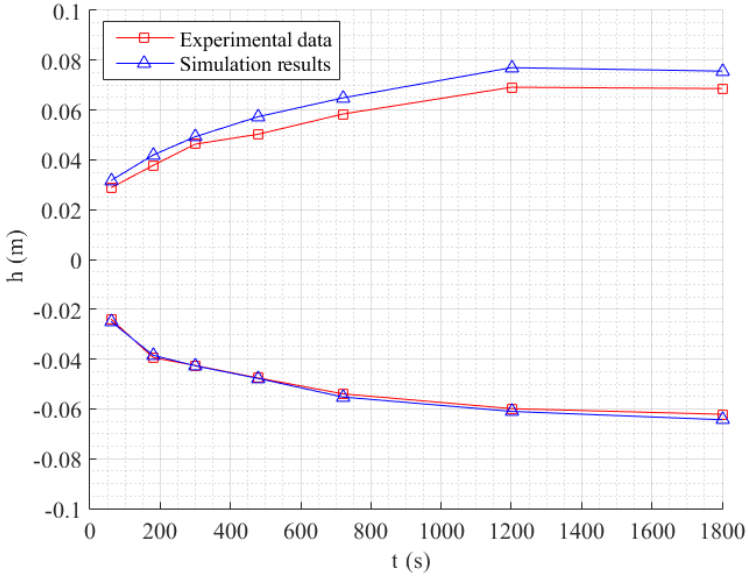

Fig. 4.11 Comparison of the simulated and measured scour depth and dune height at $t = 60\,\mathrm{s}$, $t = 180\,\mathrm{s}$, $t = 300\,\mathrm{s}$, $t = 480\,\mathrm{s}$, $t = 720\,\mathrm{s}$, $t = 1200\,\mathrm{s}$ and $t = 1800\,\mathrm{s}$.

The computed bed profile agrees reasonably well with the measured profile, with the difference between the two occurring mostly at the downstream side of the deposition dune where the form of the measured slope is different from that of the computed slope in some places. The sand-sliding mechanism in the numerical model limits the computed bed slope to the critical bed slope angle which should be the repose angle of the sediment particles. While a closer look at the experimental results shows that the bed slope in the experiments can exceed the angle of repose of the sediment at the downstream slope of the dune. The most likely explanation for this is that the reverse flow on the downstream side of the dune acts to push sand up the slope, thereby enabling the slope angle to exceed the angle of repose. To see clearer the reverse flow, the velocity profile at three positions $x = 1.2\,\mathrm{m}$, $x = 1.25\,\mathrm{m}$ and $x = 1.3\,\mathrm{m}$ on the downstream slop of the dune are plotted in Fig. (4.12). So in the sand-sliding mechanism, instead of using the repose angle of the sediment, a value obtained from studying the experimental results is used as the critical bed slope angle. However, this modification still cannot guarantee a perfect agreement with the experimental results. In principle it would be possible to include this effect in the simulation through the use of a modified angle of repose which depends on the local shear stress.

We also noticed that at the beginning point of the erodible bed, the simulated bed level height does not change while the measured bed profile shows that in this region, the sediment is also eroded and the bed level height becomes lower with time. As we mentioned above that the initial bed level is set to be $z = -0.005\,\mathrm{m}$ for the erodible bed and $z = 0\,\mathrm{m}$ for the rigid apron to compensate the mass loss of the sediment in the experiment and to avoid large distortions of the mesh cells in this region, a sudden change with a sharp angle in the computational domain still prevent the flow velocity and thus the sediment transport in this region to be accurately reproduced, and this is one of the limitations of our model.

The computed scour depths agree well with the experimental results, but the computed heights of the deposition dune are consistently a little higher than the measured values. A closer examination of the profiles of the deposition dune shows that, in the simulations, the crest of the dune is consistently sharper than in the experiments. This is probably because, in the experiments, there is a horizontal force on the dune caused by the pressure difference between the upstream and downstream faces of the dune, and this force could push some of the sediment down the slop of the dune. Currently, this effect is not included in the simulation – the sediment movement is driven entirely by the action of the shear force parallel to the bed surface.

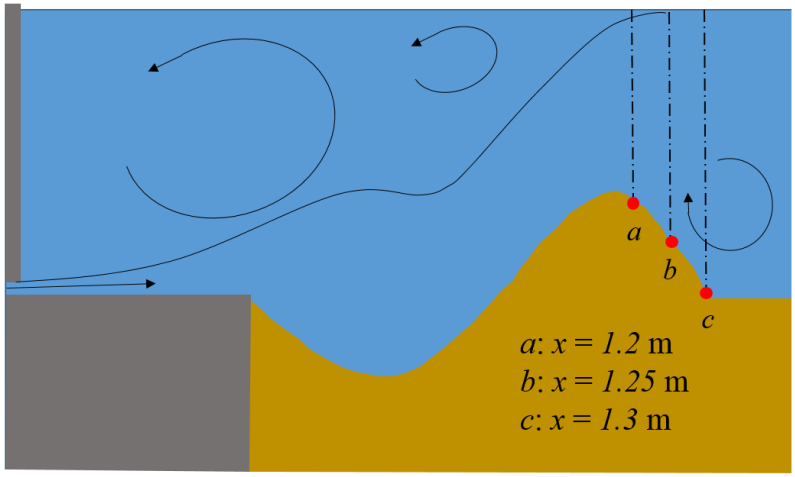

(a) Positions of the velocity profiles plotted.

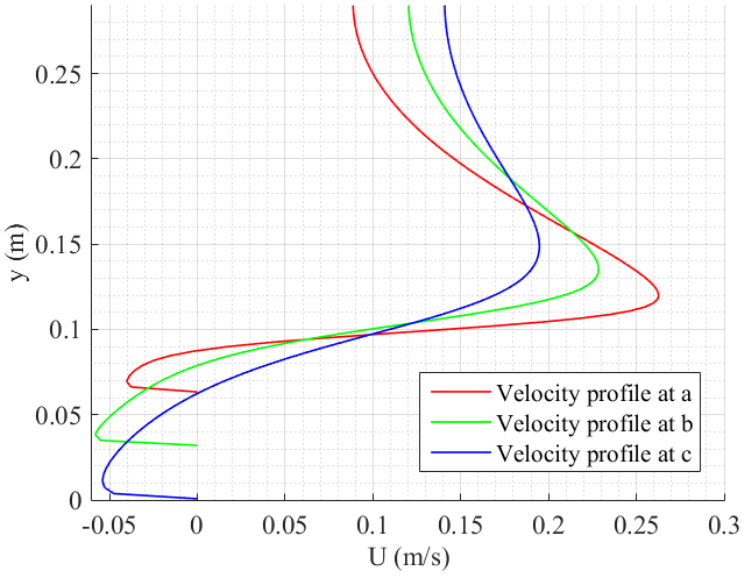

(b) Velocity profile at downstream slop of the sand dune.

Fig. 4.12 Reverse flow at $x = 1.2\,\text{m}$, $x = 1.25\,\text{m}$ and $x = 1.3\,\text{m}$ on the downstream slop of the dune.

4.4 Conclusions

A numerical simulation of a two-dimensional scour caused by submerged jet has been conducted using the model developed to test its performance. The flow field solved with k-ε turbulence model with a rough wall function shows correct flow patterns and the simulation results agree well with the experimental measurements. The computed bed profiles agree reasonably well with the measured ones, but with two important differences concerning the form of the deposition dune downstream of the scour hole: the downstream slope of the dune simulated is not totally in agreement with that in the experiments, and the computed dune's height exceeds the measured height. The first is probably caused by the existence of the reverse flow which pushes sand back up the slope, making it possible to maintain a slope steeper than the angle of repose. The second is probably the result of a horizontal force on the top of the dune, caused by a pressure difference between the upstream and downstream faces, which pushes some sand down the downstream slope of the dune.

Chapter 5

Three Dimensional Simulation of Scour Around Obstacle

In this chapter, we will present the numerical simulation of three dimensional flow and scour. Initially, the bed deformation is not activated and a steady state flow field with a horseshoe vortex is simulated to test the ability of the hydrodynamic module to simulate three dimensional flow field. Then an unsteady turbulent flow field around a single cylinder is simulated but still with a rigid bed. In both of these simulations, the flow field is simulated with and without the free surface to study the influence of the free surface on the flow field and thus by implication, on the scour process. Finally, the bed deformation is activated and the local scour around a single cylinder is simulated using the model previously validated. By comparing the simulation results and the experimental data, the overall performance of the model is tested and evaluated.

5.1 Simulation of Vortex Structure in Horseshoe

When flow meets an emerging obstacle, the flow separates around the obstacle, creating a three-dimensional structure at the foot of the obstacle called a horseshoe vortex. The horseshoe vortex plays an important role in scouring around structures built in water because of the high stresses that it imposes at bed which are likely to contribute to the erosion of sediment. This complex recirculation is also important in certain problems related to floods and river overflows. So in order to simulate the scour correctly, the horseshoe vortex also should be correctly reproduced. We choose one of the experiments done by Launay et al. (2015) which aimed at studying the structure of horseshoe vortex in shallow water with

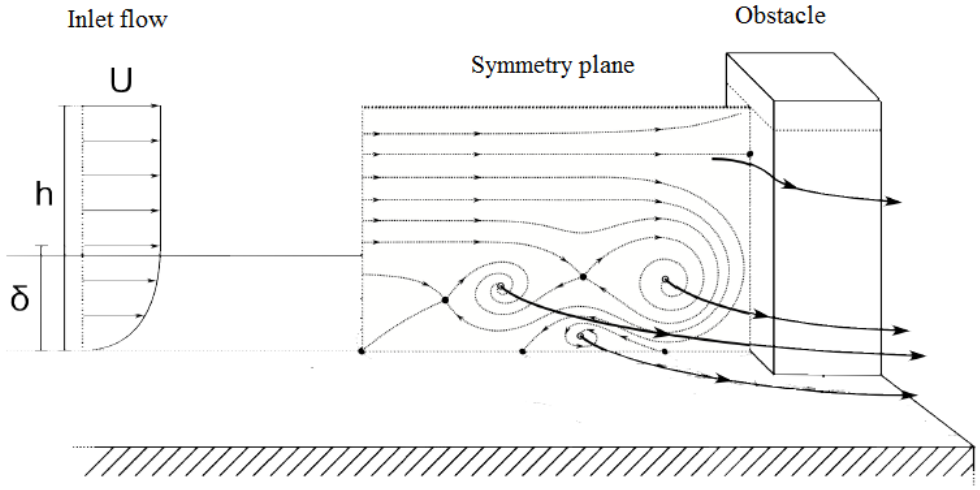

Fig. 5.1 Flow pattern of the horseshoe vortex, from Launay et al. (2015).

emerging obstacle as a test case, which is shown in Fig. (5.1), to evaluate the ability of the model to simulate three dimensional flow field.

5.1.1 Laboratory Study Details

The experimental device used to study the horseshoe vortex in Launay et al. (2015) consists of tranquillization basin and a honeycomb grid which allows the flow to be homogenized, a vertical convergent inlet which ensures a quasi-uniform distribution of the flow, and a channel entirely made of glass, which allows the optical measurements of Particle Image Velocimetry (PIV). The width of the obstacle placed in the measuring zone is adjustable. The flow rate is measured by an electromagnetic flow-meter at the outlet and the height of water is adjusted by a threshold at outlet which allows the water depth to reach a maximum value of 8 cm during the experiments. The measurements were only made in the vertical plane of symmetry, which gives a cross-section view of the horseshoe vortex and its internal structure.

The PIV measures are carried out in this experimental study with different widths of the obstacle, inlet bulk velocity and water depth and four horseshoe vortex regimes are identified:

- Stable regime which is characterized by a quasi-permanent horseshoe vortex.
- Oscillating regime which is characterized by the periodic displacement of the vortex centres around an average position.
- Cyclical regime which is characterized by a periodic behaviour different from that observed for the regime oscillating.

- Chaotic regime which results in a more or less complete disorganization of the horseshoe vortex structure.

This experimental studies also helped to understand the the complex dependence of the regimes on the Reynolds number and other non-dimensional parameters. In this thesis, to facilitate the comparison between the experimental measurements and the simulation results, a horseshoe vortex case in stable regime is chosen.

5.1.2 Numerical Set-Up of the Simulation

The sketch of the horseshoe vortex simulation is shown in Fig. (5.2). The obstacle is placed at 0.6 m after the inlet in 0.06 m deep water. The inlet bulk velocity is $0.0178\,\mathrm{m}\cdot\mathrm{s}^{-1}$. The obstacle is 0.047 69 m wide and 0.5 m long. As the flow velocity is very small, the flow field is treated as laminar flow and no turbulence model is needed.

The Froude number Fr for this case is $Fr = 0.023$, which is quite small and in this case, the variation of the free surface position should be also very small. Usually in the numerical simulation of cases with very small Froude number, the effect of the variation of the water depth is considered to be negligible. However, in this test case, the influence of the free surface on the simulation results for the horseshoe vortex is also studied. So two simulations with the same parameters are conducted: a rigid lid simulation which contains only the water domain with the water surface modelled as a slip boundary, and a free surface simulation which contains both the water phase and the air phase with the free surface tracked by VOF method as presented in Chapter 2.

The meshes used for the rigid lid and the free surface simulations were generated with mesh generator *Gmsh*. In order to reduce the computing resources required, the meshes contain only the right half of the experimental domain. So only the right half of the experimental domain is calculated in the simulation and a *symmetryPlane* boundary condition is used which assumes that the left half of the flow field is symmetrical to the right half. It should be noticed that this assumption is not true in reality as the vortices generated at the corner of the cubic obstacle are not totally symmetrical in reality. However, the experimental measurements were only conducted on the symmetry plane of the simulation domain in front of the obstacle and they showed that the flow field on this plane is in a steady state. So the numerical results with this assumption still manage to give a quite good agreement with the experimental measurement. But given enough time and calculating resources, this simulation should be done without the assumption of the symmetry.

The only difference between the mesh used for rigid lid simulation and the one used for free surface simulation is the dimension in vertical direction where the mesh for free

surface simulation contains not only the water domain but also an extra region for the air domain. In other directions, the meshes are exactly the same. Fig. (5.3) shows the horizontal plane $y = 0\,\text{m}$ of the meshes. The mesh for free surface simulation has 360 mesh cells in the x direction (horizontal axis) with $\Delta x_{min} = 0.001\,\text{m}$, 120 mesh cells in the z direction (transversal axis) with $\Delta z_{min} = 0.001\,\text{m}$ and 85 mesh cells in the y direction (vertical axis) with $\Delta y_{min} = 0.001\,\text{m}$. The mesh for the rigid lid simulation has only 60 mesh cells in the y direction. The mesh cells close to the obstacle and the symmetry plane are the finest and the maximum expansion ratio of the cell edge length in all directions between adjacent cells is controlled to be smaller than 1.05. Several mesh configurations have been used and no apparent differences were found when using a finer mesh which means the mesh is fine enough for this simulation. The details of the boundary conditions defined are presented below:

- **Top boundary**: For the rigid lid simulation, the mesh only contains the water domain and all the properties at the top boundary of the mesh are given a *slip* type of boundary condition. For the free surface simulation, the top boundary represents the atmosphere so it set to be the same as in previous similar cases.

- **Bottom boundary**: The bottom boundary for the rigid lid and the free surface simulations is set to be *wall* type of boundary and the conditions for fields on the boundary are similar to the previous simulations.

- **Inlet and outlet boundaries**: For rigid lid simulation, the inlet velocity is set to be uniform and equal to the bulk velocity and at the outlet, the velocity is set to be zero-gradient. For pressure field, as only the relative pressure is important for the rigid lid simulation, the pressure field is set to be zero-gradient at the inlet boundary and a fixed value zero at the outlet boundary. For free surface simulation, the fields at inlet and outlet boundaries are set to be the same as in the submerged jet case only with different values. This set-up is also for the purpose of fixing the outlet water depth of the flow field.

- **Left and right side boundaries**: As the simulation is in three dimensions, the *empty* boundary condition type can no longer be applied. For the right-side boundary, a *slip* type of boundary is used which imposes zero-gradient of all the properties and for the left-side boundary, a *symmetryPlane* type of boundary condition is used which assumes the planar patch is a symmetry plane of the simulation domain so that we do not need to solve the left half of the flow field.

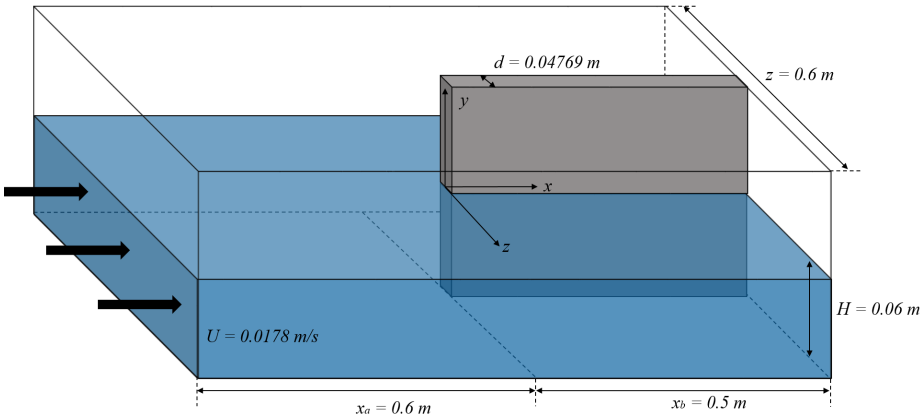

Fig. 5.2 Sketch of the horseshoe vortex simulation.

- **Obstacle surface boundary**: The surface of the obstacle is also a boundary of the mesh and a *wall* type of boundary is used which is the same as for the bottom boundary.

5.1.3 Simulation Results and Discussions

First of all, we look at the flow pattern in a horizontal plane to get an overall picture of the flow field. For this we just look at the free surface simulation results of the velocity field and the pressure field in a horizontal plane at two different heights, 0.05 m above the bed, which is close to the water surface, and 0.01 m above the bed, which is close to the bed, as shown in Fig. (5.4) and Fig. (5.5). We can identify from the figures the vortex shedding at the corner of the obstacle in flow near the water surface and the horseshoe vortex at the foot of the obstacle.

Next, in order to study in detail the horseshoe vortex, the results for both the rigid lid simulation and the free surface simulation on the symmetry plane in front of the obstacle are compared with the experimental measurements, including the vortex centre positions and the vorticity of the vortices. A vortex is a region in a fluid in which the flow rotates around an axis and a key concept in the dynamics of vortices is the vorticity, a vector that describes the local rotary motion at a point in the fluid. The direction of the vorticity vector is defined to be the direction of the axis of rotation according to the right-hand rule while its length is twice the angular velocity at this point. Mathematically, the vorticity is defined as the curl (or rotational) of the velocity field of the fluid:

$$\boldsymbol{\omega} = \nabla \times \boldsymbol{U} \tag{5.1}$$

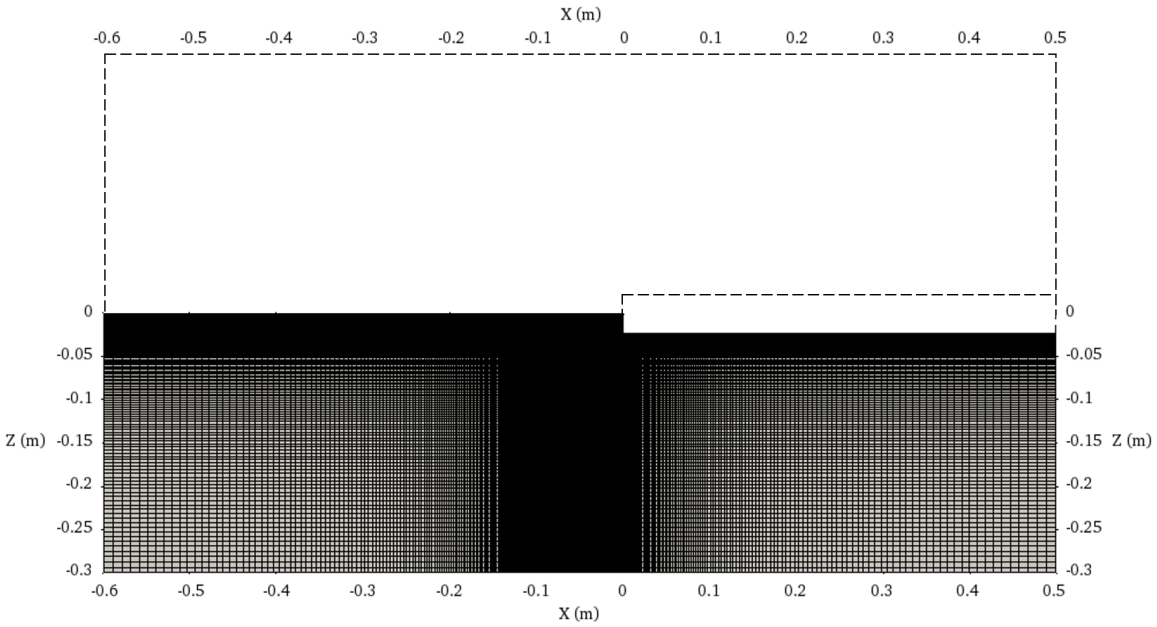

Fig. 5.3 Mesh generated for the horseshoe vortex simulation.

where $\boldsymbol{\omega}$ is the vorticity. In theory, the vorticity may vary with the distance r from the axis in many ways. There are two important special cases: a rigid-body vortex and an irrotational vortex. If the velocity increases in proportional to the distance from the axis, it is called a rigid-body vortex as the fluid rotates like a rigid body. The vorticity is uniform in such a flow and its direction is parallel to the rotation axis. If the velocity is inversely proportional to the distance from the axis, it is an irrotational vortex and in this case the vorticity is zero at any point not on the axis. Algorithms exist to identify the centres of both rotational and irrotational vortices, from velocity data. We have used the algorithm proposed by Graftieaux et al. (2001) to identify the vortices centres. The idea of this method is to identify the vortex centre by a dimensionless scalar function Γ for a fixed point P as:

$$\Gamma(P) = \frac{1}{S}\int_S \sin(\theta_M)dS = \frac{1}{S}\int_{M\in S} \frac{(\boldsymbol{PM}\wedge\boldsymbol{U_M})\cdot\boldsymbol{n}}{\|\boldsymbol{PM}\|\cdot\|\boldsymbol{U_M}\|}dS \tag{5.2}$$

where S is a two dimensional area chosen surrounding P, M represents other points lying in the area S, $\boldsymbol{n}$ is the vector normal to the measurement plane, θ_M represents the angle between the velocity vector U_M and the vector $\boldsymbol{PM}$. $\|\Gamma\|$ is bounded with a maximum possible value of 1 and this bound is reached at the location of the vortex centre. If $\Gamma < 0$, the vortex rotates in a clockwise direction, and in an anti-clockwise direction if $\Gamma > 0$. Thus, the scalar function Γ provides a way to quantify the streamline topology of the flow in the vicinity of P and the rotation sign of the vortex.

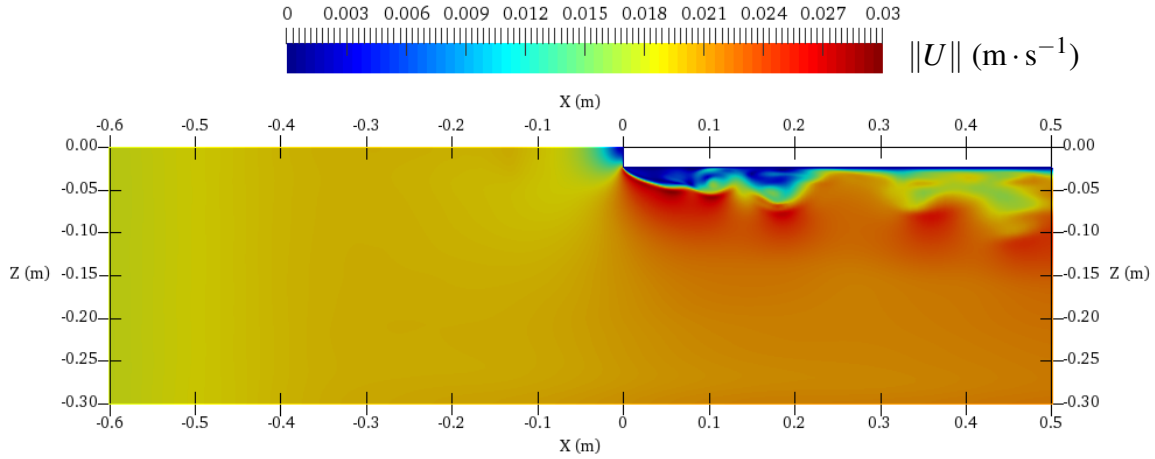

(a) Velocity field at 0.05 m above the bed.

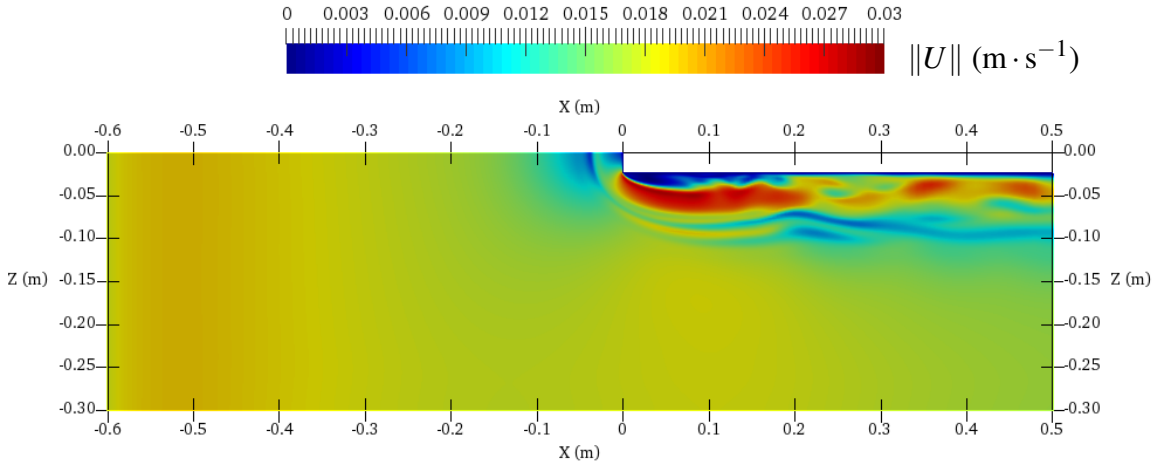

(b) Velocity field at 0.01 m above the bed.

Fig. 5.4 Simulation results of the velocity field in horizontal planes at different heights in water (from the simulation with free surface).

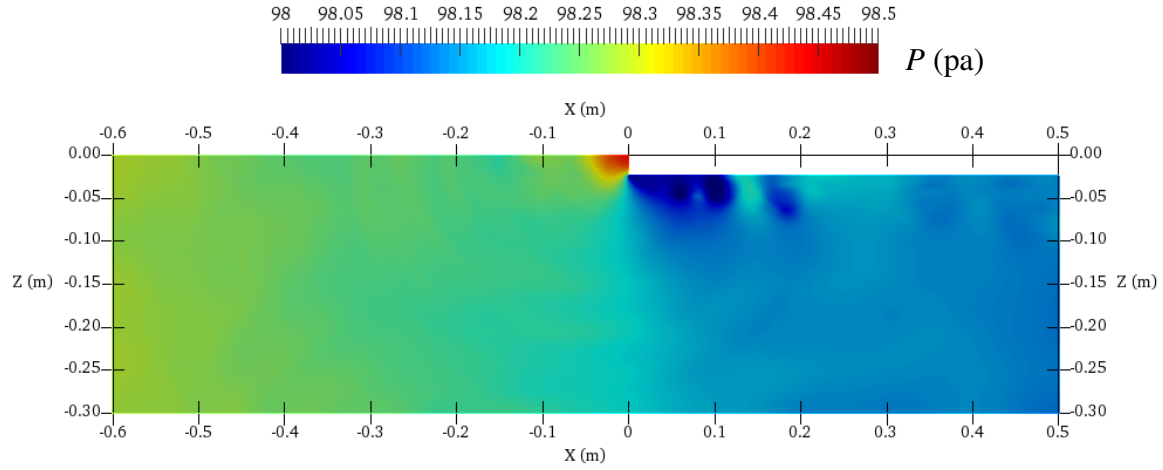

(a) Pressure field at 0.05 m above the bed.

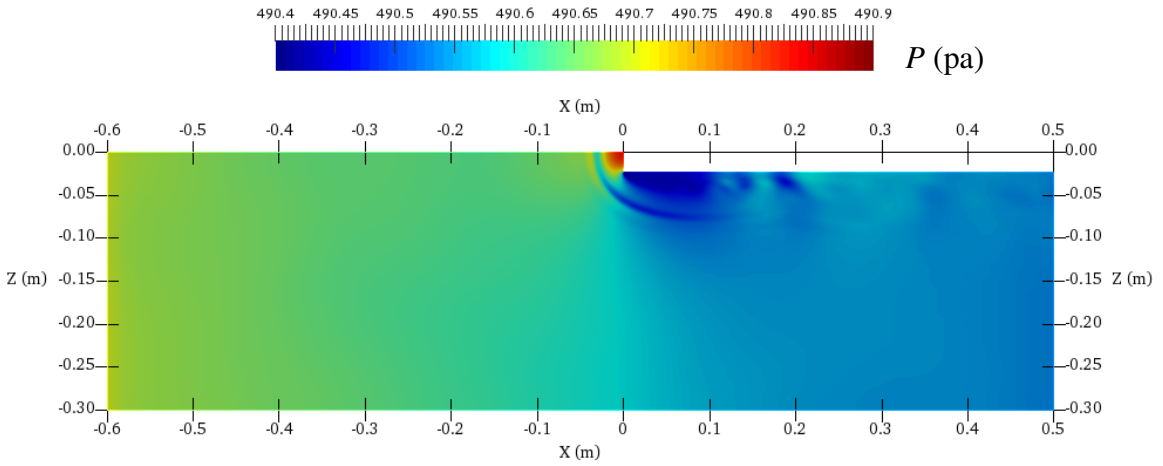

(b) Pressure field at 0.01 m above the bed.

Fig. 5.5 Simulation results of the pressure field in horizontal planes at different height in water (from the simulation with free surface).

For processing the data sampled at discrete spatial locations, S should be a rectangular domain of fixed size and geometry centred on P, and Γ then can be calculated approximately by:

$$\Gamma(P) = \frac{1}{N}\sum_{S}\sin(\theta_M) = \frac{1}{N}\sum_{S}\frac{(\boldsymbol{PM}\wedge\boldsymbol{U_M})\cdot\boldsymbol{n}}{\|\boldsymbol{PM}\|\cdot\|\boldsymbol{U_M}\|} \tag{5.3}$$

where N is the number of points M inside S. In this thesis, the same number of points has been chosen in each direction of P which makes S a square area. For a point P near the boundary, a reduced number of points in each direction is used to make sure S is always a square and for a point P at the boundary, Γ is calculated with $N = 1$ which makes Γ always equals to zero at boundaries. The parameter N plays the role of a spatial filter. This approximation affects only weakly the location of maximum $\|\Gamma\|$ and the region near vortex centre should then have values of $\|\Gamma\|$ranging from 0.9 to 1. This definition of Γ is not Galilean invariant, but as the experiment provides a steady flow field, this method is sufficient for analysing the horseshoe vortex in our case.

Comparison between the Γ calculated from velocity field obtained from experimental measurements and simulation results of the symmetrical plane just in front of the obstacle is shown in Fig. (5.6) where the black points indicate the vortex centres that have been detected.

In both the experimental measurements and the simulation results, there are three major vortices close to the bottom of the obstacle with the centres detected by $\|\Gamma\| \geqslant 0.9$, and a set of smaller vortex type of flow structures but with $\|\Gamma\| < 0.9$ which means that they don't have distinct centres. The enlarged Γ and velocity fields of this region from the experiment and simulations are shown in Fig. (5.8). By comparing the results between the rigid lid simulation and free surface simulation, we can conclude that even though the vortex centre positions simulated both agree very well with the experimental measurements, the streamline topology of the flow at these vortices from the free surface simulation agrees slightly better with the experimental results.

If we look at the flow field near the water surface close to the obstacle, we find that in experimental measurements, there is a small area where the flow velocity is not purely horizontal. The enlarged Γ and velocity fields of this region from the experiment and the simulations are shown in Fig. (5.7). This phenomenon is caused by the variation of the free surface in front of the obstacle. As the free surface varies only a little bit in this case, the vertical component of the velocity is also very small in this area. However, this phenomena can not be simulated in the rigid lid simulation as the water surface is fixed, and in the free surface simulation, a small circular flow occurs in this region with $\Gamma \sim 0.7$. There are two possible explanation for the difference between the numerical simulation and the experimental measurements – smoothing of the velocity measurements obtained from PIV

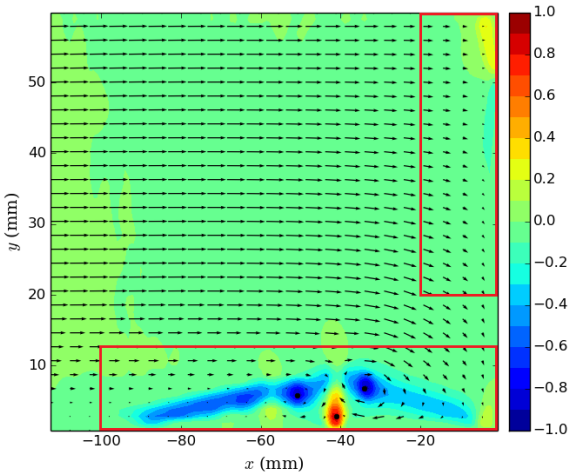

(a) Γ and the velocity field from experimental results.

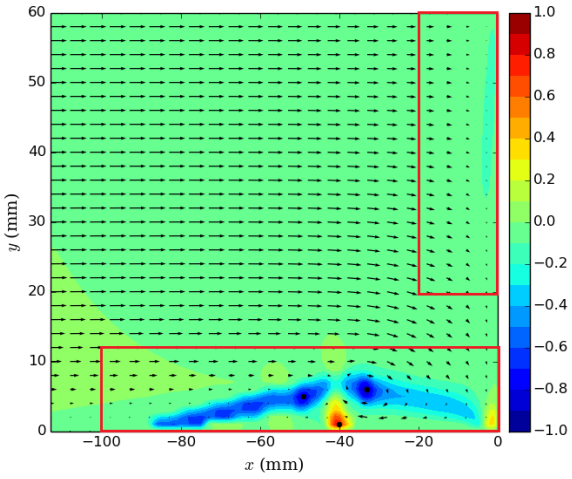

(b) Γ and the velocity field from rigid lid simulation.

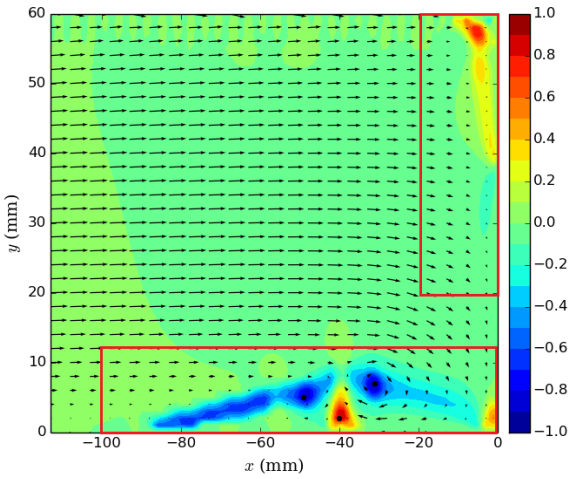

(c) Γ and the velocity field from free surface simulation results.

Fig. 5.6 Comparison of Γ and the velocity field between experimental measurements and simulation results with and without free surface, black points on the figures indicate the vortex centres detected and red squares on the figures indicates the regions enlarged in following figures.

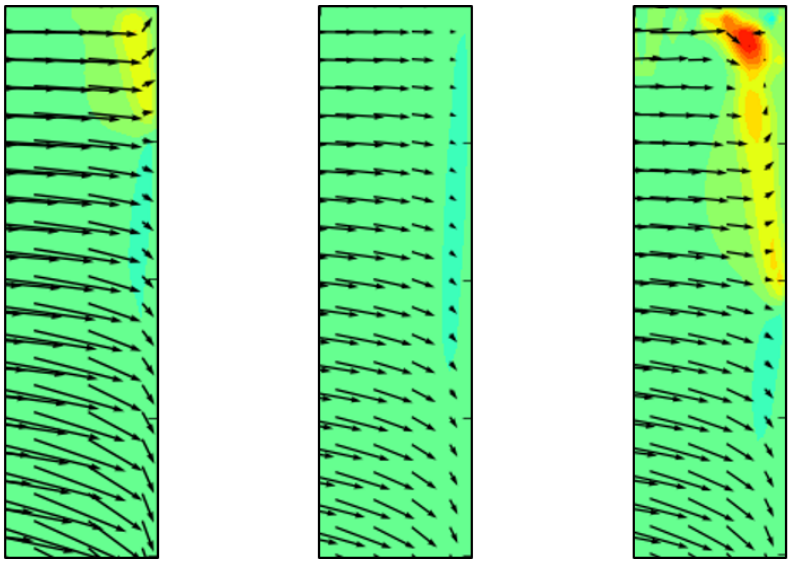

(a) Experiments. (b) Rigid lid simulation. (c) Free surface simulation.

Fig. 5.7 Comparison of Γ and the velocity field between experimental measurements and simulation results with and without free surface, the top enlarged part.

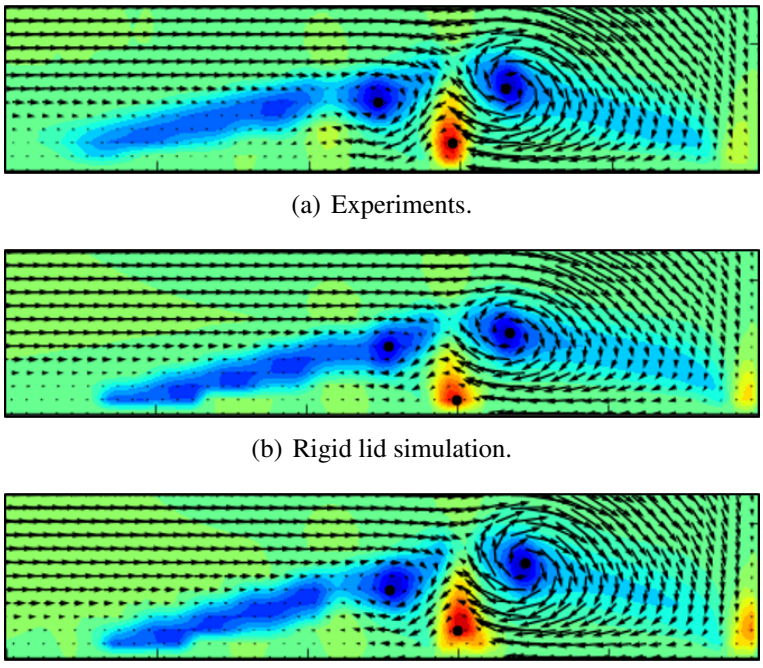

(a) Experiments.

(b) Rigid lid simulation.

(c) Free surface simulation.

Fig. 5.8 Comparison of Γ and the velocity field between experimental measurements and simulation results with and without free surface, black points on the figures indicate the vortex centres detected, the bottom enlarged part.

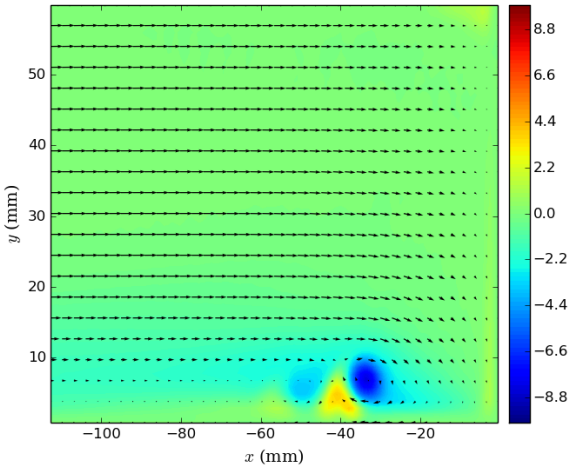

(a) Vorticity calculated from experimental results.

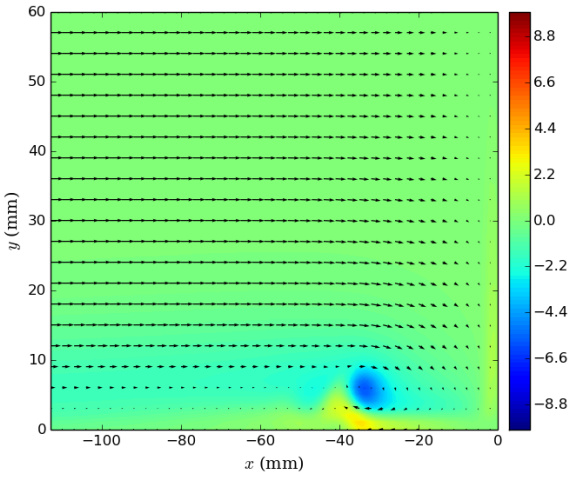

(b) Vorticity calculated from simulation results without free surface effect.

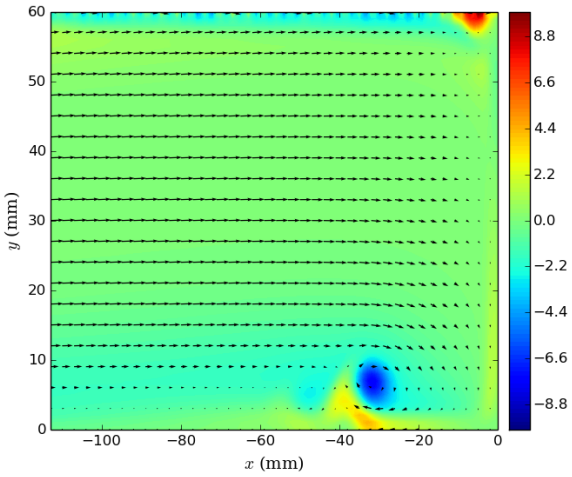

(c) Vorticity calculated from simulation results with free surface effect.

Fig. 5.9 Comparison of the velocity field and vorticity magnitude between experimental measurements and simulation results with and without free surface.

could reduce the apparent rotation by limiting velocity gradients, or the representation of the free surface in the VOF method could exaggerate the water level changes, increasing the apparent rotation. Moreover, it should be noticed that the difference in this region also has an influence on the separation point of the flow field in front of the obstacle. The separation point is the position where the flow diverges and the flow goes upward in the region above the point and downward below the point. We can see from Fig. (5.7) that the difference between the velocity field close to the free surface in front of the obstacle causes a difference between the position of the separation point and thus influences the flow field close to the bed in the horseshoe vortex region.

Comparison of the vorticity magnitude calculated from experimental and simulation results is shown in Fig. (5.9). From the results of the experiments we can see clearly the three major vortices who have the highest or the lowest vorticity. The vorticity of these three vortices in rigid lid simulation is much smaller than in the experiment, especially for the vortex located furthest from the obstacle which can barely be identified. The free surface simulation provides better agreements with the experimental results, although the vorticity magnitude is still a little smaller. This means that the simulation without a free surface will underestimate the vorticity of the horseshoe vortex whereas the simulation with a free surface will provide a better estimation of the vorticity of the horseshoe vortex.

It should be noticed, however, that the location of the maximum vorticity magnitude of the vortex closest to the bottom in the experimental measurements and in the simulation results is not exactly the same; the maximum vorticity magnitude is located closer to the bed lower in the simulation results than in the experimental measurements. As the basic structure of this vortex is still the same in the simulation results and in the experimental results and the difference between the vorticity magnitude values is very small, this difference probably not particularly important for simulating scour.

Finally, we can find that in the free surface simulation, there is a small layer near the water surface where the vorticity magnitude is around $-2.5\,\mathrm{s}^{-1}$ and there is also an area with quite strong vorticity close to the obstacle. This is consistent with the difference between the free surface simulation and the experimental measurments observed when analysing the vortex centre detection results, which is probably caused by the inaccuracy of the VOF method and the usage of the PIV method in the experiments. In this test case the variation of the free surface is very small and almost invisible during the experiment. So it is very difficult to construct a mesh fine enough to resolve accurately this small variation in the position of the free surface and this will therefore probably lead to an overestimation of the water level change. Also, in the experimental result obtained with the PIV method, the velocities have

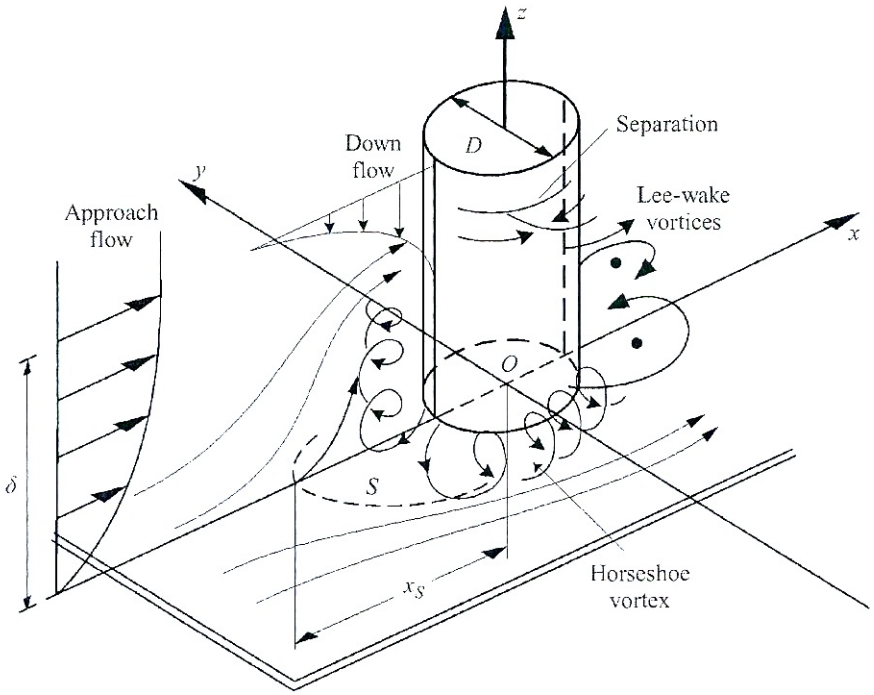

Fig. 5.10 Flow pattern around a pile in steady current, from Roulund et al. (2005).

been smoothed and this may reduce the vorticity gradients resulting in an under-estimation of the rotation of the fluid.

In conclusion, the simulation including the free surface reproduces more accurately the structure and the vorticity of the horseshoe vortex at the foot of the obstacle. The simulation without a free surface reproduces correctly the position of the vortex centres but tends to compute smaller vorticity. Moreover, in order to get very accurate flow field simulation results at the free surface, the simulation requires a very fine mesh.

5.2 Simulation of Flow Around Cylinder on Rigid Bed

When a vertical cylinder is placed on the bed in a steady current, the flow will be changed in many ways as shown in Fig. (5.10). First of all, a horseshoe vortex is formed in front of the cylinder. Secondly, the streamlines contract at the side of the cylinder. Finally, a vortex pattern is formed at the lee-side of the cylinder, usually in form of a vortex shedding. Before we start to simulate the scour formation around a cylinder, the flow field around a cylinder on a rigid bed is simulated and studied in this section.

5.2.1 Laboratory Study Details

The case we chose is provided by Roulund et al. (2005) , where measurements of flow field around a circular cylinder on a rigid bed in steady current have been conducted and presented. Roulund et al. (2005) conducted not only the experiments for a rigid bed but also for a erodible bed which were used later in this work to validate the overall performance of the numerical model for scour simulation. The measurements of flow field and scour profiles are presented in detail and have been referenced by many similar studies. So in this part of the thesis, the data obtained from this study are used to analyse and to validate the model.

In the experiments with a rigid bed, two types of rigid bed were used in the experiments:(i) a smooth bed; and (ii) a rough bed with a single layer of crushed stones. The experiments with a smooth bed were conducted in a flume of 35 m long and 3 m wide, while the experiments with a rough bed were conducted in another flume, 28 m long and 4 m wide. The water depth in experiments with both types of rigid bed was maintained at 0.54 m and the mean approach velocity was $0.326\,\mathrm{m}\cdot\mathrm{s}^{-1}$.

During the experiments, the velocity measurements were made on the plane of symmetry upstream and downstream of the pile. A two-component DANTEC laser-Doppler anemometer (LDA) was used in the measurements. The LDA system comprised a two-colour high performance fibre optic system and the dimensions of the measurement volume $d_x \times d_y \times d_z$ were $1.5\,\mathrm{mm} \times 0.12\,\mathrm{mm} \times 0.12\,\mathrm{mm}$. The bed shear stress was measured with a DANTEC one-component 55R46 hot-film probe and these measurements were conducted only with the smooth bed as the the principle of the hot-film technique breaks down for rough walls (Roulund et al., 2005).

In both the smooth-bed and rough-bed experiments, the cylinder was placed 20 m downstream of the inlet section and the undisturbed velocity profiles at the measurement sections were measured. The measurements of the undisturbed velocity profiles were used to calculate the Reynolds numbers Re_D, mean flow velocity U, equivalent roughness height k_s and some other properties which are useful to determine the characteristics of the inlet flow in the simulation. The experimental conditions for rigid-bed experiments with a smooth bed and a rough bed are summarized in Table 5.1

5.2.2 Numerical Set-Up of the Simulation

The sketch of the simulation is shown in Fig. (5.11). The cylinder with diameter $D = 0.536\,\mathrm{m}$ is placed in the centre of the simulation domain. The length and width of the simulation domain is $x = 24D$ and $y = 16D$. The inlet flow velocity is $U_0 = 0.326\,\mathrm{m}\cdot\mathrm{s}^{-1}$ and the initial water depth is $H = 0.54\,\mathrm{m}$. The corresponding Reynolds number is $Re_D = 1.75 \times 10^5$. As in

Table 5.1 Conditions for the rigid-bed experiments, from Roulund et al. (2005).

Bed	Smooth bed	Rough bed
Water depth H	0.54 m	0.54 m
Boundary layer thickness δ	0.54 m	0.54 m
Mean flow velocity $\overline{U}$	$0.326\,\mathrm{m}\cdot\mathrm{s}^{-1}$	$0.326\,\mathrm{m}\cdot\mathrm{s}^{-1}$
Pile diameter D	0.536 m	0.536 m
Froude number $Fr = \frac{\overline{U}}{\sqrt{gH}}$	0.14	0.14
Reynolds number $Re_D = \frac{\overline{U}D}{\nu}$	1.7×10^5	1.7×10^5
Friction velocity U_f	$0.013\,\mathrm{m}\cdot\mathrm{s}^{-1}$	$0.023\,\mathrm{m}\cdot\mathrm{s}^{-1}$
Bed Nikuradse equivalent sand Roughness k_s	-	0.01 m

the horseshoe vortex simulation, two simulations are conducted with the same parameters: one is a rigid lid simulation including only the water region and a *slip* boundary condition for the water surface; the other one is a free surface simulation including the air region, the water region and the free surface effect. The flow field in this simulation is highly turbulent and the k-ωSST turbulence model is used which should produce better results than k-ε model for simulating reverse flow and vortex shedding structures. Moreover, for the free surface simulation, two types of beds are used as in the experiments of Roulund et al. (2005) : (i) a smooth-bed; and (ii) a rough-bed with equivalent roughness height $k_s = 0.01$ m.

Fig. (5.12) shows the mesh constructed for free surface simulation on the horizontal plane $z = 0\,\mathrm{m}$. It should be noticed that in this simulation, unlike the simulation of scour caused by submerged jet, the y axis is the transversal direction and z axis is the vertical direction. The mesh for free surface simulation has 2.6 million mesh cells. The mesh cells close to the cylinder, to the bottom boundary and near the free surface region are the finest. The maximum expansion ratio between edge lengths of adjacent cells is controlled to be smaller than 1.05. The first mesh layer height closest to the cylinder and the bottom boundary, and the smallest mesh cell height in the free surface region is $\Delta_d = 0.005\,\mathrm{m}$. The mesh constructed for rigid lid simulation is with the same set-up but only contains 1.7 million mesh cells as it includes only the water region. The details of the boundary conditions are presented below:

- **Top and bottom boundaries**: The top and bottom boundary condition for velocity and pressure fields are set to be the same as in the horseshoe vortex test case for the rigid lid and the free surface simulation. The k and the ω field at the top boundary are set to be zero-gradient and at the bottom boundary, the corresponding wall functions for smooth or rough walls are used.

- **Inlet and outlet boundaries**: The velocity and pressure field at the inlet and the outlet boundary for the rigid lid and the free surface simulations are set to be the same as

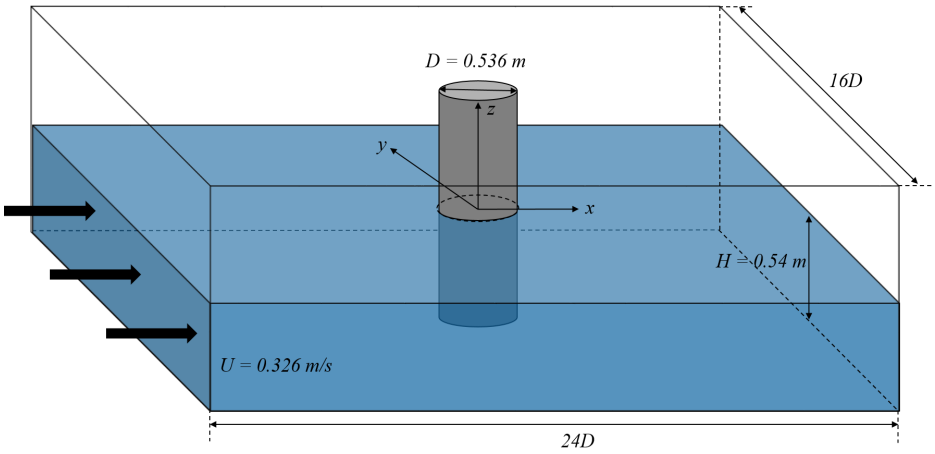

Fig. 5.11 Sketch of simulation of flow field around cylinder.

those in the horseshoe vortex simulations. For the properties of the turbulence, the *turbulentIntensityKineticEnergyInlet* type of boundary is used for the k field at the inlet and the turbulent intensity is set to be 5%. The *turbulentMixingLengthFrequencyInlet* type of boundary is used for the ω field at the inlet and the mixing length is set to be 0.54 m as indicated in Roulund et al. (2005). The k and the ω fields at the outlet are all set to be *inletOutlet* type which actually sets a zero-gradient condition at the outlet boundary.

- **Front and back boundaries**: The front and back boundaries are all set as *wall* type of boundary. The velocity field is set to be zero and corresponding wall functions are used for k, ω and ν_t fields.

- **Cylinder surface boundary**: The cylinder surface is also a boundary for the mesh and the *wall* type of boundary is used.

Both simulations, with and without a free surface, are Unsteady Reynolds Averaged Navier-Stokes (URANS) simulations which give an unsteady state of the flow field with vortex shedding in the wake behind the cylinder. The simulation continues to run for approximately 200 s after the convergence to calculate the time-averaged value of velocity field $\overline{U}$ to compare with the experimental measurements. And probes are set at different locations in the flow field to measure the variation of local U and p with time to analyse the unsteady feature of the flow field.

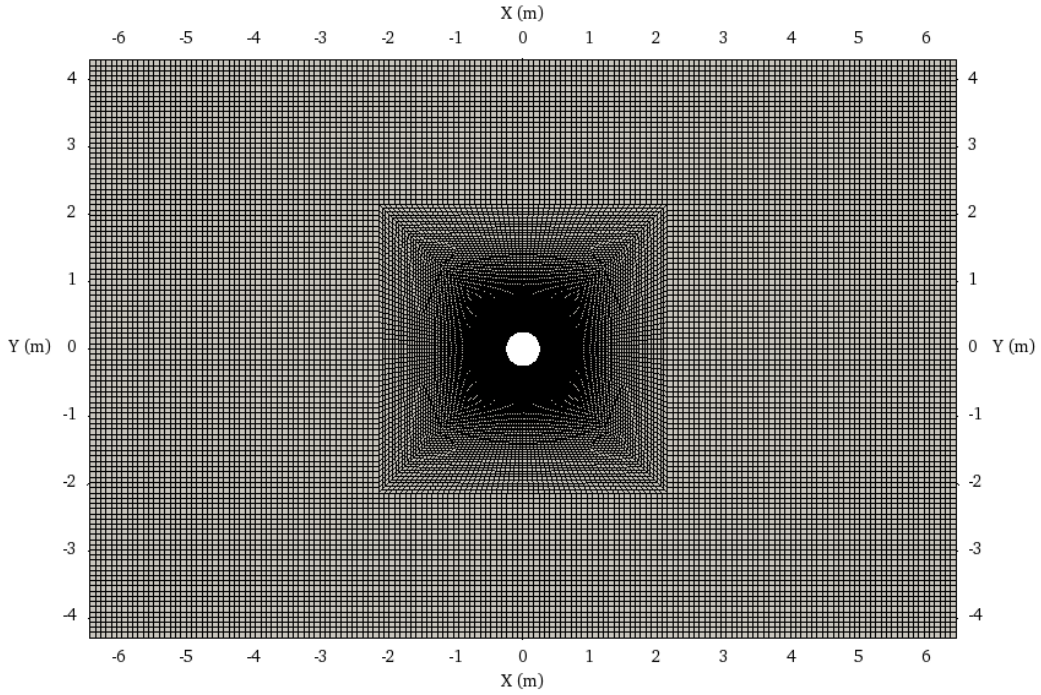

Fig. 5.12 Mesh generated for the simulation fo flow around cylinder (from the free surface simulation).

5.2.3 Simulation Results and Discussions

As presented previously, three simulations were conducted: (i) a rigid lid simulation with a smooth bed; (ii) a free surface simulation with a smooth bed; and (iii) a free surface simulation with a rough bed. To analyse the simulation results, first of all, the time-averaged velocity field obtained from the rigid lid and the free surface simulations with a smooth bed are introduced and compared with the experimental measurements to identify the influence of the free surface on the flow field. Next, the unsteady feature of the flow field are analysed by sampling the velocity and pressure fields from the simulation results. Finally, the simulation results of the free surface simulation with a rough bed are presented and compared with the experimental data to validate the performance of the hydrodynamic module with the rough wall functions.

Flow around cylinder on a smooth rigid bed

First of all, we compare the time-averaged velocity field, which is usually referred to as the mean flow field, obtained by averaging the velocity field for the rigid lid and the free surface simulations over a period of 100 s. The components of the mean velocity field in horizontal planes at two different water depth $z = -0.2\,\mathrm{m}$ and $z = -0.5\,\mathrm{m}$ obtained from the

rigid lid and the free surface simulations are shown in Fig. (5.13) and Fig. (5.14). Initially, the water surface is located at $z = 0\,\text{m}$ and the bed located at $z = -0.54\,\text{m}$, so these two depths correspond to distance $h = 0.34\,\text{m}$ and $h = 0.04\,\text{m}$ above the bed. In the rest of the thesis, we use the distance above the bed h instead of the vertical coordinate z to describe the vertical position. So in this case, the horizontal plane $h = 0\,\text{m}$ represents the bed surface and the horizontal plane $h = 0.54\,\text{m}$ represents the initial water surface.

The mean velocity fields for rigid lid simulation and free surface simulation show similar flow patterns and the velocity values before and after the cylinder in the x and y directions do not differ significantly. In the z direction, however, the flow pattern and velocity values are quite different. The difference of the mean velocity in the z direction between the free surface simulation and the rigid lid simulation is what we would expected as the free surface simulation takes into account the water surface variation and the flow at the free surface is allowed to move vertically while in the rigid lid simulation the water surface is fixed and no vertical motion is allowed.

For flow around a cylinder, the velocity component in the x direction contributes most to the scour formation as this is the direction of the undisturbed flow and it is the largest. In order to see more clearly the differences between the mean velocity in the x direction in the rigid lid and in the free surface simulation results, $\overline{U}_x$ on the symmetrical plane $y = 0\,\text{m}$ is plotted and compared in Fig. (5.15) for these two simulations. The figure shows only the simulation results in the water region. The flow field in front of the cylinder is almost the same in both of the simulations and the horseshoe vortex can be clearly identified in the figure. However, the flow pattern behind the cylinder is quite different. For the rigid lid simulation, the separation zone of the flow behind the cylinder is an almost vertical line. The flow on the downstream side of this line goes forward and merges with the current flow and the flow on the upstream side of this region goes backward and forms a reverse flow region. For the free surface simulation, the separation line however, is not vertical but curved. The bottom half of the reverse flow region is narrower than the top half. This phenomenon can be explained by the variation of the free surface. The free surface position at two random instants and the corresponding velocity magnitude on the free surface are shown in Fig. (5.16). From the figures, we can see that the cylinder has an influence on the free surface position: the free surface in front of the cylinder is higher than the initial free surface and the free surface behind the cylinder is lower than the initial free surface. Moreover, the vortex shedding behind the cylinder can cause a variation of the water depth. We can also notice that surface waves in the flow field generate a seiching effect and this is discussed in detail in the analysis of the unsteady features of the flow field later. In the simulation with a free surface, the variation of the water depth can cause a variation in the velocity and also in

the pressure field. As the flow rate is constant, the flow velocity is higher where the water depth is shallower and the pressure is smaller. So the variation of the water depth behind the cylinder causes the separation line to be curved rather than vertical. The pressure pushes the flow backwards more strongly in the free surface simulation than in the rigid lid simulation so we can see that the velocity in the x direction in the reverse flow region is stronger and the reverse flow region is wider in the free surface simulation.

Secondly, we compare the time-averaged velocity field obtained from both of the simulations with the experimental measurements and simulation results from Roulund et al. (2005). The simulation done by Roulund et al. (2005) used also the k-ω SST turbulence model but without the free surface effect. Moreover, the time-averaged velocity field is obtained directly from a steady state solver which does not reproduce the vortex shedding but only the mean flow field.

The comparison for U_x is shown in Fig. (5.17) and for U_z is shown in Fig. (5.18). All of the simulation results at the upstream side of the cylinder agree quite well with the experimental measurements except for a small area very near the cylinder where the velocity in the x direction and in the z direction is slightly underestimated by the simulations.

On the downstream side of the cylinder, in the x direction, the free surface simulation captures a reverse flow region more accurately than the rigid lid simulation although both of them underestimate slightly the width of the reverse flow region. The free surface simulation gives a better estimation of the maximum negative velocity very near the bed at $h = 0.005\,\mathrm{m}$ and $h = -0.01\,\mathrm{m}$ and away from the bed at $h = 0.1\,\mathrm{m}$ and $h = 0.2\,\mathrm{m}$, but the rigid lid simulation gives a better estimation of the maximum negative velocity value in the middle depth at $h = 0.02\,\mathrm{m}$ and $h = 0.05\,\mathrm{m}$. Comparing with the simulation results from Roulund et al. (2005), the simulations conducted in this work reproduce better the velocity downstream of the reverse flow region. As for the velocity in the z direction, the experimental measurements show a very strong negative value immediately behind the cylinder which is not reproduced by all of the simulation results. The results from both rigid lid and free surface simulations in this work produce small negative velocity in z direction close to the bed and small positive velocity away from the bed, while the simulation results from Roulund et al. (2005) produce very large positive velocity away from the bed. This difference between the simulation results and the experimental measurements has already been pointed out by Roulund et al. (2005) but no explanation was given. Moreover, later when we analyse the same velocity field obtained on a rigid rough bed, we find that the measured velocity in this area becomes positive and agrees with the simulation results, which suggests that the near-bed turbulence, which depends on the bed roughness, probably influences the vertical velocities in this region.

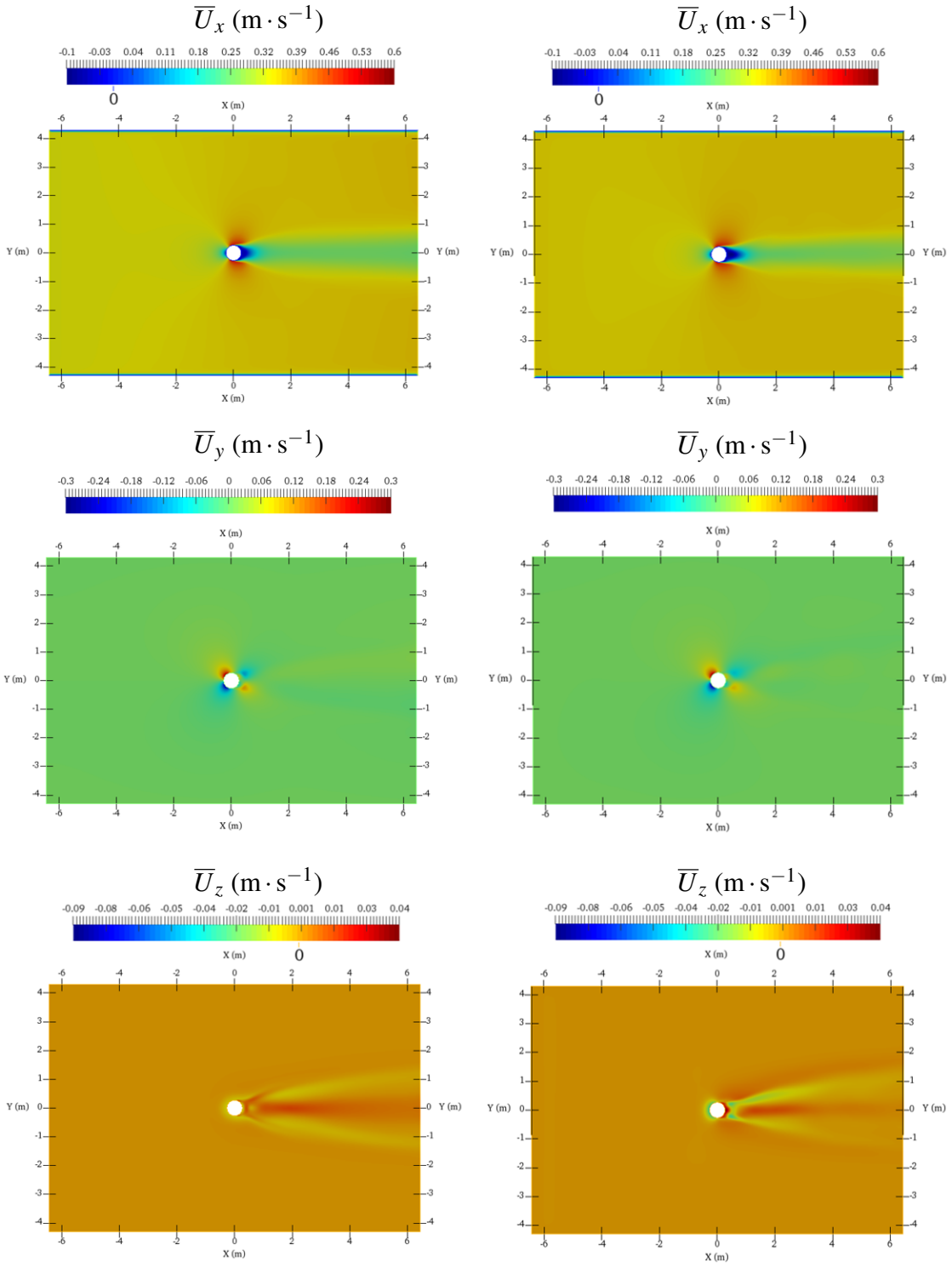

(a) Rigid lid simulation results.

(b) Free surface simulation results.

Fig. 5.13 Time-averaged velocity field for the rigid lid and the free surface simulations in a horizontal plane at depth $h = 0.34\,\mathrm{m}$.

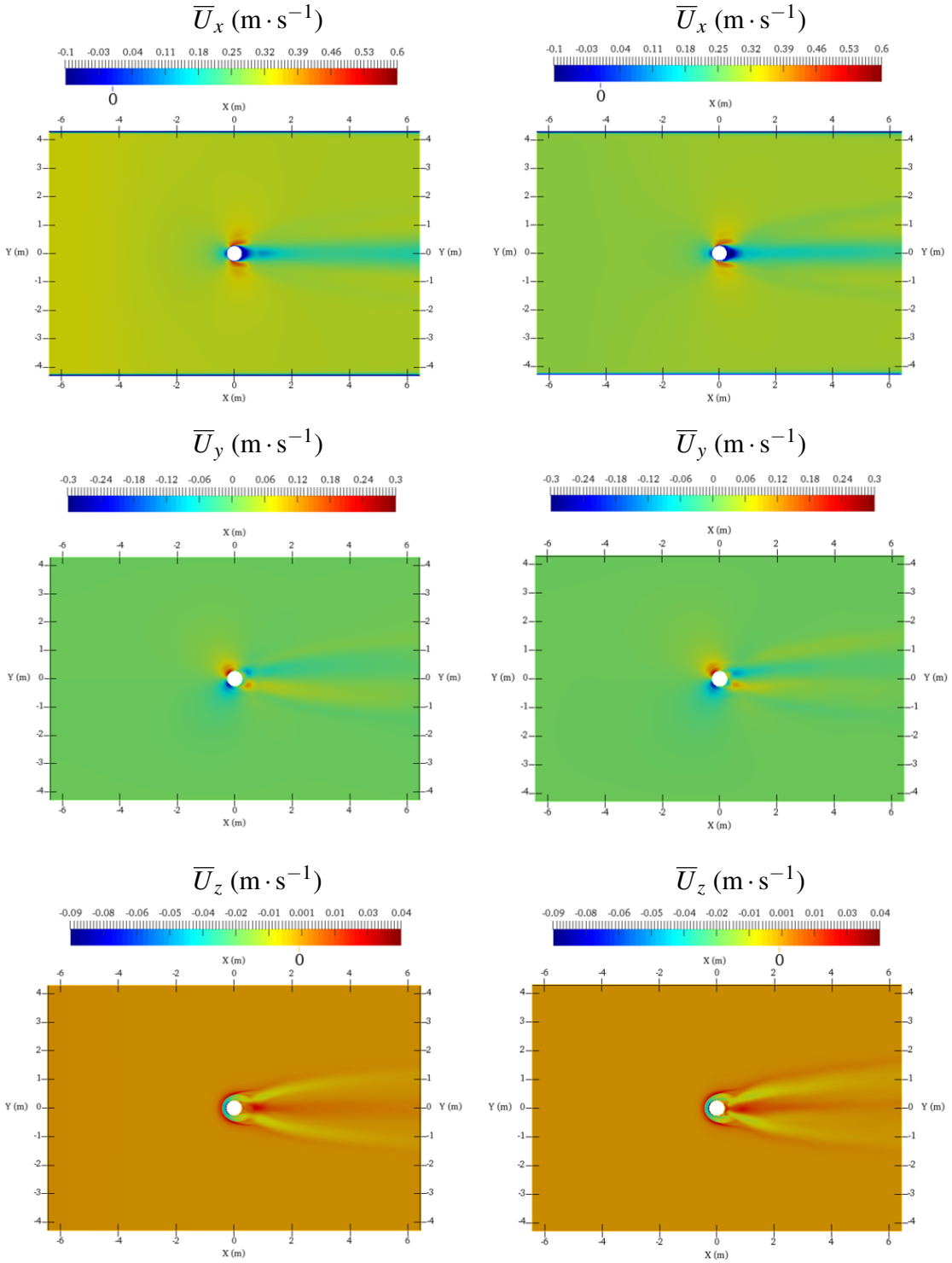

(a) Rigid lid simulation results.

(b) Free surface simulation results.

Fig. 5.14 Time-averaged velocity field for the rigid lid and the free surface simulations in a horizontal planes at depth $h = 0.04\,\mathrm{m}$.

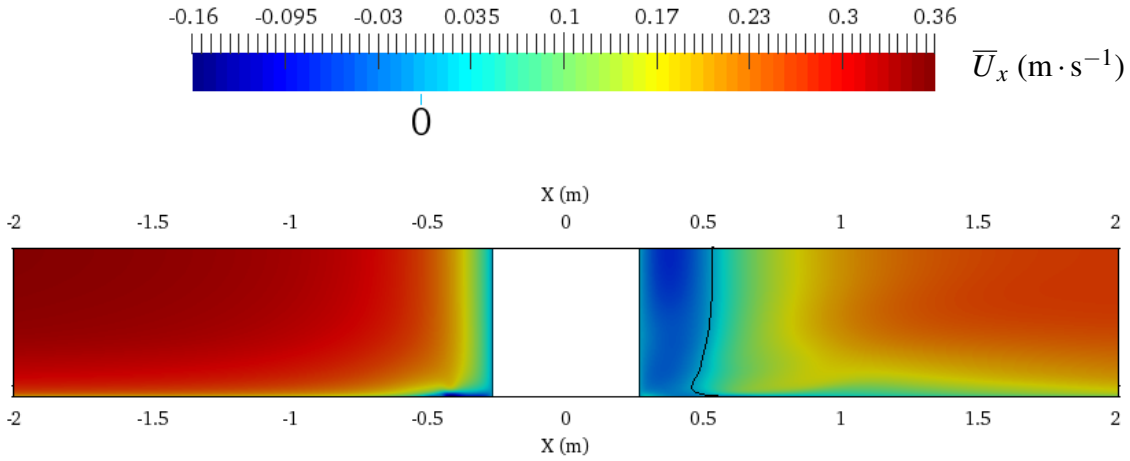

(a) $\overline{U}_x$ for the rigid lid simulation.

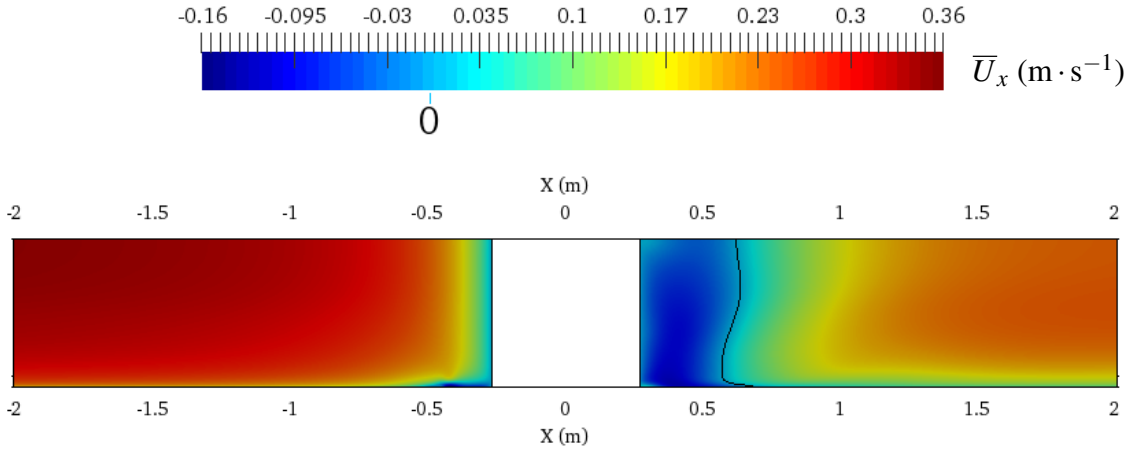

(b) $\overline{U}_x$ for the free surface simulation.

Fig. 5.15 x component of the time-averaged velocity field for the rigid lid and the free surface simulations on the symmetry plane at $y = 0\,\mathrm{m}$. Black line indicates the region where $\overline{U}_x = 0\,\mathrm{m \cdot s^{-1}}$.

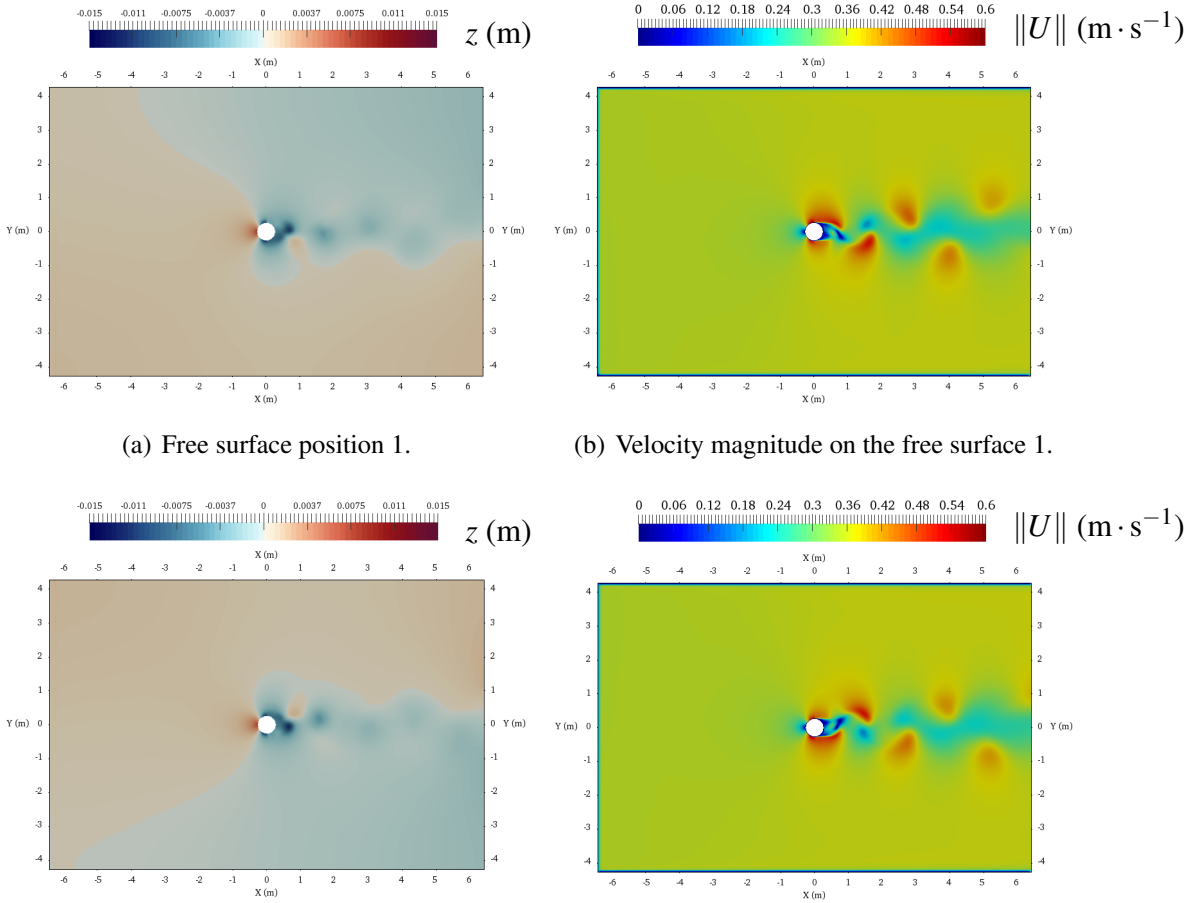

(a) Free surface position 1.

(b) Velocity magnitude on the free surface 1.

(c) Free surface position 2.

(d) Velocity magnitude on the free surface 2.

Fig. 5.16 Free surface position at two random instants and the corresponding velocity magnitude fields on the free surface.

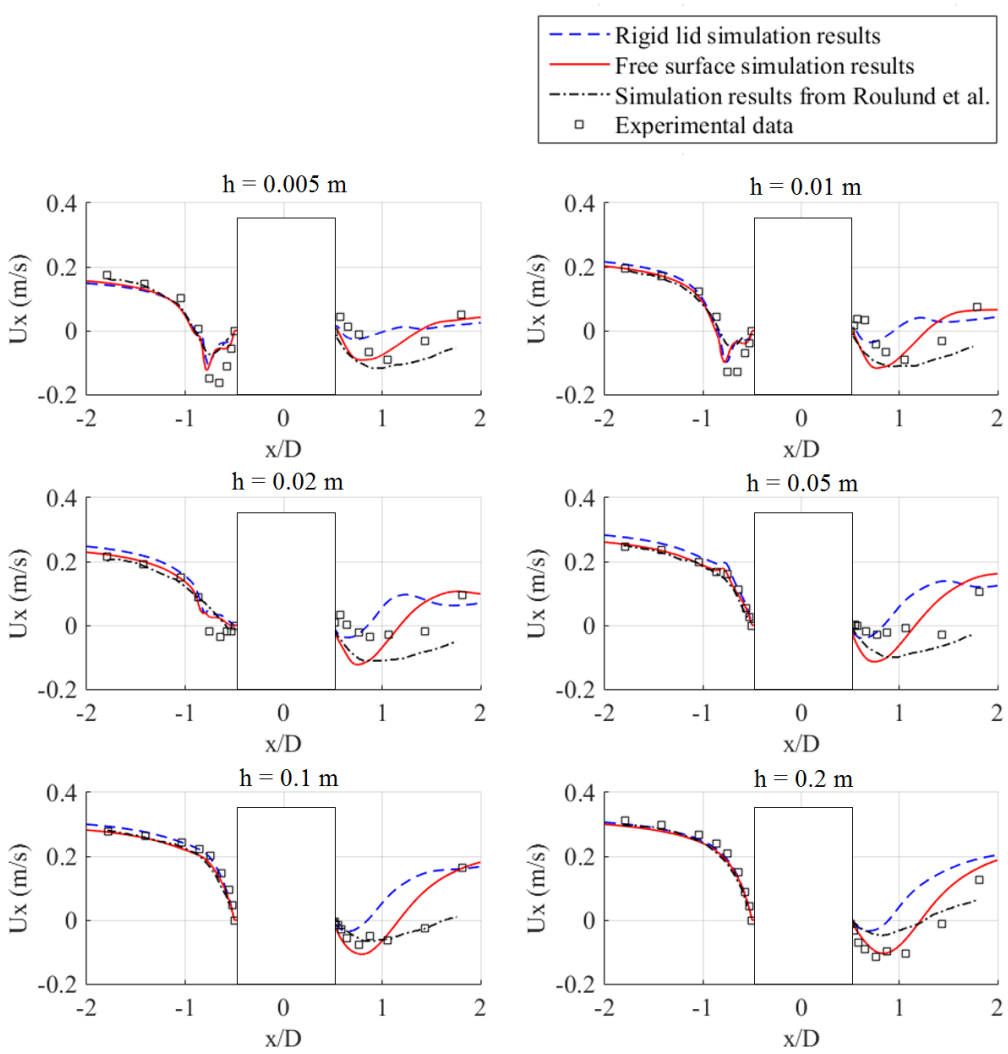

Fig. 5.17 Comparison between simulation results and experimental measurements of time-averaged velocity field U_x on plane $y = 0\,\mathrm{m}$ for flow around a cylinder on a smooth bed.

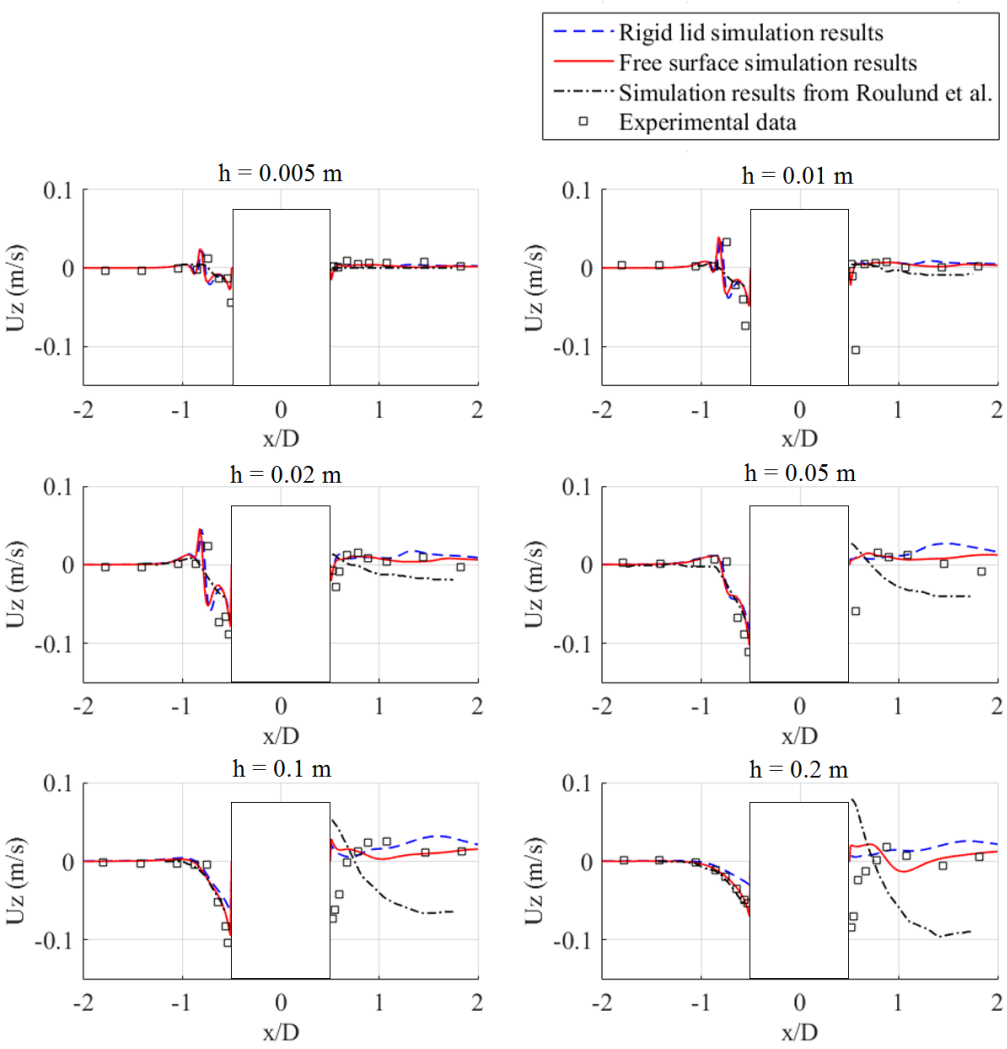

Fig. 5.18 Comparison between simulation results and experimental measurements of time-averaged velocity field U_z on plane $y = 0\,\text{m}$ for flow around a cylinder on a smooth bed.

Table 5.2 Sampling positions for measuring vortex shedding frequency.

Label	Position (m)	Description	Field sampled
1	(2.144 0.536 -0.2)	$h = 0.34$ m in the lee-wake region	Velocity
2	(2.144 0.536 -0.05)	$h = 0.49$ m in the lee-wake region	Velocity
3	(2.144 0.536 -0.49)	$h = 0.05$ m in the lee-wake region	Velocity
4	(0 0.268 -0.2)	$h = 0.34$ m on the surface of the cylinder	Pressure
5	(0 0.268 -0.05)	$h = 0.49$ m on the surface of the cylinder	Pressure
6	(0 0.268 -0.49)	$h = 0.05$ m on the surface of the cylinder	Pressure

In conclusion, the free surface simulation allows variations in the water depth and this appears to influence the flow pattern, the reverse flow region and the mean velocity field close to the bed. So the flow field obtained from a free surface simulation should give a more accurate estimation of the temporal development of local scour.

Next, we analyse the unsteady features of the flow field around the cylinder obtained from the simulations.

Fig. (5.19) shows the instantaneous velocity field on a horizontal plane at depth $h = 0.34$ m obtained from the rigid lid and the free surface simulations coloured with the velocity magnitude, and both simulations reproduce well the vortex shedding downstream of the cylinder. We begin the analysis by calculating the vortex shedding frequency in these two simulations. The simulation results are sampled at 6 positions with sampling frequency 10 Hz over a period of 100 s and a Fourier transform is applied to the sampled data to provide a frequency analysis. The sampling positions are shown in Fig. (5.20) and the details of the sampling positions can be found in Table 5.2. At positions 1, 2, 3, the velocity field is sampled and at positions 4, 5, 6, the pressure field is sampled.

The Fourier transform is calculated using MATLAB with the fast Fourier transform algorithm. Instead of directly using the sampled data of the U and P fields, the mean values of the data, $\overline{U}$ and $\overline{P}$, were subtracted and the Fourier transform was applied to the fields $U' = U - \overline{U}$ and $P' = P - \overline{P}$. Fig. (5.21) shows the results of the sampled velocity field and its amplitude spectrum obtained by the Fourier transform for the free surface simulation with the smooth rigid bed in positions 1, 2, 3 and Fig. (5.22) shows the results of the sampled pressure field and its amplitude spectrum for the same simulation in positions 4, 5, 6. The same results for the rigid lid simulation can be found in Fig. (5.23) and Fig. (5.24).

By analysing the amplitude spectrum obtained from the velocity field and the pressure field, we can conclude that the vortex shedding frequency for the free surface simulation is

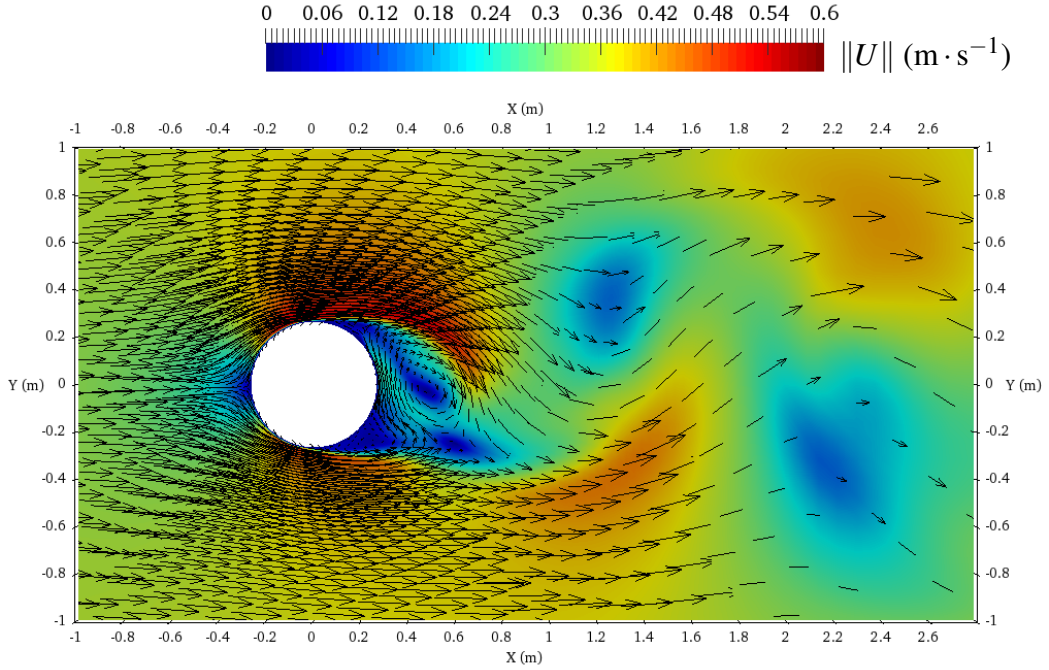

(a) Rigid lid simulation results.

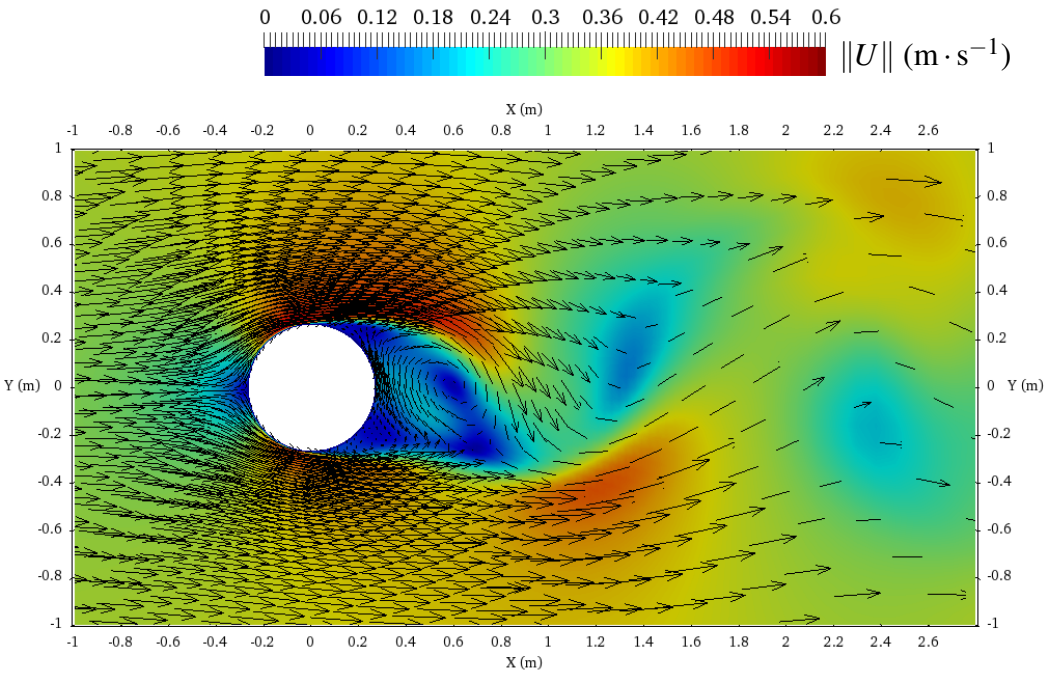

(b) Free surface simulation results.

Fig. 5.19 Instantaneous velocity vector field for the rigid lid and the free surface simulation coloured by velocity magnitude at horizontal plane $h = 0.34\,\mathrm{m}$.

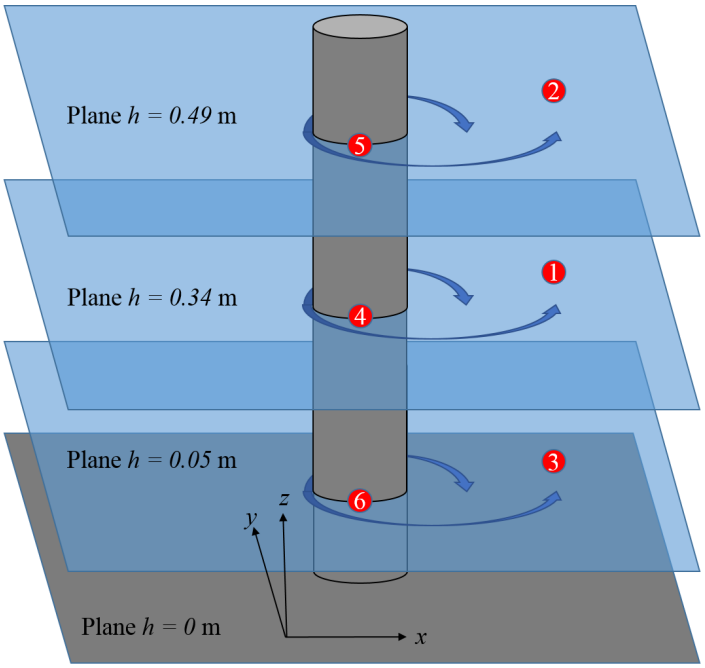

Fig. 5.20 Sampling positions for measuring vortex shedding frequency.

$f_f \approx 0.12\,\text{Hz}$ and the vortex shedding frequency for the rigid lid simulation is $f_r \approx 0.13\,\text{Hz}$. From the vortex shedding frequency, we can calculate the corresponding Strouhal number, which is a dimensionless number describing oscillating flow mechanisms, defined as:

$$St = \frac{fD}{U} \tag{5.4}$$

where f represents the frequency of vortex shedding. So the corresponding Strouhal number calculated from the free surface simulation results is $St_f \approx 0.2$ and from the rigid lid simulation results is $St_r \approx 0.21$. For vortex shedding behind a long circular cylinder with the Reynolds number $Re_D = 1.75 \times 10^5$, the Strouhal number should has a value $St \approx 0.2$ and both rigid lid and free surface simulations produce a reasonable vortex shedding frequency.

Comparing the sampled data and the amplitude spectrum obtained at different water depth, we find that the variation of the velocity field at depths $h = 0.34\,\text{m}$ and $h = 0.49\,\text{m}$ is similar while close to the bed at depth $h = 0.05\,\text{m}$, the amplitude of peak $f \approx 0.06\,\text{Hz}$ is almost the same with the expected vortex shedding frequency $f \approx 0.12\,\text{Hz}$, which makes it harder to decide which frequency should be the vortex shedding frequency at this depth. This phenomenon occurs in both rigid lid and free surface simulations. Based on the amplitude spectrum obtained from pressure field at position 4, 5 and 6, we tend to believe that the vortex shedding frequency at depth $h = 0.05\,\text{m}$ is still $f \approx 0.12\,\text{Hz}$ but the flow in the region close to the bed is not only dominated by the vortex shedding but also influenced by some

other effects probably related to the bed. However, Baykal et al. (2015) observed similar difference between frequency peaks at different water depth and they concluded that the vortex shedding frequency changes along the water depth and more frequent shedding of the vortices exists at the region far away from the bed. So this phenomenon requires further study to get a confirmed conclusion.

It should also be noticed that the Fourier transform results for velocity field from the free surface simulation in Fig. (5.21) show not only the vortex shedding frequency, which has the largest amplitude and dominates the flow field, but also several other peaks with lower amplitude. Some of them are harmonics of the vortex shedding frequency – $f \approx 0.06\,\mathrm{Hz} = 0.5 f_f$, $f \approx 0.24\,\mathrm{Hz} = 2 f_f$ and $f \approx 0.36\,\mathrm{Hz} = 3 f_f$. However, there are two frequencies who do not belong to the harmonic of the vortex shedding frequency: $f_1 \approx 0.132\,\mathrm{Hz}$ and $f_2 \approx 0.176\,\mathrm{Hz}$. A possible explanation is that they correspond to the frequency of the surface waves propagating in the simulation domain. As the front and back boundaries are set to be *wall* type of boundary, surface waves can be generated and reflected between these two boundaries. The inlet and outlet boundaries are controlled by the flow rate which also could numerically generate surface waves between them. The dimension of the computational mesh is $L = 24D = 12.864\,\mathrm{m}$ long and $W = 16D = 8.576\,\mathrm{m}$. If the surface waves have wavelengths equal to the length and width of the mesh, then the water depth $H = 0.54\,\mathrm{m}$ is much smaller than the surface wavelengths, so these waves should satisfy the shallow water condition. So the phase velocity of the surface waves can be calculated as:

$$c_p = \sqrt{gH} \tag{5.5}$$

which in our case gives $c_p = 2.3\,\mathrm{m}\cdot\mathrm{s}^{-1}$. So the corresponding frequency of the surface waves should be $f_W \approx 0.27\,\mathrm{Hz}$ and $f_L \approx 0.18\,\mathrm{Hz}$. Comparing the theoretical frequencies of the surface waves with the frequencies we obtain from Fig. (5.21), we have $f_1 \approx 0.5 f_W$, which means that the wavelength in this direction is twice the width of the domain and $f_2 \approx f_L$, which means that the wavelength in this direction equals the length of the domain. So the possible surface waves propagating in the simulation domain are shown in Fig. (5.25).

Finally, we look at the vorticity of the flow field behind the cylinder. The iso-surfaces of vorticity magnitude for the rigid lid and the free surface simulations are shown in Fig. (5.26) and Fig. (5.27). From Fig. (5.26), we see clearly the structure of the vortices behind the cylinder. From Fig. (5.27), we see that in the rigid lid simulation, the iso-surfaces for vorticity magnitude are almost vertically straight, except at the region close to the bed where the iso-surfaces curved towards the cylinder and the vorticity magnitude is larger, while in the free surface simulation the iso-surfaces are curved vertically towards the cylinder in the regions close to the bed and close to the free surface where the vorticity magnitude becomes

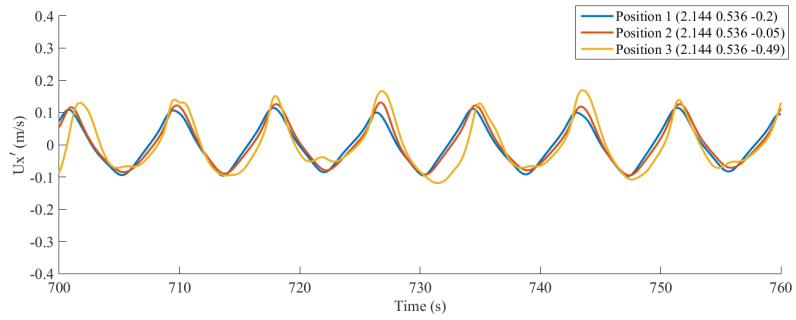

(a) $U'_x = U_x - \overline{U}_x$ field.

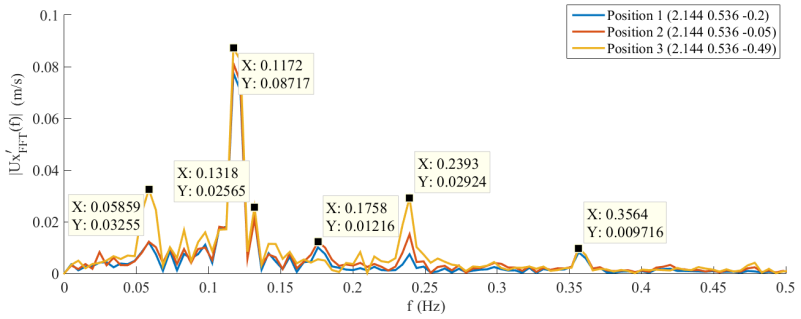

(b) Fourier transform of U'_x.

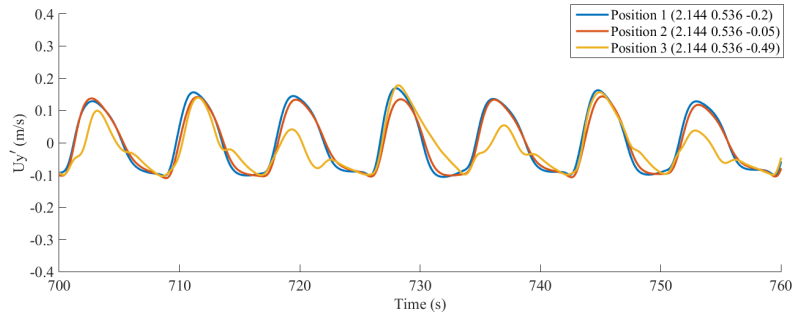

(c) $U'_y = U_y - \overline{U}_y$ field.

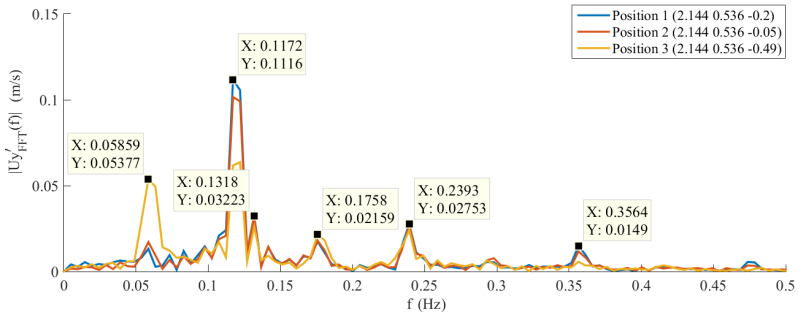

(d) Fourier transform of U'_y.

Fig. 5.21 Velocity field and its Fourier transform at positions 1, 2, 3 for the free surface simulation with a smooth bed.

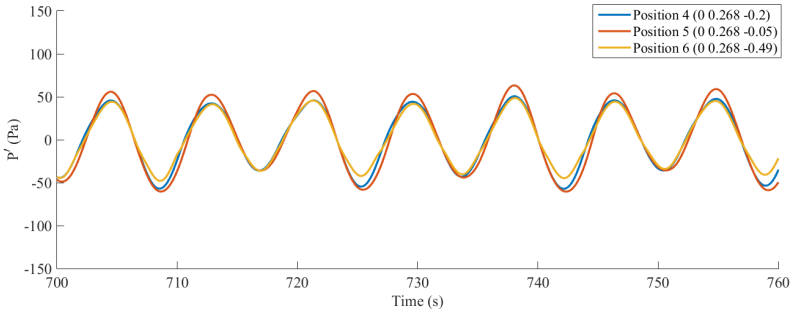

(a) $P' = P - \overline{P}$ field.

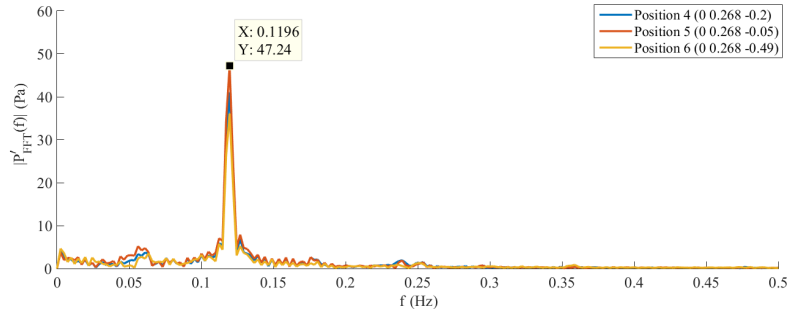

(b) Fourier transform of $P - \overline{P}$.

Fig. 5.22 Pressure field and its Fourier transform at positions 4, 5, 6 for the free surface simulation with a smooth bed.

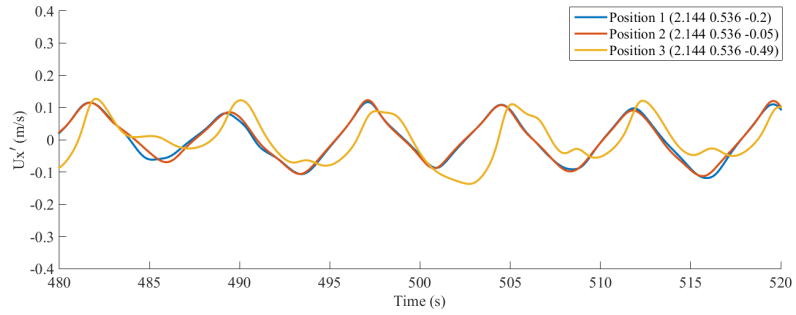

(a) $U'_x = U_x - \overline{U}_x$ field.

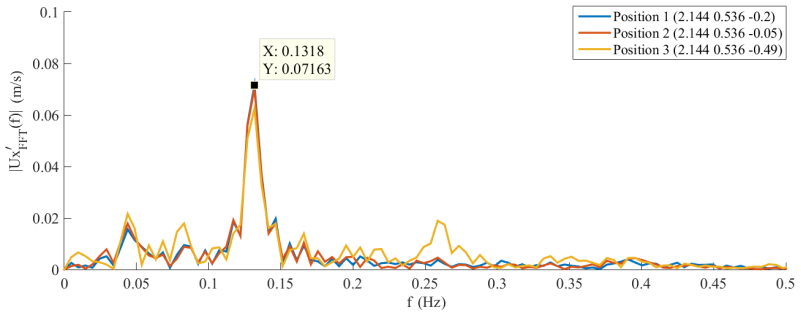

(b) Fourier transform of U'_x.

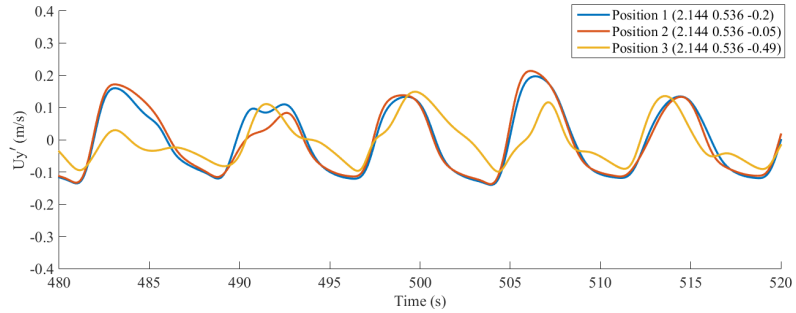

(c) $U'_y = U_y - \overline{U}_y$ field.

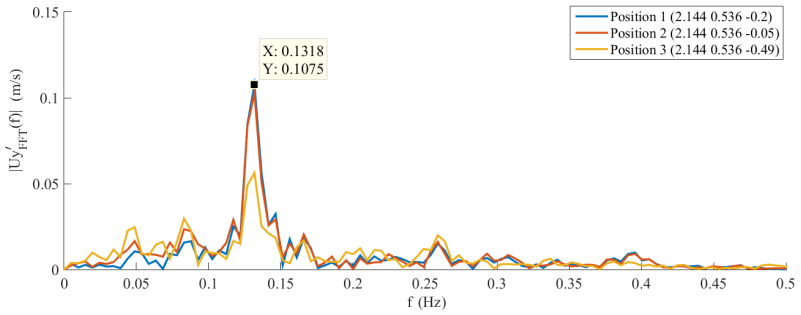

(d) Fourier transform of U'_y.

Fig. 5.23 Velocity field and its Fourier transform at positions 1, 2, 3 for the rigid lid simulation with a smooth bed.

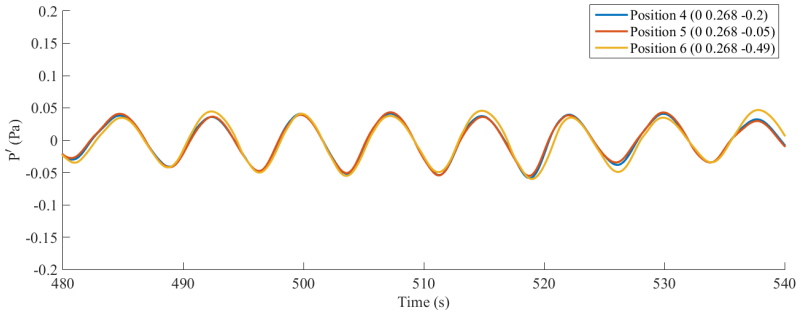

(a) $P' = P - \overline{P}$ field.

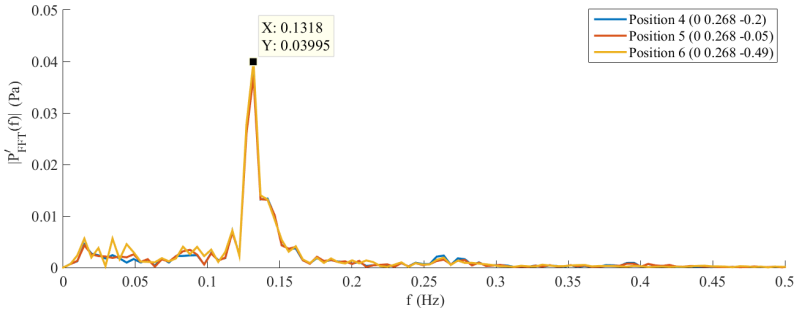

(b) Fourier transform of $P - \overline{P}$.

Fig. 5.24 Pressure field and its Fourier transform at positions 4, 5, 6 for the rigid lid simulation with a smooth bed.

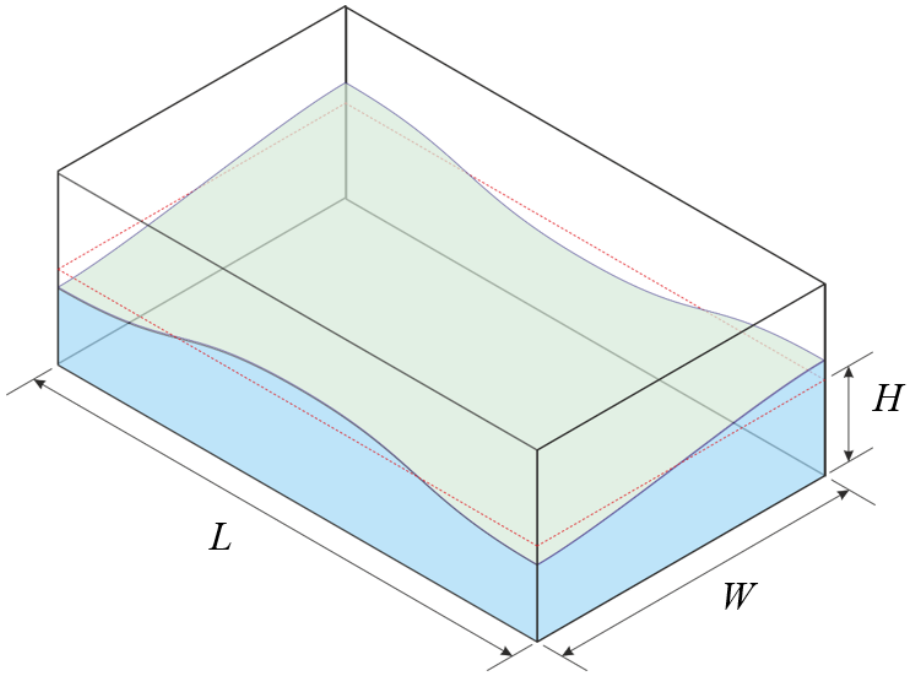

Fig. 5.25 The surfaces waves detected in the simulation domain.

also larger. This could be explained by the variation of the water depth in the free surface simulation which causes the vortex line to be stretched or compressed. Theoretically, the magnitude of the vorticity becomes smaller when the vortex line is stretched and larger when the vortex line is compressed.

Flow around cylinder on a rough rigid bed

Now we look at the simulation results for the flow around a cylinder on a rough rigid bed. For wall-bounded turbulent flows, the roughness of the wall exerts a frictional drag on the flow acting as a momentum sink. As described in Chapter 2, the roughness of the wall is modelled using the rough wall functions and the roughness of the bed will influence the calculated eddy viscosity and hence the boundary layer and the flow field. So before looking at the simulation results of the flow field around the cylinder on a rough bed, a preliminary test was done to compare the measured and simulated velocity profile of the flow field in the absence of the cylinder, which is referred to as the 'undisturbed velocity profile' in Roulund et al. (2005), on both of the smooth and rough beds.

The comparison is shown in Fig. (5.28). We can see from the figure that the simulated velocity profile on the smooth bed is consistent with the measured velocity profile represented by blue circles. However, the simulated velocity profile on the rough bed, which uses the same mean inlet velocity as in the experiment $\overline{U} = 0.326\,\mathrm{m}\cdot\mathrm{s}^{-1}$, is not in good agreement with the measured velocity profile, especially for the region close to the bed. A closer look at the measured undisturbed velocity profile reveals that the flow rate for the rough bed is larger than that for the smooth bed, while in the experiments, the mean inlet velocity and the water depth are set to be the same for the smooth and rough beds as indicated in Roulund et al. (2005). This difference could be caused by the fact that the flow in this case is three-dimensional and the measurement of the flow velocity may be conducted near the central plane where the flow rate per unit width is higher than that close to the side walls. So we increased the mean inlet velocity in the simulation without changing the equivalent roughness height and we found that with the mean inlet velocity increased to $\overline{U} = 0.365\,\mathrm{m}\cdot\mathrm{s}^{-1}$, the velocity profile close to the bed is in good agreement with the measured velocity profile, while the velocity away from the bed is overestimated. So we can conclude that the equivalent roughness height value used in the simulation is correct and the rough wall functions work fine, but the difference between the flow rate per unit width in the position measured in the experiments and in the simulation cause the difference between the measured and simulated velocity profile. In this work, we decided to follow the values given in the paper and thus the inlet mean velocity is set to be $\overline{U} = 0.326\,\mathrm{m}\cdot\mathrm{s}^{-1}$ as indicated in Roulund et al. (2005). And this difference between the inlet velocity profile can be responsible for the difference

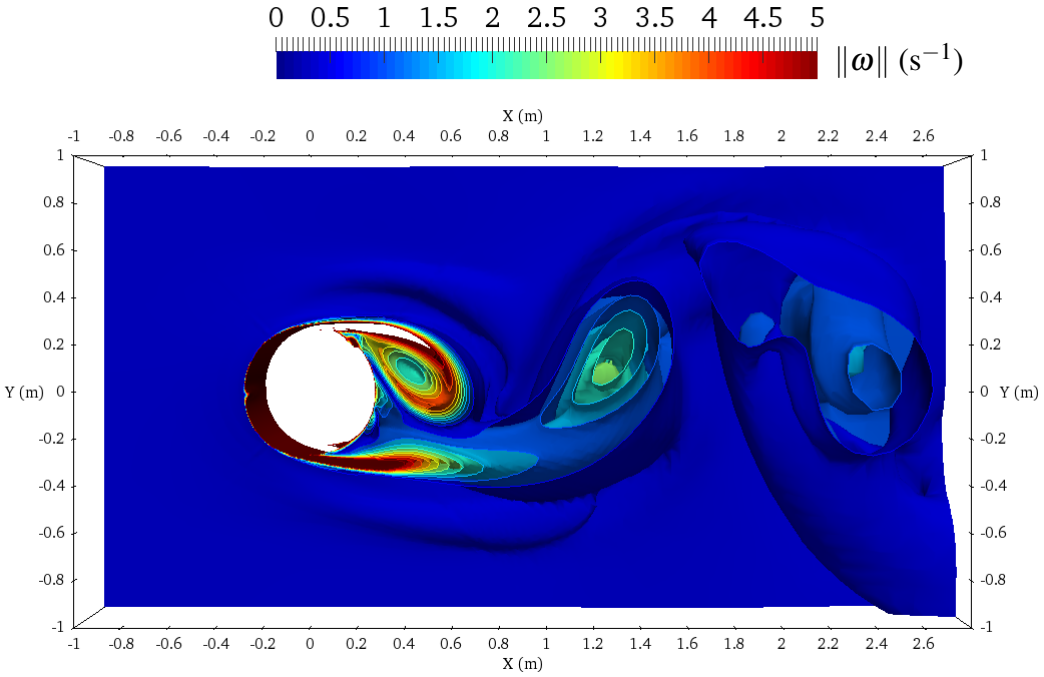

(a) Rigid lid simulation results.

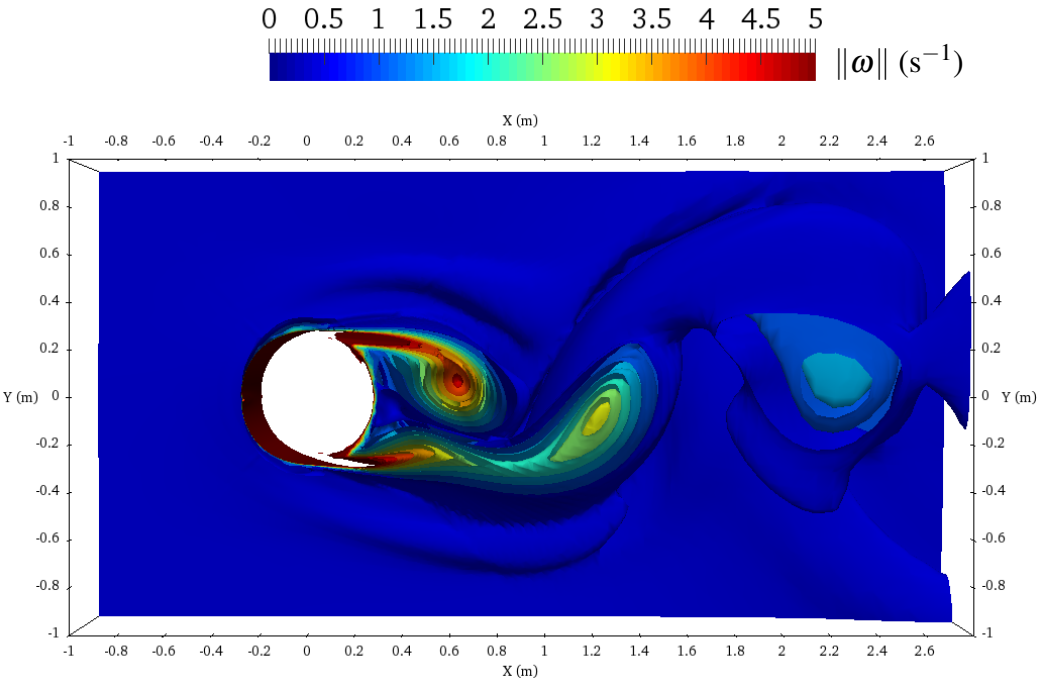

(b) Free surface simulation results.

Fig. 5.26 Iso-surfaces of instantaneous vorticity magnitude for the rigid lid and the free surface simulations, view from above.

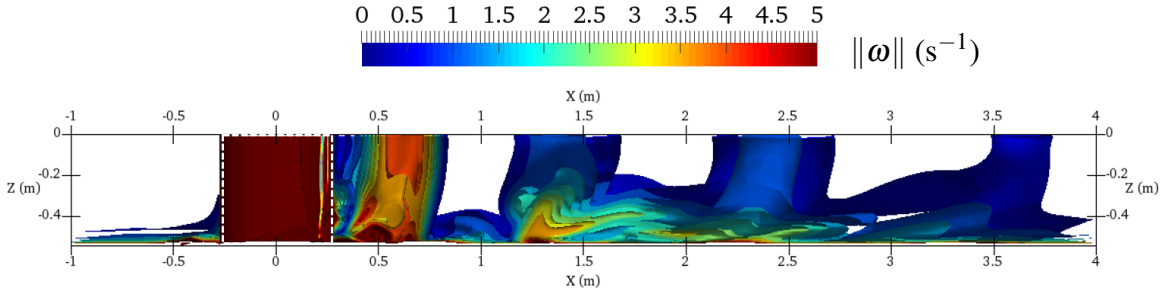

(a) Rigid lid simulation results.

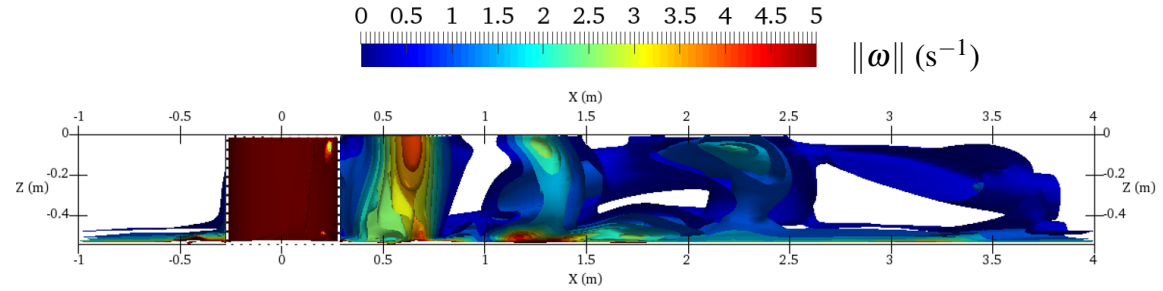

(b) Free surface simulation results.

Fig. 5.27 Iso-surfaces of instantaneous vorticity magnitude for the rigid lid and the free surface simulations, view from the central plane.

between the measured and simulated velocity field at the downstream side of the cylinder on a rough bed.

The simulation results of the mean velocity field on a rough bed show similar flow patterns to those on a smooth bed, only the values are different. So there is no need to analyse again the simulation results of the time-averaged velocity field for this simulation, and we just show here the comparison between the measured and simulated time-averaged velocity in the x and z directions at different water depths in Fig. (5.29), Fig. (5.30) and Fig. (5.31).

We see from these figures that the simulation results agree well with the experimental measurements for the flow field in both the x and the z directions at the upstream side of the cylinder. However, at the downstream side of the cylinder, the comparison for the velocity in x direction shows that the size of the reverse flow region is underestimated by the simulation in this work. This could be explained by the difference between the measured and simulated undisturbed mean inlet velocity. But the simulation results from Roulund et al. (2005), which is a rigid lid simulation and uses the same numerical set-up, agree very well with the experimental data. So this requires further investigation. The simulated and measured velocity in the z direction is quite different. However, behind the cylinder, the simulated and

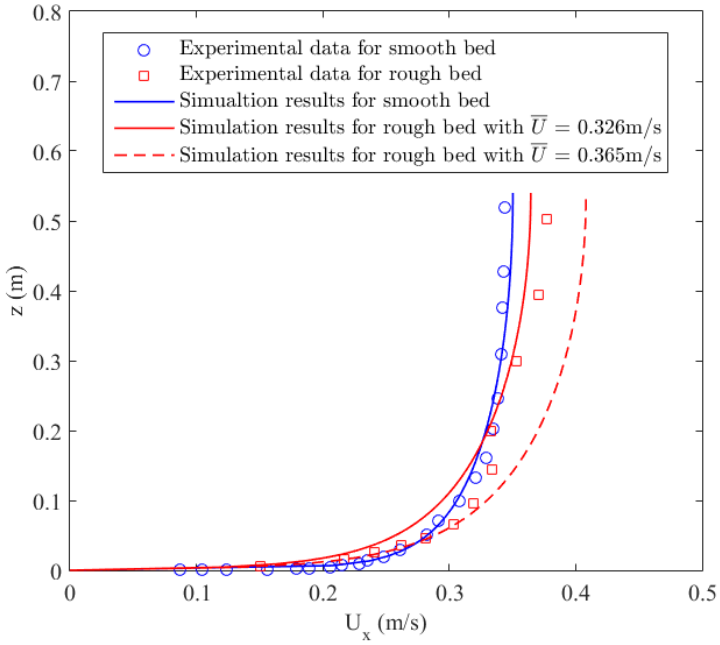

(a) Velocity profile using linear scales on the vertical and horizontal axis.

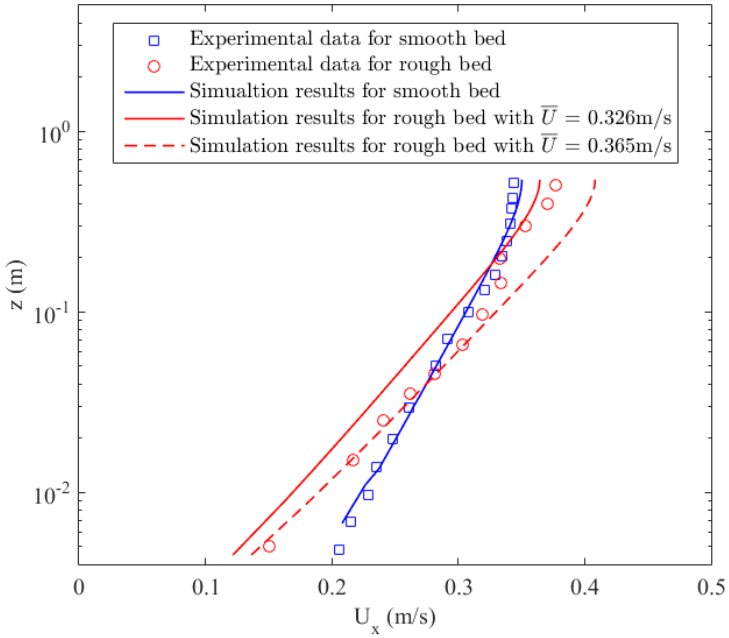

(b) Velocity profile using a logarithmic scale on the vertical axis, and a linear scale on the horizontal axis.

Fig. 5.28 Measured and simulated velocity profile of the flow field without cylinder on the smooth and rough beds.

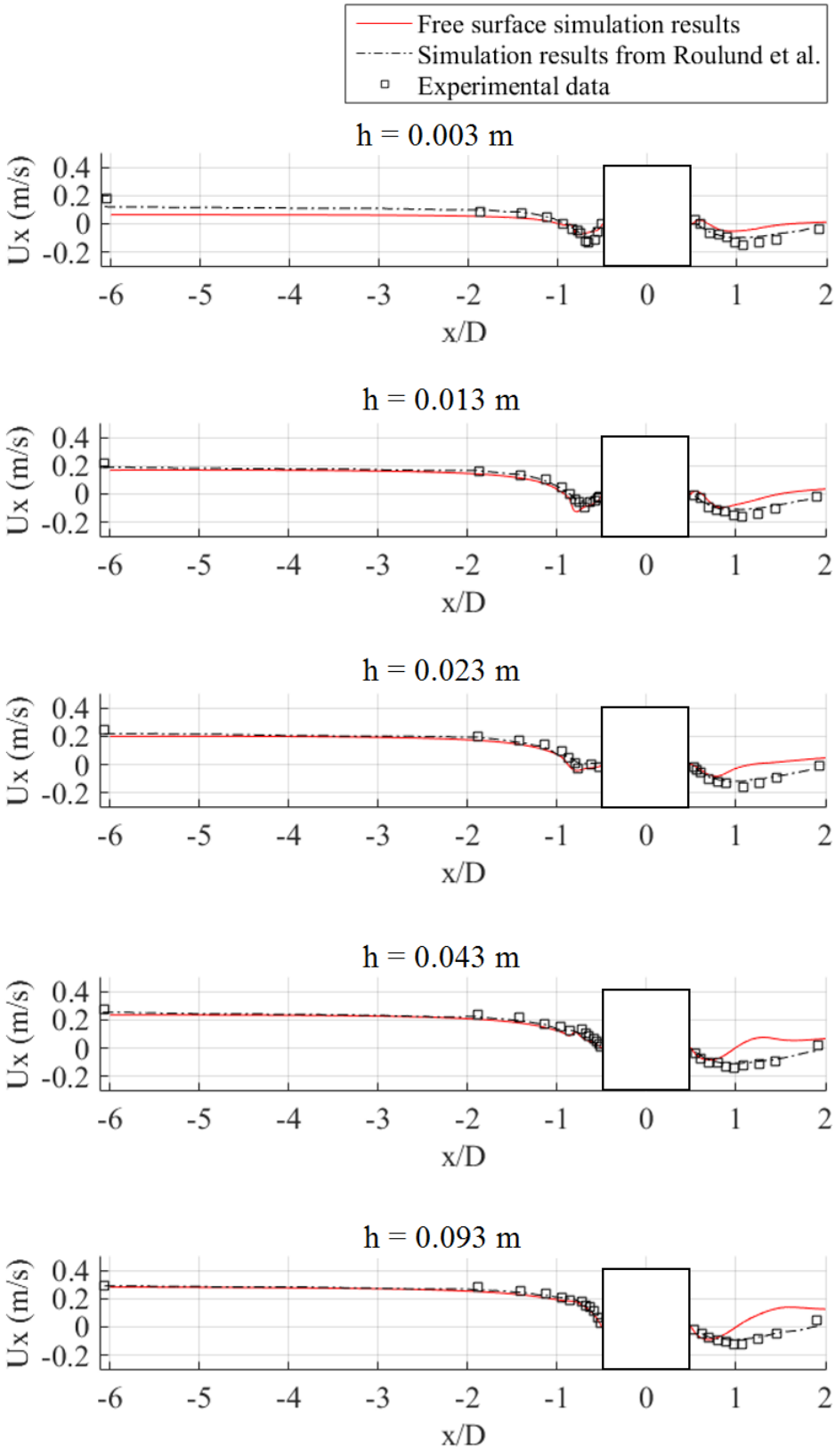

Fig. 5.29 Comparison between simulation results and experimental measurements of time-averaged velocity field U_x on plane $y = 0\,\text{m}$ for flow around a cylinder on a rough bed.

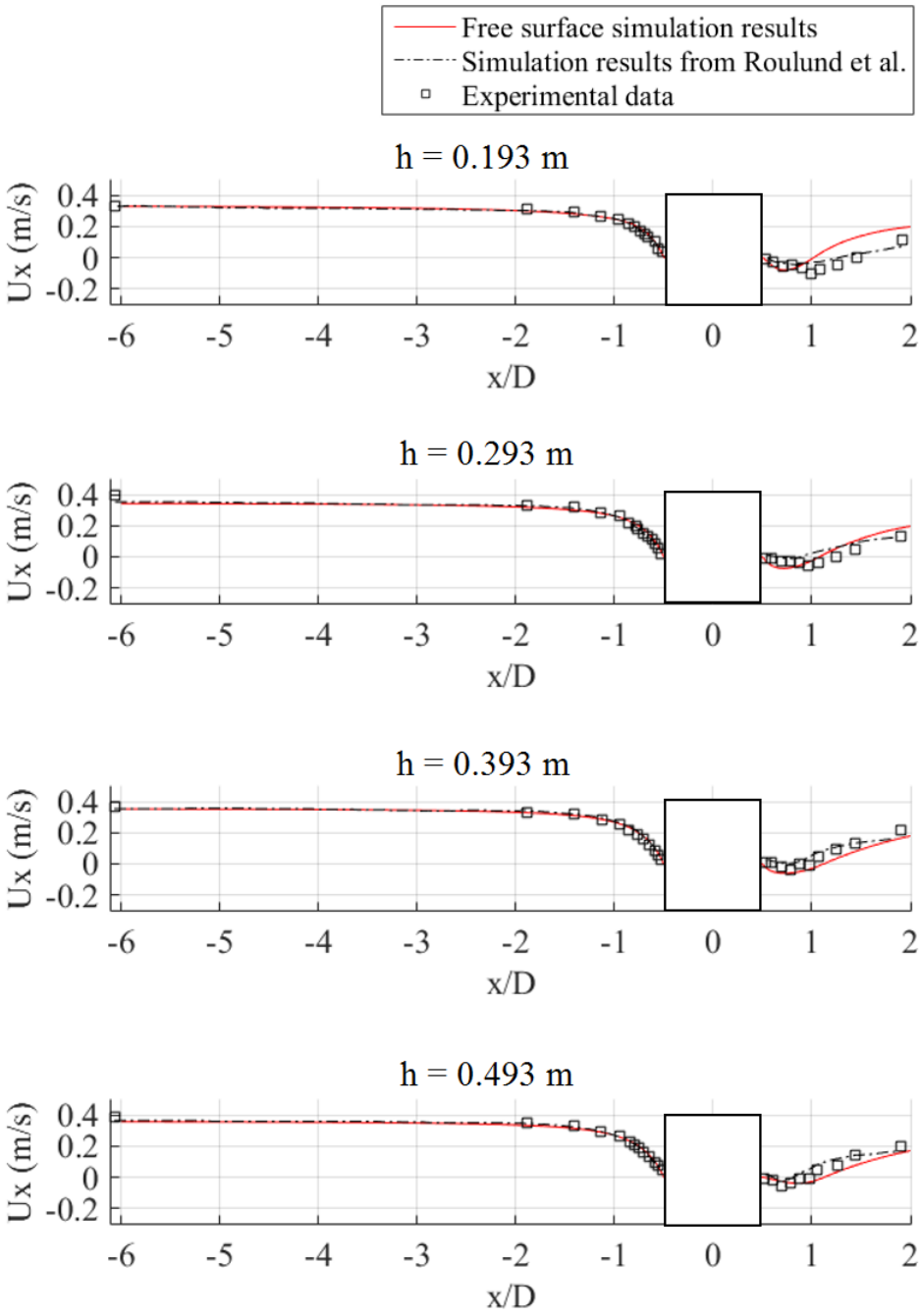

Fig. 5.30 Comparison between simulation results and experimental measurements of time-averaged velocity field U_x on plane $y = 0\,\text{m}$ for flow around a cylinder on rough bed (continue).

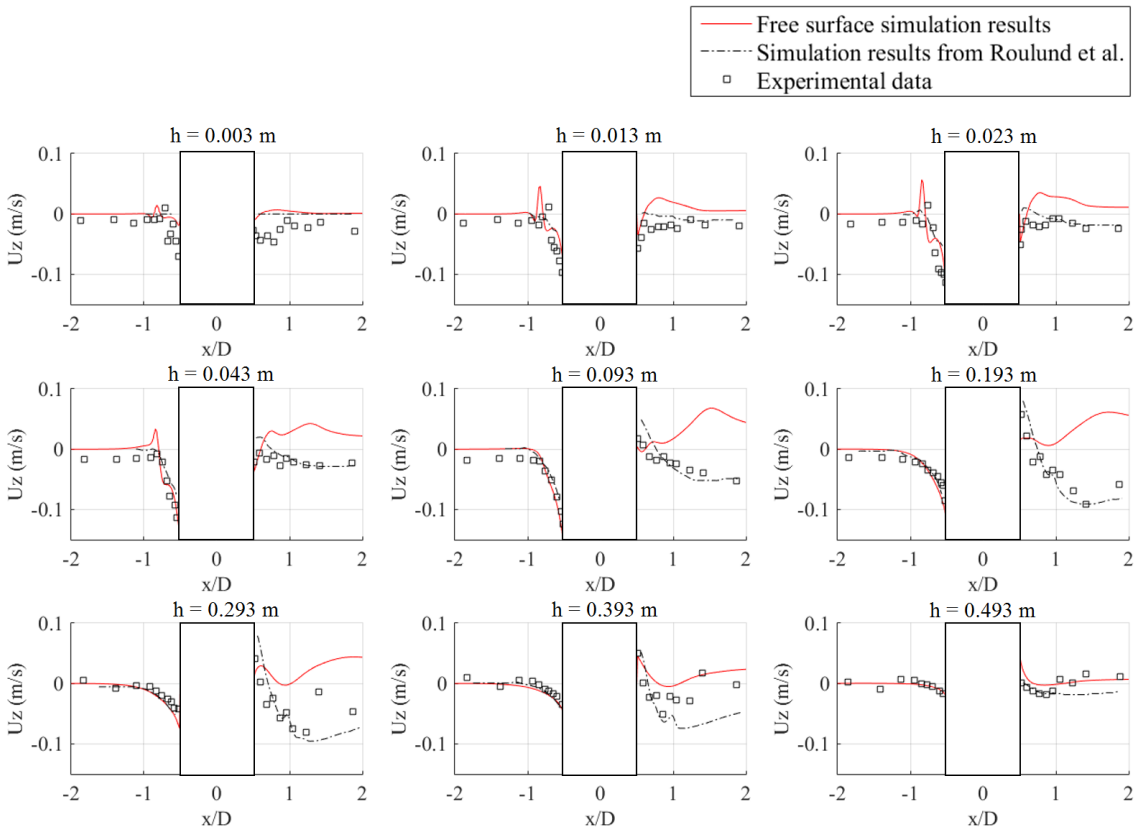

Fig. 5.31 Comparison between simulation results and experimental measurements of time-averaged velocity field U_z on plane $y = 0\,\mathrm{m}$ for flow around a cylinder on rough bed.

measured velocity in z direction are both negative in the region close to the bed, and positive in the region away from the bed close to the water surface.

Next, we look at the unsteady features of the flow field on a rough bed. The velocity field and the pressure field are sampled in the same positions as in the smooth bed simulation. The field sampled and the Fourier transform of the corresponding fields are shown in Fig. (5.32) and Fig. (5.33). We can see from the figure that the vortex shedding frequency is $f \approx 0.12\,\mathrm{Hz}$, so it is not influenced by the roughness of the bed and the Strouhal number obtained is the same as in the free surface simulation on a smooth bed $St \approx 0.2$. The amplitude spectrum shows that surface waves also exist in the flow field on a rough bed. Except for the harmonics of the vortex shedding frequency and the surface wave frequencies that have already been detected in the smooth bed simulation, some new peaks appear in the amplitude spectrum as shown in Fig. (5.34), which suggests that there could be a complex combination of the surface waves of different wavelengths.

The vorticity of the flow field on a rough bed is shown in Fig. (5.35) and Fig. (5.36). The iso-surfaces of the vorticity magnitude are also curved vertically and the vorticity magnitude at the vortex centres seems to be generally larger than that for the smooth bed simulation.

To complete the analysis of the simulation results of flow around a cylinder, we look at the simulation results of the shear stress on the bed surface. Fig. (5.37) shows the contour plot of the bed shear stress amplification A obtained from the simulation with the smooth bed and with the rough bed. The bed shear stress amplification A in this work is defined as the ratio of the local bed shear stress to the undisturbed bed shear stress with the sign of A given by the x component of the local bed shear stress:

$$A = \mathrm{sgn}(\tau_{bx}) \frac{\|\tau_b\|}{\tau_\infty} \tag{5.6}$$

where τ_∞ represents the undisturbed bed shear stress. In this way, we can see clearly the separation regions of the flow field and the shear stress magnitude at the same time. We can identify on Fig. (5.37) the horseshoe vortex region in front of the cylinder. The maximum bed shear stress occurs around $\phi = 79°$ on the smooth bed and at about $\phi = 65°$ on the rough bed, where ϕ is the angle measured from the $-x$ axis; the value of the shear stress on the rough bed is much bigger than that on the smooth bed. Moreover, the separation of the boundary layer on a rough bed is later than that on the smooth bed and the wake is closer to the cylinder on the rough bed than on the smooth bed. These phenomena agree well with the common idea that larger the roughness, larger the turbulence generated at the bed and injected into the main body of the flow, thus delaying the boundary-layer separation.

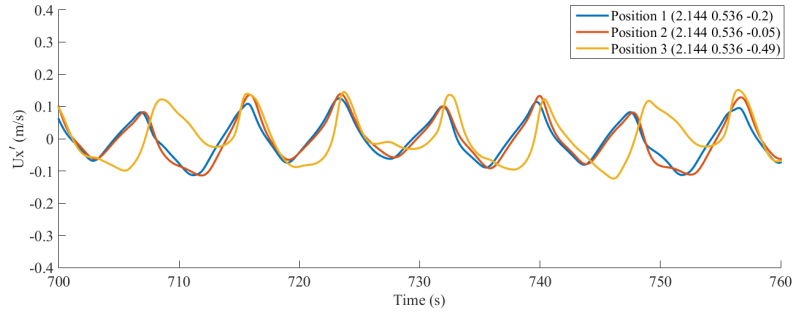

(a) $U'_x = U_x - \overline{U}_x$ field.

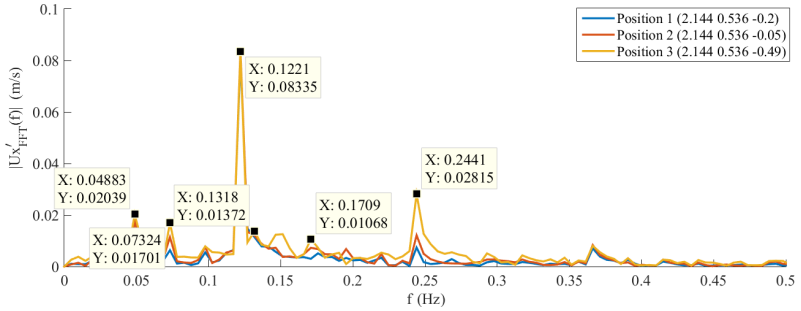

(b) Fourier transform of U'_x.

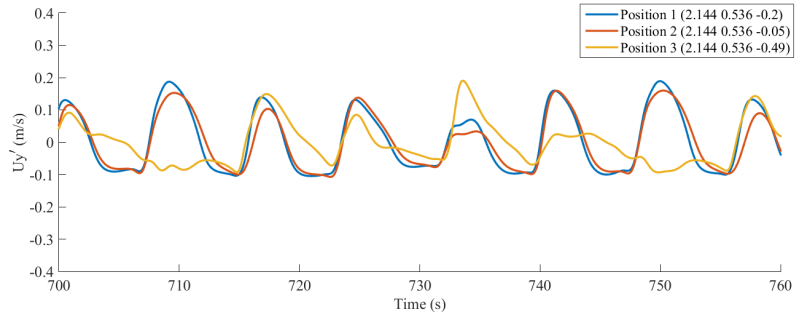

(c) $U'_y = U_y - \overline{U}_y$ field.

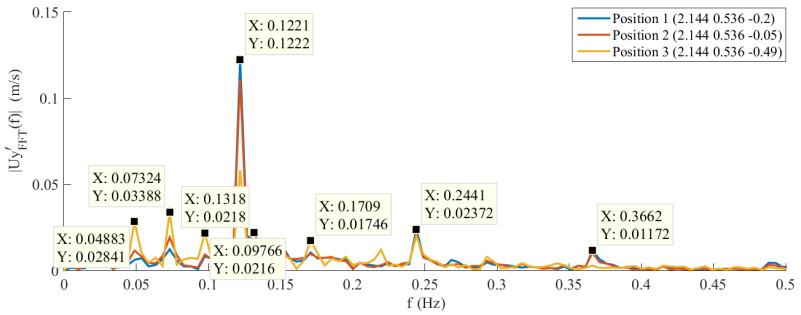

(d) Fourier transform of U'_y.

Fig. 5.32 Velocity field and its Fourier transform at positions 1, 2, 3 for the free surface simulation with a rough bed.

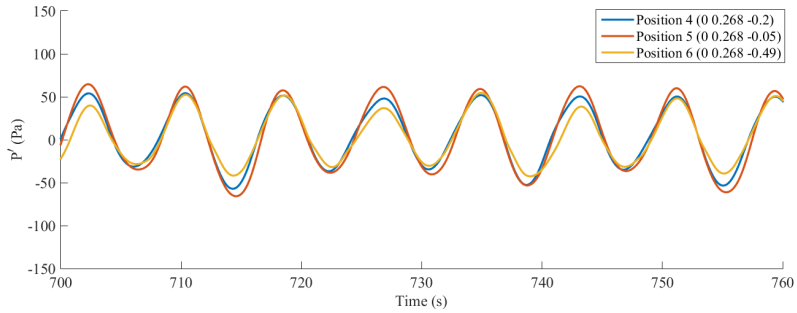

(a) $P' = P - \overline{P}$ field.

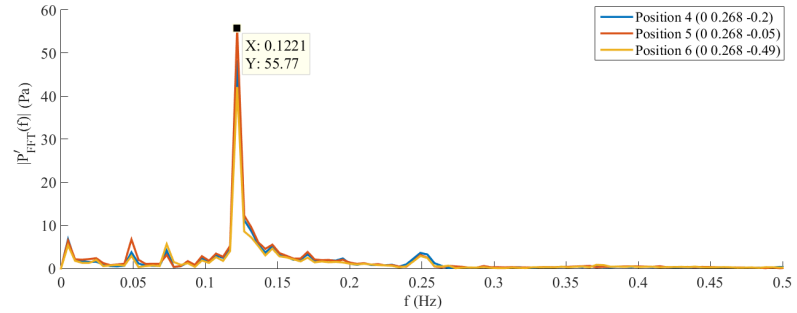

(b) Fourier transform of $P - \overline{P}$.

Fig. 5.33 Pressure field and its Fourier transform at positions 4, 5, 6 for the free surface simulation with a rough bed.

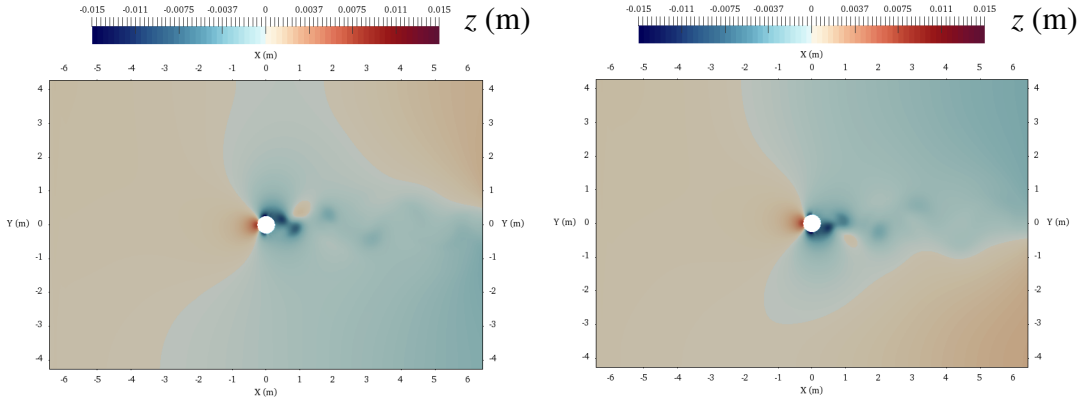

(a) Free surface position, initial at $z = 0\,\text{m}$.

(b) Free surface position, initial at $z = 0\,\text{m}$.

Fig. 5.34 Free surface position at two random instants for the rough bed simulation.

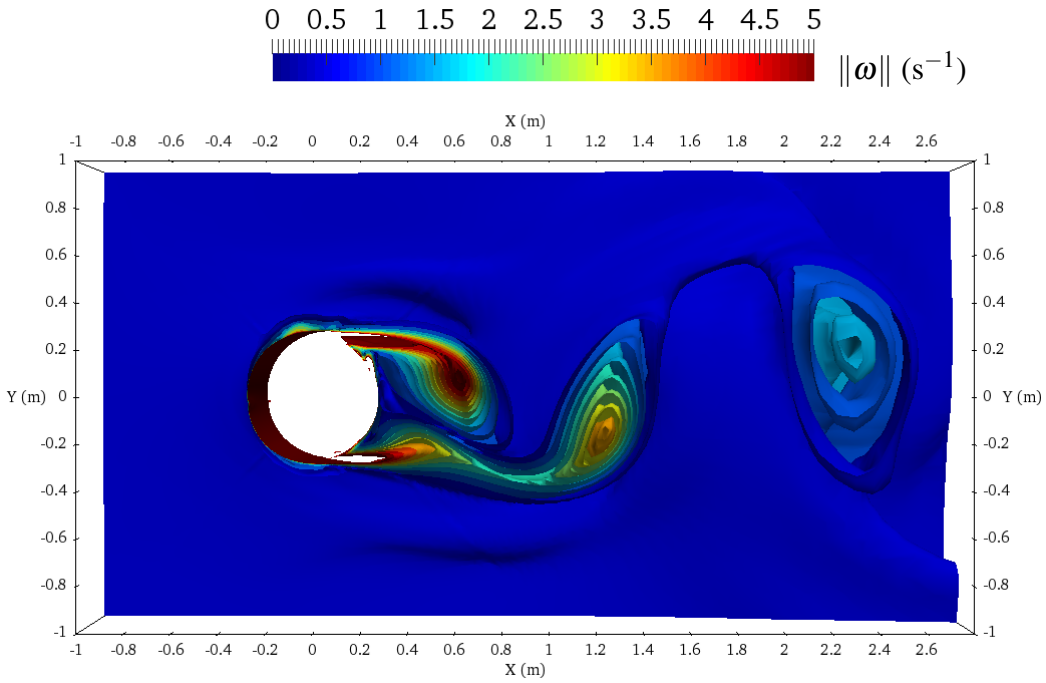

Fig. 5.35 Iso-surfaces of instantaneous vorticity magnitude for the free surface simulations with a rough bed, view from above.

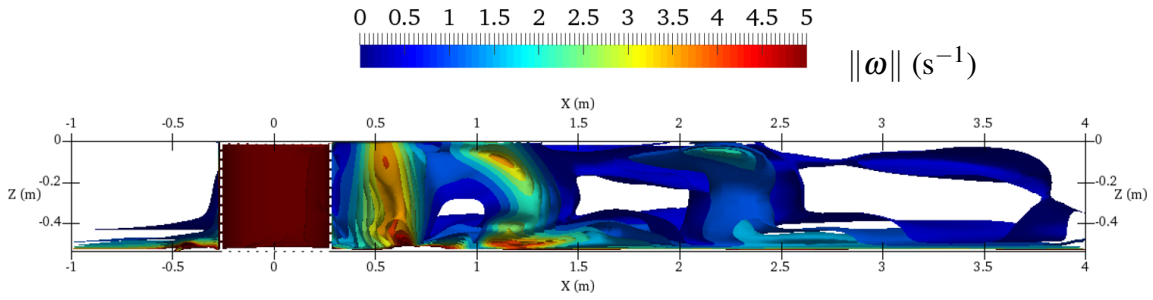

Fig. 5.36 Iso-surfaces of instantaneous vorticity magnitude for the free surface simulations with a rough bed, view from the central plane.

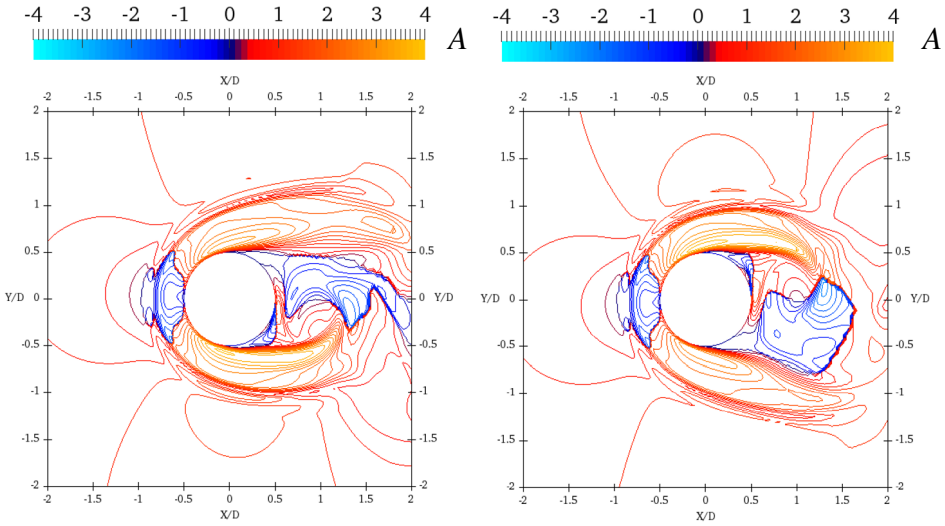

(a) Shear stress on a smooth bed at two phases of the vortex shedding.

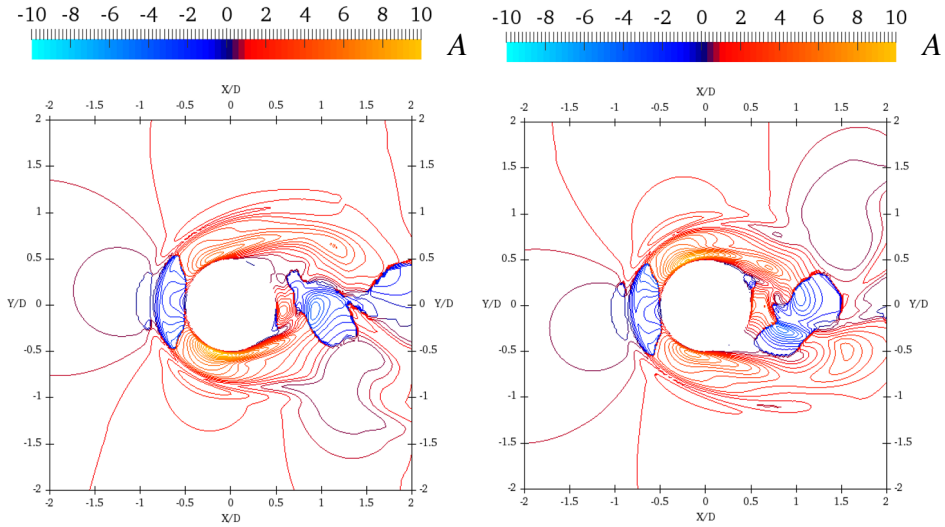

(b) Shear stress on a rough bed at two phases of the vortex shedding.

Fig. 5.37 Bed shear stress amplification A defined in Eq.(5.6) on the smooth bed and on the rough bed.

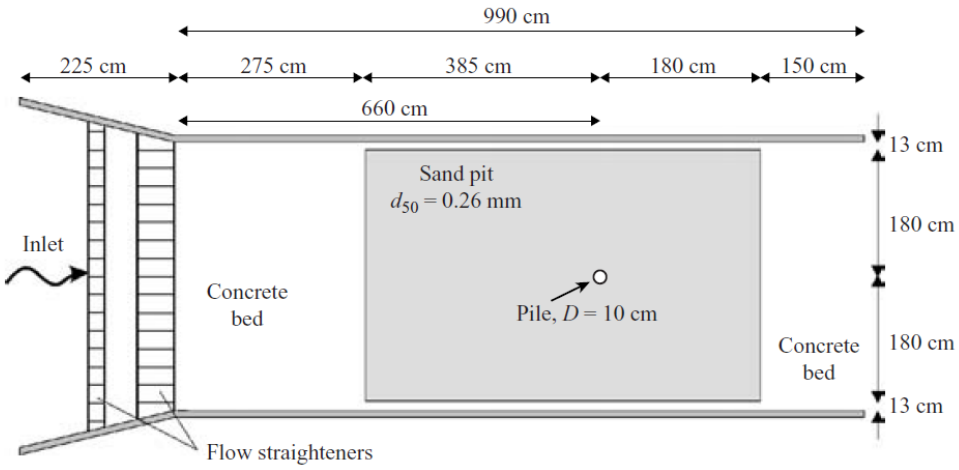

Fig. 5.38 Set-up for the scour experiment, from Roulund et al. (2005).

5.3 Simulation of Live-Bed Scour Around Cylinder

Finally, the numerical model is used to simulate the local scour around a cylinder in steady current. The free surface simulation with the k-ωSST turbulence closure is used for the flow field and the bed deformation is activated. The simulation results are compared with the experimental measurements from Roulund et al. (2005) to evaluate the performance of the model.

5.3.1 Laboratory Study Details

Fig. (5.38) shows the set-up of the scour experiment and the experimental conditions in the scour test are summarized in Table 5.3. The experiment was conducted in a current flume with a sand bed. The water depth was $H = 0.4$ m and the undisturbed mean flow velocity was $\overline{U} = 0.46$ m. A circular pile with diameter $D = 0.1$ m and hydraulically smooth surface was placed in the sediment bed. The corresponding Reynolds number was $Re = 4.6 \times 10^4$. The sand size used in the experiment is $d_{50} = 0.26$ mm with a geometric standard deviation of $\sigma_g = d_{85}/d_{50} = 1.5$. The undisturbed mean velocity profile for the scour experiment was also measured to calculate the boundary layer thickness and the bed equivalent roughness height. As the test is in live-bed conditions, the bed is covered with ripples and thus the bed roughness can be divided into two components: the roughness due to the bed form and the roughness due to the skin friction of the sediment.

The flow and scour processes around the pile were visualized using a DANTEC 2.5 mm thick vertical sheet of laser light as a light source. The flow was made visible with fluorescent dye as well as with sediment grains and an underwater video camera was used to videotape he

Table 5.3 Conditions for the scour experiment, from Roulund et al. (2005).

Bed	Loose sand
Water depth H	0.4 m
Boundary layer thickness δ	0.2 m
Mean flow velocity $\overline{U}$	$0.46\,\mathrm{m}\cdot\mathrm{s}^{-1}$
Pile diameter D	0.1 m
Froude number $Fr = \frac{\overline{U}}{\sqrt{gH}}$	0.23
Reynolds number $Re_D = \frac{\overline{U}D}{\nu}$	4.6×10^4
Grain size d_{50}	0.26 mm
Gradation σ_g	1.5
Friction velocity U_f	$0.048\,\mathrm{m}\cdot\mathrm{s}^{-1}$
Friction velocity due to skin friction U'_f	$0.028\,\mathrm{m}\cdot\mathrm{s}^{-1}$
Bed Nikuradse equivalent sand roughness k_s	0.15 m
Sand roughness due to skin friction $k'_s = 2.5d_{50}$	0.65 mm

flow and the scour processes at five radial sections (the visualisations of flow and scour at the base of the circular pile at upstream and downstream symmetry lines are shown in Roulund et al. (2005)). The time development of scour depth at both upstream and downstream side of the pile was monitored. The experiment lasted 3 hours and the experimental measurements shows that within 30 min, the scour depth on the upstream side of the cylinder reached 80% of the equilibrium scour depth and the scour depth on the downstream side of the cylinder reached 66% of the equilibrium scour depth. Because of the computational time required, our simulation only covers the first 30 min of the scour process (which takes about 1160 h). Fig. (5.39) shows the equilibrium scour hole obtained from the experiment.

5.3.2 Numerical Set-Up of the Simulation

A sketch of the simulation of scour around a circular pile is shown in Fig. (5.40). The diameter of the cylinder is $D = 0.1\,\mathrm{m}$ and the initial water depth is $H = 0.4\,\mathrm{m}$. The inlet mean flow velocity is set to be $\overline{U} = 0.46\,\mathrm{m}\cdot\mathrm{s}^{-1}$ as in the experiments.

The mesh is generated with mesh generator *Gmsh*. The view of the mesh from above and from the inlet boundary is shown in Fig. (5.41). The mesh has 952320 cells with finer resolution in the regions around the cylinder, close to the bed and near the free surface; the maximum expansion ratio between the edges of adjacent mesh cells equals 1.05. The simulation domain contains only the sand pit region in the experiment and the mean grain size of the sediment is set to be $d_{50} = 0.26\,\mathrm{mm}$. The equivalent roughness height for the rough wall functions is set to be $k_s = 2.5d_{50} = 0.65\,\mathrm{mm}$, which is the roughness height due

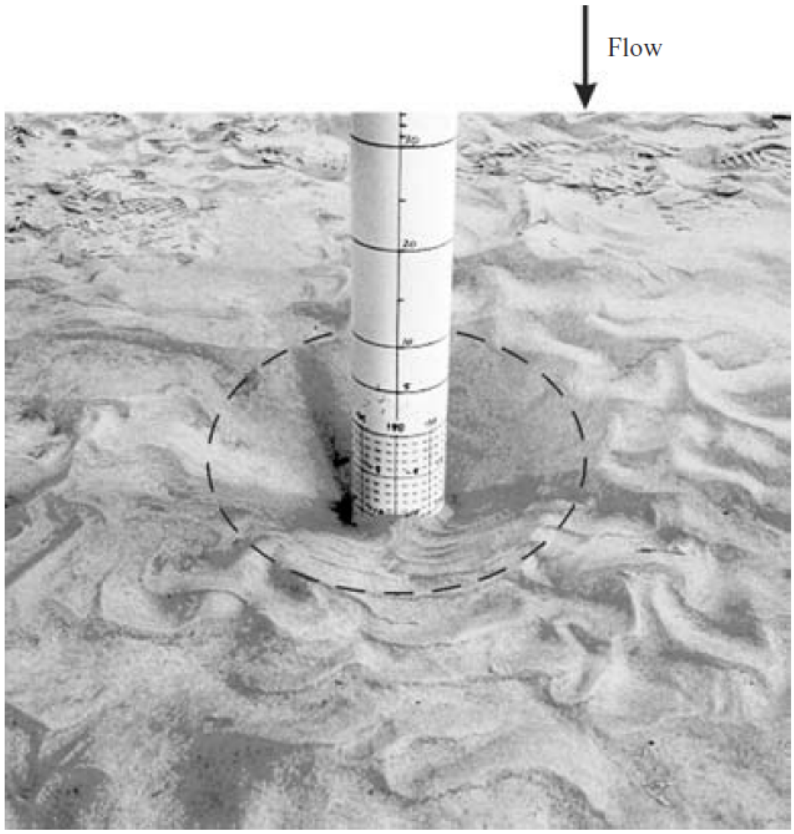

Fig. 5.39 Equilibrium scour hole in the experiment, from Roulund et al. (2005).

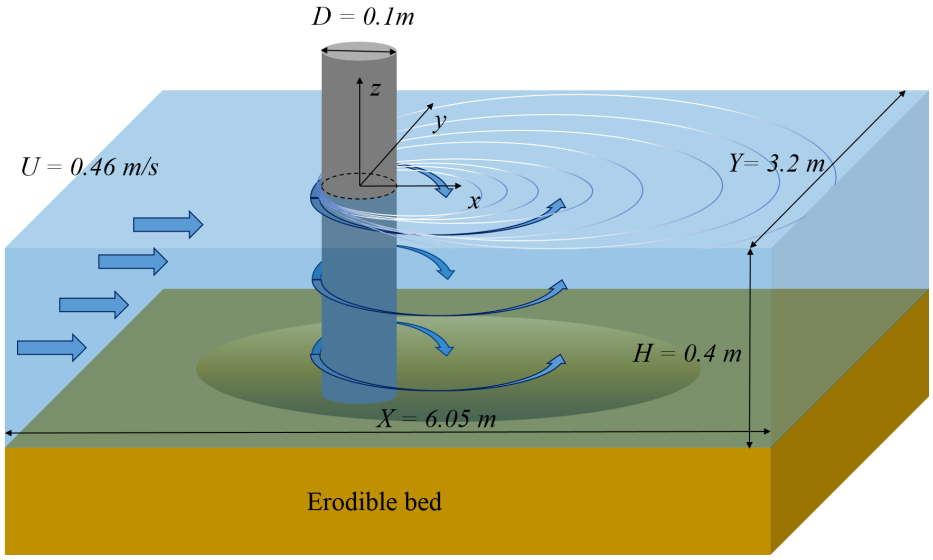

Fig. 5.40 Sketch of simulation of scour around a single cylinder.

to the skin friction of the bed and should be used in the morphological module to calculate the sediment transport. Due to the limitations of the model, the ripples which formed and propagated on the bed in the experiment can not be reproduced; so the boundary layer thickness of the flow field calculated in the simulation should be different from that of the experiment which means that the influences of the bed forms on the the sediment transport are not included in this simulation. This could be an explanation of the difference between the simulated and measured temporal development of scour hole.

The boundary conditions for the flow field are defined to be the same as in the previous simulations of the rigid bed configuration. The boundary condition for suspended load concentration is set to be zero-gradient for all boundaries except for the bottom boundary which is defined using the entrainment rate and deposition rate presented in Chapter 3.

5.3.3 Simulation Results and Discussions

First of all, we look at the temporal development of the overall scour form. A sequence of pictures illustrating the evolution of the scour hole obtained in the present simulation is shown in Fig. (5.42). Moreover, to show quantitatively the form of the scour, Fig. (5.43) shows the contour of bed elevation at $t = 180\,\mathrm{s}$, $t = 300\,\mathrm{s}$, $t = 600\,\mathrm{s}$ and $t = 900\,\mathrm{s}$.

From the simulation result, several topographic bed features can be observed:

- The scour hole starts to form at the upstream side of the cylinder, then the hole becomes larger and expands to the downstream side of the cylinder.

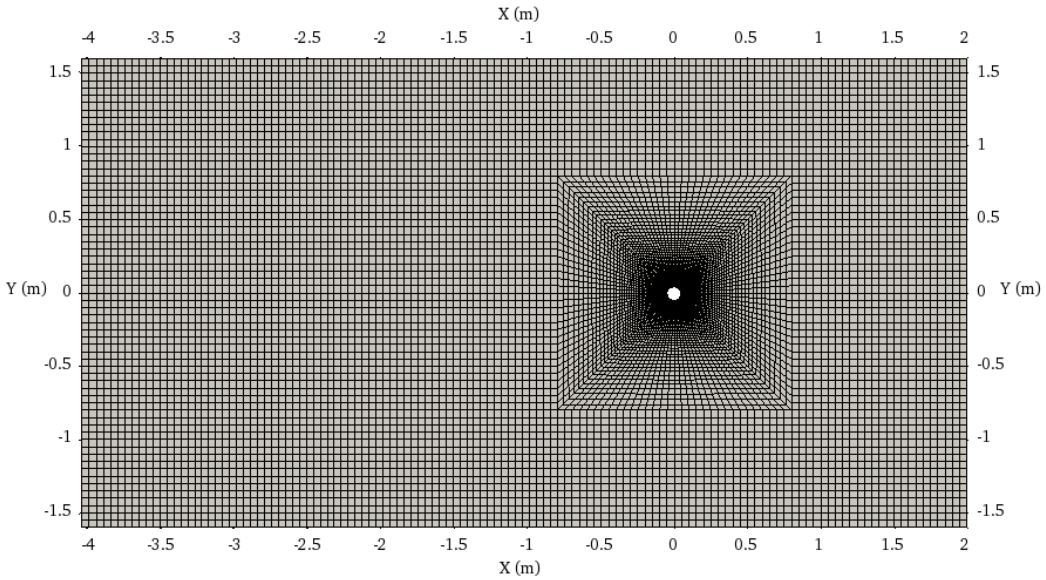

(a) A horizontal slice of the mesh (view from above).

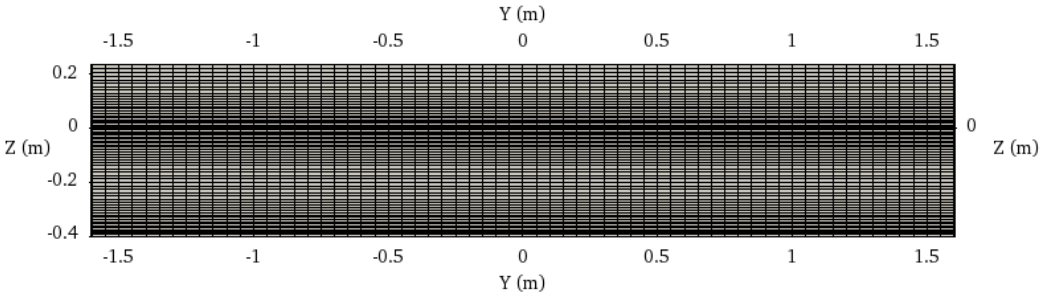

(b) A vertical slice of the mesh (view from inlet).

Fig. 5.41 Mesh generated for simulation of scour around a single cylinder.

- The scour hole upstream of the cylinder becomes deeper and deeper until finally it is semi-circular in shape and the slope of the hole approximately equals the repose angle of the sediment while the slope of the hole at the downstream side of the cylinder is quite gentle.

- The sand is deposited and forms two dunes positioned almost symmetrically at the downstream side of the cylinder. The sand dunes then migrate with the flow and become higher and higher as the scour hole around the cylinder becomes deeper and deeper.

- Along the central plane, a small 'ridge' is formed behind the cylinder, and its height becomes smaller as the scour hole becomes deeper; it separates the scour hole downstream of the cylinder into two parts. This ridge seems to have an important influence on the flow field in the simulation and its formation will be discussed later in this section. It should be noticed that in the experiment, this ridge also exits but its height is very small so it was not discussed in Roulund et al. (2005).

- In the early stages of the scour, the two parts of the scour hole are symmetric, as are the sand dunes behind them. However, in the later stages, the two parts lose this symmetry and the scour hole on one side and the corresponding sand dune behind it are larger than those on the other side. This feature also has an influence on the flow field which will be discussed later.

- In the simulation, no ripples are formed on the bed in contrast to what was observed in the experiment. It could be because that the computational mesh is not fine enough to reproduce the early stages of ripple formation, or the current sediment transport model might not capable of reproducing the formation of ripples on bed.

Comparing the bed form obtained from this three dimensional scour around cylinder with the bed form obtained from the two dimensional scour caused by the submerged jet, as presented in Chapter 4, we find that for scour around cylinder, the height of the sand dunes is much smaller than the depth of the scour hole and the profile of the sand dunes at the crest is smooth instead of being very sharp. The main differences between these two simulations are: (i) the cylinder scour is in three dimensions; and (ii) the suspended load transport in the cylinder scour case is not negligible as the sand size is small, and this enhances the migration of the sand dunes with the flow. So in the simulation of scour around cylinder, the sediment transport rate is not zero on the surface of the sand dunes and the sand slide mechanism is not the only mechanism that controls the form of the sand dunes. The details of the suspended load concentration obtained from this simulation will be discussed in detail later.

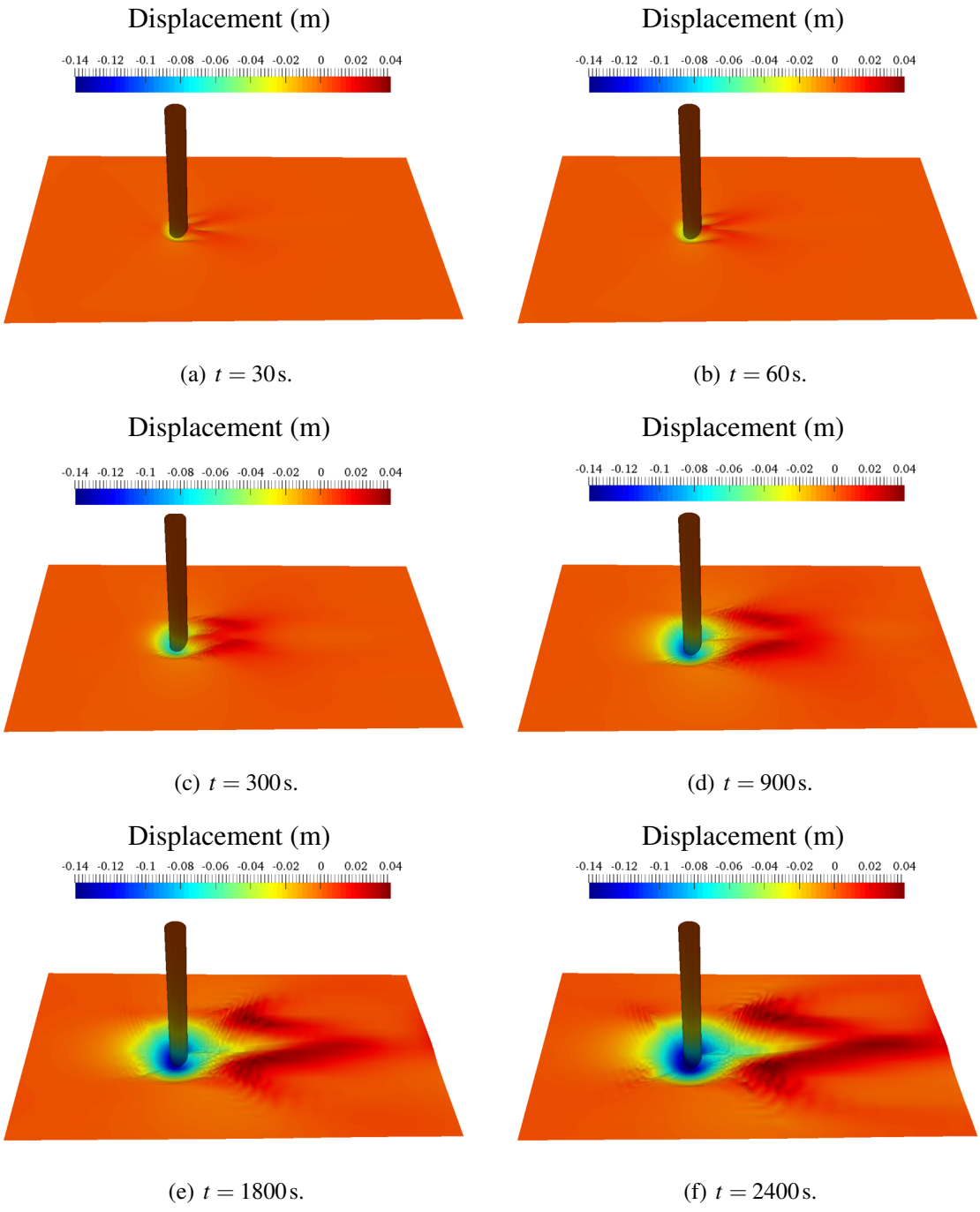

(a) $t = 30\,\mathrm{s}$. (b) $t = 60\,\mathrm{s}$.

(c) $t = 300\,\mathrm{s}$. (d) $t = 900\,\mathrm{s}$.

(e) $t = 1800\,\mathrm{s}$. (f) $t = 2400\,\mathrm{s}$.

Fig. 5.42 Scour development simulation results at time $t = 30\,\mathrm{s}$, $t = 60\,\mathrm{s}$, $t = 300\,\mathrm{s}$, $t = 900\,\mathrm{s}$, $t = 1800\,\mathrm{s}$ and $t = 2400\,\mathrm{s}$.

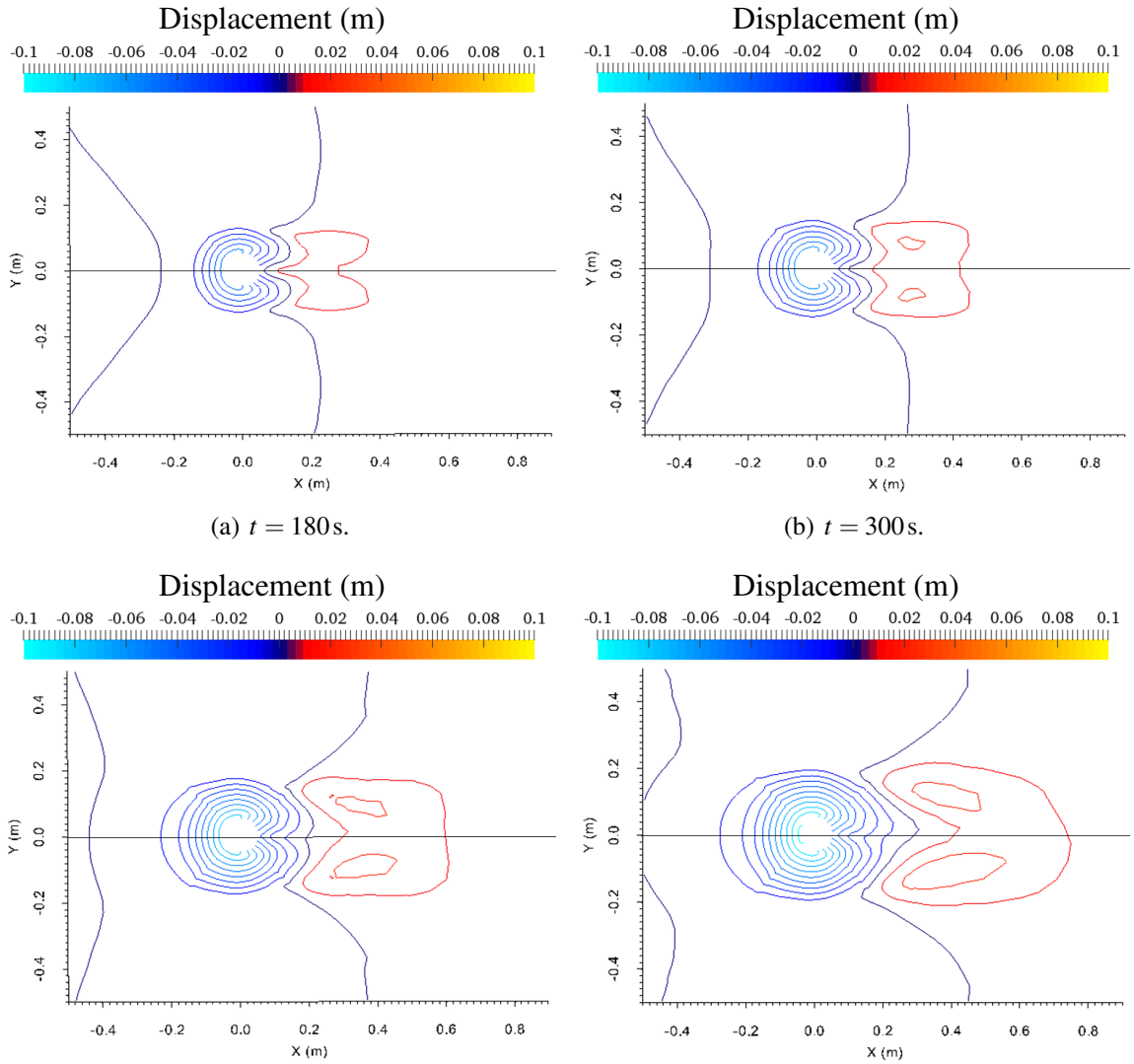

(a) $t = 180\,\mathrm{s}$.

(b) $t = 300\,\mathrm{s}$.

(c) $t = 600\,\mathrm{s}$.

(d) $t = 900\,\mathrm{s}$.

Fig. 5.43 Contour of bed elevation at time $t = 180\,\mathrm{s}$, $t = 300\,\mathrm{s}$, $t = 600\,\mathrm{s}$ and $t = 900\,\mathrm{s}$.

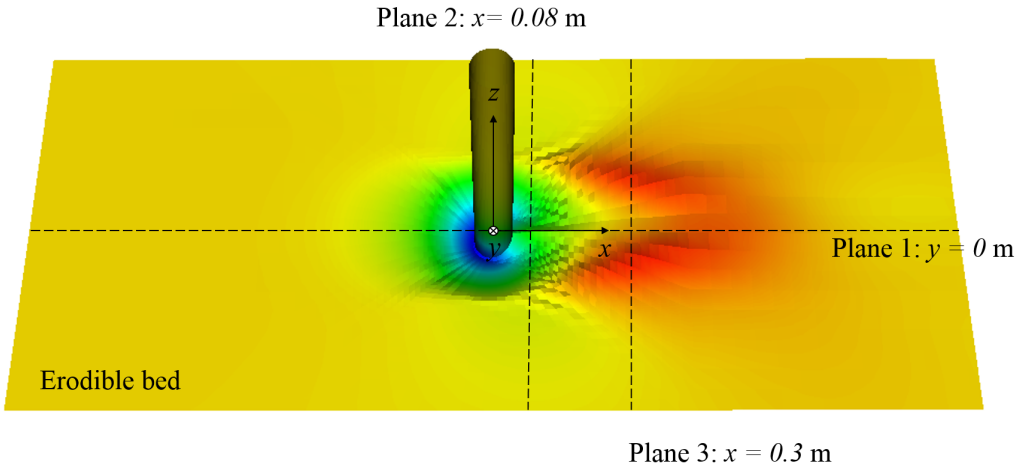

Fig. 5.44 Three planes sampled to analyse the flow field for scour simulation.

Next, we look at the influence of the scour on the flow field and simulation results on three planes are plotted and analysed as shown in Fig. (5.44): (1) x-z plane at $y = 0\,\text{m}$ which is the central plane; (2) y-z plane at $x = 0.08\,\text{m}$ which corresponds to the region of scour hole downstream of the cylinder; and (3) y-z plane at $x = 0.3\,\text{m}$ which corresponds to the region of sand dunes.

Flow field on plane (1)

We start the analysis of the flow field by looking at the variation of the free surface position. Fig. (5.45) shows the position of the water surface on the central plane $y = 0\,\text{m}$ (plane 1) at $t = 180\,\text{s}$ and $t = 1800\,\text{s}$. We can see from the figure that the free surface at the upstream side of the cylinder is higher than its initial position and the free surface position at the downstream side of the cylinder seems to be unchanged. Moreover, the development of the scour hole around the cylinder does not have an obvious influence on the free surface position.

Then we look at the velocity field in the same central plane at $t = 180\,\text{s}$ and $t = 1800\,\text{s}$ as shown in Fig. (5.46) and Fig. (5.47). The flow upstream of the cylinder goes towards the cylinder and into the scour hole at the foot of the cylinder, then a reverse flow forms downstream of the cylinder. The differences between the bed form at $t = 180\,\text{s}$ and $t = 1800\,\text{s}$ are principally the depth of the scour hole around the cylinder and the height of the ridge and the dunes behind the cylinder. And these differences seem to have a strong influence on the velocity component in the y direction. The figure shows that there is flow circulation across the central plane. It is caused by the asymmetry of the flow field in transversal plane where the vortex on one side dominates the flow field near the bed and it can be seen more clearly

later on the flow field on planes (2) and (3) (Fig. (5.50) and Fig. (5.53)). As the scour hole becomes deeper, the dominant vortex becomes larger and stronger and the velocity of this transverse flow increases.

Finally, we look at the suspended load concentration on the central plane as the flow field has a direct influence on the transport of the suspended load. Fig. (5.48) and Fig. (5.49) show the suspended load concentration at an early stage of the scour ($t = 180\,\mathrm{s}$) and at a later stage of scour ($t = 1800\,\mathrm{s}$) on the central plane, together with the photos taken in the experiment at similar times from Roulund et al. (2005). We can see from the figure that the features of the suspended load concentration obtained from the experiment and the simulation are similar. Upstream of the cylinder, the suspended load concentration is strongest on the downward slope of the scour hole. The suspended sediments transported from upstream are trapped by the scour hole in front of the cylinder, and at the foot of the cylinder, the flow velocity is small and downwards so the sediments here fall quickly. As a result, the highest suspended load concentration occurs before the foot of the cylinder on the downward slope of the scour hole. Downstream of the cylinder, the reverse flow behind the cylinder is upwards, which pushes a small amount of the suspended sediments behind the cylinder up and allows them to be transported further away. Moreover, we can see that in both simulation and experimental results, the suspended load concentration downstream of the cylinder in the early stages of the scour is higher than that in the later stages of the scour.

Flow field on plane (2)

The analysis of the flow field on plane (2) follows the same procedure as for the plane (1). Firstly, Fig. (5.51) shows the velocity field on plane (2) at $t = 1800\,\mathrm{s}$ together with the free surface position. We can see from the figure that near the bed, the flow in the scour hole close to the foot of the cylinder from both sides of the scour hole goes upwards and towards the central plane, which corresponds to the transport of the horseshoe vortex to the downstream of the cylinder. The flow then encounters at the central plane, and then is deflected upwards until reaches to the region near the water surface. Then The flows go outward and downwards to the bed separately, meets the upwards flow at the foot of the cylinder and forms a vortex on each side. This flow pattern should generate two symmetrical vortices in the flow near the bed. However, the figure shows that the flow field is not symmetrical near the bed as the vortex close to the bed on one side is larger than the one on the other side and the form of the reverse flow region behind the cylinder is then curved. The asymmetry of the flow field is caused by the asymmetry of the bed forms, which has already been discussed previously. At $t = 1800\,\mathrm{s}$, the right side ($y > 0\,\mathrm{m}$) of the scour hole is sightly deeper and larger than the left side ($y < 0\,\mathrm{m}$), and the vortex on left side is stronger and dominates the flow field. In

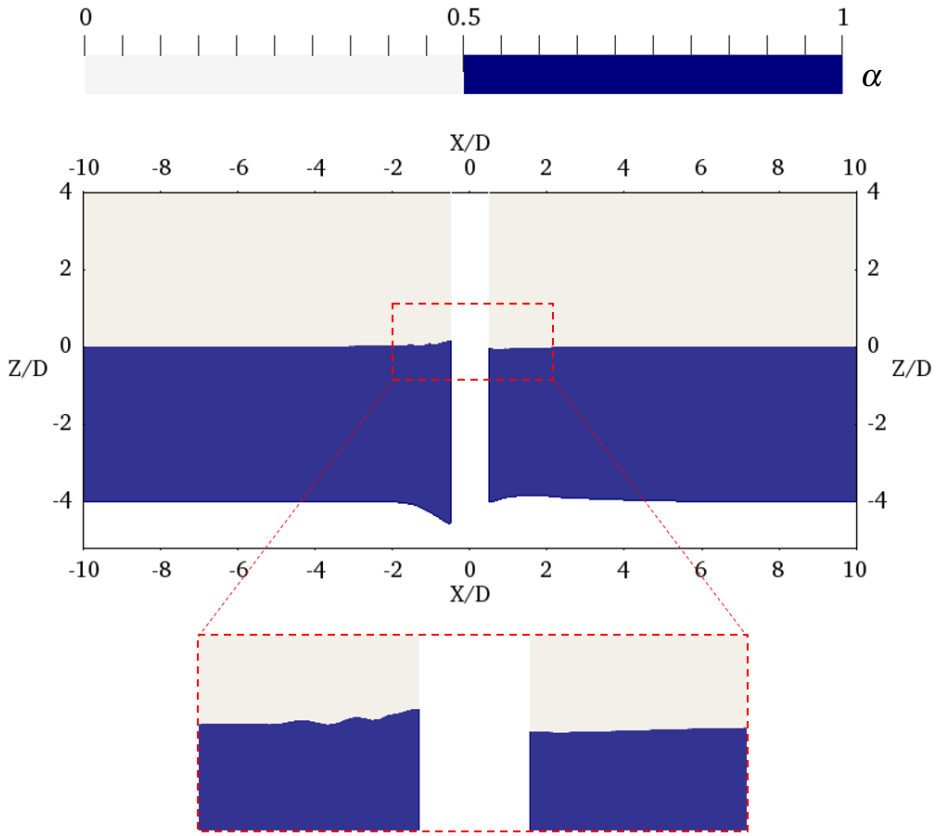

(a) $t = 180\,\mathrm{s}$.

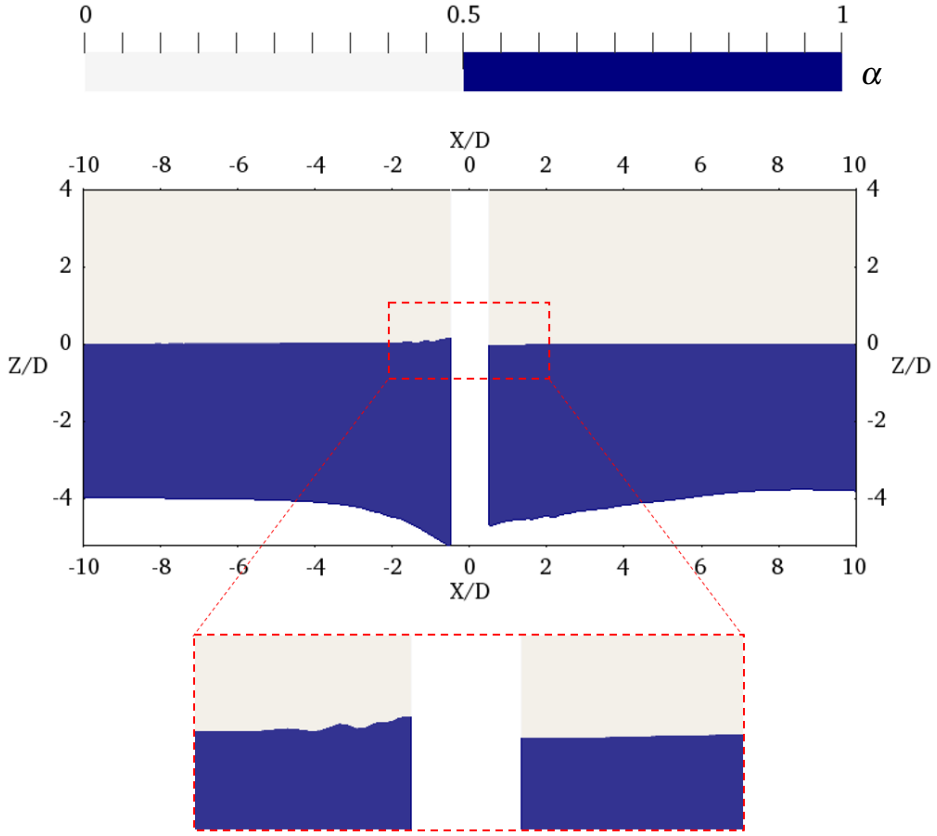

(b) $t = 1800\,\mathrm{s}$.

Fig. 5.45 Free surface position on the central plane $y = 0\,\mathrm{m}$ at $t = 180\,\mathrm{s}$ and $t = 1800\,\mathrm{s}$.

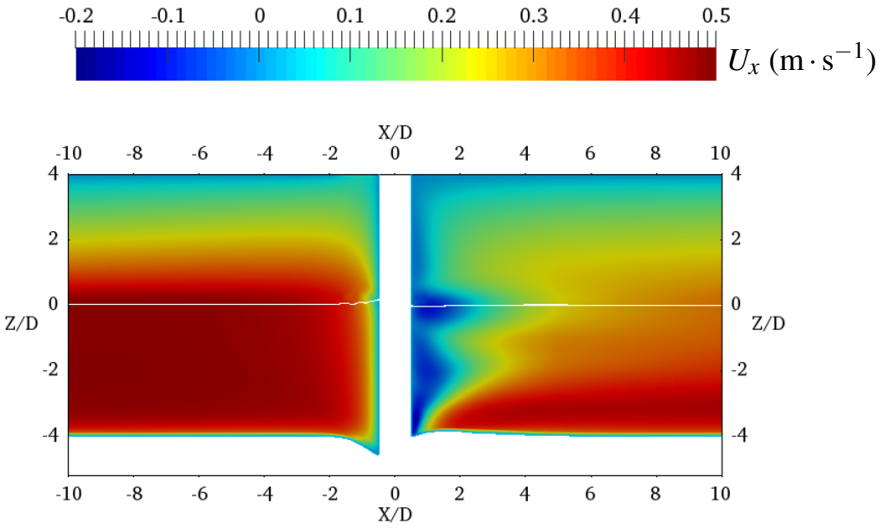

(a) U_x at $t = 180$ s.

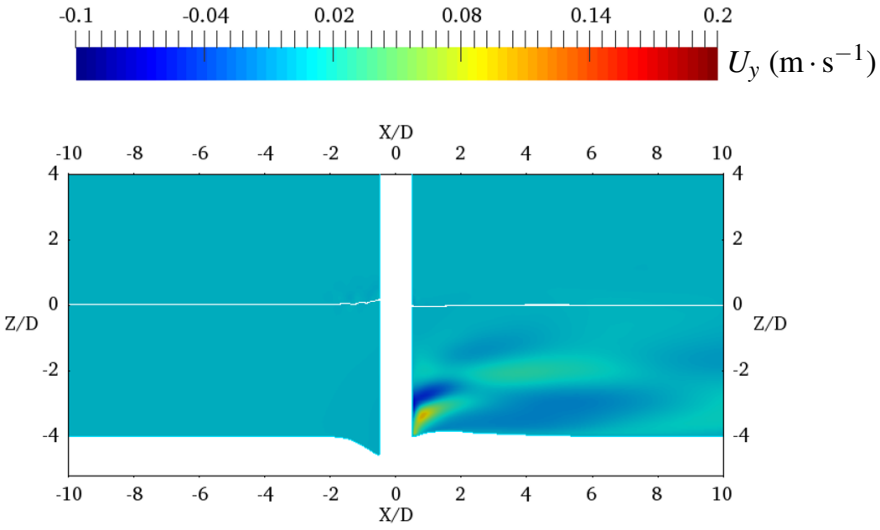

(b) U_y at $t = 180$ s.

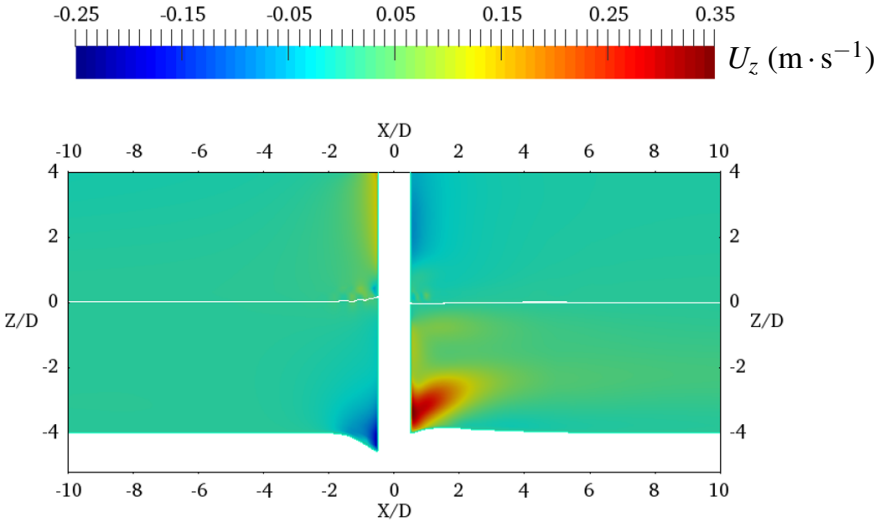

(c) U_z at $t = 180$ s.

Fig. 5.46 Velocity field on the central plane $y = 0$ m at $t = 180$ s, white line indicates the position of the free surface.

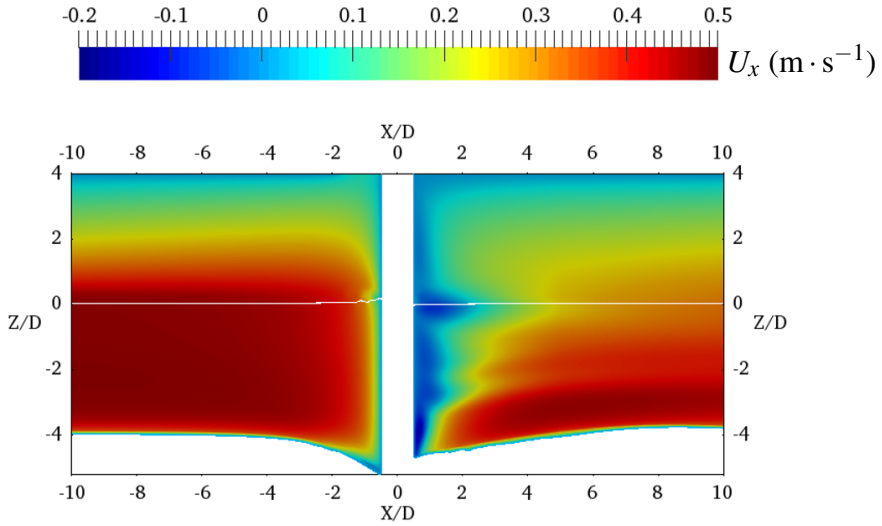

(a) U_x at $t = 1800$ s.

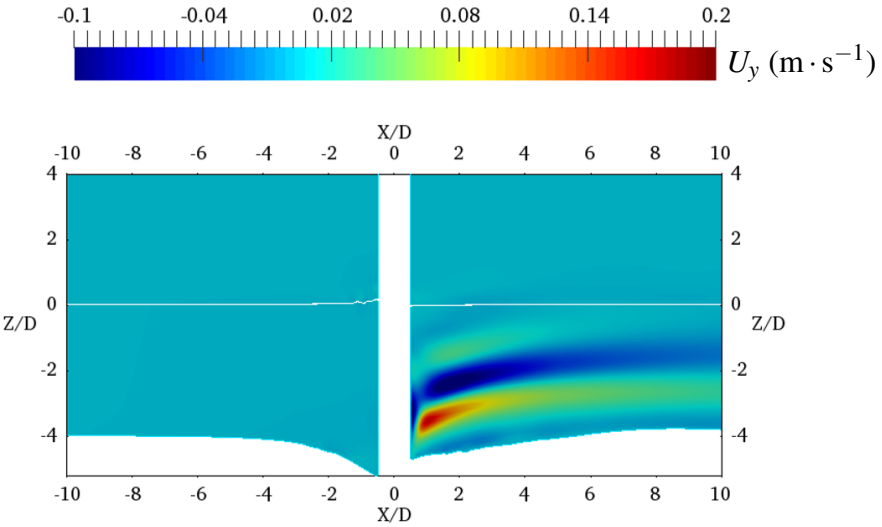

(b) U_y at $t = 1800$ s.

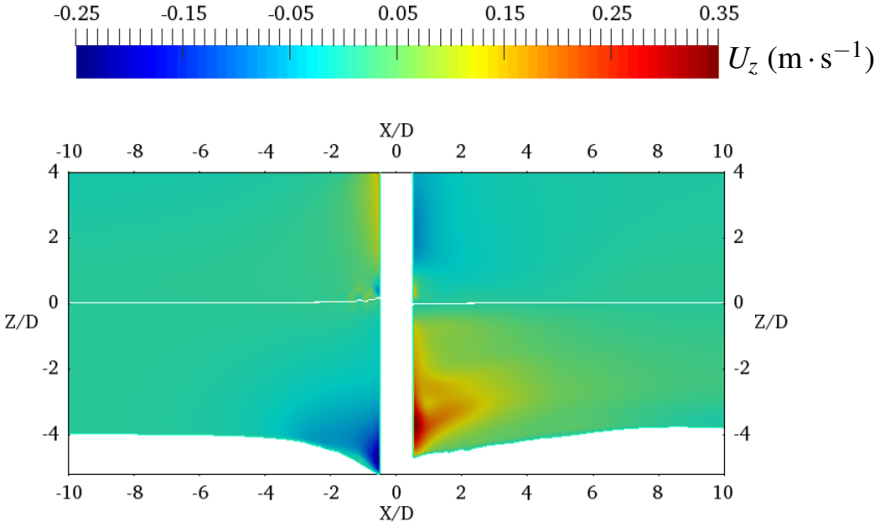

(c) U_z at $t = 1800$ s.

Fig. 5.47 Velocity field on the central plane $y = 0$ m at $t = 1800$ s, white line indicates the position of the free surface.

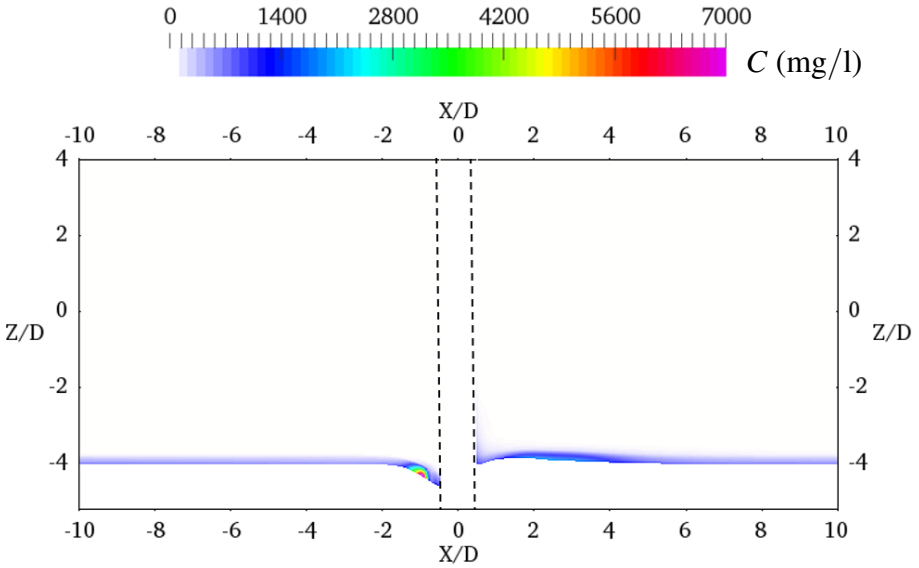

(a) Simulation results at $t = 180\,\mathrm{s}$.

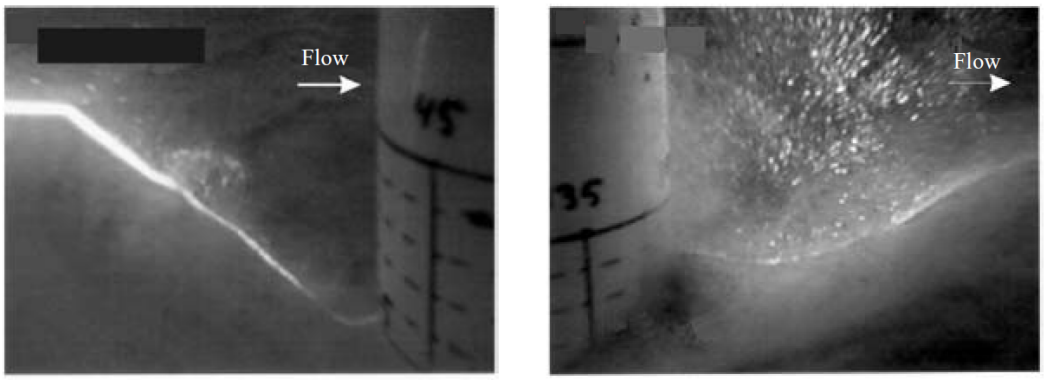

(b) Photos from Roulund et al. (2005) at $t = 120\,\mathrm{s}$.

Fig. 5.48 Suspended load concentration on the central plane $y = 0\,\mathrm{m}$ in the early stages of the scour.

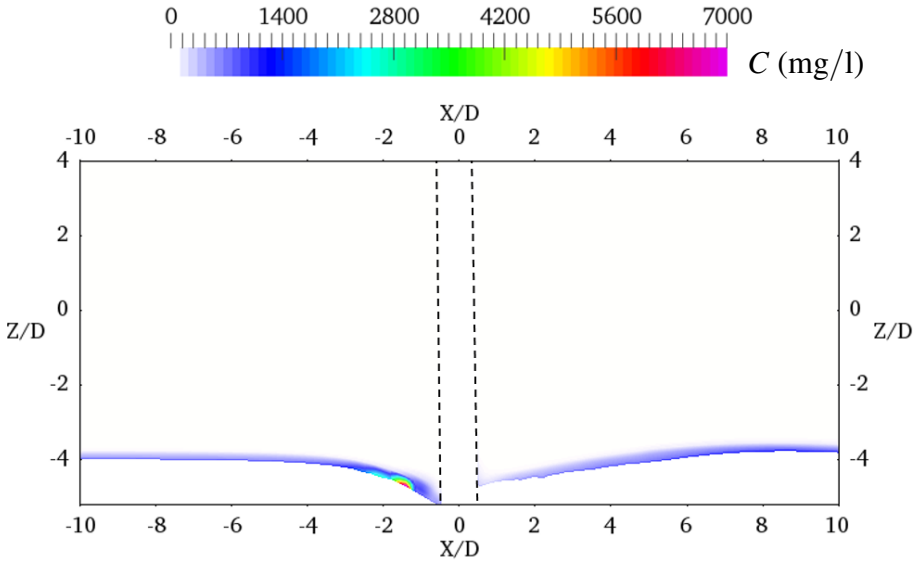

(a) Simulation results at $t = 1800\,\mathrm{s}$.

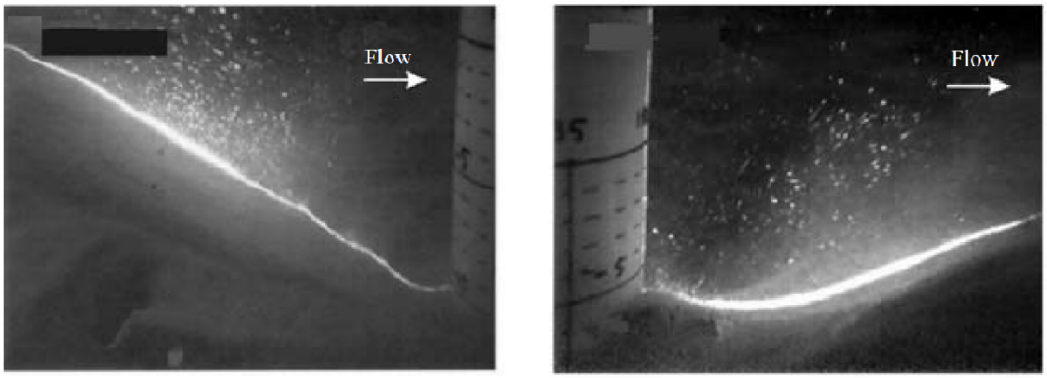

(b) Photos from Roulund et al. (2005) at $t = 1800\,\mathrm{s}$.

Fig. 5.49 Suspended load concentration on the central plane $y = 0\,\mathrm{m}$ in the later stages of the scour.

the early stages of the scour – at $t = 180\,\mathrm{s}$, for example – the two parts of the scour hole downstream of the cylinder are almost symmetrical and the simulation results show that in this condition, the dominant vortex near the bed flaps between the two parts of the scour hole as shown in Fig. (5.51). So we can conclude that the asymmetry of the scour hole, once formed, stops the flapping of the dominant vortex near the bed. The variation of the free surface is very small, but we can still see that in the early stages of the scour, the free surface position is slightly higher in the region where the scour hole starts to form.

Next, we look at the suspended load concentration on plane (2). Fig. (5.52) shows the suspended load concentration and the corresponding velocity field in the z direction at an early stage of the scour ($t = 180\,\mathrm{s}$) and a later stage of the scour ($t = 1800\,\mathrm{s}$). The reason for showing the velocity field in the z direction is to provide an explanation for the high sediment concentration near the central plane. As mentioned before, we can see that the flow from both sides of the scour hole meets near the central plane and is deflected upwards with a relatively high velocity, which transports the suspended load upwards away from the bed. As the flow from both sides converges near the central plane, the directions of the bed load and suspended load are all towards the central plane, which may explain the formation of the ridge on the central plane behind the cylinder. By comparing the suspended sediment concentration at the early and later stages of scour, we see that in the scour hole region, as the scour hole becomes larger and deeper, the concentration of the suspended sediment becomes generally smaller.

Flow field on plane (3)

Fig. (5.53) shows the velocity field on plane (3) at $t = 1800\,\mathrm{s}$ together with the free surface position. We can see from the figure that at $x = 0.3\,\mathrm{m}$, the flow all goes downstream of the cylinder, however, the velocity in the x direction in the region which corresponds to the reverse flow region on plane (2) is still slower than the surrounding flow. The dominant vortex close to the bed we find on plane (2) propagates to plane (3) and its surface becomes larger.

Fig. (5.54) shows the suspended load concentration and the corresponding velocity field in the z direction at $t = 180\,\mathrm{s}$ and $t = 1800\,\mathrm{s}$ on plane (3). We can see from the figure that the free surface does not vary much on plane (3) and the vertical flow velocity near the central plane is smaller than that on plane (2). So the corresponding suspended sediment concentration away from the bed is smaller. But the suspended sediment concentration near the bed becomes larger, which means that most of the suspended sediments will just settle out in this region instead of being transported further away and that's what we would expect at the region where the sand dunes are formed.

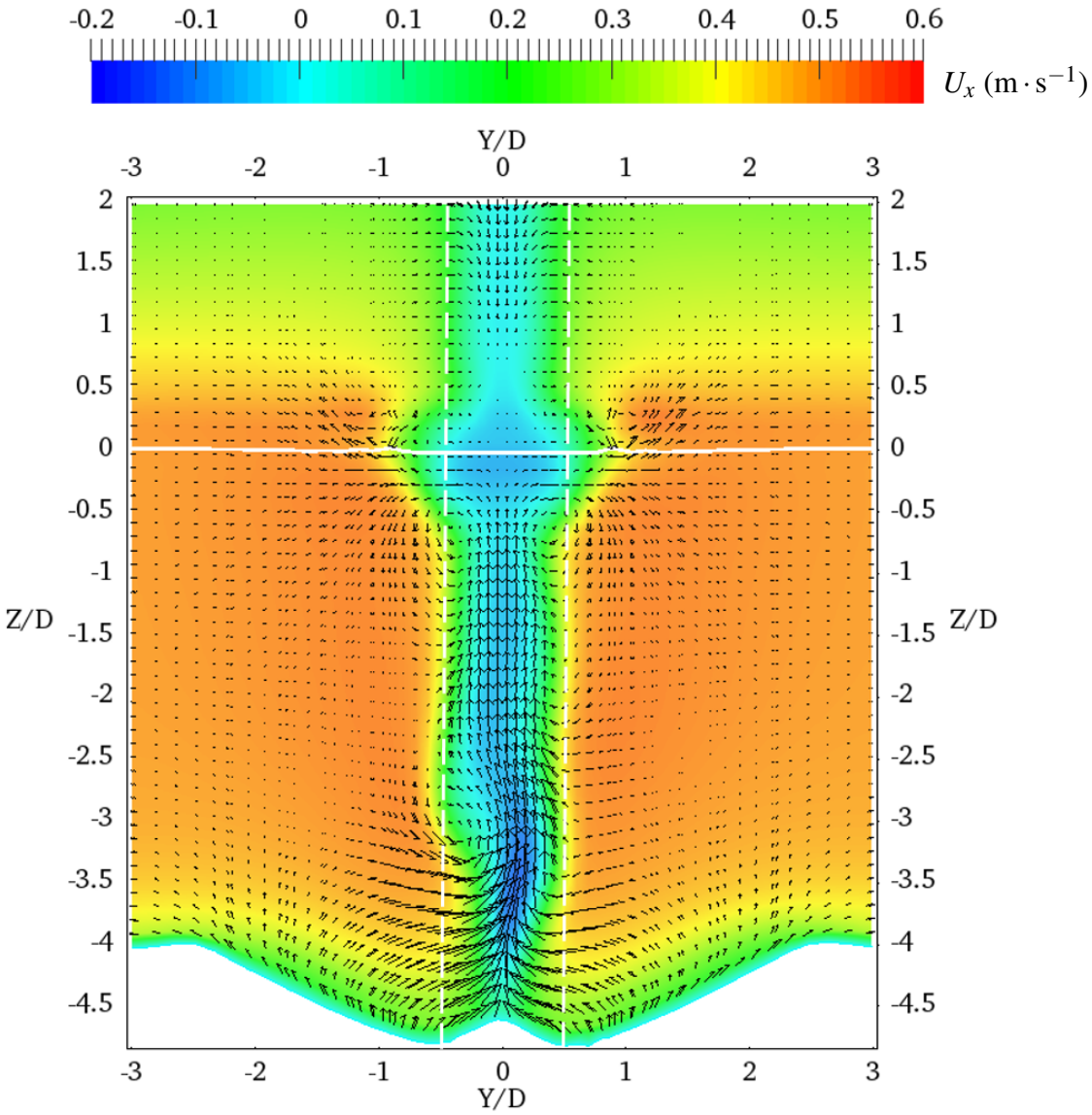

Fig. 5.50 Velocity field on plane (2) at $t = 1800\,\mathrm{s}$, the figure is coloured by the value of the x component of the velocity field and the vectors indicate the velocity field in y-z plane. The white solid line indicates the position of the free surface and the white dashed line indicates the position of the cylinder.

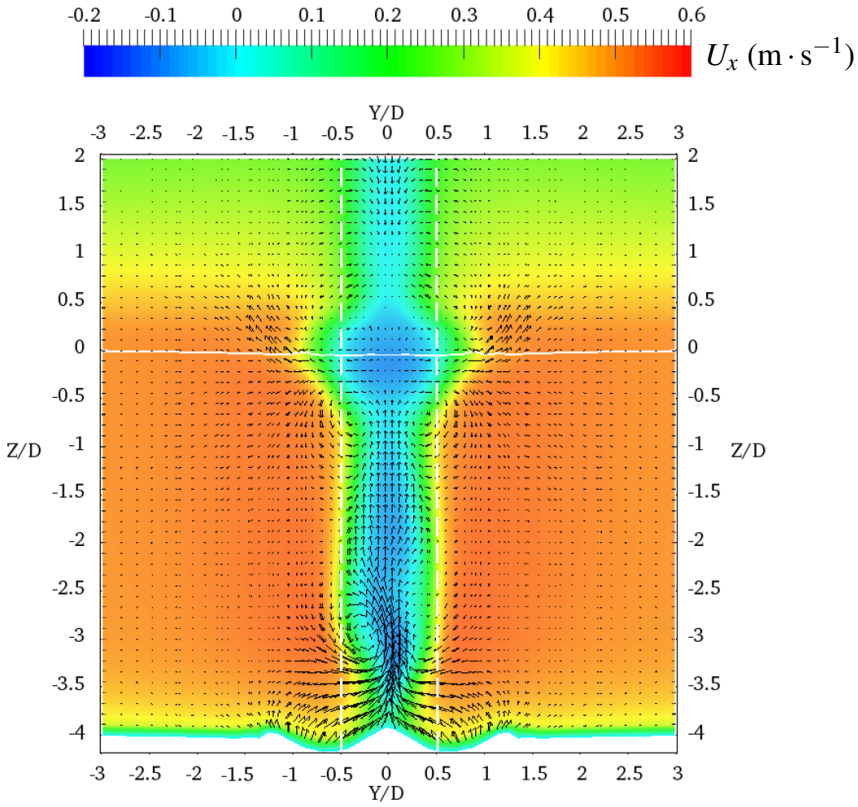

(a) $t = 180$ s.

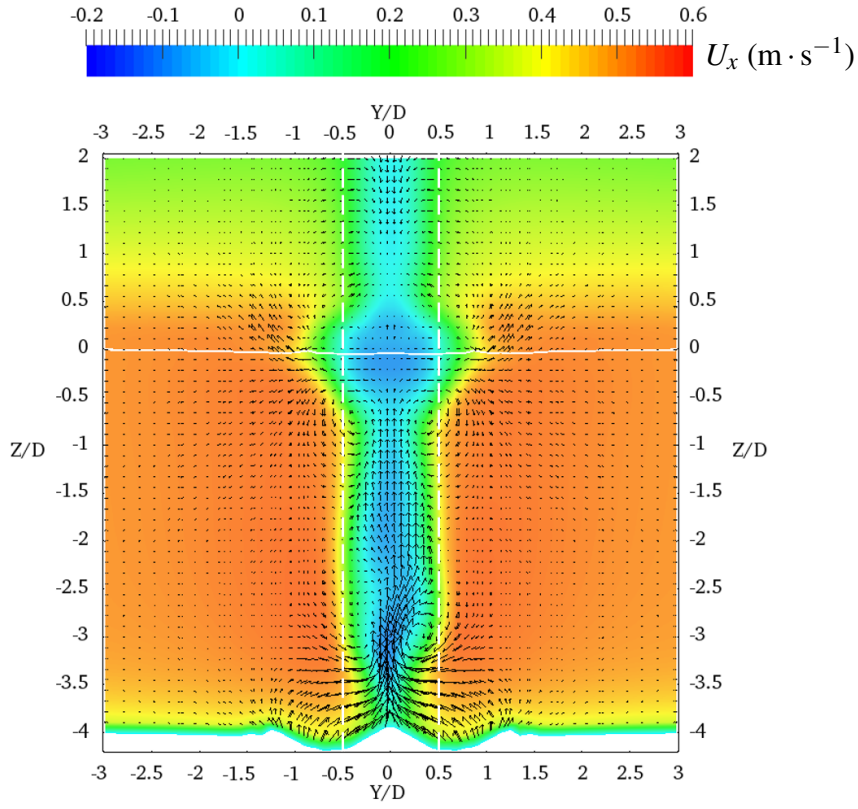

(b) $t = 200$ s.

Fig. 5.51 Flapping of the vortex near the bed, the figure is coloured by the value of the x component of the velocity field and the vectors indicate the velocity field in y-z plane. The white solid line indicates the position of the free surface and the white dashed line indicates the position of the cylinder.

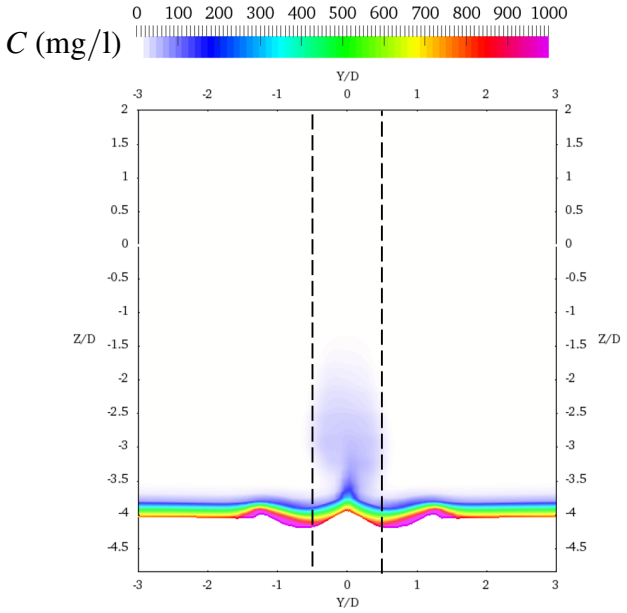

(a) Suspended load concentration at $t = 180\,\mathrm{s}$.

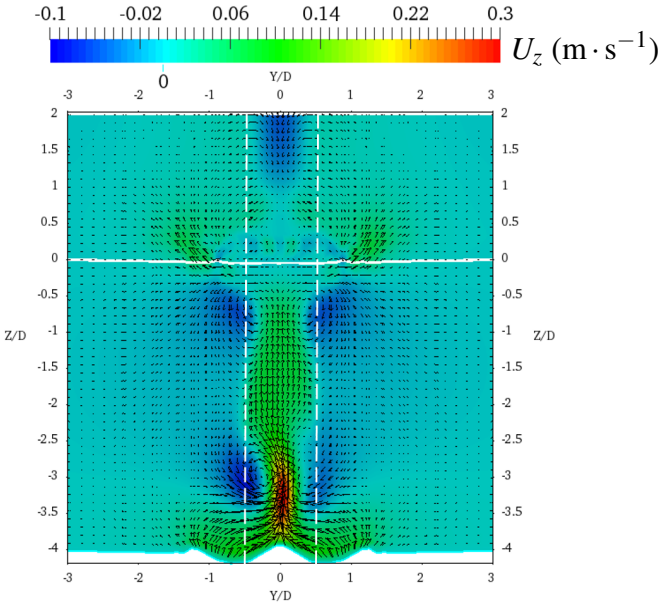

(b) Velocity field at $t = 180\,\mathrm{s}$.

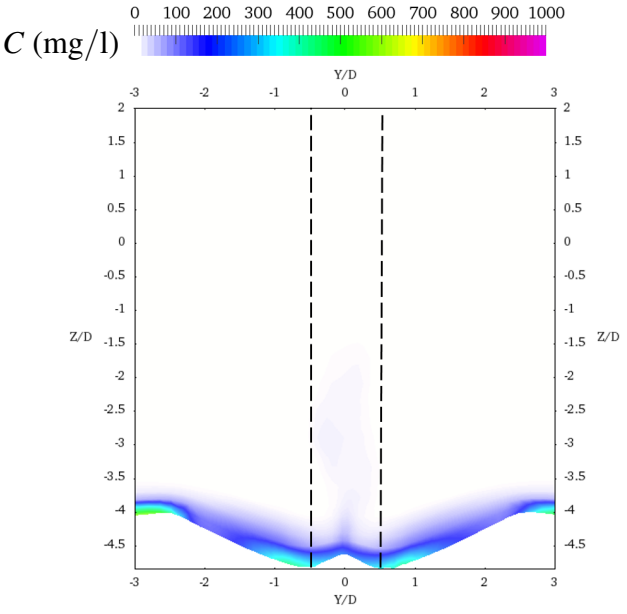

(c) Suspended load concentration at $t = 1800\,\mathrm{s}$.

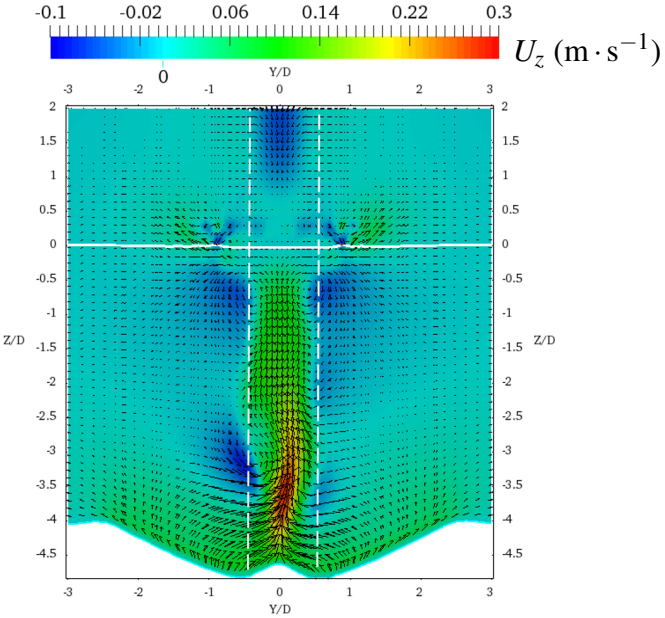

(d) Velocity field at $t = 1800\,\mathrm{s}$.

Fig. 5.52 Suspended load concentration and the corresponding velocity field in the z direction on plane (2) at $t = 180\,\mathrm{s}$ and $t = 1800\,\mathrm{s}$, the solid line indicates the position of the free surface and the dashed line indicates the position of the cylinder.

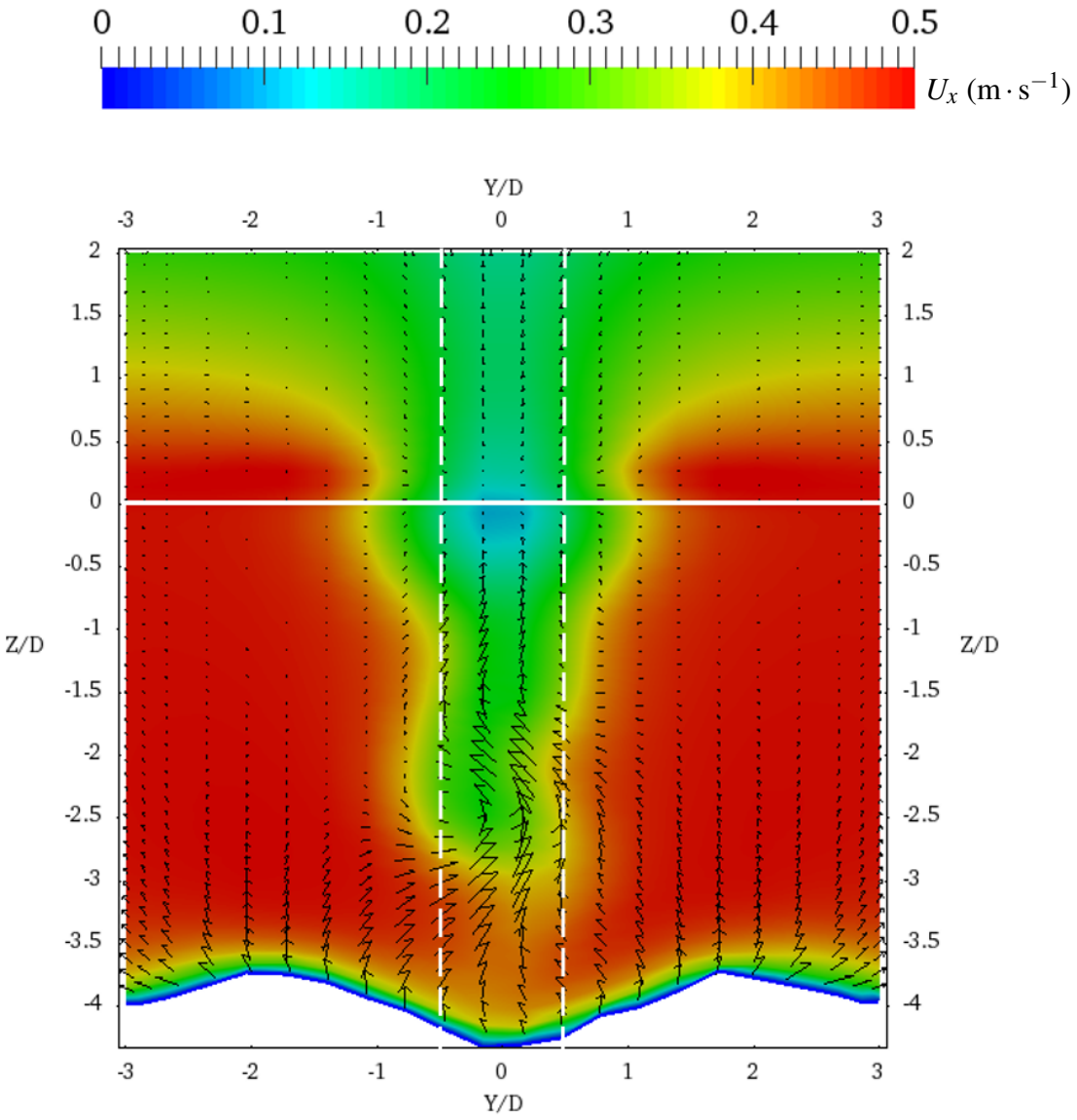

Fig. 5.53 Velocity field on plane (3) at $t = 1800$ s, the figure is coloured by the value of the x component of the velocity field and the vectors indicate the velocity field in y-z plane. The solid white line indicates the position of the free surface and the white dashed line indicates the position of the cylinder.

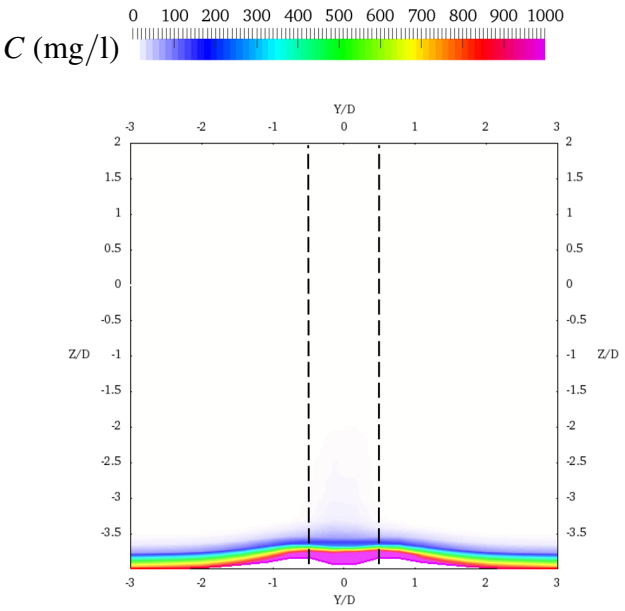

(a) Suspended load concentration at $t = 180\,\mathrm{s}$.

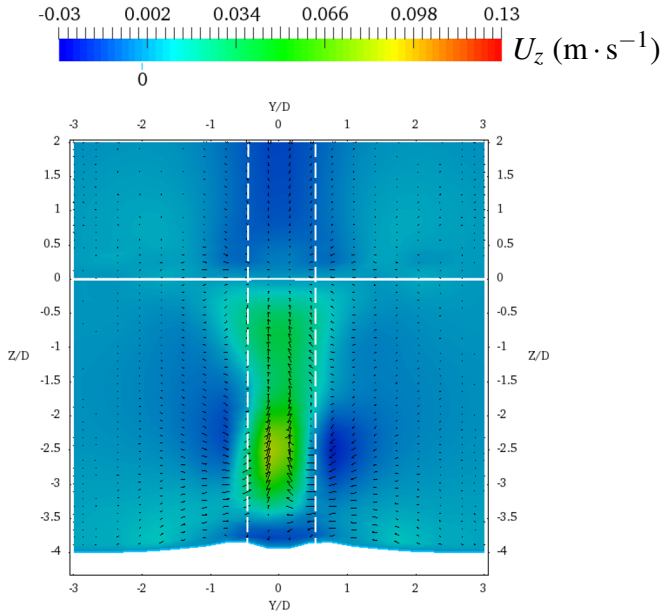

(b) Velocity field at $t = 180\,\mathrm{s}$.

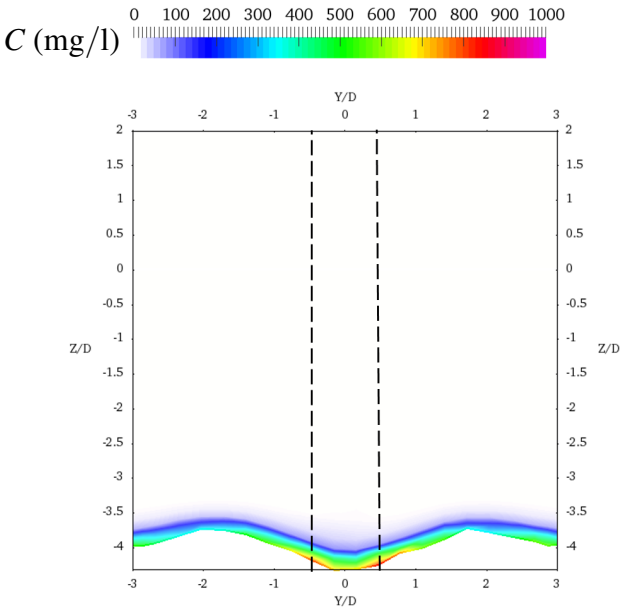

(c) Suspended load concentration at $t = 1800\,\mathrm{s}$.

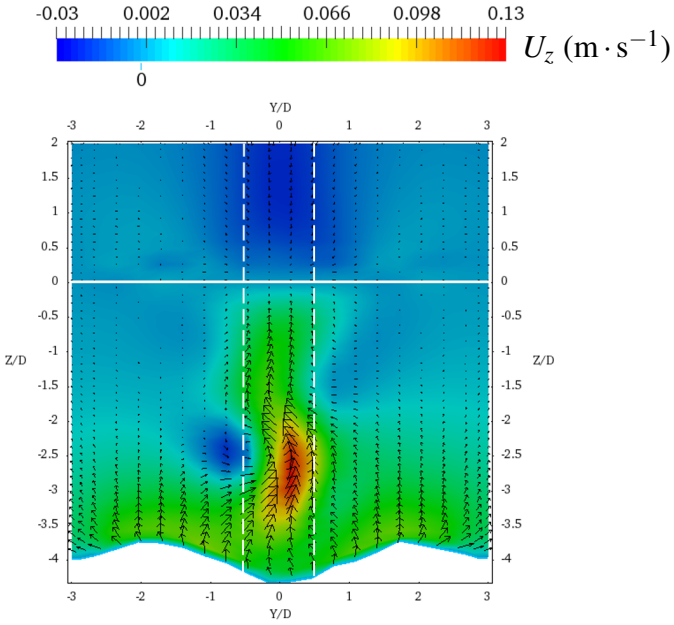

(d) Velocity field at $t = 1800\,\mathrm{s}$.

Fig. 5.54 Suspended load concentration and the corresponding velocity field in the z direction on plane (3) at $t = 180\,\mathrm{s}$ and $t = 1800\,\mathrm{s}$. The solid line indicates the position of the free surface and the dashed line indicates the position of the cylinder.

Finally, we compare the measured and simulated temporal development of the scour depth at the upstream and downstream edges of the cylinder. Fig. (5.55) shows the experimental measurements of the scour depth in central plane at time $t = 60\,\mathrm{s}$, $t = 120\,\mathrm{s}$, $t = 300\,\mathrm{s}$, $t = 600\,\mathrm{s}$, $t = 1800\,\mathrm{s}$, $t = 3600\,\mathrm{s}$ along with the simulated temporal development of scour depth up to $t = 2400\,\mathrm{s}$. The simulation results from Roulund et al. (2005) are also plotted. The simulation done by Roulund et al. (2005) used a steady-state solver to simulate the flow field with k-ω turbulence closure and the bed load transport model introduced in 3 which takes into account the effect of the bed slope on the direction of the bed load transport. But no suspended load transport model was included. The simulation results from Roulund et al. (2005) are presented here just to give a reference and further analysis of these simulation results can be found in their paper. This thesis focuses only on the analysis of the simulation results from this work.

The scour depth at the upstream side of the cylinder simulated in this work at $t = 60\,\mathrm{s}$ and $t = 120\,\mathrm{s}$ agrees well with the experimental measurements. However, after $t = 300\,\mathrm{s}$, the scour depth is overestimated by the simulation. On the downstream side of the cylinder, we can see that the simulated scour depth on the central plane underestimates the scour depth in the early stages of the scour, and in the later stages of the scour, the model also overestimates the maximum scour depth at the downstream side of the cylinder.

There are several possible explanations for these disagreements. First of all, no vortex shedding was detected at the downstream side of the cylinder. This could be because the mesh used in this simulation is not fine enough to reproduce the vortex shedding. Roulund et al. (2005) compared the bed shear stress amplification obtained from the steady-state-flow simulation and the time-averaged unsteady-flow simulation and found the results are quite similar. So in order to reduce the time needed for calculation, Roulund et al. (2005) used a steady-state solver for the prediction of flow in connection with the numerical simulation of scour. In our simulation, the vortex shedding is not reproduced due to the resolution of the mesh and the simulation gives directly the mean flow field. The lack of the vortex shedding behind the cylinder could explain the ridge formed in the central plane as the flow field is almost symmetrical behind the cylinder, especially at the early stages of the scour. In the simulation, the ridge is higher than the one formed in the experiment, so the bed behind the cylinder on the central plane only starts to be eroded at about $t = 140\,\mathrm{s}$. Secondly, the ripples migrating on the bed, once they have entered the scour hole from the upstream side, could slide down the slope of the scour hole and decrease the scour depth. Finally, the mesh distortion becomes larger and larger and the limitation of the mesh resolution around the scour area could also be responsible for the difference between the simulated and measured scour depth. We can also notice that the temporal development of the maximum scour depth

after about $t = 1000\,\mathrm{s}$ starts to become fluctuating instead of being smooth. A possible explanation is that as the scour hole in front of the cylinder becomes deeper than some critical depth, the slope of the scour hole collapses regularly and refills the scour hole slightly.

Fig. (5.56) shows the simulated bed profile at $t = 900\,\mathrm{s}$, $t = 1500\,\mathrm{s}$, $t = 2400\,\mathrm{s}$ and the measured bed profile at equilibrium state of the scour. As the scour at $t = 2400\,\mathrm{s}$ has not yet reached equilibrium, the differences between the compared and measured scour depths are to be expected. Upstream of the cylinder, the slope angle of the scour hole is correctly reproduced by the simulation, which also justifies the value imposed for the critical bed slope in the sand-sliding mechanism. At the downstream side of the cylinder, the slope of the scour hole is gentler than the measured slope. As pointed out in Roulund et al. (2005), the lack of vortex shedding causes an underestimation of the maximum bed shear stress amplification and the differences mainly occur in the wake region. This could explain the gentle slope produced at the downstream side of the cylinder by the simulation. Moreover, the large difference between the simulated scour depth and the equilibrium scour depth at the downstream side of the cylinder is to be expected, because in the experiment, the upstream scour hole reaches its equilibrium depth after 2 hours, whereas it takes 3 hours for the downstream scour hole to reach its equilibrium depth.

5.4 Conclusions

The numerical model that we developed, and which was validated in previous chapters has been used to simulate the three dimensional flow field around a cubic obstacle and a cylinder in free surface flow to test the performance of the hydrodynamic module and to study the influence of the free surface on the flow field. Comparisons with experimental data show that: (1) The hydrodynamic module simulates the horseshoe vortex and the lee-wake vortex shedding structure rather well, both with and without a free surface. (2) The variation of the free surface, caused by the presence of the obstacle in the flow and the surface waves propagating in the flow field, has a significant influence on the flow field. (3) The free surface simulation which includes the variation of free surface provides a more accurate estimation of the position of the centres of the horseshoe vortex and of the mean velocity field. (4) The influence of the roughness of the bed can be correctly included in the simulation using rough wall functions; it modifies the mean flow field but not the vortex shedding frequency.

The bed deformation is then activated and the development of scour around a cylinder in a steady current is simulated. The formation and the development of the scour hole and other topographic bed features are successfully reproduced by the numerical model. The influence of the scour formation on the flow field and thus on the suspended load transport

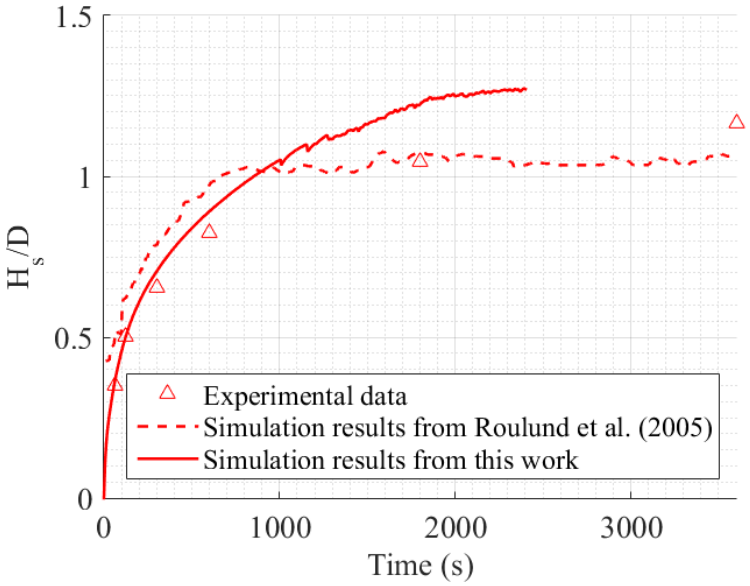

(a) Upstream of the cylinder.

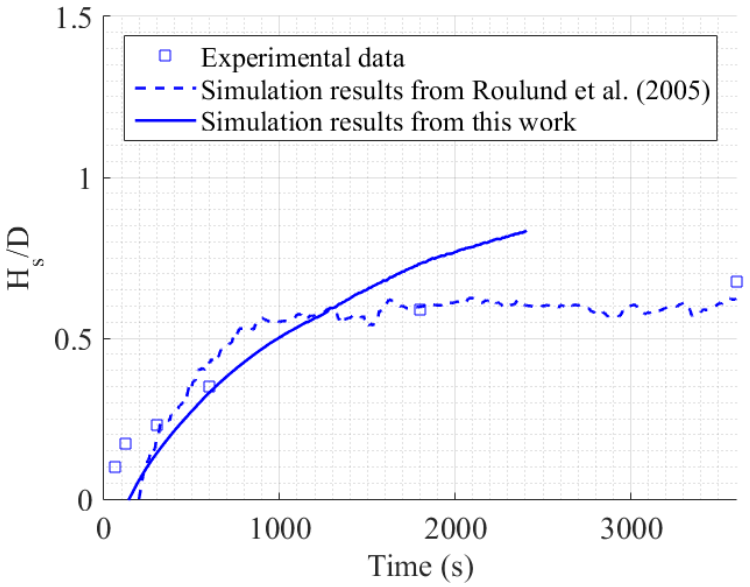

(b) Downstream of the cylinder.

Fig. 5.55 Comparison of the measured and simulated temporal development of scour depth upstream and downstream of the cylinder.

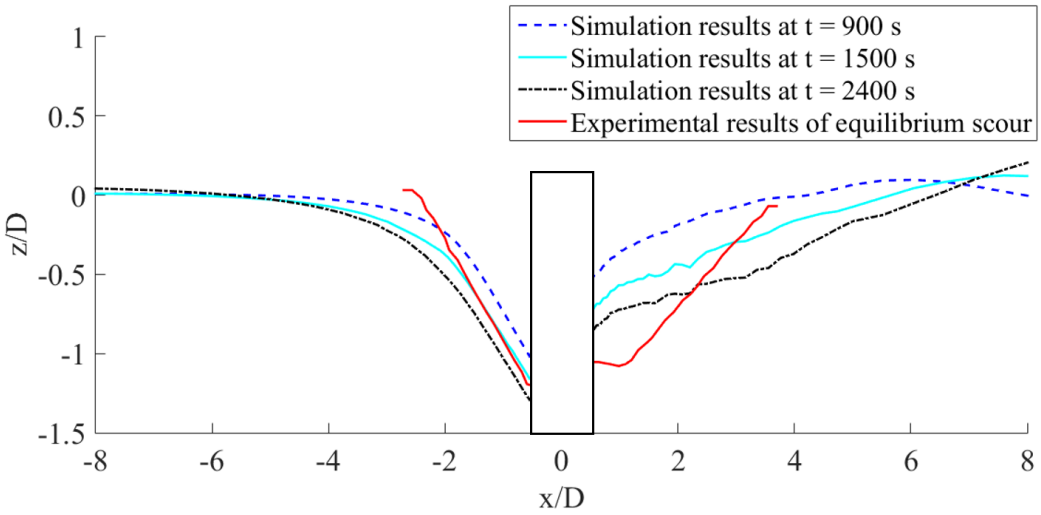

Fig. 5.56 Comparison of the simulated bed profile on the central plane at $t = 900\,\mathrm{s}$, $t = 1500\,\mathrm{s}$, $t = 2400\,\mathrm{s}$ and the bed profile at equilibrium scour measured by Roulund et al. (2005).

has been studied. The strong vertical velocity on the central plane in the simulation can cause the sediment to be gathered behind the cylinder and form a ridge there. The height of this ridge seems to be greater than that of the ridge formed in the experiment and influences the simulated scour depth in the early stages of the scour.

The simulation results for the temporal development of scour depth at the upstream edges of the cylinder agree rather well with the experimental results in the early stages of the scour formation but they overestimate it in the later stages. Downstream of the cylinder, the formation of a ridge behind the cylinder prevents the model from reproducing correctly the scour depth on the central plane in the early stages of the scour. These problems could all be because that the mesh used in the simulation is not fine enough and thus the simulation fails to reproduce the ripples on the bed and the vortex shedding behind the cylinder. But the cost to reproduce these effects can be vary large and probably won't make a big progress as the model with present mesh still can give a reasonable results compared with the experimental measurements.

In order to improve the performance of the model, a finer mesh could be used or, in order to avoid large mesh distortions, the dynamic immersed boundary method, which isn't fully implemented in OpenFOAM® could be developed and used in this model to replace the dynamic mesh method.

Chapter 6

Conclusions and Perspectives

Conclusions

In this thesis, the local scour caused by bed-mounted obstacles has been studied and a numerical model for simulating scour has been developed which combines the hydrodynamic and morphological processes.

The hydrodynamic module of the model solves the governing equations of the flow field using the RANS model with k-ε or k-ω SST turbulence models as closure to the Navier-Stokes equations. Free surface effects are also included in the model by tracking the water surface using the VOF method; the effects of the bed roughness on the flow field is simulated using rough wall function. The hydrodynamic module is based on the multiphase flow solver *interDyMFoam* of the open-source CFD tool OpenFOAM® . To implement the model, the Finite Volume Method is used to discretize the simulation space and Euler implicit time discritization method is chosen. The SIMPLE algorithm is used for solving the pressure-momentum coupling for steady-state problems and the PIMPLE algorithm is used for transient problems.

Two preliminary tests have been conducted for validating the components of the hydrodynamic module. The performance of the rough wall functions has been validated by simulating the flow over homogeneous bed with different equivalent roughness heights. Good agreement was obtained between the simulated and the theoretical velocity profiles obtained from the law of the wall. Next, the dam break case was simulated to test the ability of the model to reproduce the free surface and the computations were compared with the experimental results from Koshizuka (1995). The simulation proves that a fine mesh can reproduce more accurately the details of the free surface while a coarse mesh can still give a reasonable approximation to the form of the free surface.

The hydrodynamic module has also been used to study the flow field around obstacles. It is first used to simulate the horseshoe vortex in front of a cubic obstacle on the bed in laminar flow (comparing with the experiments of Launay et al. (2015)) and then to simulate the vortex shedding on the downstream side of a cylinder on a smooth or a rough bed in turbulent flow (comparing with experiments of Roulund et al. (2005)). Three general conclusions can be drawn from analysing the simulation results:

- The obstacles in flow cause some perturbations of the water surface, i.e. variation of the water depth at the upstream and downstream sides of the obstacle, and this can explain the differences between the simulation results from the rigid lid and free surface simulations.
- The comparison between the results obtained from the rigid lid and free surface simulations shows that the variation of the water depth has detectable influences on the mean flow field and also the vorticity field even with a small Frounde number, and the results from the free surface simulation agree better with experimental measurements.
- The roughness of the bed can be correctly included into the model using the rough wall functions; it influences the boundary layer thickness and thus the mean flow field, but the vortex shedding frequency is not modified.

The morphological module which is added into the numerical model calculates the sediment transport, including both the suspended load and the bed load; the changes in bed level are obtained by solving the Exner equation, and a sand-sliding mechanism to restrict the bed slope to the repose angle of the sediment. The suspended load concentration is calculated by solving the advection-diffusion equation with a correction at the free surface region and a boundary condition defined with the entrainment and deposition rates. The empirical formula proposed by Engelund and Fredsøe (1976) is used to calculate the bed load. The morphological module works with a finite area mesh constructed from the bottom boundary of the finite volume mesh which represents the bed, and it interacts with the hydrodynamic module through dynamic mesh deformation. After the finite area mesh is deformed, the finite volume mesh is then smoothed by solving the Laplace equations and the updated finite volume mesh is used to calculate the flow field for the new time step.

The components of the morphological module have also been tested separately. The suspended load transport model has been validated by the net entrainment case experimentally studied by Van Rijn (1987). The sand-sliding mechanism has been tested by simulating the avalanche of a sand heap and it correctly modified the bed slope angle. Additional efforts have also been devoted to the parallelization of the model. The finite area mesh in

OpenFOAM® does not support the deformation in parallel so the morphological module can not be parallelized, and the deformation of the finite volume mesh also causes problems when calculating the hydrodynamic module in parallel. A correction mechanism has been added to correct the displacements of the mesh points on processor boundaries.

The model has been used to reproduce the scouring process. The two-dimensional scour caused by a submerged jet issuing from an opening under the sluice gate is simulated. The velocity field at the equilibrium state of the scour hole and the temporal development of the bed profile have been compared with the experimental measurements from Chatterjee and Ghosh (1980) and Chatterjee et al. (1994) and the good agreement between the simulation results and the experimental data confirms the validity of the numerical model. Finally, the model is applied to simulate the three-dimensional scour formed around a cylinder on live-bed in a current. The computed temporal variations of the maximum scour depth upstream and downstream of the cylinder are compared with the experimental measurements from Roulund et al. (2005). Several conclusions can be made from analysing the simulation results of the model:

- In the two-dimensional scour simulation, the temporal development of the bed form and the maximum scour depth are satisfactorily predicted. However, the form of the dune in the simulation is totally controlled by the sand-sliding mechanism and thus can not reproduce exactly the bed profile measured during the experiment.

- In the three-dimensional scour simulation, the formation and the development of the scour hole can be successfully reproduced by the numerical model. The flow coming from both sides of the cylinder meets at the central plane and is deflected upwards, causing the sediment to be gathered behind the cylinder and forms a ridge there which separates the scour hole into two parts. A dominant vortex close to the bed behind the cylinder exists and flaps between the two parts of the scour hole when they are symmetrical, and the flapping stops as the two parts of the scour hole become asymmetrical at the later stages of the scour.

- The computed maximum scour depth upstream of the cylinder agrees well with the experimental results in the early stages of the scour, but it tends to overestimates the scour depth in the later stages. Downstream of the cylinder, the formation of the ridge behind the cylinder prevents the model from reproducing correctly the scour depth on the central plane in the early stages of the scour. However, in the later stages, the height of the ridge decreases and the model also overestimates the scour depth.

Perspectives

Even though the model which has been developed in this work produces acceptable simulation results for the flow field and the temporal development of scour, the model still has several limitations.

First of all, the parallelization of the model could be improved. The version of OpenFOAM® used by the model is Foam-extend-3.1 for which the finite area mesh does not support calculation with deformation in parallel and the parallelization of the simulation on finite volume mesh needs corrections. However, the Foam-extend-4.0 (which was released in 2017) has already partially corrected the parallelization problem of the deforming finite volume mesh in a more efficient way. So if in a latter version of Foam-extend, the parallelization of the calculation on deforming finite area mesh is fully implemented, this will definitely accelerate the simulation.

Secondly, the sand-sliding mechanism in the model dominates the form of the sand dune after the scour hole and limits the bed slope to the critical bed slop, which is usually the repose angle of the sediment. However, the experimental measurements show that the bed slope in the reverse flow region can exceed the repose angle of the sediments. So a more realistic formula to define the critical bed slope should be used instead which calculates the critical bed slope with the local shear stress. Moreover, as the sand-sliding mechanism must work in loop and this can be very slow in certain situations, an optimized algorithm to achieve the sand-sliding could also accelerate the simulation.

Thirdly, the dynamic mesh method used in the model to couple the hydrodynamic and morphological modules is straightforward and simple. However, when the scour hole is deep, large distortions can be found in the mesh. So a better way of coupling the two modules should be found. The immersed boundary method is very promising for solving this difficulty. But the dynamic immersed boundary method which allows the immersed boundary to deform automatically during the simulation and conserves the mass of water is not yet available in OpenFOAM® .

The overestimation of the scour depth as the scour hole becomes deeper indicates that the sediment transport model needs improving. The empirical formula used is a basic and general formula; a more complex and complete model should give a better estimation of the bed profile. Several factors can be added into the sediment transport model: (i) the fractions of the sand particles with different diameters; (ii) the influence of the suspended sediment on the flow field and its corresponding influence on the wall shear stress.

Finally, the model developed, especially after the improvements mentioned above, can be used in future for studying more complex scour processes or to test the techniques for protecting hydraulic structures against scour and bed erosion. For example, the scour formed

around a group of piles instead of one (case studied experimentally by Sumer and Fredsøe (1998)), or the reduction of bend scour by an outer bank footing (case studied experimentally by Roca et al. (2007)).

Appendix A

The Derivation of the Transport Equation for Volume Fraction Indicator

The conventional transport equation for the indicator α, which represents the volume fraction of one phase, is:

$$\frac{\partial \alpha}{\partial t} + \nabla \cdot (\alpha \boldsymbol{U}) = 0 \tag{A.1}$$

In VOF method, if we have two phases: phase 1 and phase 2, and α represents the volume fraction of phase 1, we assume that the velocity of the effective fluid $\boldsymbol{U}$ can be calculated from the weighted average of the velocity of the two phases, which leads to the following equation:

$$\boldsymbol{U} = \alpha \boldsymbol{U}_1 + (1-\alpha)\boldsymbol{U}_2 \tag{A.2}$$

where $\boldsymbol{U}_1$ is the velocity of phase 1 and $\boldsymbol{U}_2$ is the velocity for phase 2. This assumption is adopted in OpenFOAM® , but actually no conclusions have been made about how the velocity of the two phases should influence the velocity of the effective fluid. The transport equations for each phase are:

$$\frac{\partial \alpha}{\partial t} + \nabla \cdot (\alpha \boldsymbol{U}_1) = 0 \tag{A.3}$$

$$\frac{\partial (1-\alpha)}{\partial t} + \nabla \cdot \{(1-\alpha)\boldsymbol{U}_2\} = 0 \tag{A.4}$$

In OpenFOAM® , instead of solving the conventional transport equation, a modified equation is used which includes an extra term to compress the interface in the discrete formulation. The derivation of the modified transport equation is presented below.

First of all, the velocity $\boldsymbol{U}$ in Eq.(A.1) is replaced with its definition as a weighted average in Eq.(A.2):

$$\frac{\partial \alpha}{\partial t} + \nabla \cdot \{[\alpha \boldsymbol{U}_1 + (1-\alpha)\boldsymbol{U}_2]\,\alpha\} = 0 \tag{A.5}$$

Now, we define a relative velocity between the two phase $\boldsymbol{U}_r$:

$$\boldsymbol{U}_r = \boldsymbol{U}_1 - \boldsymbol{U}_2 \tag{A.6}$$

Then we replace the velocity of phase 2 $\boldsymbol{U}_2$ with the relative velocity in Eq.(A.5):

$$\frac{\partial \alpha}{\partial t} + \nabla \cdot \{[\boldsymbol{U}_1 - (1-\alpha)\boldsymbol{U}_r]\,\alpha\} = 0 \tag{A.7}$$

If we rearrange the terms, we get:

$$\frac{\partial \alpha}{\partial t} + \nabla \cdot (\alpha \boldsymbol{U}_1) - \nabla \cdot [(1-\alpha)\alpha \boldsymbol{U}_r] = 0 \tag{A.8}$$

The first two terms on the left side of the Eq.(A.8) equals to zero according to the transport equation for phase 1, so the rest of the equation is :

$$\nabla \cdot [(1-\alpha)\alpha \boldsymbol{U}_r] = 0 \tag{A.9}$$

At last, we add Eq.(A.9) onto Eq.(A.1) and we can get the modified transport equation for volume fraction indicator:

$$\frac{\partial \alpha}{\partial t} + \nabla \cdot (\alpha \boldsymbol{U}) + \nabla \cdot [(1-\alpha)\alpha \boldsymbol{U}_r] = 0 \tag{A.10}$$

This modified equation with the an extra term depending on the velocity defined by Eq.(A.2) achieved a strong coupling between the classical VOF method and the two-fluid model. The additional term also contributes to a higher interface resolution without effecting the solution outside of the interface region.

Appendix B

Algorithm of the Sand-Sliding Mechanism

The sand-sliding mechanism used in the model established is the same with the one introduced by Jacobsen (2015). The details of algorithm is presented here. The two dimensional mesh in OpenFOAM® is actually a three dimensional mesh but not solved in a certain direction. So the sand-sliding mechanism works the same in both two and three dimensional simulations.

For a given face, the unit normal vector of the face is represented by $\boldsymbol{n}$ and it can be defined as:

$$\boldsymbol{n} = \boldsymbol{n}_h + \boldsymbol{n}_z \tag{B.1}$$

where $\boldsymbol{n}_h$ is the horizontal component and $\boldsymbol{n}_z$ is the vertical component of vector $\boldsymbol{n}$. We define also $\boldsymbol{e}_z$ the unit vector along the positive vertical direction.

Sand-sliding mechanism is used to restrict the bed slope to the critical bed slope, which is typically taken as the angle of repose ϕ_r. So the sand-sliding mechanism should find the faces on the bottom boundary of the mesh which have a slope angle larger than ϕ_r. That is the same as finding the face where $\boldsymbol{n} \cdot \boldsymbol{e}_z > \cos\phi_r$. And the desired vertical component of the unit normal vector after correction $\boldsymbol{n}'_z$ should be:

$$\boldsymbol{n}'_z = \cos\phi_r \boldsymbol{e}_z \tag{B.2}$$

Then the corresponding horizontal component after correction $\boldsymbol{n}'_h$ should be:

$$\boldsymbol{n}'_h = \sqrt{\frac{1-\cos^2\phi_r}{1-(\boldsymbol{n}\cdot\boldsymbol{e}_z)^2}}\boldsymbol{n}_h \tag{B.3}$$

This horizontal component corrected ensures that the normal vector after correction $\boldsymbol{n}'$ is still a unit vector and the steepest slope direction of the face corrected is the same before and after the sand-sliding mechanism. Physically, that means the sand will slide down along the steepest slope direction of the face. So the unit normal vector after correction $\boldsymbol{n}'$ should be:

$$\boldsymbol{n}' = \boldsymbol{n}'_h + \boldsymbol{n}'_z = \sqrt{\frac{1-\cos^2\phi_r}{1-(\boldsymbol{n}\cdot\boldsymbol{e}_z)^2}}\boldsymbol{n}_h + \cos\phi_r \boldsymbol{e}_z \tag{B.4}$$

The face needs correction should be rotated with its unit normal vector changes from $\boldsymbol{n}$ to $\boldsymbol{n}'$ around its face centre, which is represented by $\boldsymbol{P}_0$ and the the vertices of the face, which are mesh points, are represented by $\boldsymbol{P}_i$ where for hexahedral mesh (so the finite area mesh is quadrilateral mesh) $i = 1,2,3,4$. To simplify the calculation, two hypothesis are made here. First of all, for each mesh points, the displacement is only in the vertical direction but not in the horizontal direction. So if we define a unit vector $\boldsymbol{e}_h$, which is in the same direction of $\boldsymbol{n}_h$, then the value $(\boldsymbol{P}_i - \boldsymbol{P}_0)\cdot\boldsymbol{e}_h$ is constant. Secondly, the sand-sliding is considered to be instantaneous. As a result, considering the plane defined by $(\boldsymbol{P}_i - \boldsymbol{P}_0)\cdot\boldsymbol{n} = 0$, the vertical displacement for each points, Δh_{P_i}, can be calculated by:

$$\Delta h_{P_i} = \frac{(\boldsymbol{P_i} - \boldsymbol{P}_0)\cdot\boldsymbol{n}_h}{\boldsymbol{n}\cdot\boldsymbol{e}_z} - \frac{(\boldsymbol{P_i} - \boldsymbol{P}_0)\cdot\boldsymbol{n}'_h}{\boldsymbol{n}'\cdot\boldsymbol{e}_z} \tag{B.5}$$

As the mesh points only move in the vertical direction but not in the horizontal direction, the projected area of the face on horizontal plan is constant. So as long as the centre of the face does not move, the mass conservation of this face is satisfied. However, the displacements of the mesh points due to the sand-sliding mechanism influence not only the face corrected, but also the neighbour faces. If the finite area mesh is uniform in every direction, the mass conservation is still satisfied. Otherwise, the mass conservation error needs to be eliminated by extra correcting algorithms.

Consider a part of the finite area mesh where face f_0 with area A_0 needs to be corrected by sand-sliding mechanism. The neighbour faces and the areas of the neighbor faces are shown in Fig.(B.1).

If points P_2 and P_3 are displaced due to the sand-sliding mechanism, then face f_2, f_3, f_5, f_4, f_6, f_7 are all influenced. As the finite area mesh is not uniform, the areas of each surface are not same and therefore the mass conservation cannot be satisfied. In order to guarantee the conservation of the mass, the displacements of the mesh points Δh_{P_i} need to be corrected by:

$$\Delta h^{\star}_{P_i} = \Delta h_{P_i} - \frac{\sum_i \sum_{j\in S_{P_i}} A_j \Delta h_{P_i}}{\sum_i \sum_{j\in S_{P_i}} A_j} \tag{B.6}$$

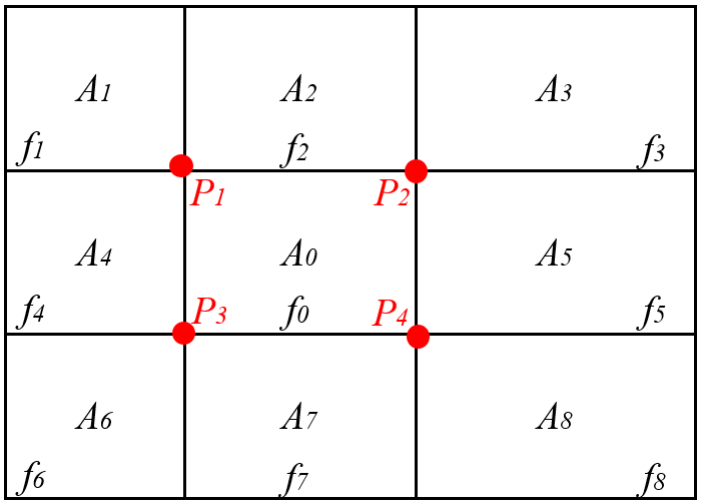

Fig. B.1 A part of finite area mesh with face f_0 needs correction of sand-sliding mechanism

where S_{P_i} represents all the faces contains point P_i except for the face being corrected.

Finally, the new positions of the mesh points on the face corrected by sand-sliding mechanism are given as:

$$P_i^\star = P_i + \Delta h_{P_i}^\star \boldsymbol{e}_z \tag{B.7}$$

Moreover, the correction of one face may cause the neighbour faces to exceed critical bed slope. So all neighbouring faces should also be tested after the correction. And if the neighbouring faces are corrected, the original face can also be effected. As a result, the sand-sliding mechanism will loop over all the faces on the finite area mesh as many times as necessary to guarantee that no faces have a bed slope larger than the critical value. This procedure can be slow as sometimes more than two hundred iterations are needed to finish the sand-sliding. However, no possible faster method has been found so far and as the finite area mesh is a two dimensional mesh which only contains the bottom boundary of the finite volume mesh, the number of surfaces needs to be checked is quite small. As a consequence, in most cases, the time consumed for sand-sliding mechanism in our model is acceptable.

References

Abdelaziz, S., Bui, M., and Rutschmann, P. (2010). Numerical simulation of scour development due to submerged horizontal jet. In *River Flow 2010. Proc. of the Intern. Conf. on Fluvial Hydraulics*, pages 1597–1604.

Aghaee, Y. and Hakimzadeh, H. (2010). Three dimensional numerical modeling of flow around bridge piers using les and rans. *River Flow, Dittrich, Koll, Aberle and Geisenhainer (eds)*, P(2010):211–218.

Aureli, F., Maranzoni, A., and Mignosa, P. (2004). Experimental modeling of rapidly varying flows on wet bed and in presence of submersible obstacles. In *River Flow*.

Balachandar, R., Kells, J., and Thiessen, R. (2000). The effect of tailwater depth on the dynamics of local scour. *Canadian Journal of Civil Engineering*, 27(1):138–150.

Baykal, C., Sumer, B. M., Fuhrman, D. R., Jacobsen, N. G., and Fredsøe, J. (2015). Numerical investigation of flow and scour around a vertical circular cylinder. *Philosophical Transactions of the Royal Society of London A: Mathematical, Physical and Engineering Sciences*, 373(2033):20140104.

Baykal, C., Sumer, B. M., Fuhrman, D. R., Jacobsen, N. G., and Fredsøe, J. (2017). Numerical simulation of scour and backfilling processes around a circular pile in waves. *Coastal Engineering*, 122:87–107.

Berberović, E., van Hinsberg, N. P., Jakirlić, S., Roisman, I. V., and Tropea, C. (2009). Drop impact onto a liquid layer of finite thickness: Dynamics of the cavity evolution. *Physical Review E*, 79(3):036306.

Blocken, B., Stathopoulos, T., and Carmeliet, J. (2007). CFD simulation of the atmospheric boundary layer: wall function problems. *Atmospheric environment*, 41(2):238–252.

Boroomand, M. R., Salehi Neyshabouri, S. A. A., and Aghajanloo, K. (2007). Numerical simulation of sediment transport and scouring by an offset jet. *Canadian Journal of Civil Engineering*, 34(10):1267–1275.

Breusers, H. (1965). *Conformity and time scale in two-dimensional local scour*. Waterloopkundig Laboratorium.

Breusers, H. (1967). Two-dimensional scour in loose sediments. *Publ. 64, Delft Hydraulics, Delft, The Netherlands*.

Breusers, H., Nicollet, G., and Shen, H. (1977). Local scour around cylindrical piers. *Journal of Hydraulic Research*, 15(3):211–252.

Brørs, B. (1999). Numerical modeling of flow and scour at pipelines. *Journal of Hydraulic Engineering*, 125(5):511–523.

Callaghan, D. P., Saint-Cast, F., Nielsen, P., and Baldock, T. E. (2006). Numerical solutions of the sediment conservation law; a review and improved formulation for coastal morphological modelling. *Coastal Engineering*, 53(7):557–571.

Camenen, B., Larson, M., and Bayram, A. (2009). Equivalent roughness height for plane bed under oscillatory flow. *Estuarine, Coastal and Shelf Science*, 81(3):409–422.

Carsons, M., Neilson, F. M., and Altinbilek, H. D. (1929). Bed forms generated in the laboratory under an oscillatory flow: Analytical and experimental study. Technical report, DTIC Document.

Cavar, D., Réthoré, P.-E., Bechmann, A., Sørensen, N. N., Martinez, B., Zahle, F., Berg, J., and Kelly, M. C. (2016). Comparison of openfoam and ellipsys3d for neutral atmospheric flow over complex terrain. *Wind Energy Science Discussions*.

Celik, I. and Rodi, W. (1991). Suspended sediment-transport capacity for open channel flow. *Journal of Hydraulic Engineering*, 117(2):191–204.

Çevik, E. and Yüksel, Y. (1999). Scour under submarine pipelines in waves in shoaling conditions. *Journal of waterway, port, coastal, and ocean engineering*, 125(1):9–19.

Chatterjee, S. S. and Ghosh, S. N. (1980). Submerged horizontal jet over erodible bed. *Journal of the Hydraulics Division*, 106(11):1765–1782.

Chatterjee, S. S., Ghosh, S. N., and Chatterjee, M. (1994). Local scour due to submerged horizontal jet. *Journal of Hydraulic Engineering*, 120(8):973–992.

Chen, X., Li, Y., Niu, X., Li, M., Chen, D., and Yu, X. (2011). A general two-phase turbulent flow model applied to the study of sediment transport in open channels. *International Journal of Multiphase Flow*, 37(9):1099–1108.

Engelund, F. and Fredsøe, J. (1976). A sediment transport model for straight alluvial channels. *Hydrology Research*, 7(5):293–306.

Faruque, M. A. A., Sarathi, P., and Balachandar, R. (2006). Clear water local scour by submerged three-dimensional wall jets: Effect of tailwater depth. *Journal of Hydraulic Engineering*, 132(6):575–580.

Fernandez Luque, R. and Van Beek, R. (1976). Erosion and transport of bed-load sediment. *Journal of hydraulic research*, 14(2):127–144.

Finn, J. R., Li, M., and Apte, S. V. (2016). Particle based modelling and simulation of natural sand dynamics in the wave bottom boundary layer. *Journal of Fluid Mechanics*, 796:340–385.

Fowler, J. E. (1992). Scour problems and methods for prediction of maximum scour at vertical seawalls. Technical report, DTIC Document.

Fredsøe, J. and Deigaard, R. (1992). *Mechanics of coastal sediment transport.*, volume 3. World scientific.

Fredsøe, J. and Sumer, B. M. (1997). Scour at the round head of a rubble-mound breakwater. *Coastal engineering*, 29(3):231–262.

Frisch, U. (1989). Lectures on turbulence and lattice gas hydrodynamics. *Lecture notes on turbulence*, page 219.

Fuhrman, D. R., Baykal, C., Sumer, B. M., Jacobsen, N. G., and Fredsøe, J. (2014). Numerical simulation of wave-induced scour and backfilling processes beneath submarine pipelines. *Coastal Engineering*, 94:10–22.

Gao, F.-P., Yang, B., Wu, Y.-X., and Yan, S.-M. (2006). Steady current induced seabed scour around a vibrating pipeline. *Applied Ocean Research*, 28(5):291–298.

García, M. H. and Parker, G. (1991). Entrainment of bed sediment into suspension. *Journal of Hydraulic Engineering*, 117(4):414–435.

Graftieaux, L., Michard, M., and Grosjean, N. (2001). Combining piv, pod and vortex identification algorithms for the study of unsteady turbulent swirling flows. *Measurement Science and Technology*, 12(9):1422.

Greaves, D. M. (2006). Simulation of viscous water column collapse using adapting hierarchical grids. *International Journal for Numerical Methods in Fluids*, 50(6):693–711.

Guo, J., Suaznabar, O., Shan, H., and Shen, J. (2012). Pier scour in clear-water conditions with non-uniform bed materials (no. fhwa-hrt-12-022). Technical report, Turner-Fairbank Highway Research Center (TFHRC).

Hassanzadeh, Y. (2012). *Hydraulics of sediment transport*. INTECH Open Access Publisher.

Hirt, C. W. and Nichols, B. D. (1981). Volume of fluid (vof) method for the dynamics of free boundaries. *Journal of computational physics*, 39(1):201–225.

Hoffmans, G. J. and Verheij, H. (1997). *Scour manual*, volume 96. CRC Press.

Hughes, S. A. and Kamphuis, J. W. (1996). Scour at coastal inlet structures. *Coastal Engineering Proceedings*, 1(25).

Irie, I., Kuriyama, Y., and Asakura, H. (1986). Study on scour in front of breakwaters by standing waves and protection methods. *Report of the Port and Harbour Research Institute*, 25(1):3–86.

Irie, I. and Nadaoka, K. (1984). Laboratory reproduction of seabed scour in front of breakwaters. *Coastal Engineering Proceedings*, 1(19).

Issa, R. I. (1986). Solution of the implicitly discretised fluid flow equations by operator-splitting. *Journal of computational physics*, 62(1):40–65.

Jacobsen, N. G. (2011). *A full hydro-and morphodynamic description of breaker bar development*. PhD thesis, DTU Mechanical Engineering.

Jacobsen, N. G. (2015). Mass conservation in computational morphodynamics: uniform sediment and infinite availability. *International Journal for Numerical Methods in Fluids*, 78(4):233–256.

Jacobsen, N. G., Fredsoe, J., and Jensen, J. H. (2014). Formation and development of a breaker bar under regular waves. part 1: Model description and hydrodynamics. *Coastal Engineering*, 88:182–193.

Jasak, H. (1996). *Error analysis and estimation for the finite volume method with applications to fluid flows*. PhD thesis, Imperial College London (University of London).

Jasak, H. (2012). Handling parallelisation in openfoam. In *Cyprus Advanced HPC Workshop*, volume 101.

Jasak, H. and Tukovic, Z. (2006). Automatic mesh motion for the unstructured finite volume method. *Transactions of FAMENA*, 30(2):1–20.

Jensen, J. H., Madsen, E. s., and Fredsøe, J. (1999). Oblique flow over dredged channels. ii: Sediment transport and morphology. *Journal of Hydraulic Engineering*, 125(11):1190–1198.

Jha, S. K. and Bombardelli, F. A. (2010). Toward two-phase flow modeling of nondilute sediment transport in open channels. *Journal of Geophysical Research: Earth Surface*, 115(F3).

Johnson, H. K. and Zyserman, J. A. (2002). Controlling spatial oscillations in bed level update schemes. *Coastal Engineering*, 46(2):109–126.

Khosronejad, A., Kang, S., Borazjani, I., and Sotiropoulos, F. (2011). Curvilinear immersed boundary method for simulating coupled flow and bed morphodynamic interactions due to sediment transport phenomena. *Advances in water resources*, 34(7):829–843.

Khosronejad, A., Kang, S., and Sotiropoulos, F. (2012). Experimental and computational investigation of local scour around bridge piers. *Advances in Water Resources*, 37:73–85.

Kjeldsen, S., Gjorsvik, O., Bringaker, K., and Jacobsen, J. (1973). Local scour near offshore pipelines. In *Proceedings of the Second International Conference on Port and Ocean Engineering Under Arctic Conditions (POAC), August 27-30, 1973*.

Koshizuka, S. (1995). A particle method for incompressible viscous flow with fluid fragmentation. *Comput. Fluid Dynamics J.*, 4:29–46.

Kothyari, U., Ranga Raju, K., and Garde, R. (1992). Live-bed scour around cylindrical bridge piers. *Journal of Hydraulic Research*, 30(5):701–715.

Kraus, N. C. (1988). The effects of seawalls on the beach: an extended literature review. *Journal of coastal Research*, pages 1–28.

Larsen, B. E., Fuhrman, D. R., and Sumer, B. M. (2016). Simulation of wave-plus-current scour beneath submarine pipelines. *Journal of Waterway, Port, Coastal, and Ocean Engineering*, 142(5):04016003.

Launay, G., Riviere, N., and Mignot, E. (2015). Interaction entre un écoulement à surface libre et un obstacle émergent: Étude expérimentale de la structure du tourbillon en fer à cheval. *S27 Turbulence*.

Launder, B. E. and Spalding, D. B. (1974). The numerical computation of turbulent flows. *Computer methods in applied mechanics and engineering*, 3(2):269–289.

Li, M., Pan, S., and O'Connor, B. A. (2008). A two-phase numerical model for sediment transport prediction under oscillatory sheet flows. *Coastal Engineering*, 55(12):1159–1173.

Li, Y., Kelly, D. M., Li, M., and Harris, J. M. (2014). Development of a new 3d euler-lagrange model for the prediction of scour around offshore structures. *Coastal Engineering Proceedings*, 1(34):31.

Liang, D., Cheng, L., and Li, F. (2005a). Numerical modeling of flow and scour below a pipeline in currents: Part i. flow simulation. *Coastal engineering*, 52(1):25–42.

Liang, D., Cheng, L., and Li, F. (2005b). Numerical modeling of flow and scour below a pipeline in currents: Part ii. scour simulation. *Coastal engineering*, 52(1):43–62.

Lillycrop, W. J. and Hughes, S. A. (1993). Scour hole problems experienced by the corps of engineers; data presentation and summary. Technical report, DTIC Document.

Lim, S.-Y. (1997). Equilibrium clear-water scour around an abutment. *Journal of Hydraulic Engineering*, 123(3):237–243.

Liu, X. (2008). *Numerical Models for Scour and Liquefaction around Object under Currents and Waves*. PhD thesis, University of Illinois at Urbana and Champaign.

Liu, X. and García, M. H. (2008). Three-dimensional numerical model with free water surface and mesh deformation for local sediment scour. *Journal of waterway, port, coastal, and ocean engineering*, 134(4):203–217.

Liu, X., Osher, S., and Chan, T. (1994). Weighted essentially non-oscillatory schemes. *Journal of computational physics*, 115(1):200–212.

Lofquist, K. E. (1986). Drag on naturally rippled beds under oscillatory flows. Technical report, DTIC Document.

Lopes, P. (2013). *Free-surface flow interface and air-entrainment modelling using OpenFOAM*. PhD thesis, University of Coimbra.

Marieu, V., Bonneton, P., Foster, D., and Ardhuin, F. (2008). Modeling of vortex ripple morphodynamics. *Journal of Geophysical Research: Oceans*, 113(C9).

Martinez, B. (2011). Wind resource in complex terrain with openfoam. *Risø DTU, National Laboratory for Sustainable Energy*.

Melville, B. and Sutherland, A. (1988). Design method for local scour at bridge piers. *Journal of Hydraulic Engineering*, 114(10):1210–1226.

Melville, B. W. (1997). Pier and abutment scour: integrated approach. *Journal of Hydraulic Engineering*, 123(2):125–136.

Melville, B. W. and Coleman, S. E. (2000). *Bridge scour*. Water Resources Publication.

Menter, F. (1992). Influence of freestream values on k-omega turbulence model predictions. *AIAA journal*, 30(6):1657–1659.

Menter, F. and Esch, T. (2001). Elements of industrial heat transfer predictions. In *16th Brazilian Congress of Mechanical Engineering (COBEM)*, volume 109.

Menter, F., Kuntz, M., and Langtry, R. (2003). Ten years of industrial experience with the sst turbulence model. *Turbulence, heat and mass transfer*, 4(1):625–632.

Miller, M., McCave, I., and Komar, P. (1977). Threshold of sediment motion under unidirectional currents. *Sedimentology*, 24(4):507–527.

Moncada-M, A. T. and Aguirre-Pe, J. (1999). Scour below pipeline in river crossings. *Journal of Hydraulic Engineering*, 125(9):953–958.

Nielsen, P. (1992). *Coastal bottom boundary layers and sediment transport*, volume 4. World scientific.

Niemann, S., Fredsøe, J., and Jacobsen, N. G. (2011). Sand dunes in steady flow at low froude numbers: Dune height evolution and flow resistance. *Journal of Hydraulic Engineering (new York)*.

Nikuradse, J. (1933). Laws of flow in rough pipes. In *VDI Forschungsheft*. Citeseer.

Orszag, S. A. (1970). Analytical theories of turbulence. *Journal of Fluid Mechanics*, 41(02):363–386.

Oscar, L., Pfleger, F., and Zanke, U. (2008). Characteristics of developing scour-holes at a sand-embedded cylinder. *International Journal of Sediment Research*, 23(3):258–266.

Patankar, S. V. and Spalding, D. B. (1972). A calculation procedure for heat, mass and momentum transfer in three-dimensional parabolic flows. *International journal of heat and mass transfer*, 15(10):1787–1806.

Pješivac-Grbović, J., Angskun, T., Bosilca, G., Fagg, G. E., Gabriel, E., and Dongarra, J. J. (2007). Performance analysis of mpi collective operations. *Cluster Computing*, 10(2):127–143.

Preiss, B. R. (2008). *Data structures and algorithms with object-oriented design patterns in C++*. John Wiley & Sons.

Rahman, M. M. and Haque, M. A. (2003). Local scour estimation at bridge site: modification and application of lacey formula. *International Journal of Sediment Research*, 18(4):333–339.

Rance, P. (1980). The potential for scour around large objects. *Scour Prevention Techniques Around Offshore Structures*, pages 41–53.

Raudkivi, A. J. (1998). *Loose boundary hydraulics*. CRC Press.

Ribberink, J. S. (1998). Bed-load transport for steady flows and unsteady oscillatory flows. *Coastal Engineering*, 34(1):59–82.

Richardson, J. and Zaki, W. (1997). Sedimentation and fluidisation: Part i. *Chemical Engineering Research and Design*, 75:S82–S100.

Rijn, L. C. v. (1984). Sediment transport, part ii: suspended load transport. *Journal of hydraulic engineering*, 110(11):1613–1641.

Roca, M., Martín-Vide, J. P., and Blanckaert, K. (2007). Reduction of bend scour by an outer bank footing: Footing design and bed topography. *Journal of Hydraulic Engineering*, 133(2):139–147.

Roulund, A., Sumer, B. M., Fredsøe, J., and Michelsen, J. (2005). Numerical and experimental investigation of flow and scour around a circular pile. *Journal of Fluid Mechanics*, 534:351–401.

Rusche, H. (2002). *Computational fluid dynamics of dispersed two-phase flows at high phase fractions.* PhD thesis, Imperial College London (University of London).

Sarathi, P., Faruque, M. A. A., and Balachandar, R. (2008). Influence of tailwater depth, sediment size and densimetric froude number on scour by submerged square wall jets. *Journal of Hydraulic Research*, 46(2):158–175.

Schields, A. (1936). Application of similarity mechanics and turbulence research for bed-load transport. *Mitt. der Preussischen Versuchsanstalt für Wasserbau und Schiffbau, Berlin*.

Soulsby, R. (1997). *Dynamics of marine sands: a manual for practical applications*. Thomas Telford.

Soulsby, R. L. (1993). The reference concentration for suspended sand in a steady current. In *Proc. of MAST-II G8 Coast. Morphodyn. Overall Workshop*.

Sousa, J. and Bastos, L. (2013). Multi-temporal sar interferometry reveals acceleration of bridge sinking before collapse. *Natural Hazards and Earth System Sciences*, 13(3):659.

Sui, J., Faruque, M. A. A., and Balachandar, R. (2008). Influence of channel width and tailwater depth on local scour caused by square jets. *Journal of Hydro-environment Research*, 2(1):39–45.

Sumer, B. M., Christiansen, N., and Fredsøe, J. (1997). The horseshoe vortex and vortex shedding around a vertical wall-mounted cylinder exposed to waves. *Journal of Fluid Mechanics*, 332:41–70.

Sumer, B. M., Chua, L. H., Cheng, N.-S., and Fredsøe, J. (2003). Influence of turbulence on bed load sediment transport. *Journal of Hydraulic Engineering*, 129(8):585–596.

Sumer, B. M. and Fredsøe, J. (1990). Scour below pipelines in waves. *Journal of waterway, port, coastal, and ocean engineering*, 116(3):307–323.

Sumer, B. M. and Fredsøe, J. (1997). Scour at the head of a vertical-wall breakwater. *Coastal Engineering*, 29(3):201–230.

Sumer, B. M. and Fredsøe, J. (1998). Wave scour around group of vertical piles. *Journal of waterway, port, coastal, and ocean engineering*, 124(5):248–256.

Sumer, B. M. and Fredsøe, J. (2001a). Scour around pile in combined waves and current. *Journal of Hydraulic Engineering*, 127(5):403–411.

Sumer, B. M. and Fredsøe, J. (2001b). Wave scour around a large vertical circular cylinder. *Journal of waterway, port, coastal, and ocean engineering*, 127(3):125–134.

Sumer, B. M. and Fredsøe, J. (2002). *The mechanics of scour in the marine environment*. World Scientific.

Sumer, B. M., Mao, Y., and Fredsøe, J. (1988). Interaction between vibrating pipe and erodible bed. *Journal of Waterway, Port, Coastal, and Ocean Engineering*, 114(1):81–92.

Sumer, B. M., Petersen, T. U., Locatelli, L., Fredsøe, J., Musumeci, R. E., and Foti, E. (2012). Backfilling of a scour hole around a pile in waves and current. *Journal of Waterway, Port, Coastal, and Ocean Engineering*, 139(1):9–23.

Sun, R. and Xiao, H. (2016). Sedifoam: A general-purpose, open-source cfd–dem solver for particle-laden flow with emphasis on sediment transport. *Computers & Geosciences*, 89:207–219.

Tsai, C.-H. and Tsai, C.-T. (2000). Velocity and concentration distributions of sediment-laden open channel flow1. *JAWRA Journal of the American Water Resources Association*, 36(5):1075–1086.

Tukovic, Z. and Jasak, H. (2008). Simulation of free-rising bubble with soluble surfactant using moving mesh finite volume/area method. In *Proceedings of 6th International Conference on CFD in Oil & Gas, Metallurgical and Process Industries, no. CFD08-072*.

Ubbink, O. (1997a). *Numerical prediction of two fluid systems with sharp interfaces*. PhD thesis, University of London.

Ubbink, O. (1997b). *Numerical prediction of two fluid systems with sharp interfaces*. PhD thesis, University of London.

van Rijn, L. C. (1986). Mathematical modeling of suspended sediment in nonuniform flows. *Journal of Hydraulic Engineering*, 112(6):433–455.

Van Rijn, L. C. (1987). *Mathematical modelling of morphological processes in the case of suspended sediment transport*. Waterloopkundig Laboratorium Delft.

van Rijn, L. C. (2005). *Principles of sedimentation and erosion engineering in rivers, estuaries and coastal seas including mathematical modelling package (toolkit on CD-ROM)*. Aqua Publications.

van Rijn, L. C. (2013). Local scour near structures. *Taken from: www. leovanrijnsediment. com*.

Wang, S. and Jia, Y. (1999). Computational simulations of local scour at bridge crossings and limitations. In *Proc. of international water resources engineering conference*, pages Session BS–06.

Weller, H. (2002). Derivation, modelling and solution of the conditionally averaged two-phase flow equations. *Nabla Ltd, No Technical Report TR/HGW/02*.

Whitehouse, R. (1998). *Scour at marine structures: A manual for practical applications*. Thomas Telford.

Zhou, L. and Perkins, R. J. (2016). Numerical modelling of scour – the influence of small scale morphological processes. In *River Sedimentation: Proceedings of the 13th International Symposium on River Sedimentation*, pages 528–535.

Zyserman, J. and Fredsøe, J. (1988). Numerical simulation of concentration profiles of suspended sediment under irregular waves. *Institute of Hydrodynamics and Hydraulic Engineering, Technical University of Denmark, Progress Report*, 68:15–26.